

APPLIED RADAR METEOROLOGY

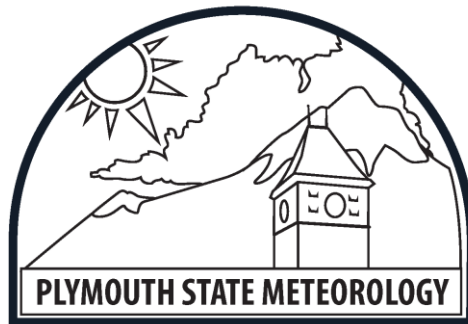
by

Sam Miller

AMS Certified Consulting Meteorologist

Professor of Meteorology

Plymouth State University



With contributions from:

Stephen Baron, Jason Cordeira, Christopher Hohman, Bryan Rand, and Abbie Small

Plymouth State University

Alex Jacques

University of Utah

Paul Johnston

University of Colorado Cooperative Institute for Research in Environmental Sciences

NOAA Earth System Research Laboratory, Physical Sciences Division

and

Phil Poyner and Dan St. Jean

NOAA National Weather Service

This text is dedicated to weather forecasters everywhere.

This work is licensed as an Open Educational Resource under the Creative Commons. Others may distribute, remix, adapt, and build upon this work, as long as they credit the authors.



Acknowledgments

We send our sincere thanks to:

- Justin Arnott, Science and Operations Officer at the Gray, Maine WFO (NOAA/National Weather Service), for his assistance in pulling together some of the materials for this text.
- Allen White (of NOAA's Earth System Research Laboratory, Physical Sciences Division) and our current and former colleagues in the Plymouth State University Meteorology Program - Lourdes Avilés, Eric Hoffman, Eric Kelsey, and Brendon Hoch - for their input and assistance with the Snow Level Radar.

And most of all, to our students in the Plymouth State University Meteorology Program.

Table of Contents

<i>Dedication and Creative Commons License</i>	2
<i>Acknowledgments</i>	3
<i>Preface</i>	5
<i>A note about units</i>	7
1. Historical overview of U.S. weather radar	8
2. Properties of electromagnetic radiation	22
3. The WSR-88D Radar Data Acquisition module and archive Level I data	38
4. The rest of the WSR-88D system, the Doppler Dilemma, and the production of Level II data	63
5. Velocity field interpretation	94
6. Dual-wavelength and dual-polarization variables and products	118
7. Level III derived products	149
8. Radar estimates of precipitation	203
9. More weather radar systems	230
10. The future of weather radar	263
<i>Appendix 1: Current WSR-88D and TDWR systems in the United States</i>	280
<i>Appendix 2: Forecasting skill</i>	283
<i>Appendix 3: Visualizing radar data with IDV and GR2Analyst</i>	288
<i>References</i>	322
<i>Index</i>	335
<i>About the Author</i>	342

Preface

S. Miller

This is a textbook focused on operational and other aspects of applied radar meteorology. Its primary purpose is to serve as a text for upper-level undergraduates and graduate students studying meteorology, who wish to work as professional operational meteorologists in the U.S. National Weather Service or the Air Force Weather Agency. In addition to a detailed description of operational weather radar systems operating in the United States, this text also provides a brief historical overview of the subject as well as a basic review of the physics of electromagnetic radiation and other theoretical aspects of weather radar. The last two chapters discuss a sample of other radar systems (such as the Doppler on Wheels and the Canadian and European operational networks), and future directions of weather radar, including its use as an input for high-resolution, rapid refresh computer models.

I attended the National Weather Service's radar course in Norman, Oklahoma, in 2005, shortly before joining the meteorology faculty at Plymouth State, and when originally asked to develop a radar course, I began with the materials I obtained when taking the NWS course. I added additional materials from Rinehart's (2004) text, as well as from many other sources. Over 14 years of teaching the course, I gradually added updated and supplementary materials to account for the dual-polarization retrofit to the WSR-88D network, and other advances in weather radar. By 2019, it was past time for a complete overhaul of the course, and so I began the careful process of researching recent material on meteorological applications of radar. This text is the result of that work.

Chapter 1 begins with a brief history of radar, focusing on the origins of the current United States operational weather radar systems. Chapter 2 is a review of the basic properties of electromagnetic radiation. Chapter 3 introduces the Weather Surveillance Radar - 1988 Doppler (WSR-88D) system and the production of Level I base moments. Chapter 4 completes the description of the WSRs, and explains the Doppler Dilemma and the production of Level II data. Chapter 5 is a tutorial on interpreting radial velocity fields. Chapter 6 describes the dual-polarization retrofit of the WSR system and introduces dual-pol variables and products. Chapter 7 contains an overview of Level III derived products, such as the Mesocyclone Detection Algorithm. Chapter 8 discusses WSR-88D precipitation estimates, both before and after the dual-polarization

retrofit. Chapter 9 describes a few other types of weather radar, such as the Center for Severe Weather Research's Doppler on Wheels, the FAA's Terminal Doppler Weather Radar, and operational weather radar networks in other countries. Finally, Chapter 10 explores weather radar in the near future, including its use as an input for high-resolution, rapid refresh computer models used as tools during severe weather outbreaks. Each chapter includes a list of key terms and concepts, as well as study prompts to help students review the contents of the chapter.

A note about units

The literature about weather radar goes back many decades. In the early papers, a combination of British Imperial and nautical units were used for length and speed measurements. In more recent publications, SI units have been generally (but not universally) adopted. For that reason, this book uses a sometimes awkward combination of all these measurement systems. In most cases, if the older unit is used to describe something, the conversion to the equivalent SI unit is also provided.

The following conversions are used here:

1 nautical mile	1.1508 statute miles
	6076.12 feet
	1852 meters (1.852 kilometers)

1 knot	1 nautical mile per hour
	1.1508 statute miles per hour
	1.852 kilometers per hour
	0.5144 meters per second

1. Historical overview of U.S. weather radar.

With contributions from Abbie Small

This chapter starts with some early discoveries which make radar possible, proceeds through a sample of early radar systems from WWII through the 1970s, and ends with a description of the present state-of-the-art operational weather radar systems in the United States.

1.1. The 19th Century.

1.1.1. Christian Andreas Doppler (Austrian mathematician and physicist): In 1842, Doppler first described the observed frequency shift of light (and sound) that results when a source is moving with respect to the observer (Rinehart 2004). This was independently discovered by French physicist H. Louis Fizeau, who also formalized the mathematical theorem for the effect (Houdas 1991). The Doppler Effect is described in more detail in Chapter 2.

1.1.2. James Clerk Maxwell (Scottish physicist): In 1865, Maxwell showed that electrical and magnetic fields travel through space as “waves,” moving at the speed of light. He also proposed that light can be described as a wave in the same “medium.” This was his classical theory of electromagnetic radiation, unifying electricity, magnetism, and radiation as different manifestations of the same thing (Maxwell 1864). This is discussed in greater detail in Chapter 2.

1.1.3. Heinrich Rudolf Hertz (German physicist): In 1886, Hertz determined that an electric current swinging rapidly back and forth in a conducting wire would cause the wire to emit electromagnetic radiation (EMR). He is also known for *proving* the existence of electromagnetic waves, which had been proposed by James Clerk Maxwell (O’Connor and Robertson 2007). EMR emission by a dipole antenna is described further in Chapter 2.

1.1.4. Guglielmo Marconi (Italian electrical engineer): In the early 1890s, Marconi developed a system for the practical transmission and reception of radio waves, or “wireless” systems. By the end of the decade, he was able to transmit and receive

signals over a distance of more than 60 nautical miles, and by 1902 he was able to transmit and receive signals over more than 1,500 miles (public domain sources).

1.2. **Into the 20th Century.** In 1904, the first radar-like device was patented by German inventor and physicist Christian Hülsmeyer, based on the published work of Heinrich Hertz. Hülsmeyer's device, called a "telemobiloscope," transmitted pulses of EMR generated using a spark gap, and listened for its own back-scattered radiation, but was unable to directly measure the range to a given target (*e.g.* Wiesbeck *et al.* 2015).

Eighteen years later in the United States, electrical engineers Albert Taylor and Leo Young were testing wireless radio for the Navy, with the transmitter and receiver on opposite sides of the Potomac River. A wooden steamship, the *Dorchester*, sailed up the river, temporarily attenuating the signal strength at the receiver. Realizing that such a system could be used to remotely detect the presence of enemy vessels, they proposed establishing an "electromagnetic curtain" in the nation's coastal rivers and seaports but received no response from the Navy (Rinehart 2004; Parry 2010).

1.2.1. The next year the Naval Research Laboratory was established with Taylor appointed the head of the radio division. In the early 1930s, Taylor and Young realized that a single antenna could be used as both transmitter and receiver, provided a "duplexer" (switch) was added to toggle the system between modes. (The same idea had also occurred to German and Russian engineers working on the same problem.) In 1934, they constructed a system that was able to detect the location of an aircraft at a distance of one mile. By 1937, Taylor, Young, and their team had developed a practical system for detecting aircraft from naval vessels (Parry 2010).

1.2.2. The term RADAR was created by the Navy in 1940 as an acronym for RAdio Detection And Ranging *or* RAdio Direction And Ranging. The word "radar" has since entered English and other languages as a common noun, losing its capitalization (Lapedes 1976).

1.3. Prior to and during World War Two, radar was simultaneously under development in several countries (Rinehart 2004; Wiesbeck *et al.* 2015)¹. These countries fell into several categories:

¹ A highly entertaining (and detailed) insider's story of radar development during the last years of WWII, written by J. Fletcher (a pilot and radar researcher of the period), can be found in Atlas (1990).

- The *Western Allies*, consisting of the United States, Great Britain, France, and Holland (although the latter two dropped out of the effort early in the war)
- The *Axis Powers*, consisting of Germany, Italy, and Japan.
- *Other countries*, including the Soviet Union, Australia, Canada, New Zealand, South Africa and Hungary.

1.3.1. Robert Alexander Watson-Watt (Scottish physicist) was a key figure in the British Met Office (and a Fellow of the Royal Meteorological Society), who worked with the British Air Ministry to develop aircraft-detecting radar. He is also known for using radio devices to detect lightning, and for naming the ionosphere (Rinehart 2004; Whiten *et al.* 1998).

1.3.2. In 1940, John Randall and Henry Boot (English physicists), at the University of Birmingham (England), invented the cavity magnetron transmitter tube (an improvement on an earlier design), making it possible to construct relatively light-weight radar devices, which could be mounted on trucks and operated at higher microwave frequencies, making them more accurate (Rinehart 2004). It also significantly increased the transmitted power of the radar at 10 cm wavelengths. Another type of transmitter tube, called a klystron, was invented in 1937 by Russell and Sigurd Varian (Pond 2008).

1.3.3. Also in 1940, J.W. Ryde of the General Electric Corporation Research Laboratory, in Wembley, England, investigated returned power from clouds and precipitation in radar displays, when backscattered EMR from weather targets was considered “clutter” (noise) that obscured the targets of interest (aircraft) (Rinehart 2004; Whiten *et al.* 1998). Weather clutter is visible in the right-hand image in Figure 1.1 (below).

1.3.4. In 1944, the APQ-13 radar system was jointly developed by Bell Telephone Laboratories and the Massachusetts Institute of Technology (MIT), to help guide bombing and assist with aircraft navigation (Whiten *et al.* 1998). It was an X-band (~3 cm wavelength) radar, and highly sensitive to precipitation echoes. It was later adapted as an early ground-based weather radar, and a network of these systems was fielded as the first system for storm detection (Whiten *et al.* 1998; Swingle 1990). While it was replaced by the National Weather Service (then called the Weather Bureau) in 1946, it

remained one of the USAF's base weather radar systems until the AN/FPS-77 system was deployed in the 1960s. The last of these remained in operation until October, 1977 (Small 2005; Whiten *et al.* 1998). (See Figure 1.1.)

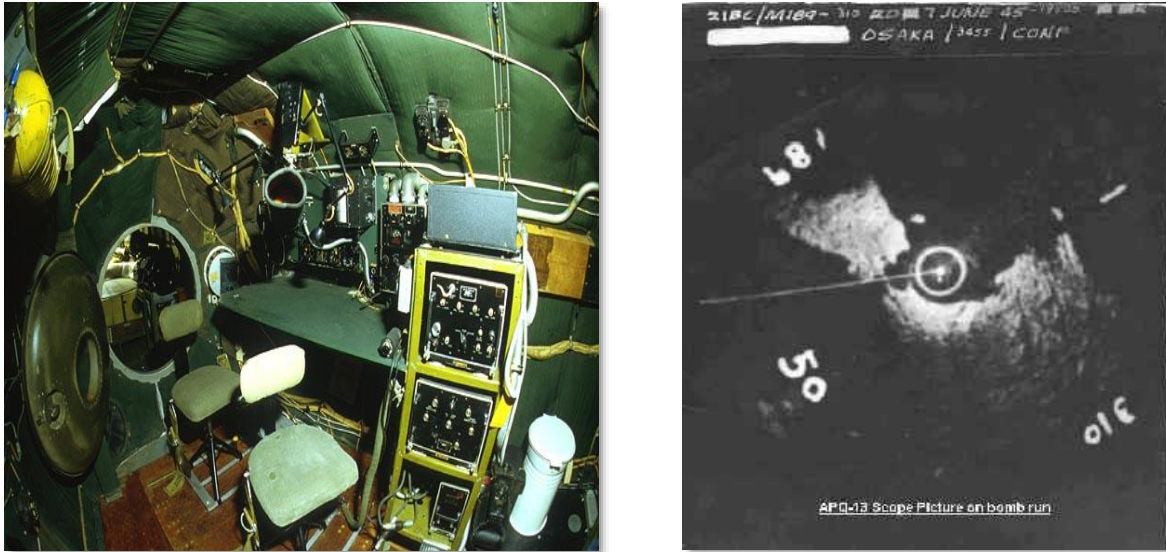


Fig. 1.1. APQ-13 radar. Left: Display/control console. Right: Image from screen. (Credits: Small 2005.)

1.4. After World War Two, surplus radar equipment became available for experimentation by civilians. Studies conducted during the last three years of the war at MIT's Radiation Laboratory had determined that "weather" could be detected by C- and S-band radars out to a range of 150 miles (Whiten *et al.* 1998; Katz and Henry 1990). Work began to examine the kinds of information that could be extracted from what had previously been thought of as noise.

1.4.1. In 1946, the National Weather Service obtained 25 S-band AN/APS-2F radars from the United States Navy, and began modifying them for meteorological use. Modifications included equipping them with larger antennas, and adding a converter that allowed them to run on conventional power systems. The modified radars (the first of which was installed at Washington National Airport in 1947) were renamed WSR-1, WSR-1A, WSR-3, and WSR-4, depending on the year of deployment and minor variations in design (Whiten *et al.* 1998). The invention of semiconductors (transistors) in the late 1940s and early 1950s was immediately useful, and increased the reliability of radar systems.

1.4.2. The first radar system specifically designed for weather purposes was the AN/CPS-9 (1954), designed by the U.S. Army Signal Corp and built by Raytheon (which would later build the WSR-57 and the Federal Aviation Administration's Terminal Doppler Weather Radar). It was an X-band (3 cm wavelength) system, with a beamwidth of 1° , and transmitted pulses of both $5 \mu\text{s}$ and $0.5 \mu\text{s}$ in duration. The choice to make it an X-band, rather than an S-band (which is less prone to attenuation by precipitation), was made to make the overall system reasonably portable and to contain costs. The first was installed at Maxwell AFB, Alabama in 1954, and the last remained in operation until 1984 (Small 2005; Whiten *et al.* 1998). (See Figure 1.2.)

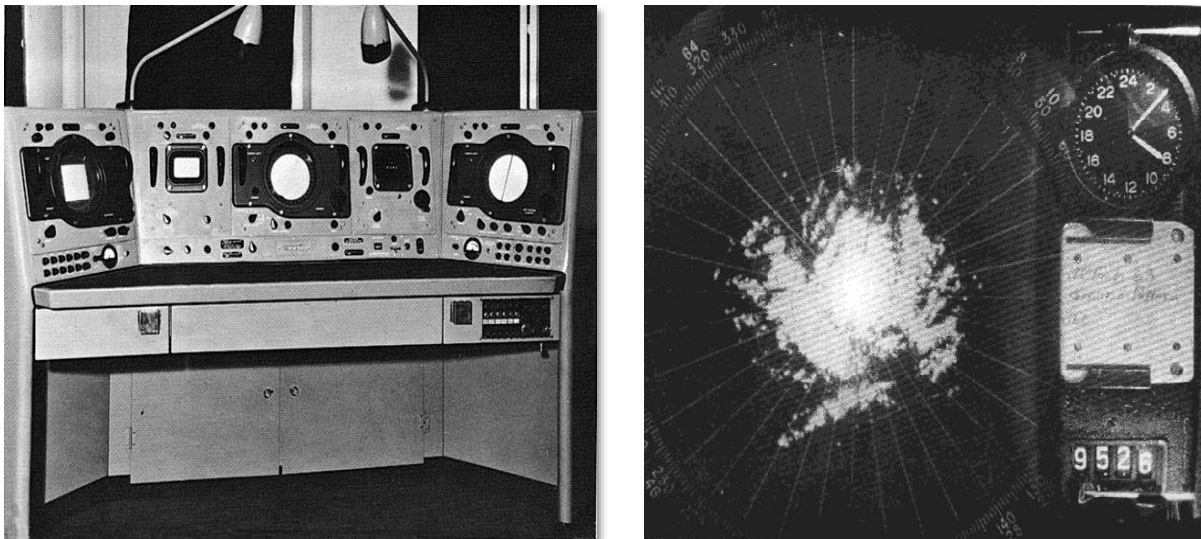


Fig. 1.2. CPS-9 radar. Left: Display/control console. Right: Image from screen. (Credits: Small 2005; Whiten *et al.* 1998.)

1.4.3. A later generation of operational weather radar was called Weather Surveillance Radar 1957 (WSR-57), originally built by Raytheon in 1957 to track hurricanes for the National Hurricane Center. It remained the primary civilian weather radar system in the United States for more than 35 years. It was an S-band (10.3 cm wavelength) system, and had a beamwidth of 2° . It also had a backup power system, and a "repeater PPI display." The acronym PPI means Plan Position Indicator, which is the name given to a "plan view" display of reflectivity. The repeater was used for Polaroid or 35-mm photographs of the radar display. (Thousands of feet of film of these displays are available at the National Centers for Environmental Information.) The first

of these systems was installed in Miami, Florida, in June, 1959, and the last remained in use until December, 1996 (Small 2005; Whiten *et al.* 1998). (See Figure 1.3.)

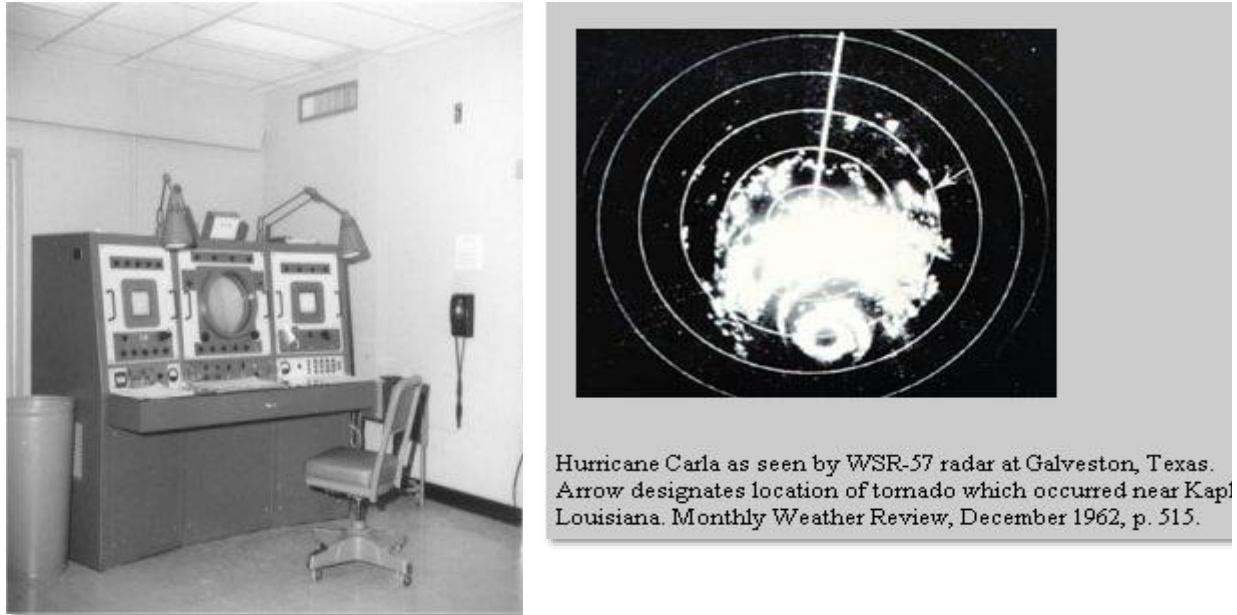


Fig. 1.3. WSR-57 radar. Left: Display/control console. Right: Image from screen. (Credits: Small 2005.)

1.4.4. In the early days, the cost of purchasing a radar system made it prohibitively expensive for all except government agencies, but remote displays (such as the WSR-57's repeater PPI display) which showed output from an existing radar site were more affordable, and installed in airline weather centers (Whiten *et al.* 1998).

By the 1960s, improvements in the manufacturing of all components of radar (transmitters, receivers, control systems and information displays) made them lightweight and affordable enough to be installed in non-government aircraft, such as commercial airliners. Some of these were later adapted for use in ground-based installations. By the late 1960s, commercial television stations in different parts of the United States were purchasing their own small X-band radar systems, for use in weather broadcasts (Whiten *et al.* 1998).

1.4.5. The U.S. Air Force developed its own radar system in 1964, called the AN/FPS-77, to replace the aging fleet of AN/APQ-13s and CPS-9s. This system was a C-band radar (wavelength 5.4 cm), and remained in use through the 1980s. The first unit was installed at Griffiss AFB, New York, in 1964, and by 1969, the network of more

than 100 sites was nearly complete. Like all previous radar systems, it was analog and manually operated. Images were “painted” on a screen, and archived using a Polaroid camera (Small 2005; Whiten *et al.* 1998). (See Figure 1.4.)

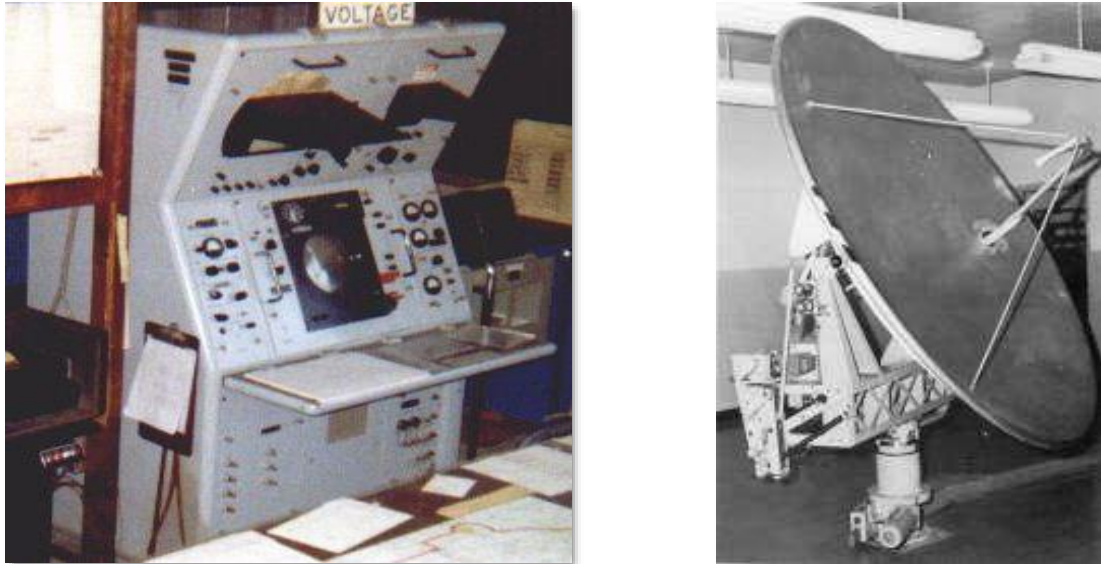


Fig. 1.4: FPS-77 Radar. Left: Control/Display console. Right: Antenna. This radar was entirely manually operated and contained more than 200 vacuum tubes. The round screen at the bottom was used for creating plan-view images of reflectivity, called Plan-Position Indication (PPI) images. The smaller screen to the upper left was used to create profile-view cross-sections of a reflectivity center, called Range Height Indicator (RHI) images. (Photo credit <http://www.radartutorial.eu/19.kartei/11.ancient/karte166.en.html>)

1.5. By the late 1970s, the United States weather radar network had become an uneven patchwork of several legacy systems. Some were quite old and unreliable, although the NWS had added a handful of newer systems (such as the WSR-74C and WSR-74S) to fill in the coverage gaps in the existing network. All required manual operation by a human technician, and none took advantage of advances in computer technology. Then, a spectacular series of unwarned convective events occurred during radar outages, resulting in loss of life and property damage, which motivated the U.S. government to commission an entirely new system.

1.5.1. In 1981, the Next-Generation Radar (NEXRAD) program office was established, and began coordination for the development and construction of the new Weather Surveillance Radar - 1988 Doppler (WSR-88D) network. In 1988, the first

WSR-88D was delivered to Norman, OK, and by 1996, the network was fully installed (WDTB 2005). A general description of the system included:

- It was an S-band system, with a wavelength of 10.3 cm.
- It was natively Doppler-capable, enabling the system to detect the radial velocity (V_r) of a meteorological target. Previous systems did not have this ability.
- It was entirely digital and computer controlled. Human beings could send the radar system special commands, but these were still interpreted and carried out by computers.
- Data produced by the system were archived as digital data on computer hard drives, and could be easily recalled using many different platforms.

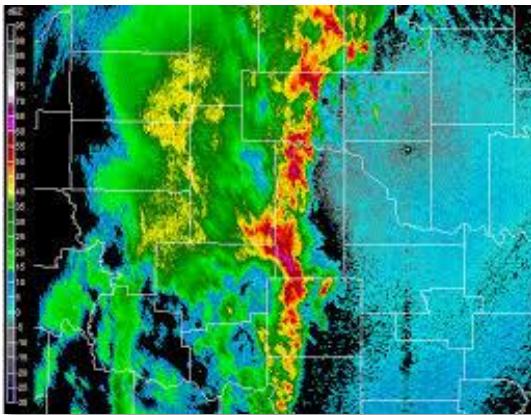


Fig. 1.5: WSR-88D Radar. Left: Typical computer-screen display (photo credit: <https://www.researchgate.net/publication/267381624>). Right: Antenna (photo credit: NOAA). This radar system is computer operated and consists mostly of solid-state components.

1.5.2. There are about 160 WSR-88D installations in the country and U.S. territories (WDTB 2005). There are more than 135 in the CONUS alone. Locations of these installations are shown in Figures 1.6 and 1.7. Appendix 1 lists them all by location. The WSR network is operated jointly by the U.S. National Weather Service (NWS), Federal Aviation Administration (FAA), and Department of Defense (DoD). Single- and composite-radar data are disseminated to users by the NEXRAD Imagery Dissemination System (NIDS), as well as via the Internet (Whiten *et al.* 1998).

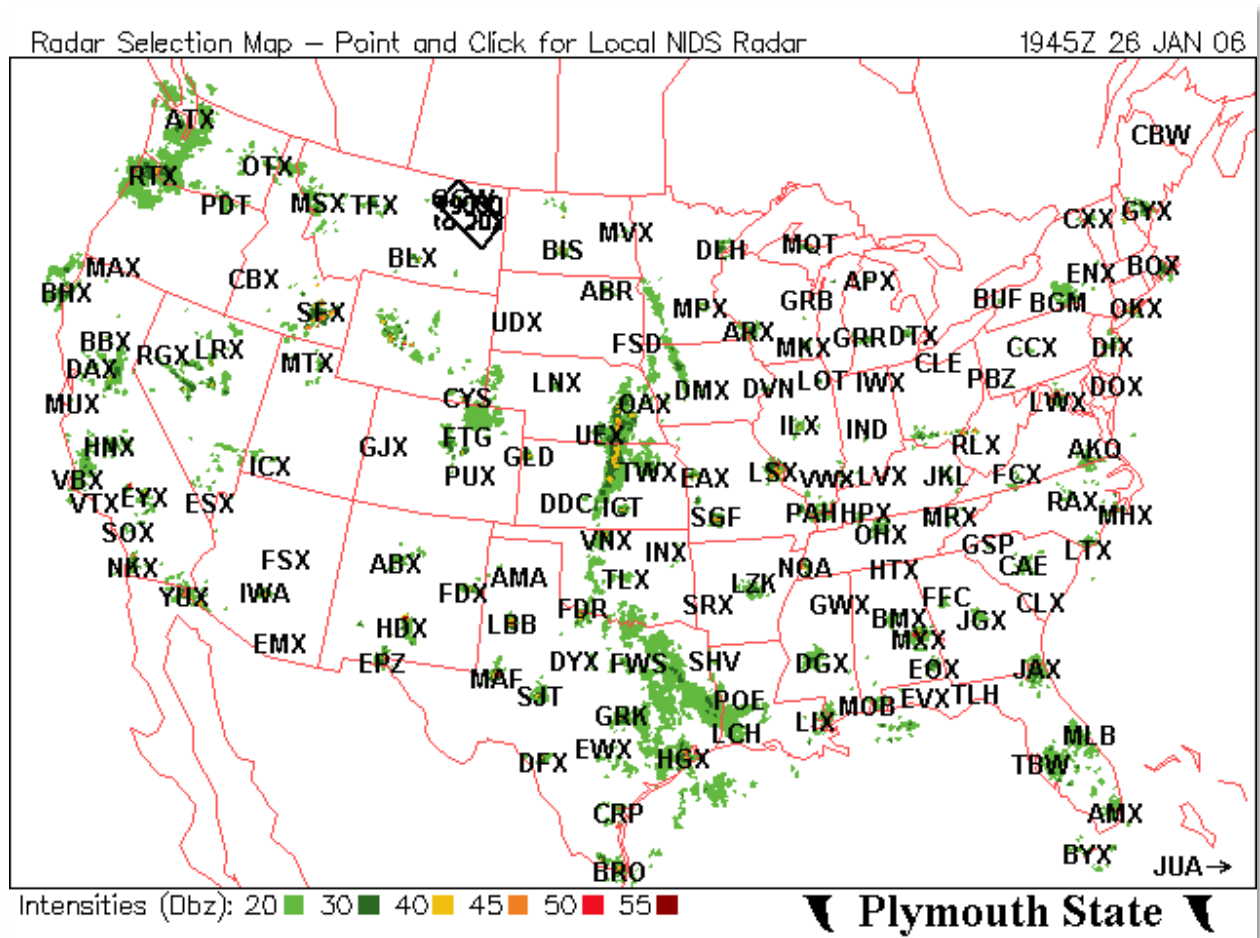


Fig. 1.6: WSR-88D installations in the CONUS. Note that the station identified as “JUA” is located in San Juan, Puerto Rico, which is not shown on the map. (Image credit: Plymouth State University).

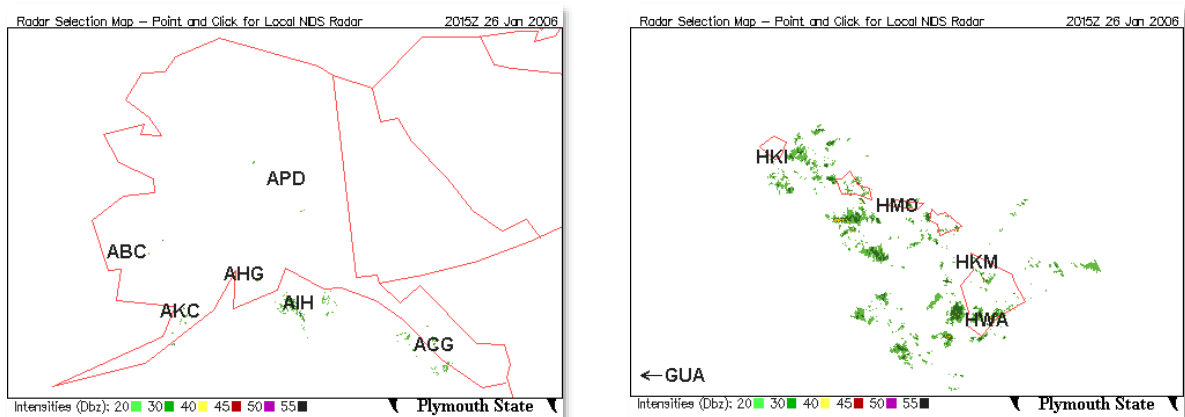


Fig. 1.7: WSR-88D installations in the Alaska and Hawai'i. The station indicated as “GUA” is Guam, not shown on the map. (Image credit: Plymouth State University).

1.5.3. In 2013, the entire WSR-88D network was retrofitted with dual polarization capability, enabling improved rainfall-rate estimates as well as better estimates of the *type* of hydrometeors inside a storm cell (rain, snow, graupel, etc.). The network is currently undergoing a Service Life Extension Program (SLEP) that will extend its lifetime through at least 2030 (ROC 2019).

1.6. In the early 21st Century, The National Weather Service began working together with the Federal Aviation Administration to retrofit a network of airport weather radars called Terminal Doppler Weather Radar (TDWR). Originally designed with the primary goal of identifying wind shear within about 70 nautical miles of busy airports, the NWS reprogrammed the network of about 45 installations to perform both its original function, as well as new functions very similar to those carried out by the WSR-88D network (NCEI 2019). Appendix 1 lists these installations by location. The TDWRs, and several other radar networks, are discussed in greater detail in Chapter 9.

This concludes our brief history of weather radar. In the next chapter, we review the basic properties of electromagnetic radiation.

Summary. Advances in theoretical physics during the 19th Century by Doppler, Maxwell, and Hertz, led to early developments in practical radio and radar systems in the late 19th and early 20th Centuries by Marconi and Hülsmeyer. By the 1920s and early 1930s, Taylor and Young had developed a practical radar system for tracking aircraft. Prior to and during World War Two, several countries scrambled to develop and field radar-based aircraft tracking systems, including both the Allied and Axis powers.

Originally, backscattered radar energy from clouds and precipitation were considered noise (or “clutter”) in radar data, because they partially obscured information about aircraft. But shortly after the war, scientists began retrofitting aircraft-detection radars to study weather. They found that C- and S-band radars could be used to detect and visualize precipitation out to a range of 150 miles from the radar antenna.

The first radar system in the U.S. specifically designed for weather detection was the AN/CPS-9, in 1954. The first was installed in Alabama, and the last remained in operation until the mid-1980s. In 1957, an even more advanced system, called the WSR-57, was brought on-line, and (along with a few WSR-74s) remained the primary civil

weather radar system in the United States for almost 40 years. It was replaced in the late 1980s and early 1990s by the WSR-88D, which remains in operation today. The U.S. Air Force developed its own system in the 1960s, called the AN/FPS-77, which remained operational through the 1980s.

The current generation of operational U.S. weather radars consists of two separate systems. The first is the WSR-88D, which has now surpassed 30 years of operational service, and is undergoing a Service Life Extension Program designed to keep it operational through 2030. The WSR-88D is Doppler-enabled and fully computer controlled, and, as of 2013, capable of dual-polarization interrogation of meteorological targets. There are about 160 of these systems deployed throughout the CONUS, Alaska, Hawai'i, Puerto Rico, and other United States territories. The second system is the Terminal Doppler Weather Radar network, which has many of the same capabilities as the WSR-88D. There are about 45 TDWRs deployed in the United States.

Terms and concepts:

- APQ-13
- Cavity magnetron transmitter tube
- CPS-9
- Department of Defense (DoD)
- Dipole antenna
- Doppler Effect
- Electromagnetic radiation and relationship to electrical and magnetic fields
- Federal Aviation Administration (FAA)
- FPS-77
- Klystron transmitter tube
- National Hurricane Center
- National Weather Service (NWS)
- NEXRAD Imagery Dissemination System (NIDS)
- NEXRAD/WSR-88D
- Plan Position Indicator (PPI)
- RADAR and radar
- Radio Detection and Ranging
- Radio Direction and Ranging
- Range Height Indicator (RHI)
- S-band, C-band, and X-band
- Service Life Extension Program (SLEP)

- Steamship Dorchester
- Telemobiloscope
- Terminal Doppler Weather Radar (TDWR)
- Transmitter, receiver, and duplexer
- Weather clutter
- WSR-1, -1A, -3, and -4
- WSR-57

Study prompts:

1. Summarize the 19th Century contributions of Doppler, Maxwell, and Hertz toward the physics of radar and radio.
2. What were the contributions toward early radar by Christian Hülsmeier, Albert Taylor, and Leo Young?
3. What are the two types of transmitter tubes discussed in the chapter? Who invented them?
4. What was the name of the first U.S. radar system fielded as a network for storm detection?
5. Discuss the origins of the WSR-1 through WSR-4 radar systems.
6. What was the name of the first U.S. radar system specifically designed for detecting weather? What was its wavelength? Who built it? When and where was the first one installed?
7. Discuss the origins and characteristics of the WSR-57.
8. Discuss the origins and characteristics of the FPS-77.
9. What do PPI and RHI stand for? What are good meteorological uses for them?
10. When did the NEXRAD program begin? When was the first of these units delivered? How does it differ from previous radar systems? How many of these

systems are there in the United States inventory? Who operates them? Describe a relatively recent improvement to this network?

11. Describe a second network of radar systems in the United States, deployed at airports to monitor weather conditions.

2. Properties of electromagnetic radiation

In this chapter we review some basic properties of electromagnetic radiation, including its dual nature as wave and a particle, how it gets generated in an antenna, wavelength bands, absorption, scattering, reflection, and refraction. We also discuss polarization and the Doppler Effect.

2.1. Light, or electromagnetic radiation (EMR), can be described as both waves and particles. In the early part of the 20th Century, experiments were conducted that confirmed this dual nature. With the right experiment, EMR manifests as a wave. With another suitable experiment, it manifests as a stream of particles. This apparent contradiction can only be reconciled when one realizes that the descriptions of EMR as particles and waves are both incomplete, and further, that both are *analogies*. Put another way, EMR *cannot* be composed of particles *or* waves in the way that we usually think of particles and waves. (If it is particles, how do you explain its behavior in diffraction gratings? If it's waves, what *exactly* is waving? EMR can propagate through a perfect vacuum!) We do not have a word in any of the ancient human languages for what EMR actually is, so we resort to simplified descriptions that seem appropriate for the situation. Fortunately, EMR can be described *mathematically* to a very high degree of precision, and, for *most* of the applications relevant to radar meteorology, the mathematical properties of waves are appropriate.

2.1.1. Using the wave analogy, we can describe the waves of EMR as ranging in wavelength from near zero to infinitely long. Longer wavelengths are associated with lower energy sources, and shorter wavelengths are associated with higher energy sources. Figure 2.1 shows the Electromagnetic Spectrum.

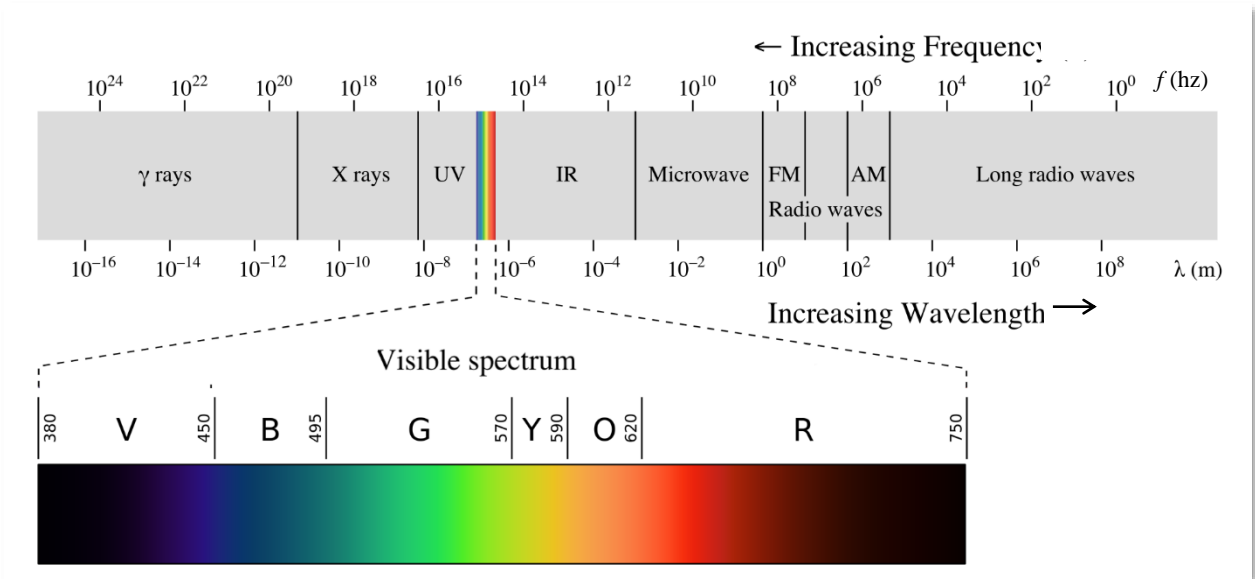


Fig 2.1: Electromagnetic Spectrum. Radar wavelengths are near 10^{-1} meters, in the microwave range. Numbers shown in the expanded window for visible light indicate wavelength in nanometers. (Source: https://commons.wikimedia.org/wiki/File:EM_spectrumrevised.png)

2.2. Separation of charge in a conducting wire. If positive and negative charges are separated in a wire, an electrical field (E) is created that points from the positive charge center to the negative charge center. Electrons from the negative charge center begin to move toward the positive charge center. The moving electric charges then create a magnetic field (B), pointing in a direction at a right angle to the direction of the E -field (Ohanian 1987).

2.2.1. When an oscillating external force (in this case, an oscillating electrical field, or “alternating current”) is applied to the wire, the electrical charges in the wire are separated. As the external field reverses direction, the flow of electrons from one end of the wire also reverses directions. The resulting B -field (in a plane at a right angle to the oscillating E -field) responds by continuously reversing direction as well. Part of the energy from the external force is radiated away as EMR (with the same wavelength and period as the originating E - and B -fields) and some is dissipated as heat in the wire. This is a description of a simple dipole antenna (Figure 2.2) (Rauber and Nesbitt 2018).

EMR consists of propagating E - and B -fields (Figure 2.3), and while both the E - and B -waves propagate together in the same direction, their planes of oscillation are orthogonal (Figure 2.3).

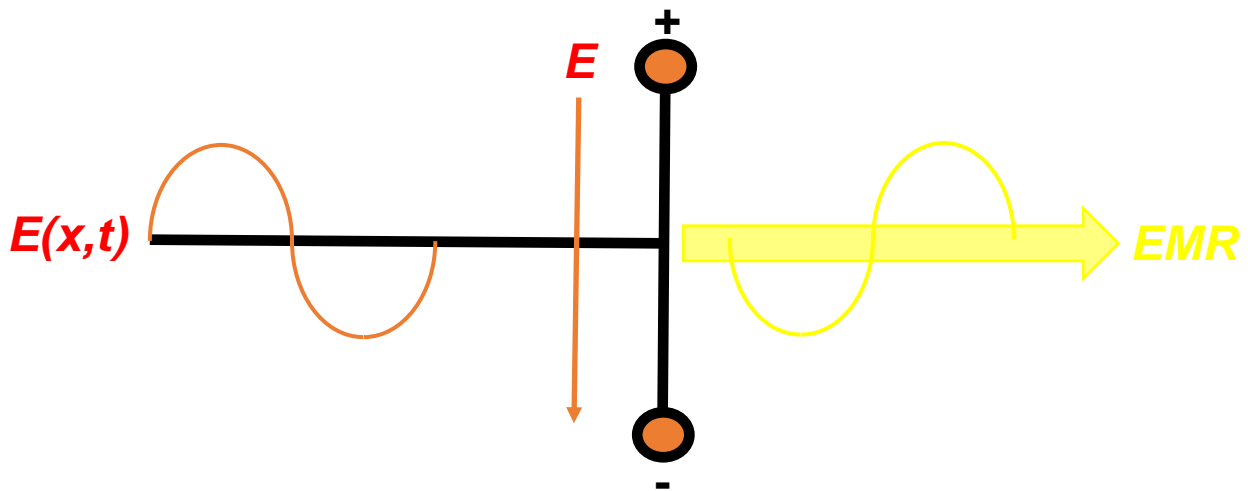


Fig. 2.2: A Simple Dipole Antenna. An externally-imposed oscillating electrical field $E(x,t)$ creates a separation of charge in a conducting wire. Under the right circumstances, free electrons (-) are forced to one end of the wire, leaving behind positive ions (+) at the other end. At this moment, the E-field between the separated charges points from the positive charge concentration to the negative charge concentration. Electrons in the wire begin moving toward the positive ions at the other end, generating a magnetic field (not shown). The wire radiates away some the excess energy imposed by the oscillating E-field in the form of EMR.

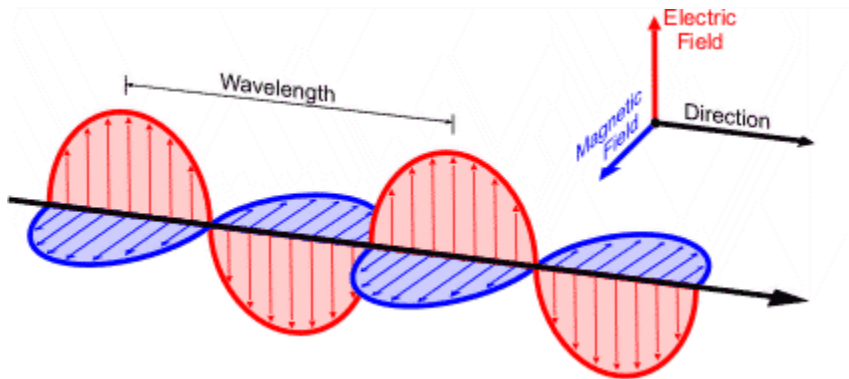


Fig. 2.3: EMR as combination of propagating E- and B-waves. (Credit: <https://www.ices-emfsafety.org/electromagnetic-energy/>)

2.2.2. Electromagnetic waves propagate away from the oscillating dipole antenna at the speed of light (c) when in a vacuum, or slower than c when in some medium such as air. From Maxwell's equations, c is defined by:

$$c = \frac{1}{\sqrt{\mu_0 \epsilon_0}} \quad (2.1)$$

where μ_0 is the magnetic permeability of vacuum ($1.26 \times 10^{-6} \text{ J A}^{-2} \text{ m}^{-1}$), and ϵ_0 is the electrical permittivity of free space ($8.85 \times 10^{-12} \text{ C}^2 \text{ J}^{-1} \text{ m}^{-1}$). With enough decimal places of accuracy on the RHS of (2.1), the function produces the usual value of c , that is 299, 792, 458 ms^{-1} (Ohanian 1987).

The speed of the EMR through a medium (v_c) is defined by the Index of Refraction (n), where:

$$n = \frac{c}{v_c} \quad (2.2)$$

For EMR in the microwave range used by radar, the Index of Refraction of air at standard sea-level temperature and pressure is about 1.0003, and decreases with altitude. The macroscale determinant of n is the density of the air mass, which (at constant pressure) is a function of its temperature and water vapor mixing ratio (Kidder and Vonder Harr 1995). Some sample values of n are shown in Table 2.1.

Table 2.1: Method of computing and sample values of n for the Electromagnetic Spectrum, between 200 and 2000 nm (UV to near IR). (Reproduced from Lide 1997.)

INDEX OF REFRACTION OF AIR

This is a table of the index of refraction n of dry air at 15°C and a pressure of 101.325 kPa and containing 0.03% by volume of carbon dioxide ("standard air"). The index of refraction is defined by $n = \lambda_{vac} / \lambda_{air}$, where λ is the wavelength of the radiation. The index is calculated from the expression:

$$(n - 1) \times 10^8 = 8342.13 + 2406030(130 - \sigma^2)^{-1} + 15997(38.9 - \sigma^2)^{-1}$$

where $\sigma = 1 / \lambda_{vac}$ and λ_{vac} has units of μm . The equation is valid for λ_{vac} from 200 nm to 2 μm .

The table also gives the correction $(n - 1)\lambda_{air}$ which must be added to the wavelength in air to obtain λ_{vac} .

If the air is at a temperature t in °C and a pressure p in pascals, a value of $(n - 1)$ from this table should be multiplied by

$$\frac{p[1 + p(61.3 - t) \times 10^{-10}]}{96095.4(1 + 0.003661t)}$$

REFERENCE

Edlen, B., *Metrologia*, 2, 71, 1966.

λ_{vac}	$(n - 1) \times 10^8$	$\lambda_{vac} - \lambda_{air}$	λ_{vac}	$(n - 1) \times 10^8$	$\lambda_{vac} - \lambda_{air}$	λ_{vac}	$(n - 1) \times 10^8$	$\lambda_{vac} - \lambda_{air}$
200 nm	32408	0.0648 nm	540	27803	0.1501	880	27461	0.2416
210	31746	0.0666	550	27782	0.1528	890	27457	0.2443
220	31224	0.0687	560	27763	0.1554	900	27452	0.2470
230	30799	0.0708	570	27745	0.1581	910	27448	0.2497
240	30445	0.0730	580	27728	0.1608	920	27444	0.2524
250	30146	0.0753	590	27712	0.1635	930	27440	0.2551
260	29890	0.0777	600	27697	0.1661	940	27436	0.2578
270	29669	0.0801	610	27682	0.1688	950	27432	0.2605
280	29475	0.0825	620	27669	0.1715	960	27429	0.2632
290	29306	0.0850	630	27656	0.1742	970	27425	0.2660
300	29155	0.0874	640	27643	0.1769	980	27422	0.2687
310	29022	0.0899	650	27631	0.1796	990 nm	27419	0.2714 nm
320	28902	0.0925	660	27620	0.1822			
330	28795	0.0950	670	27609	0.1849	1.00 μm	27416	0.000274 μm
340	28698	0.0975	680	27599	0.1876	1.05	27401	0.000288
350	28611	0.1001	690	27589	0.1903	1.10	27389	0.000301
360	28531	0.1027	700	27579	0.1930	1.15	27378	0.000315
370	28458	0.1053	710	27570	0.1957	1.20	27368	0.000328
380	28392	0.1079	720	27562	0.1984	1.25	27360	0.000342
390	28331	0.1105	730	27553	0.2011	1.30	27352	0.000355
400	28275	0.1131	740	27545	0.2038	1.35	27346	0.000369
410	28223	0.1157	750	27538	0.2065	1.40	27340	0.000383
420	28175	0.1183	760	27530	0.2092	1.45	27334	0.000396
430	28131	0.1209	770	27523	0.2119	1.50	27330	0.000410
440	28090	0.1236	780	27516	0.2146	1.55	27325	0.000423
450	28052	0.1262	790	27510	0.2173	1.60	27321	0.000437
460	28016	0.1288	800	27504	0.2200	1.65	27318	0.000451
470	27983	0.1315	810	27498	0.2227	1.70	27314	0.000464
480	27952	0.1341	820	27492	0.2254	1.75	27311	0.000478
490	27923	0.1368	830	27486	0.2281	1.80	27309	0.000491
500	27896	0.1394	840	27481	0.2308	1.85	27306	0.000505
510	27870	0.1421	850	27476	0.2335	1.90	27304	0.000519
520	27846	0.1448	860	27471	0.2362	1.95	27302	0.000532
530	27824	0.1474	870	27466	0.2389	2.00 μm	27300	0.000546 μm

2.3. The propagation of EMR can be described using separate equations for the electrical and magnetic components. For the E-wave propagating in the x-direction during time t ,

$$E(x, t) = E_m \sin[\kappa x - \omega t + \phi] \tag{2.3a}$$

and for the B wave,

$$B(x, t) = B_m \sin[\kappa x - \omega t + \phi] \quad (2.3b)$$

where:

κ = Wave number = $2\pi/\lambda$ [m^{-1}]

ω = Angular frequency = $2\pi/T$ [s^{-1}]

λ = Wavelength [m]

T = Period [s]

ϕ = Phase angle [radians]

and E_m, B_m are the amplitudes of the E- and B-waves, respectively (Ohanian 1987).

2.3.1. The phase angle (ϕ), can be thought of as an angular offset. Normally, the sine function has a value of zero if the rotation angle is zero. If ϕ has a non-zero value, the function can also have a non-zero value at a rotation angle of zero. This is illustrated (for a time-dependent sine wave) in Figure 2.4.

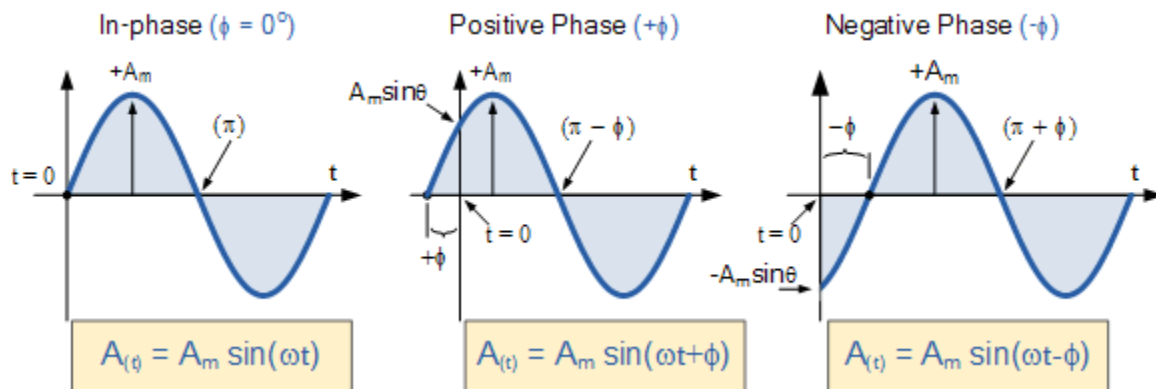


Fig. 2.4: Phase angle. Illustration assuming a sine wave oscillating in time (t). In the first example, there is a zero phase, so the function equals zero at $t = 0$. Adding or subtracting a phase shifts the zero point of the function either forward or backward in time. (Credit: <https://www.electronicstutorials.ws/accircuits/phase-difference.html>)

2.3.2. The speed of light is also equal to the ratio of the amplitudes of the E- and B-waves, that is:

$$c = \frac{E_m}{B_m} \quad (2.4)$$

indicating that the amplitude of the E-wave is almost 300 million times greater than the amplitude of the B-wave (Ohanian 1987).

2.3.3. Note that the angular frequency (ω) is also given by:

$$\omega = 2\pi f \quad (2.5)$$

where f is the more conventionally-used frequency, with units of cycles per second [Hz]. The inverse of f is the period (T) of the wave ($f = 1/T$).

2.3.4. The speed of light is related to f and λ by:

$$c = f\lambda \quad (2.6)$$

so that:

$$c = \frac{\lambda}{T} \quad (2.7)$$

Combining (2.5) and (2.6), one obtains:

$$c = \frac{\omega\lambda}{2\pi} \quad (2.8)$$

but $\kappa = 2\pi/\lambda$, so that:

$$c = \frac{\omega}{\kappa} \quad (2.9)$$

2.4. Meteorological radars are designed to transmit EMR at wavelengths that interact with various hydrometeors, but not with the molecular constituents of dry air (N_2 and O_2). These radars are classified with a band (letter) designation as shown in Table 2.2.

Table 2.2: Meteorological radars by band, wavelength, and frequency. Wavelength is often used by meteorologists, for easy size comparison to hydrometeors. Frequency is more commonly used by radar engineers. The lettered band designations (column 1) for these ranges of wavelength and frequency were originally created during WW II, and standardized by the Institute of Electrical and Electronics Engineers (IEEE) in the mid-1980s (Whiten *et al.* 1998).

Band	Range of Wavelengths [cm]	Central Frequency [GHz]
S	7.5 – 15	2.8
C	3.7 – 7.5	5.5
X	2.5 – 3.7	9.4

2.4.1. EMR interactions with matter (such as hydrometeors) depend on the wavelength (or frequency) of the radiation, and the size, shape and distribution of the matter. The first two types of interactions are absorption and scattering (Rauber and Nesbitt 2018).

2.4.1.1. When EMR is *absorbed* by matter, its energy is converted to random motion (heat) in the matter. The energy (E) of a photon (particle of EMR) is given by:

$$E = \frac{hc}{\lambda} \tag{2.10}$$

where E has units of Joules [J], and h is Planck's constant (after Max Planck, a German physicist of the 19th and 20th Centuries), equal to 6.63×10^{-34} [J•s].

Microwave ovens are designed to operate on this principle. Absorption occurs when photons with a specific frequency are absorbed by an atom or a molecule, corresponding to the energy levels of the electrons surrounding the atoms or forming the molecular bonds in the molecules. Absorption by hydrometeors is far greater in short-wavelength radars (such as X-band) than it is for long-wavelength radars (such as S-band), limiting the range of the former as compared to the latter (Rauber and Nesbitt 2018).

2.4.1.2. *Scattering* occurs when EMR is absorbed but immediately re-radiated at the same wavelength, in the same (or a different) direction. Scattering is classified as Rayleigh, Mie, or geometric scattering depending on the relative sizes of the EMR's wavelength and the circumference of the scattering particle. The size parameter (X) is used to combine the two independent variables, and is defined by:

$$\chi = \frac{2\pi r}{\lambda} \quad (2.11)$$

where r is the radius of the scattering particle. Rayleigh scattering occurs when $X < 0.1$, that is, the scattering particle is much smaller than the wavelength of the EMR. An example of this is the interaction of visible (and ultraviolet) sunlight with molecules of dry air, producing a blue sky. Rayleigh scattering forms the basis for the Probert-Jones Radar Equation, described later in this text (Kidder and Vonder Harr 1995; Rauber and Nesbitt 2018).

Mie scattering occurs when $0.1 \leq X \leq 50$, indicating that the scattering particle is very roughly the same size as the wavelength of the EMR. An example is the interaction of infrared light with cloud droplets. For EMR at the wavelengths of meteorological radar, the objects of concern are cloud droplets, raindrops, ice crystals, snowflakes, hailstones, and insects. Because of its inherent non-linearity, it's preferable to avoid Mie scattering by using meteorological radar wavelengths that are much larger than the hydrometeors one is trying to measure (Kidder and Vonder Harr 1995; Rauber and Nesbitt 2018).

Geometric scattering occurs when $X > 50$, that is, the spherical scatterer is large compared to the wavelength of the EMR. This form of scattering is responsible for rainbows and halos, produced by the interaction between visible sunlight and either precipitation-sized droplets or ice crystals (Kidder and Vonder Harr 1995; Rauber and Nesbitt 2018).

2.4.1.3. A special type of scattering, called Bragg scattering, occurs when electromagnetic waves are incident on regularly-spaced objects, or regions of air with different indices of refraction, leading to constructive interference between the scattered waves. Bragg scattering can develop in the atmosphere when turbulence *mixes* air with different indices of refraction (caused by different temperature or humidity), creating eddies at all scales, one of which may correspond to half the wavelength of the radar EMR. It may also occur in clouds when some droplets have the appropriate half-wavelength spacing along the beam (Rauber and Nesbitt 2018).

2.4.2. Refraction occurs when an electromagnetic wave crosses from an airmass with one Index of Refraction (n_1) into another airmass with a different Index of Refraction (n_2). This implies a change in the *speed* with which the EMR is propagating, and the result, described by Snell's Law, is also a change in the *direction* of the EMR's propagation. Snell's Law is given by:

$$\frac{n_1}{n_2} = \frac{\sin\theta_2}{\sin\theta_1} = \frac{v_{c2}}{v_{c1}} \quad (2.12)$$

where θ_1 is the angle of the incidence (with speed v_{c1}) of the EMR on the boundary between the two different airmasses, and θ_2 is the angle of refraction (with speed v_{c2}). Figure 2.5 illustrates the relationship between these variables. Refraction is not a desirable characteristic in meteorological radars and is a common source of error. Refracted radar EMR can result in Anomalous Propagation (discussed later), and in extreme cases, ducting (Kidder and Vonder Harr 1995; Rauber and Nesbitt 2018).

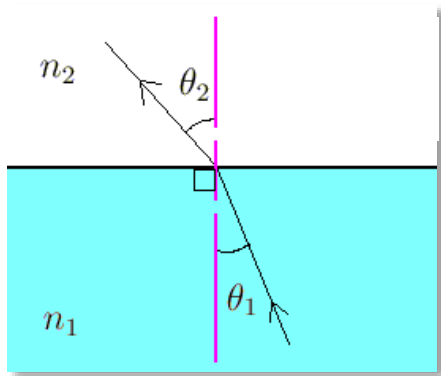


Fig. 2.5: Illustration of Snell's Law. (Credit: <https://www.math.ubc.ca/~cass/courses/m309-01a/chu/Fundamentals/snell.htm>)

2.4.3. Reflection occurs when an electromagnetic wave is incident on a boundary between two different media, and the boundary has a thickness much greater than the wavelength of the EMR. In this case, the incident EMR returns back into the medium where it originated. Reflection may be specular (mirror-like) or diffuse (blurring caused by the reflection of the EMR into many different directions). Like refraction, reflection is not a desirable characteristic in meteorological radars. Reflected radar EMR results in Ground Clutter (Rauber and Nesbitt 2018).

2.5. Polarization is another characteristic of EMR, and refers to the plane in which the E- or B-wave is oscillating. Because the amplitude of the E-wave is so much greater than that of the B-wave, the former is usually referenced. An electromagnetic wave may be linearly or circularly polarized. Linear polarization may be either vertical or horizontal, meaning that the plane in which the E-field oscillates remains either

vertically- or horizontally-oriented as the electromagnetic wave propagates. Circular polarization (Figure 2.6) may be right-handed or left-handed. In the former case, the plane of E-field oscillations rotates in the clockwise direction as the EMR wave propagates. In the latter case, the plane of the E-field rotates in a counter-clockwise direction as the EMR wave propagates (Rinehart 2004).

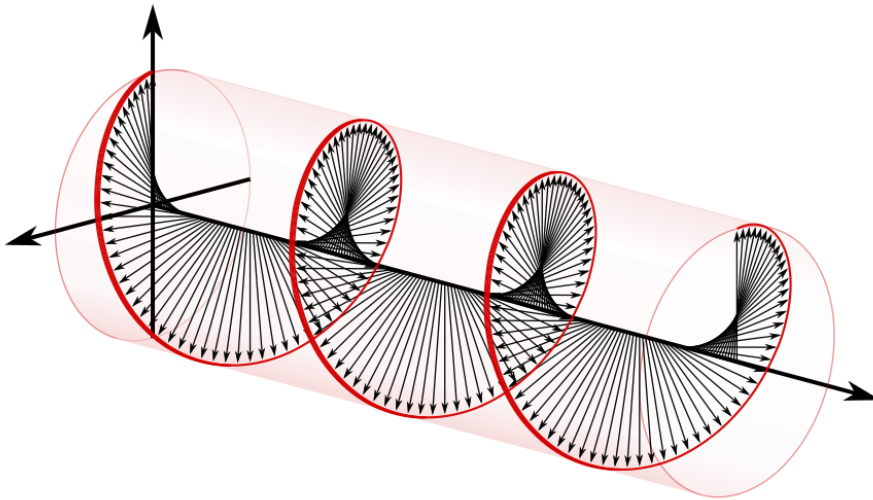


Fig. 2.6. Right-Handed Circular Polarization. Arrows indicate orientation of the E-field plane, rotating in a clockwise direction as it propagates to the right. (Credit: http://www.wikiwand.com/en/Circular_polarization)

2.5.1. Most operational meteorological radars were originally horizontally-polarized. In the mid-2010s, all members of the United States operational weather radar network were retrofitted with new modules making them polarization diverse, meaning they still transmit with a fixed (*linear-diagonal*) polarization, but are able to receive at all linear polarizations (Raubert and Nesbitt 2018).

2.5.2. The polarization of EMR has consequences for how it interacts with matter. For example, large raindrops are larger in the horizontal dimension than they are in the vertical dimension. Thus, a vertically-polarized wave “perceives” a smaller raindrop than a horizontally-polarized wave. The vertically-polarized wave experiences less absorption, and a different degree of scattering than the horizontally-polarized wave. By comparing the relative scattering in the horizontal plane to that observed in the vertical plane, the average shape of the raindrops can be estimated.

Because a raindrop's shape is related to its size, this can lead to better estimates of rainfall rate (Rinehart 2004).

2.6. The Doppler Effect describes the change in frequency that occurs in EMR when its source is moving with respect to the observer. If the source is approaching the observer, its velocity must be added to the speed of the EMR itself. This causes the crests of the electromagnetic waves to bunch up closer together, reducing their wavelength and increasing their frequency. In sound (also described as waves), the result is higher pitch. In EMR, the result is a shift toward the blue end of the spectrum, that is, a change in color. The opposite occurs when the source is moving away from the observer. This concept is illustrated in Figure 2.7.

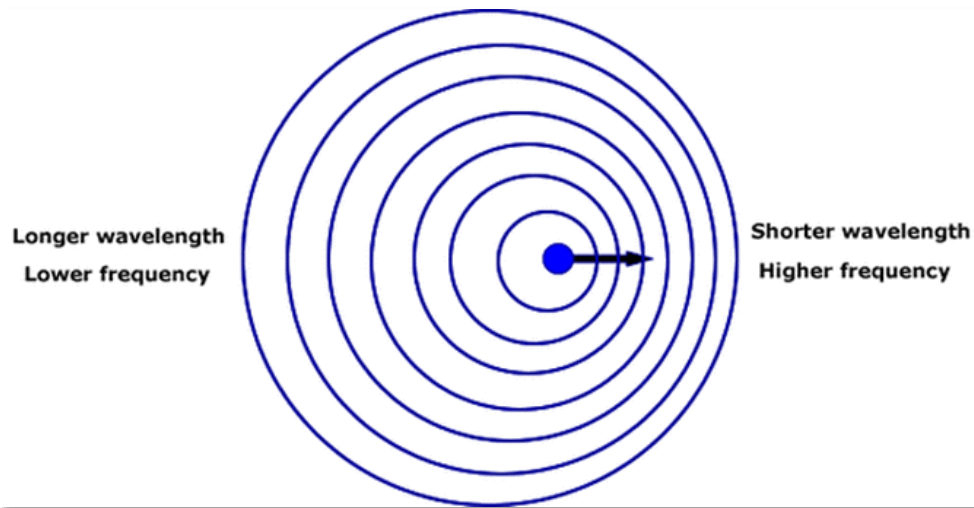


Fig. 2.7: Illustration of the Doppler Effect. Concentric circles indicate crests of oscillating sound or light waves, emitted from a source moving to the right. An observer to the left of the moving source would see longer wavelengths, corresponding to lower pitch sounds or redder colors. An observer to the right of the moving source would see shorter wavelengths, corresponding to higher pitch sounds or bluer colors. (Credit: <https://soundwavesreillymckennaaly.weebly.com/doppler-effect.html>)

2.6.1. Mathematically, the change in frequency that results from the Doppler Effect (as seen by a stationary observer) is given by:

$$\Delta f_{dop} = \frac{-2V_r}{\lambda} \quad (2.13)$$

where Δf_{dop} is the change in frequency resulting from the source's motion [Hz], λ is the original wavelength of the EMR [m], and V_r is the source's radial velocity [ms^{-1}]. The radial velocity is that component of the source's total velocity vector that corresponds to its approach or recession from the position of the observer. If no part of its total velocity vector is either toward or away from the observer, the Doppler frequency shift will be zero (Ohanian 1987).

2.6.2. In the context of radar meteorology, the stationary "observer" is the radar installation itself (while in listening mode), and the "source" consists of meteorological "targets," such as storm cells. We can consider the targets as sources of radar EMR, because they scatter the microwave radiation back toward the radar installation.

2.6.3. The radial velocity of a meteorological target is *negative* if the target is *inbound* (approaching the radar installation). V_r is *positive* if the target is *outbound* (receding from the radar installation). This can easily be remembered by appealing to the finite-difference definition of velocity:

$$V_r = \frac{(x_f - x_i)}{\Delta t} \quad (2.14)$$

where x_f and x_i are the final and initial distances from the radar, respectively. If x_f is greater than x_i , V_r is a positive number, and the target is outbound. If x_f is less than x_i , V_r is a negative number, and the target is inbound.

2.6.4. Implications of (2.13) and (2.14):

- The Doppler frequency shift is *positive* (the frequency increases; therefore, the wavelength of the backscattered radiation decreases), if the radial velocity is *negative* (indicating targets are inbound). Because the EMR wavelengths are shifting toward the *shorter* end, this is also called *blueshifting*.
- The Doppler frequency shift is *negative* (the frequency decreases; therefore, the wavelength of the backscattered radiation increases), if the radial velocity is *positive* (indicating targets are outbound). Because the EMR wavelengths are shifting toward the *longer* end, this is also called *redshifting*.

2.6.5. How much Doppler shift is imposed on radar EMR by meteorological targets? Let's assume an outbound target (positive V_r) moving at 50 knots (which is about 25 ms^{-1} , and fast, but not unheard of for weather), imaged by a 10.5-cm (0.105 m; S-band) radar installation. Using (2.13), we see that:

$$\frac{-2(25)}{(0.105)} = -476.2 \text{ Hz}$$

From Table 2.2., the transmitted frequency of the radar is about $2.8 \times 10^9 \text{ Hz}$, so the percentage change is:

$$\left(\frac{-476.2}{2.8 \times 10^9}\right) \times 100 \% = -1.7007 \times 10^{-5}$$

or, about two 100,000^{ths} of a percent. This is obviously not detectable, so the Doppler Effect as defined in (2.13) cannot be used in radar meteorology. The method actually used is described in Chapter 3.

This concludes our brief review of electromagnetic radiation. In the next chapter, we begin a detailed discussion of the WSR-88D.

Summary. Electromagnetic Radiation can be described as both waves and particles, although both of these are incomplete analogies. The wave analogy works best for most applications in radar meteorology. EMR waves are generated when an electrical field oscillates back and forth in a conducting wire, and are composed of an electrical wave and a magnetic wave, propagating in the same direction, but oscillating in planes at a right angle to each other.

EMR propagates at the speed of light in a vacuum, equal to almost exactly 300 million meters per second. It slows down when propagating through a physical medium, such as air or water, according to the medium's Index of Refraction, which is a function of density. EMR propagates with a characteristic wavelength, which - for visible light - corresponds to color. Short wavelengths are on the blue end of the spectrum, and extend into ultraviolet, x-rays, and gamma-rays. Longer wavelengths are on the red end, and extend into infra-red, microwaves, and radio waves.

Microwaves are in the region of wavelengths between 1 mm and 1 meter.

Meteorological radars operate in three microwave bands: S-band (7.5 to 15 cm), C-band

(3.7 to 7.5 cm), and X-band (2.5 to 3.7 cm). These designations were originally developed during WW II, and finalized by the IEEE in the 1980s.

When EMR interacts with matter, it may be absorbed, scattered, refracted, or reflected. Scattering may be Rayleigh, Mie, geometric, or Bragg. Reflection may be specular or diffuse. The details of the interactions, and how they affect the EMR, depend on the wavelength of the EMR, the angle at which it strikes the matter, the size of the particles in the matter, the energy levels of the electrical bonds in the molecules of the matter, the density of matter and whether it is well mixed or stratified, and several other factors.

Polarization describes the behavior and orientation of the plane in which the EMR's associated electrical field oscillates. The oscillation plane of the electrical field is used instead of that of the corresponding magnetic field, because of the multiple order-of-magnitude difference in their relative amplitudes. Polarization may be either circular or linear. Circular polarization may be either left-handed or right-handed, rotating either counter-clockwise or clockwise, respectively. Linear polarization can be used to estimate the shape, and therefore the size of precipitation particles, which can be used to improve radar-based estimates of rainfall rate.

The Doppler Effect describes the shortening or lengthening of EMR wavelengths, caused when the source of the EMR is moving either toward or away from an observer. This effect is far too small to be used directly in meteorological applications, given the relatively low velocities involved.

Terms and concepts:

- Absorption
- Alternating current
- Angular frequency (ω)
- Anomalous Propagation
- Blueshifting
- Bragg scattering
- Circular polarization
- Constructive interference
- Diffuse reflection
- Doppler Effect
- Ducting
- Electrical field
- Electrical permittivity of free space (ϵ_0)

- Electromagnetic radiation (EMR)
- Electromagnetic spectrum
- EMR wave-particle duality
- Frequency (f)
- Geometric scattering
- Ground Clutter
- Index of Refraction (n)
- Linear polarization
- Magnetic field
- Magnetic permeability of vacuum (μ_0)
- Mie scattering
- Phase angle (ϕ)
- Polarization
- Polarization diverse
- Radial velocity
- Rayleigh scattering
- Redshifting
- Reflection
- Refraction
- Scattering
- Size parameter (X)
- Snell's Law
- Specular reflection
- Speed of light (c)
- Period (of wave) (T)
- Planck's constant (h)
- Wave number (κ)
- Wavelength (λ)

Study prompts:

1. What is the EMR "wave analogy?"
2. Describe the Electromagnetic Spectrum in terms of bands (such as visible light) and their respective wavelengths. Where does microwave fall?
3. Discuss the operation of a dipole antenna.

4. Discuss the propagation of EMR with respect to the oscillating planes of its constituent electrical and magnetic waves.
5. Write several mathematical relationships describing the speed of light (c).
6. What happens to EMR's velocity when it passes through a medium? What is the relationship to c ?
7. What is the relationship between wave number and wavelength? What is the relationship between angular frequency and period?
8. Describe the effect of phase angle on sinewave oscillation.
9. What are the three *bands* discussed that are used by weather radar? List them by name, wavelength, and frequency. Based on what you read in Chapter 1, what are the relative advantages of each band?
10. Discuss the physical process by which an atom or molecule absorbs EMR.
11. Discuss Rayleigh, Geometric, and Mie scattering in terms of the size parameter. List an example of each.
12. What is Bragg scattering?
13. What is refraction? What is Snell's Law?
14. What is reflection? What are two types of reflection and how do they differ?
15. Discuss two different classes of EMR polarization. Why is this useful in meteorological radar?
16. How does the Doppler Effect work? Write a mathematical description for it that includes wavelength and radial velocity. Describe blueshifting and redshifting. Then explain why this cannot be directly used in meteorological applications.

3. The WSR-88D Radar Data Acquisition Module and archive Level I data.

Unless otherwise noted, material for this chapter was drawn from WDTB (2005).

In this chapter we introduce the basic components of the WSR-88D system, and go into detail about the generation of Level I base moments (reflectivity, radial velocity, and spectrum width).

We also discuss the relationship between reflectivity and rainfall rate.

3.1. There are three “levels” of data produced by the WSR-88D system. These are Archive Level I, which consists of raw base moments (defined below); Archive Level II, which consists of high-resolution, quality-controlled base moments; and Archive Level III, which consists of products derived from Archive Level II data, such as automated storm-cell tracking and forecasting, hail size, and many others. This chapter will focus on the hardware and operating principles of the United States operational WSR-88D system as it collects Archive Level I data. It is not intended as an engineering manual, but is meant to familiarize meteorologists and other physical scientists with the system, so it will necessarily take a somewhat simplified, schematic approach.

Rinehart’s Radar for Meteorologists text begins with the following “block diagram” of the radar system:

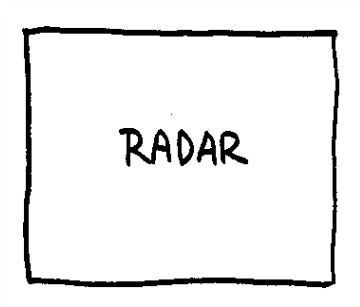


Fig. 3.1: Rinehart’s “Simplified Block Diagram of Radar System.” (Rinehart 2004.)

...which is probably *too* simplified for our purposes here. Instead, we will build our understanding of our current operational weather radar system from the block diagram shown in Figure 3.2.

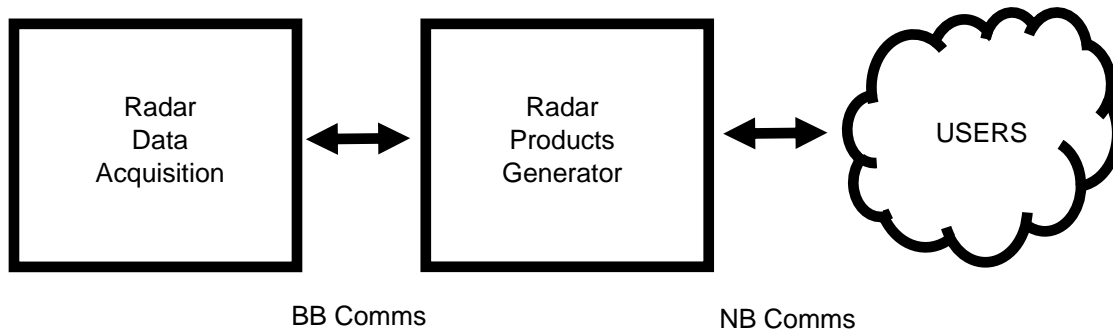


Fig. 3.2: Block diagram of a WSR-88D system.

Figure 3.2 shows that the present system has three main components, connected by two modes of communications. Radar data are initially generated by the Radar Data Acquisition (RDA) module on the left. This is essentially the antenna, associated structures, and electronics needed to make it operate. From there, data are transmitted by a broad-band communications link (BB Comms), which may take one of several forms, to the Radar Products Generator (RPG) module. Together, the RDA and RPG produce Archive Levels I, II, and III products. The RPG includes the Human Control Interface (HCI; also known as the Master System Control Function), that permits interaction with the entire system. The HCI can be used to change several settings at the RDA by transmitting instructions back along the BB Comms. The third major component consists of the users of radar data, including the Advanced Weather Interactive Processing System (AWIPS), which is the NWS's main forecaster workstation (located in WFOs). Other users include the Federal Aviation Administration and other government agencies, as well as universities and private companies. The users are connected to the RPG via narrow-band communications (NB Comms) links.

3.2. Radar Data Acquisition (RDA) module. The RDA module is usually located at some distance from its associated NWS Weather Forecast Office (WFO), and consists of the antenna (mounted on a tower, beneath a spherical dome), and the blockhouse. Functional subcomponents of the RDA are the transmitter (XMTR), duplexer (DUPL),

receiver (RCVR), signal processor (PROC), RDA maintenance terminal (RDA MT), and antenna (ANT). Figure 3.3 shows a typical RDA and an antenna schematic, and Figure 3.4 is a functional schematic of the RDA.

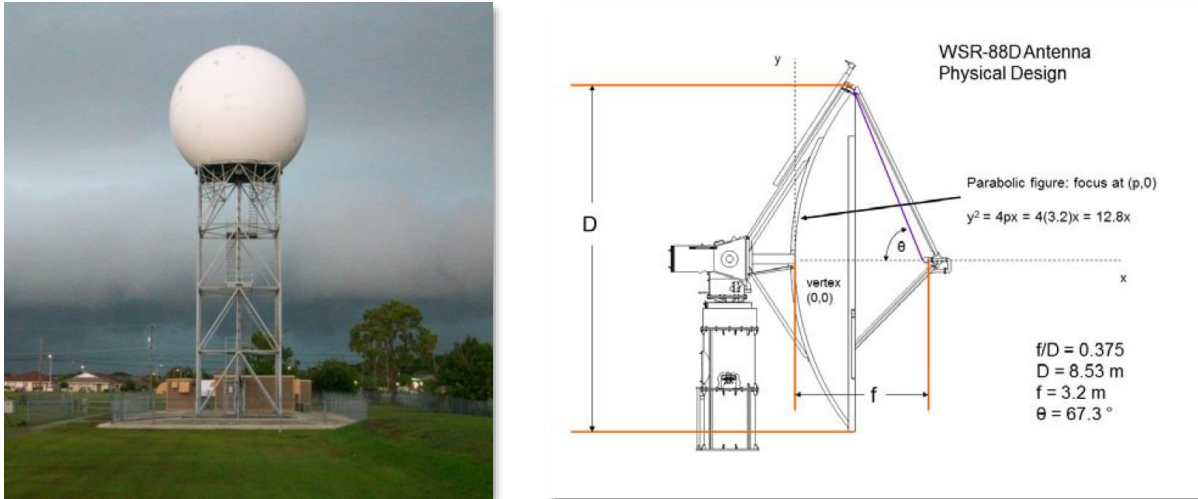


Fig. 3.3: RDA antenna, tower and dome. The blockhouse can be seen near the base of the antenna tower in the left image. (Left Image credit: <https://en.wikipedia.org/wiki/NEXRAD>; Right image credit: Ice et al. 2015)

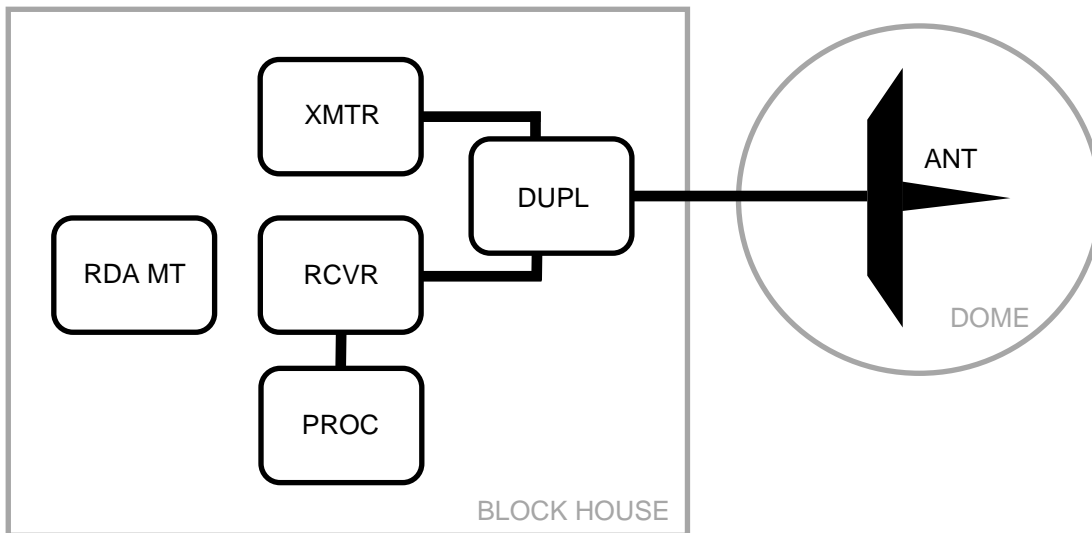


Fig. 3.4: RDA schematic.

3.2.1. The **RDA maintenance terminal** allows control of all RDA functions from within the blockhouse. It is not normally used by meteorologists.

3.2.2. The transmitter generates pulses of EMR. Pulses have a wavelength of 10.3 cm (making the WSR-88D an S-band radar) and a peak transmitted power of 750 kW (which is equivalent to five thousand 150-Watt lightbulbs). The average transmitted power is much lower than this – on the order of 1 kW. There are several types of transmitter tubes currently used by weather radars. One of them is called a magnetron, which is part of a transmitting system called a Power-Oscillator-Transmitter (POT). Another type of tube is called a klystron, which is part of a system called a Power-Amplifier-Transmitter (PAT) (radartutorial.eu 2019). There are others as well, including entirely solid-state transmitters in low-power and phased array systems. The WSR-88D uses a klystron transmitter tube (Radar Operations Center 2019).

3.2.3. The duplexer switches the antenna function back and forth between transmit and receive mode. When in transmit mode, the transmitter-generated pulse is funneled to the antenna via a wave guide (metal ducting) and sent out into the atmosphere around the RDA. When in receive mode, the antenna listens for “echoes” consisting of its own EMR backscattered from meteorological targets within range of the radar.

3.2.4. The antenna is 28 feet in diameter, rests on a turntable that rotates through 360 degrees of azimuth, and is also equipped with gearing that allows it to adjust its vertical (tilt) angle (Figure 3.3). Typically, the antenna base is 20 or 30 meters above the local terrain level; although, in some cases, it is as low as five meters AGL (see Appendix 1). It operates in a Volume Control Pattern (VCP)² that systematically scans the three-dimensional volume of space around the antenna, out to its Maximum Unambiguous Range (R_{max}). A typical VCP starts with the antenna at the lowest tilt angle (0.5° above the horizon), and the turntable rotates through 360 degrees of azimuth. Next, the tilt is increased to the next higher angle, and the turntable rotates through another full circle. This continues until all the tilt angles in the VCP are completed.

3.2.5. As the antenna rotates through azimuth angles, the duplexer switches the radar back and forth between transmit and receive mode. It transmits pulses between

² The word “control” is used here to mean that it “monitors” this volume of space. Obviously, it can’t really “control” what’s going on in the region around the antenna.

322 and 1282 times per second (this is called the radar's Pulse Repetition Frequency, or PRF), waiting for backscattered EMR (also known as returned power) (P_r) from meteorological targets between transmitted pulses. The radar's maximum range for a given PRF is given by:

$$R_{max} = \frac{c}{2 \times PRF} \quad (3.1)$$

where c is the speed of light [ms^{-1}], and PRF has units of s^{-1} . If the PRF is set to 322 pulses per second, R_{max} is slightly more than 465 km (252 nautical miles). If the PRF is set to its maximum of 1282 pulses per second, this is reduced to 116 km (63 nautical miles).

- The pulses of EMR transmitted by the antenna are linearly, diagonally polarized: The E-field associated with the EMR oscillates in a plane tilted 45 degrees from the vertical, consisting of both vertical and horizontal components.
- Backscattered EMR from targets may have vertical and horizontal components of *different* magnitudes than those of the components in the transmitted pulses, allowing the calculation of useful information about the nature of the targets. This will be discussed further in Chapter 6.

3.2.6. The width of the beam of pulses is *nominally* one degree of azimuth (so a full circumferential sweep consists of 360 beams), but the story is actually more complicated than that³. Microwave pulses are not coherent like lasers. The pulses spread out in a complex pattern that includes the main lobe (containing about 90 percent of the transmitted power), and a series of side lobes, containing less and less power as the angular distance from the beam centerline increases (Figure 3.5).

³ The width of the beam, defined by the 50 percent power points, is about 1.4 degrees (Brown and Wood 2012), however data are collected at 1-degree increments. For the remainder of this text, we will use the 1-degree data collection increment as the effective beam width.

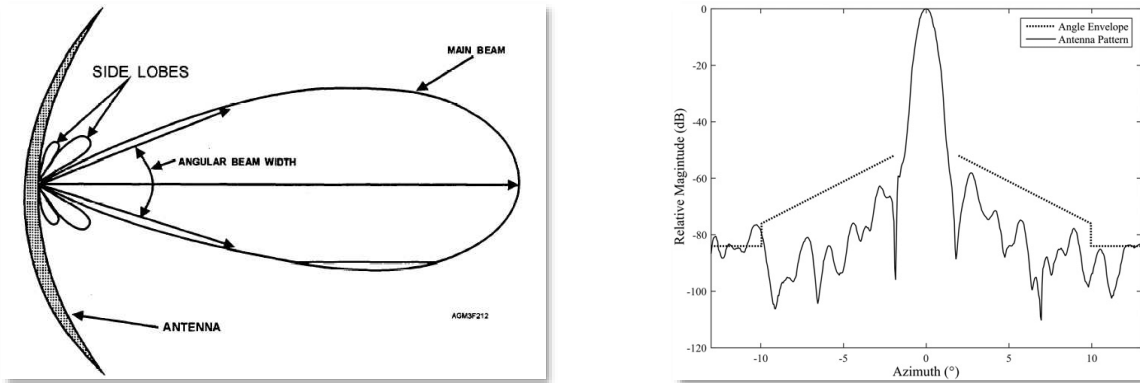


Fig. 3.5: Main and side lobes of a transmitted microwave beam. (Left image credit: http://meteorologytraining.tpub.com/14271/css/14271_61.htm; Right image credit: https://www.researchgate.net/publication/316260843_Requirement-Driven_Design_of_Pulse_Compression_Waveforms_for_Weather_Radars)

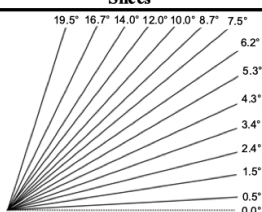
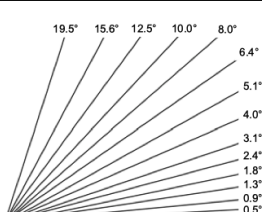
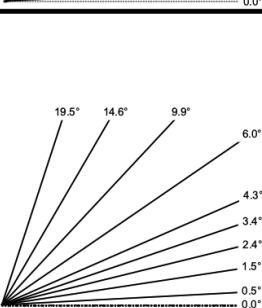
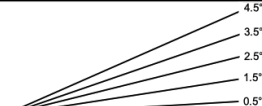
3.2.7. A Volume Control Pattern is defined by its combination of Antenna Scan Strategies and Pulse Lengths. An Antenna Scan Strategy consists of a certain number of antenna tilt angles completed in a certain period of time. Pulse lengths are either “long” or “short.” Table 3.1 lists the Antenna Scan Strategies, and Table 3.2 lists the Pulse Lengths. Figure 3.6 describes the VCPs as combinations of Scan Strategies and Pulse Lengths, as well as their uses and limitations. Note also that the description of VCPs shown in Figure 3.6 is *not* exhaustive. There are several relatively recent innovations that elaborate on these VCPs by adding more complex scan strategies, for the purpose of rapid updates. One example of this is called Supplemental Adaptive Intra-Volume Low-Level Scan (SAILS), which inserts an extra low-tilt scan at several points during the volume scan (Chrisman 2012).

Table 3.1: WSR-88D Antenna Scan Strategies.

Scan Strategy No.	No. of Tilt Angles	Time to Complete [min]
1	14	5
2	9	6
3	5	10
4	14	4.5

Table 3.2: WSR-88D Pulse Lengths.

Pulse Type	Duration [μsec]	Length [km]
Short	1.57	0.47
Long	4.5	1.35

Quick Reference VCP Comparison Table for RPG Operators					February 2008
Slices	Tilts	VCP	Time*	Usage	Limitations
	14	11	5 mins	Severe and non-severe convective events. Local 11 has Rmax=80nm. Remote 11 has Rmax=94nm.	Fewer low elevation angles make this VCP less effective for long-range detection of storm features when compared to VCPs 12 and 212.
		211	5 mins	Widespread precipitation events with embedded, severe convective activity (e.g. MCS, hurricane). Significantly reduces range-obscured V/SW data when compared to VCP 11.	All Bins clutter suppression is NOT recommended. PRFs are not editable for SZ-2 (Split Cut) tilts.
	14	12	4 ½ mins	Severe convective events. Extra low elevation angles increase low-level vertical resolution when compared to VCP 11.	High antenna rotation rates slightly decrease accuracy of the base data estimates.
		212	4 ½ mins	Rapidly evolving, widespread severe convective events (e.g. squall line, MCS). Increased low-level vertical resolution compared to VCP 11. Significantly reduces range-obscured V/SW data when compared to VCP 12.	All Bins clutter suppression is NOT recommended. PRFs are not editable for SZ-2 (Split Cut) tilts. High antenna rotation rates slightly decrease accuracy of the base data estimates.
	9	21	6 mins	Non-severe convective precipitation events. Local 21 has Rmax=80nm. Remote 21 has Rmax=94nm.	Gaps in coverage above 5°.
		121	6 mins	VCP of choice for hurricanes. Widespread stratiform precipitation events. Significantly reduces range-obscured V/SW data within 230 km when compared to other VCPs.	All Bins clutter suppression is NOT recommended. High antenna rotation rates slightly decrease accuracy of the base data estimates. PRFs are not editable. Gaps in coverage above 5°.
		221	6 mins	Widespread precipitation events with embedded, possibly severe convective activity (e.g. MCS, hurricane). Reduces range-obscured V/SW data out to 300 km when compared to other VCPs.	All Bins clutter suppression is NOT recommended. PRFs are not editable for SZ-2 (Split Cut) tilts. Gaps in coverage above 5°.
	5	31	10 mins	Clear-air, snow, and light stratiform precipitation. Best sensitivity. Detailed boundary layer structure often evident.	Susceptible to velocity dealiasing failures. No coverage above 5°. Rapidly developing convective echoes aloft might be missed.
		32	10 mins	Clear-air, snow, and light stratiform precipitation.	No coverage above 5°. Rapidly developing convective echoes aloft might be missed.

*VCP update times are approximate.

Fig. 3.6: Description of WSR-88D Volume Control Patterns. Clutter and clutter suppression are discussed later in the text. (Credit: WDTB 2008.)

3.2.8. As shown in Figure 3.6, the highest tilt angle the WSR-88D antenna ever reaches is 19.5 degrees above the horizon, and some of the VCPs don't even go that high. VCPs 31 and 32 only extend up to 4.5 degrees above the horizon. This results in a region directly above the antenna called the Cone of Silence (Figure 3.7). No information is returned to the radar from this blind area. At a range of 30 nautical

miles, and a maximum tilt of 19.5 degrees, the base of the Cone of Silence is 10 nm (61,000 feet), which is the radar's operating ceiling.

3.2.9. Looking at Figure 3.7, it is also evident that there is *another* silent area in the volume control region: Below the *lowest* tilt angle (0.5 degrees). At a range of 30 nautical miles, the top of this region is only about one quarter of a nautical mile (about 1,600 feet) ARL, but at the radar's *maximum* range of 252 nautical miles, the top of this wedge-shaped region is just over two nautical miles (about 12,000 feet) ARL. This can result in a significant loss of information, and for this reason some of the WSR system's derived products, such as precipitation estimates, suffer from pronounced degradation at extreme ranges.

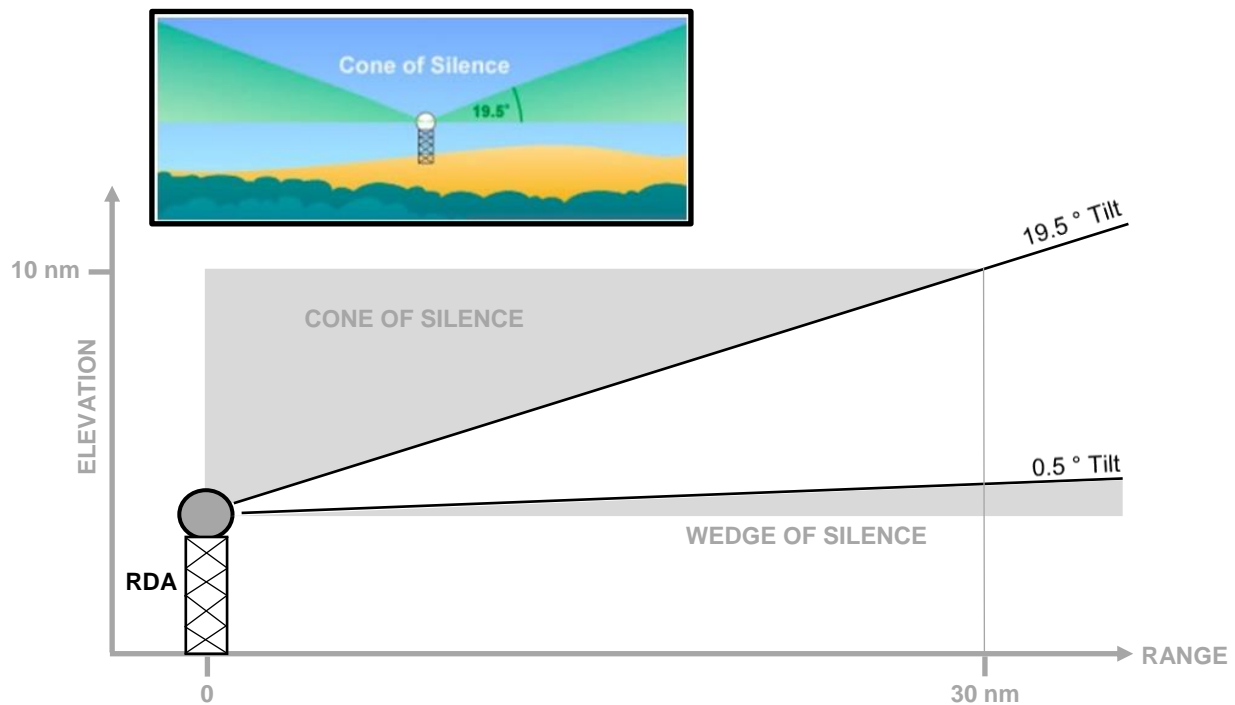


Fig. 3.7: WSR-88D Cone of Silence and Wedge of Silence. At a range of 30 nautical miles and a max tilt angle of 19.5°, the base of the *Cone* of Silence is about 10 nm ARL, which is the operating ceiling of the radar. The *Wedge* of Silence below the lowest tile angle becomes increasingly important with increasing range. (Small image credit: <https://www.roc.noaa.gov/>)

3.3. The receiver and signal processor are in operation when the duplexer is in the receive mode. The receiver captures polarized, backscattered returned power from the

system’s transmitted pulses. The processor then carries out analog-to-digital (A2D) conversion, which yields P_r in each range bin along the radial, along with its horizontal and vertical components. From returned power and its associated phase shift, Archive Level-I base moments are computed: reflectivity (Z), first-guess radial velocity (V_r), and spectrum width (w). (Reflectivity is the *zeroth moment*, radial velocity is the *first moment*, and spectrum width is the *central moment*.) The next several paragraphs describe each of these base moments in detail.

3.3.1. By converting the analog P_r to digital values, the light-travel time of the returned pulse can be used to place the returned power in the correct range bin along the radial. Range bins begin immediately outside the radome, and extend to the radar’s R_{max} . Each bin is 250-meters deep in the radial direction, and 1-degree wide in the circumferential direction⁴. Therefore, they get wider as the distance from the RDA increases, resulting in a loss of spatial resolution.

3.3.2. When the radar is set to R_{max} of 465 kilometers, there are 1860 bins along a single radial, or 669,600 bins in a single tilt angle. (At a range of 465 kilometers, the range bins are more than eight kilometers wide.) If the radar is using a VCP with 14 tilts, there are 9,374,400 range bins in a full volume scan, completed in as little as 4 ½ minutes. Once each range bin is populated with values of P_r , a very large number of calculations must be completed for each range bin before the next volume scan is completed. Some of these calculations are completed by the RDA’s own processors. Many additional calculations are completed by the processors in the RPG.

3.4. The first of the three base moments to be computed is reflectivity (Z), which is defined by:

$$Z \equiv \int_0^{\infty} N(D) D^6 dD \tag{3.2}$$

where $N(D)$ is the dropsize distribution (a function describing the number of drops with a given diameter per unit volume) [m^{-3}], and D is the drop diameter [mm]. The

⁴ There has been some recent work to improve this resolution, using the WSR-88D at the National Severe Storms Laboratory (NSSL) in Norman, Oklahoma. The radar was adjusted so that range bins were reduced to one quarter the standard size: ½ degree wide, and 125 meters deep in the radial direction. This means that, where there is one range bin in standard radar data, there are four in the high-res data. “Super Resolution” data are now available for all three base moments, in some Volume Control Patterns, at some tilt angles. See WDTB (2018) for more.

function is integrated over all drop diameters from zero to infinity, although, in practical terms, raindrops are rarely larger than 5 mm in diameter, and *never* have a diameter of zero (Rogers and Yau 1989). Z is the resulting linear reflectivity and has units of $\text{mm}^6 \text{m}^{-3}$.

3.4.1. For example, let's suppose that we are imaging a cubic meter of space inside a cloud, and it contains one 3-mm drop, and 729 one-mm drops (Figure 3.8). In this case, (3.2) becomes:

$$Z = [(1)(3^6)] + [(729)(1^6)] = 729 + 729 = 1458 \frac{\text{mm}^6}{\text{m}^3}$$

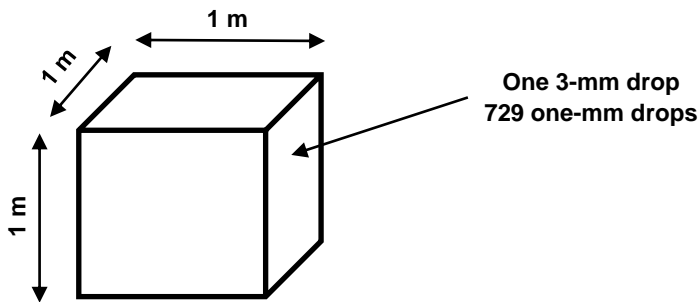


Fig. 3.8: Example 1 showing a cubic meter volume with two different sized raindrops.

This example shows that the contribution to the overall reflectivity from the single 3-mm drop is equal to that of all 729 one-mm drops. This is because of the strong dependence on drop diameter.

3.4.2. Reflectivity is usually converted to a logarithmic scale (dBZ) by:

$$\text{dBZ} \equiv 10 \log_{10}(Z) \tag{3.3}$$

which has units of decibels (dB). Z is the linear reflectivity as computed by (3.2). For the example shown above, the logarithmic reflectivity is:

$$10 \log_{10}(1458) = 31.64 \text{ dBZ}$$

which is equivalent to a very light rainshower.

3.4.3. In practice, we don't know the dropsize distribution, so cannot compute the reflectivity using (3.2). Instead, the Probert-Jones Radar Equation is used to estimate reflectivity from returned power:

$$P_r = \frac{P_t G^2 \theta \phi H \pi^3 k^2 L}{1024 (\ln 2) \lambda^2} \cdot \frac{Z}{x^2} \quad (3.4)$$

where P_r is the returned (backscattered) power, P_t is transmitted power (750 kW), G is antenna gain, and θ and ϕ are the beamwidths in the horizontal and vertical dimensions (respectively). H is the Pulse Length (see Table 3.2), k is a physical constant related to the target character, L is signal loss factors (related to attenuation), λ is the radar wavelength (10.3 cm), x is the target range, and Z is reflectivity. Of these, G , k , θ , ϕ and L are approximations. Reflectivity is computed by solving (3.4) for Z (Rinehart 2004).

3.4.4. The use of a single returned pulse to compute P_r in a given range bin would result in large errors, that is, a "noisy" pattern. Instead, the following two steps are taken that act as a low-pass filter to smooth out noise and compute a more representative reflectivity field:

- Six to 64 pulses (depending on the PRF in use) are analyzed for returned power in each range bin. An average P_r is computed for each range bin using this information.
- The average P_r from four successive 250-meter range bins are then averaged together, creating an average P_r in a larger 1-km ensemble range bin (Fig. 3.9).

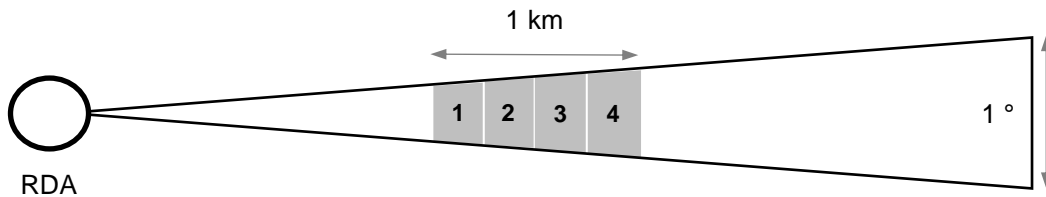


Fig. 3.9: Four successive 250-m range bins along a 1°-wide radial, creating a larger 1-km deep reflectivity range bin (plan view).

Mathematically, this is given by:

$$\bar{P}_r^{1km} = \frac{\bar{P}_{r1}^{250m} + \bar{P}_{r2}^{250m} + \bar{P}_{r3}^{250m} + \bar{P}_{r4}^{250m}}{4} \quad (3.5)$$

where the averaged P_r values on the right-hand side (RHS) represent the values computed for each of the four range bins in the ensemble. The average returned power for the 4-bin ensemble is then put in the Probert-Jones Radar Equation to compute one reflectivity for the entire ensemble. The resulting computed reflectivity has an error of less than 1 dBZ (WDTB 2005).

3.4.5. Rainfall rate (R) is one of the most important quantities derived from reflectivity data⁵. Unfortunately, R is physically quite different than Z, and there is no one-to-one relationship between the two. Mathematically, R [mm s⁻¹] is given by:

$$R \equiv \frac{\pi}{6} \int_0^{\infty} N(D) D^3 w_t(D) dD \quad (3.6)$$

where $N(D)$ is the dropsize distribution (as in (3.2.)) [m⁻³], D is the drop diameter [mm], and $w_t(D)$ is the terminal fall speed for spherical raindrops, as a function of their diameters [ms⁻¹] (WDTB 2005). Table 3.3 lists values of $w_t(D)$.

⁵ R is an Archive Level III derived product.

Table 3.3: Terminal Fall Speed as a Function of Drop Diameter. (Credit: Rogers and Yau 1989.)

Diameter [mm]	Fall Speed [ms^{-1}]	Diameter [mm]	Fall Speed [ms^{-1}]
0.1	0.27	2.6	7.57
0.2	0.72	2.8	7.82
0.3	1.17	3.0	8.06
0.4	1.62	3.2	8.26
0.5	2.06	3.4	8.44
0.6	2.47	3.6	8.60
0.7	2.87	3.8	8.72
0.8	3.27	4.0	8.83
0.9	3.67	4.2	8.92
1.0	4.03	4.4	8.98
1.2	4.64	4.6	9.03
1.4	5.17	4.8	9.07
1.6	5.65	5.0	9.09
1.8	6.09	5.2	9.12
2.0	6.49	5.4	9.14
2.2	6.90	5.6	9.16
2.4	7.27	5.8	9.17

3.4.6. For example, let's suppose that we have a cubic meter of space inside a cloud, and it contains 600 1-mm drops (Figure 3.10). Table 3.3 indicates these drops would have a terminal velocity of about 4 ms^{-1} . In this case, (3.6) becomes:

$$\begin{aligned}
 R &= \frac{\pi}{6} \left[\frac{600}{\text{m}^3} \right] [(1 \text{ mm})^3] \left[4 \frac{\text{m}}{\text{s}} \right] \\
 &= \frac{\pi}{6} \left[\left(\frac{600}{\text{m}^3} \right) \left(\frac{\text{m}^3}{10^9 \text{ mm}^3} \right) \right] [(1 \text{ mm})^3] \left[\left(4 \frac{\text{m}}{\text{s}} \right) \left(\frac{1000 \text{ mm}}{\text{m}} \right) \right] \\
 &= \frac{\pi}{6} \left(\frac{600}{10^9} \right) \left(\frac{4000}{1} \right) \left(\frac{\text{mm}}{\text{s}} \right) = 1.257 \times 10^{-3} \frac{\text{mm}}{\text{s}}
 \end{aligned}$$

where the terms in red are conversion factors necessary to obtain the correct units for R.

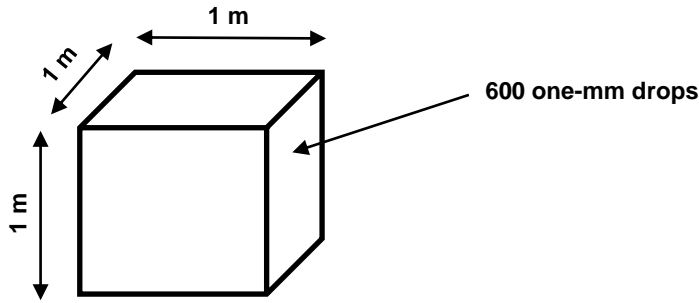


Fig. 3.10: Example 2 showing a cubic meter volume with 600 one-mm drops.

Since R is more commonly expressed in inches per hour (in hr^{-1}), a few more conversion factors (shown in red) can be applied:

$$R \left[\frac{\text{in}}{\text{hr}} \right] = R \left[\frac{\text{mm}}{\text{s}} \right] \times \left(\frac{3600 \text{ s}}{\text{hr}} \right) \times \left(\frac{0.03937 \text{ in}}{\text{mm}} \right) \quad (3.7)$$

For the example shown above, the result of (3.6) is $\approx 0.18 \text{ in hr}^{-1}$. Next, let's consider two examples that show the poor correlation between reflectivity and rainfall rate.

Example 3: Same Z , different R . Let's assume we have two 1-m^3 volumes. In the first, there are 729 one-mm drops with a terminal velocity of 4 ms^{-1} . In the second, there is one 3-mm drop with a terminal velocity of 8 ms^{-1} .

- By (3.2), both volumes have a Z -value of $729 \text{ mm}^6 \text{ m}^{-3}$ ($\approx 29 \text{ dBZ}$).
- By (3.6) and (3.7), the first volume has an R -value of $\approx 0.22 \text{ in hr}^{-1}$. The second has an R -value of $\approx 0.01 \text{ in hr}^{-1}$.

Example 4: Different Z , same R . Let's assume we have two 1-m^3 volumes. In the first, there are 600 one-mm drops with a terminal velocity of 4 ms^{-1} . In the second, there are 50 2-mm drops with a terminal velocity of about 6 ms^{-1} .

- By (3.2), the first volume has a Z -value of $600 \text{ mm}^6 \text{ m}^{-3}$ ($\approx 28 \text{ dBZ}$). The second has a Z -value of $3200 \text{ mm}^6 \text{ m}^{-3}$ ($\approx 35 \text{ dBZ}$).
- By (3.6) and (3.7), both volumes have an R -value of $\approx 0.18 \text{ in hr}^{-1}$.

3.4.7. So, how is rainfall rate estimated from reflectivity, given the very poor relationship between the two? This will be discussed in much greater detail in Chapter 8, but for now, here is a short answer: We use what are called Z-R Relationships, derived empirically from long-term climatological data relating the observed reflectivity in a given range bin to the rainfall measured by a precipitation can, located somewhere on the ground in that range bin. Z-R Relationships take the following general form:

$$Z = \alpha R^\beta \quad (3.8)$$

where Z is the linear reflectivity (computed from the Probert-Jones Radar Equation), R is the rainfall rate [mm hr^{-1}], and α and β are coefficients to be determined by a least-squares fit. This is the form for unpolarized reflectivity, and it produces large errors in rainfall rate estimates. These large errors were the primary motivation for retrofitting the WSR-88D radar network with dual-pol capability. For the updated WSR-88D network, there are more sophisticated expressions involving dual-pol data, described in Chapter 8.

3.5. The second of the three base moments to be computed is radial velocity (V_r). In Chapter 2, it was shown that using a direct application of the Doppler Effect (2.13) would not work for meteorological applications. Thus, the WSR-88D radar uses an alternative method that enables an estimate of the inbound or outbound velocity components for meteorological targets, but also:

- Necessitates additional algorithms that attempt to resolve two different types of introduced ambiguity, which will be discussed later;
- Limits the Maximum Unambiguous Range (R_{\max}) of the radar when there are high-velocity circulations (such as mesocyclones and tornadic vortex signatures) in the volume scan area; *and*,
- Propagates error through many of the suite of Archive Level III (derived) products.

3.5.1. The method used is called Pulse-Pair Processing, which compares the phase shift of two successive backscattered pulses. The explanation of this is helped by

using phasor diagrams, which are an alternative method of illustrating the oscillations of the E- or B-fields in EMR. Often, EMR is described graphically using a diagram similar to the one shown in Figure 2.3, which explicitly shows the sinewave pattern. Another method is to assume that the wave's oscillation can be described by dividing its wavelength up into radians, so that each full oscillation of the wave has a length of 2π radians. A phasor diagram shows the EMR's oscillations in terms of radians on a circular graph (Figure 3.11). One complete oscillation constitutes a complete trip around the circle. A given location in the EMR's propagation path corresponds to a phase angle (ϕ).

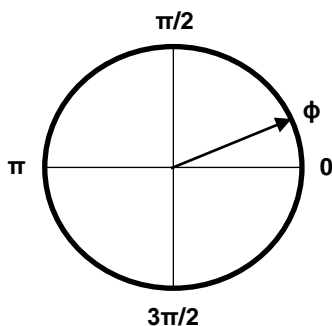


Fig. 3.11: Sample phasor diagram. The arrow indicates a given location in the propagation path of the EMR, called the phase angle.

3.5.2. The WSR is a coherent radar. When it generates and transmits a pulse, it stores a twin copy (called a reference pulse) internally. When the transmitted pulse encounters a target (such as a raindrop), it does so at a specific phase angle. This phase angle is encoded onto the backscattered pulse. When the backscattered pulse is received at the radar, the phase angle (ϕ_1) at which it encountered the target is determined by comparing the pulse to its stored twin. The radar then generates another pair of pulses - one to be transmitted, and one to be stored for comparison. If the target has moved radially, either closer to the radar or farther away, then the second pulse will encounter it at a *different* phase angle, which is then determined by comparing it to *its* stored twin (ϕ_2). Figure 3.12 shows an example of this.

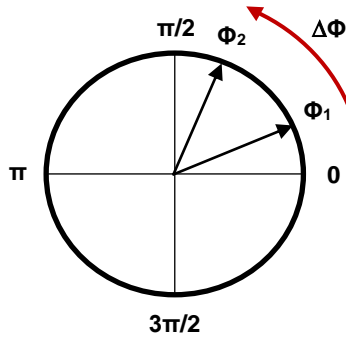


Fig. 3.12: Sample phasor diagram showing the phase shift for two successive pulses when a target is inbound. Curved red arrow indicates the *pulse-to-pulse phase shift* ($\Delta\phi$).

3.5.3. The pulse-to-pulse phase shift ($\Delta\phi$) is the difference between the two pulse phases, measured from the first phase shift to the second (Figure 3.12). This quantity, when divided by the time between the two successive pulses (Δt), is equal to the Doppler frequency shift, that is:

$$\Delta f_{dop} = \frac{\Delta\phi}{\Delta t} \quad (3.9)$$

But, by (2.13), we also have:

$$\Delta f_{dop} = \frac{-2V_r}{\lambda}$$

Combining these two, we now have:

$$\frac{\Delta\phi}{\Delta t} = \frac{-2V_r}{\lambda} \quad (3.10)$$

or,

$$V_r = -\frac{\lambda\Delta\phi}{2\Delta t} \quad (3.11)$$

which provides an alternative method of computing the radial velocity of meteorological targets. The time difference (Δt) is selected by choosing a PRF, which is described later.

Equation (3.11) implies the following:

- If the pulse-to-pulse phase shift is negative (rotating in a *clockwise* direction), then radial velocity is *positive*, and the target is *outbound*.
- If the pulse-to-pulse phase shift is positive (rotating in a *counter-clockwise* direction) then the radial velocity is *negative*, and the target is *inbound*.

Another way of remembering this is to use the Right-Hand Rule (RHR): Using your right hand, wrap your fingers in a direction pointing from ϕ_1 to ϕ_2 . (Test this on Figure 3.12.)

- If your thumb is pointing *out of the page* (toward you), the target is *inbound*.
- If your thumb is pointing *into the page* (away from you), the target is *outbound*.

3.5.4. This might seem to solve the problem of computing radial velocity (and it does to a limited extent), but it introduces a new problem: *What if the target radial velocity is so large that the pulse-to-pulse phase shift is 180 degrees (π radians) or more?* If this happens, then it's impossible to know *a priori* the direction and magnitude of $\Delta\phi$, and the first-guess radial velocity (also known as the zeroth alias), *which always uses the smaller of the two possible rotation angles* (going in opposite directions around the circle), will be incorrect.

3.5.5. The radial velocity associated with a 180-degree pulse-to-pulse phase shift is called the Maximum Unambiguous Velocity (V_{\max}), and it is computed by:

$$V_{\max} = \frac{\lambda \times PRF}{4} \quad (3.12)$$

where λ is the wavelength of the radar (converted to meters). PRF has units of s^{-1} . If the PRF is set to its minimum value of 322 pulses per second, V_{\max} is about 8 ms^{-1} (16 knots).

If the PRF is set to 1282 pulses per second, V_{\max} becomes 33 ms^{-1} (about 64 knots). All first-guess radial velocities are related to V_{\max} by:

$$\frac{V_r}{|V_{\max}|} = \frac{-\Delta\phi}{\pi} \quad (3.13)$$

where the vertical bars indicate absolute value. This means that:

$$V_r = |V_{\max}| \frac{-\Delta\phi}{\pi} = -\left(\frac{\lambda \times PRF}{4}\right) \frac{\Delta\phi}{\pi} \quad (3.14)$$

3.5.6. As with P_r (and Z), the use of a single pair of returned pulses to compute V_r in a given range bin would result in large errors and a “noisy” velocity field. Instead, 40 to 50 pulse-pairs are used for each range bin, and the resulting 40 to 50 values for $\Delta\phi$ are placed into a power-weighted average:

$$\overline{\Delta\phi} = \sum_{n=1}^N \frac{P_{rn} \Delta\phi_n}{P_{rn}} \quad (3.15)$$

where $\Delta\phi_n$ are the pulse-to-pulse phase shifts from each individual measurement, and P_{rn} is the returned power associated with each pulse-pair. N is the number of pulse-pairs in the average. This means that targets within a given range bin returning the most backscattered power have the greatest influence in the calculation of the radial velocity. The result of (3.15) is then placed into (3.14) to compute the first-guess radial velocity in each 250-m range bin, with an error of less than 1 ms^{-1} . Note that V_r has a higher spatial resolution than Z , because the former is assigned one value for each 250-m range bin, while the latter is assigned one value for an ensemble of *four* 250-m range bins.

3.6. The third of the three base moments to be computed is spectrum width (w), which is the range of radial velocities computed in each range bin from all 40 to 50 pulse-pairs. Spectrum width’s relationship to returned power and radial velocity is shown in Figure 3.13.

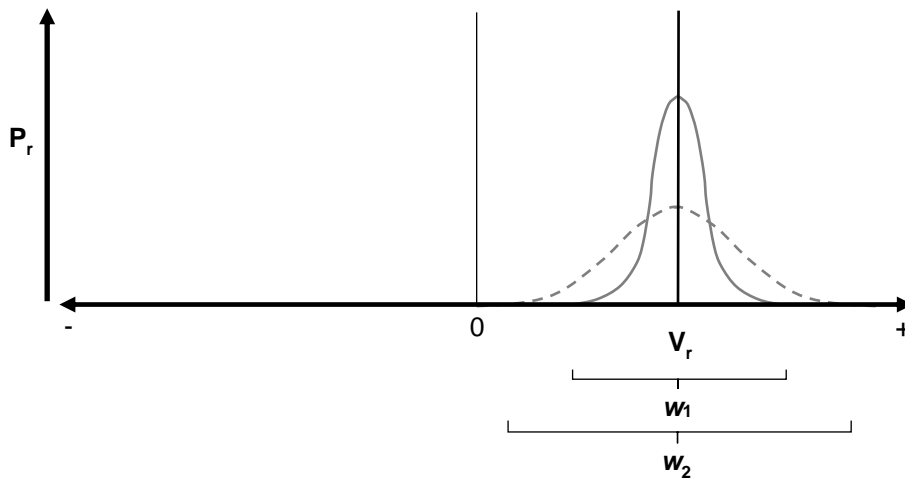


Fig. 3.13: Relationship between w , V_r , and P_r in each range bin. Horizontal axis is radial velocity, with inbounds on the left and outbounds on the right. Zero radial velocity is in the center. Vertical axis is returned power. Radial velocity for an outbound target computed by the power-weighted average (3.13) is indicated with V_r . A spectrum width associated with a typical high- P_r target is shown as a narrow Gaussian (w_1). A spectrum width associated with a typical low- P_r target is shown as a wider Gaussian (w_2).

3.6.1. The spectrum width in a given range bin can be affected by both meteorological and non-meteorological factors. Non-meteorological factors are:

- **Range:** As the distance from the RDA increases, the width of each range bin (in the circumferential direction) increases, which increases the likelihood of a larger variation in radial velocity.
- **Signal-to-noise ratio:** Signals from very weak returns (near the “grass level” of the radar, or the lower limit of detection) have a high spectrum width.
- **Ground Clutter and Anomalous Propagation:** These will be discussed in greater detail later, but for now, understand that Ground Clutter is backscattered energy from objects on the surface of the Earth – usually near the RDA, and Anomalous Propagation (AP) is Ground Clutter at a distance, caused by refraction of the radar beam by a temperature inversion.
 - Range bins that contain buildings or mountains in calm wind conditions have high returned power, radial velocities centered near zero, and narrow spectrum width. Under high wind conditions, eddies around the

edges of the stationary objects may also be imaged by the radar, broadening the spectrum width but leaving radial velocities centered at zero.

- Range bins that contain cars on highways have high returned power, radial velocities with two non-zero maxima, and a broad spectrum width.

3.6.2. Meteorological conditions associated with a broad spectrum width are:

- **Boundaries** (outflow, fronts, etc.)
- **Thunderstorms**
- **Wind shear regions**
- **Turbulence**

This completes the overview of the RDA and the radar's three base moments. In the next chapter, we will discuss the remaining components shown in Figure 3.2.

Summary. A WSR-88D system consists of three major components, connected by two modes of communication. The first component is the Radar Data Acquisition module, which includes the transmitter, wave guides, duplexer, antenna, receiver, antenna tower and dome, block house, and RDA maintenance terminal. The other two components are the Radar Products Generator and the Users. The RDA and RPG are linked by broad-band communications, and the RPG and users are linked by narrow-band communications.

Radar data fall into three levels. Level I consists of raw base moments, Level II of quality-controlled base moments, and Level III of derived products. The RDA obtains Level I data and begins the quality control process to generate high-resolution Level II data. (The QC process is discussed in detail in the next chapter.)

The RDA antenna is about 7 ½ meters in diameter, and rests on a turntable underneath a dome, standing on a tower up to 30 meters high. The turntable rotates that antenna through a full 360-degree circle, and also tilts the antenna from nearly horizontal to a maximum elevation angle of about 19 degrees above the horizon. The transmitter (which uses a Klystron tube) generates pulses with a peak power of 750 kW, at a wavelength of 10 cm (making the WSR-88D an S-band radar). The pulses are linearly, diagonally polarized. The beam of pulses is approximately 1° wide.

The RDA scans the three-dimensional volume of space around the radar using a Volume Control Pattern. A VCP consists of combinations of Antenna Scan Strategies and Pulse Lengths. Every VCP has a Cone of Silence above the highest tilt angle, and a Wedge of Silence below the lowest tilt angle.

There are three base moments generated by the RDA. This first is reflectivity, which is estimated for a given 1-km range bin using returned power from up to 60 pulses in four successive 250-m range bins, and the Probert-Jones Radar Equation. The second is radial velocity, and the third is spectrum width.

The radar's Maximum Unambiguous Range varies between 116 and 465 km, corresponding to Pulse Repetition Frequencies of 1282 and 322 pulses per second. The relationship between the two is *inverse*, so *decreasing* the PRF *increases* the maximum range, but has the *opposite* effect on radial velocity, since PRF and Maximum Unambiguous Velocity are *directly* related. This is a consequence of using Pulse-Pair Processing to compute radial velocity, which compares the phase shift of two successive pulses interacting with a given target to estimate Doppler velocity. Up to 50 pulse-pairs are used to compute radial velocity in each 250-m range bin.

Spectrum width is the range of radial velocities in a given range bin. The spectrum width can vary, depending on the type of targets in the range bin, the distance between the range bin and the RDA, the amount of returned power, and the presence of Ground Clutter or Anomalous Propagation.

Rainfall rate is estimated using Z-R Relationships, which are determined statistically based on geographic location and the type of weather conditions present. There is no one-to-one relationship between reflectivity and rainfall rate, so these estimates are often handicapped by large errors. Newer precipitation estimation techniques are now in use that include conventional reflectivity and several dual-pol parameters. These are discussed in greater detail in Chapter 8.

Terms and concepts:

- Advanced Weather Interactive Processing System (AWIPS)
- Analog-to-digital conversion (A2D)
- Anomalous Propagation
- Antenna
- Antenna Scan Strategy
- Archive levels I, II, and III
- Average transmitted power
- Base moments

- Broad-band communications links
- Coherent radar
- Cone of Silence
- Decibel (dB)
- Doppler frequency shift (Δf_{dop})
- Dropsize distribution ($N(D)$)
- Duplexer (DUPL)
- First-guess radial velocity
- Grass level
- Ground Clutter
- Human Control Interface (HCI)
- Klystron (transmitter tube)
- Linear reflectivity
- Magnetron (transmitter tube)
- Main lobe
- Master System Control Function (MSCF)
- Maximum Unambiguous Range (R_{max})
- Maximum Unambiguous Velocity (V_{max})
- Narrow-band communications links
- Peak transmitted power
- Phase angle (ϕ)
- Phase shift ($\Delta\phi$)
- Phasor diagram
- Power-Amplifier-Transmitter (PAT)
- Power-Oscillator-Transmitter (POT)
- Probert-Jones Radar Equation
- Pulse Length
- Pulse-Pair Processing
- Pulse Repetition Frequency (PRF)
- Pulse-to-pulse phase shift ($\Delta\phi$)
- Radar Data Acquisition module (RDA)
- Radar Products Generator module (RPG)
- Radial velocity (V_r) (first moment)
- Rainfall rate (R)
- Range bin
- RDA Maintenance Terminal

- Receiver (RCVR)
- Reference pulse
- Reflectivity (Z) (zeroth moment)
- Returned power (P_r)
- Right-Hand Rule (RHR)
- Side lobes
- Signal processor (PROC)
- Signal-to-noise ratio
- Spectrum width (w) (central moment)
- Supplemental Adaptive Intra-Volume Low-Level Scan (SAILS)
- Terminal fall speed ($w_t(D)$)
- Transmitter (XMTR)
- Volume Control Pattern (VCP)
- Wave guide
- Weather Forecast Office (WFO)
- Z-R Relationships

Study prompts:

1. Describe the three levels of radar data.
2. Sketch a block diagram of a WSR-88D system, including two major modules, two communication channels, and any other components necessary.
3. Create a schematic diagram of the RDA, listing its subcomponents. Briefly describe the characteristics and functions of each subcomponent. Note aspects such as antenna size, polarization, peak and average transmitted power, wavelength, beamwidth, etc.
4. What is a Volume Control Pattern? How is it carried out? What does it consist of? Discuss the variations available in each of a VCP's two defining components.
5. Discuss PRF and Maximum Unambiguous Range. How does R_{\max} vary with PRF?
6. Discuss main and side lobes of a microwave beam.

7. What is the cause of the Cone of Silence? Where is it found?
8. What is a range bin?
9. Define reflectivity and rainfall rate (mathematically), then define each of its individual terms. Explain why there is no one-to-one relationship between the two.
10. How does the terminal fall speed of a raindrop vary with its diameter?
11. Explain why the Probert-Jones Radar Equation is used to compute reflectivity. Discuss some of the approximations used in the equation. How many pulses are used to compute the reflectivity in a range bin? What kind of averaging is applied to the process?
12. Use a phasor diagram to describe Pulse-Pair Processing. Explain in detail how this is used to estimate radial velocity. What kind of averaging process is applied to the calculation?
13. What is Maximum Unambiguous Velocity and why does it occur? How does it relate to PRF and phase shift? What happens if the radial velocity of a target exceeds V_{\max} ?
14. How does the radial resolution of radial velocity differ from the radial resolution of reflectivity?
15. How are spectrum width and radial velocity related? How are they both related to returned power?
16. List and describe some non-meteorological factors affecting spectrum width.

4. The rest of the WSR-88D system, the Doppler Dilemma, and the production of Level II data.

In this chapter we discuss the Radar Products Generator, Broad- and narrow-band communications channels, and the radar data users. Then we go into detail describing three important filters (and the problems they address) applied to Level I data to produce Level II data.

4.1. Figure 4.1 shows the block diagram of a WSR-88D installation again. In Chapter 3, the RDA and production of Archive Level I were discussed in detail. In this chapter, we'll go through the remainder of the system, and discuss the production of Archive Level II data. But first, we'll look at one very fundamental problem: The conflict between maximizing the radar's effective range and its ability to unambiguously resolve radial velocities.

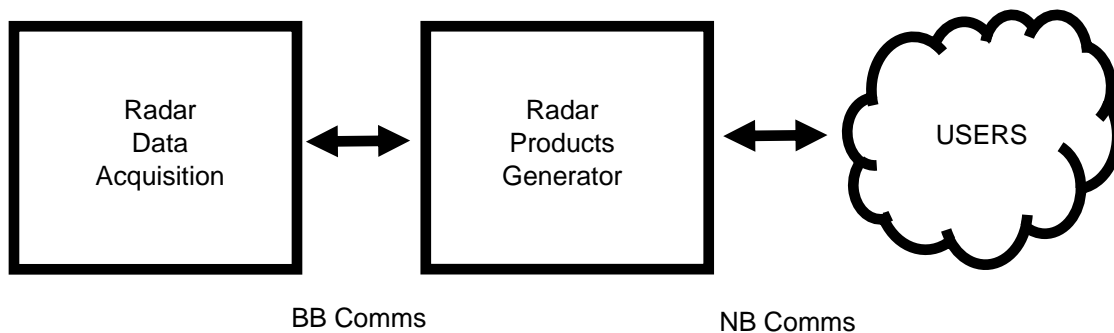


Fig. 4.1: Block diagram of a WSR-88D system.

4.2. **The Doppler Dilemma.** Recall the expressions for Maximum Unambiguous Range (R_{max}) and Maximum Unambiguous Velocity (V_{max}), originally introduced in Chapter 3:

$$R_{max} = \frac{c}{2 \times PRF}$$

$$V_{max} = \frac{\lambda \times PRF}{4}$$

While increasing the PRF increases V_{max} (they are *directly* proportional), it also has the unfortunate effect of decreasing R_{max} (they are *inversely* proportional). This means that, in meteorological scenarios associated with severe weather, such as thunderstorms (with rotating updrafts called mesocyclones) or tornadoes, adjustments to the radar to help clearly resolve these features will also limit its range. This is the Doppler Dilemma, and it can be summed up by saying “there is no single PRF that maximizes both R_{max} and V_{max} ” (WDTB 2005).

4.2.1. There is no complete solution to the Doppler Dilemma, but it *can* be managed. This is done by switching the radar between a slow PRF, which is used to collect Archive Level I reflectivity data, and a rapid PRF, which is used to collect Archive Level I (first guess) radial velocity and spectrum width data. These two modes are called Continuous Surveillance (CS) and Continuous Doppler (CD), respectively. During the first volume scan, the RDA will use the slow PRF for CS, and in the next, it will switch to the rapid PRF for CD. Then, it will switch back to the CS mode.

4.2.2. There are eight different PRFs in the WSR-88D’s toolbox. These are listed in Table 4.1, along with their associated R_{max} and V_{max} values. The table also includes the area of Earth’s surface monitored by each PRF. The top three are generally used for CS, and the bottom five are used for CD (WDTB 2005).

It’s worth spending a little more time with the table. The maximum area monitored, when the radar is using the *slowest* PRF, is nearly 200,000 square nautical miles (or about 680,000 square kilometers). When using the *fastest* PRF, this is reduced to about 12,500 square nautical miles (about 43,000 square kilometers). *The area associated with the fastest PRF is only about six percent of the area associated with the slowest PRF.* We are forced to make this rather dramatic sacrifice because of the Doppler Dilemma.

Table 4.1: Pulse Repetition Frequencies used by the WSR-88D system. The top three are used for CS (reflectivity); bottom five are used for CD (radial velocity and spectrum width). All values of R_{\max} and V_{\max} have been rounded to the nearest whole number. Equivalent areas refer to a disk shaped region with radius R_{\max} on a flat Earth.

PRF No.	Pulses per second	R_{\max} [km]	Equivalent Area [km ²]	R_{\max} [nm]	Equivalent Area [nm ²]	V_{\max} [ms ⁻¹]	V_{\max} [kts]
1	322	465	679,290	252	199,500	8	16
2	446	336	354,670	182	104,060	11	22
3	644	233	170,550	126	49,876	17	32
4	857	175	92,110	95	28,353	22	43
5	1014	148	68,813	80	20,106	26	51
6	1095	137	58,965	74	17,203	28	55
7	1181	127	50,671	69	14,957	30	59
8	1281	117	43,005	63	12,469	33	64

4.3. The RDA produces Archive Level I data, switching back and forth between CS and CD mode every other volume scan. It then executes the first two of three primary filters required to compute the corresponding Archive Level II data. (These are discussed in detail below.) The data are then shipped to the RPG via the broad-band communications link, while the RDA gets to work on collecting the raw data for the next volume scan.

4.3.1. The data transmission rate of any communications link can be described by the Shannon-Hartley Theorem, which states:

$$C = B \log_2 \left(1 + \frac{S}{N} \right) \quad (4.1)$$

where C is the channel capacity [bits per second], B is the band width [hertz], S is the average received signal power [Watts], and N is the average noise in the channel [Watts]. Together, S/N are the signal-to-noise ratio (Taub and Schilling 1986). Channel capacities for some means of communications are:

- **Direct wire:** 10 gigabytes⁶ s⁻¹
- **T1 line:** 1.544 megabytes s⁻¹
- **Microwave line-of-sight (MLOS):** 30 megabytes s⁻¹

⁶ A "byte" is 8 bits. A "bit" is a single digit (1 or 0). One megabyte is a million (10⁶) bytes; one gigabyte is a billion (10⁹) bytes; one terabyte is a trillion (10¹²) bytes.

4.3.2. The broad-band communications link between the RDA and the RPG may be accomplished by the following means, depending on the distance between the two:

- **Direct wire:** Distance between RDA and RPG is less than 400 feet (120 m). This is used in those cases where the WSR is operated by the FAA or DoD, and the RPG is actually within the RDA blockhouse.
- **Private T1 line:** Distance is between 400 feet (120 m) and 3000 feet (about 1 km). This configuration is used for some WSRs operated by the NWS.
- **Telco T1 line:** Distance is too far for a private T1 line. About half of the WSRs operated by the NWS use this configuration.
- **MLOS:** Rarely used; distances between one and 40 km. One example of this configuration is the WSR on Middleton Island, in the Gulf of Alaska. The associated RPG is located in the Anchorage, AK WFO.

About half of the installed WSRs also have a backup broad-band link, in the event the primary fails for some reason. These are usually either cellular modem or Very Small Aperture Terminal (VSAT). The latter is a two-way satellite ground station using dish antennas (WDTB 2005; WDTD 2019).

4.4. The **Radar Products Generator (RPG)** is a multi-function unit that ingests partially completed Archive Level II data, and applies the final filter to produced finished Archive Level II, processes Archive Level II data into Archive Level III data, and distributes Archive Level II and III data (via the narrow-band communications link) to all users. The RPG accepts One Time Requests (OTR) from AWIPS, and creates the requested product from the available Archive Level II data. For WSR-88D installations under the management of the NWS, it is a rack of servers located in the WFO's computer server room. For FAA and DoD WSRs, the RPG is located in the same blockhouse as the RDA (WDTB 2005).

The Human Control Interface (HCI)/Master System Control Function (MSCF) is a desktop computer that sits on the WFO forecast floor, and provides an interface for meteorologists to interact with the entire system. (Figure 4.2 shows the top-level graphical user interface that appears on the HCI screen.) Using the HCI, forecasters can control (1) non-maintenance changes in the operational state of the RDA, such as selecting the VCP or the clutter suppression pattern; (2) broad- and narrow-band communications links; and (3) Archive Level III products generation. These changes to

the overall system are made via a “point and click” interface and a series of dialog boxes into which a forecaster can enter data and settings. The HCI also provides comprehensive system status for the WFO’s WSR-88D installation (WDTB 2005).

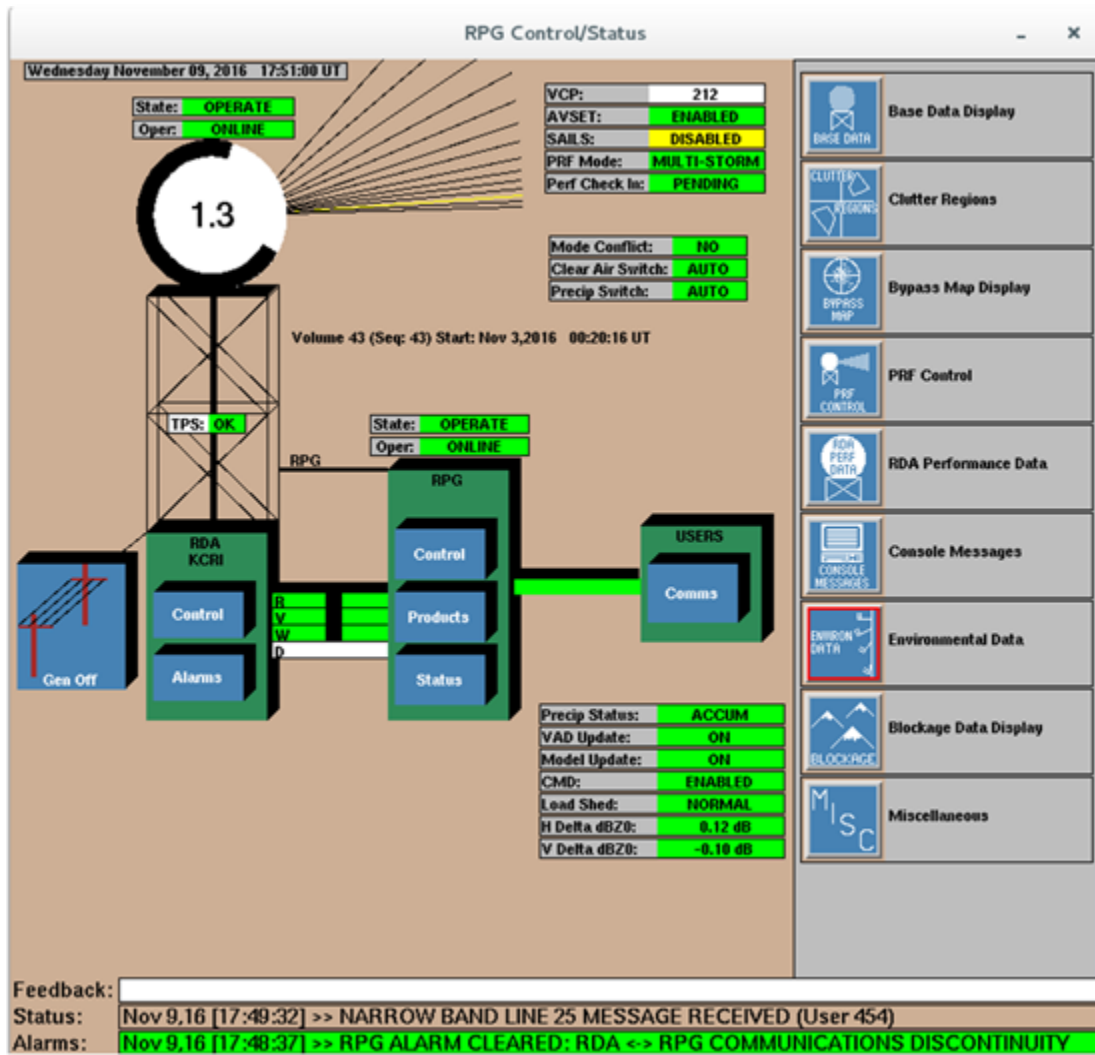


Fig. 4.2: HCI/MSCF graphical user interface. (Credit: <https://training.weather.gov/wtdt/courses/rac/intro/mscf/rpg-hci.html>)

4.5. Narrow-band communications (also known as the Product Distribution Communications) distribute products from the RPG to the end users. For NWS offices with a dedicated RPG, this link is via Local Area Network (LAN). For FAA or DoD (or NWS offices without an RPG), this link is via a dedicated IP connection. Additional

users, such as private industry or universities, access data via a dedicated satellite downlink (called a NOAAPort), NIDS, or the internet.

4.6. Users consist of AWIPS, other government agencies (such as the FAA, which uses the Weather and Radar Processor (WARP)), universities, and private companies. Radar data are also shared with other elements of the National Oceanic and Atmospheric Administration (NOAA), and are ultimately archived by the National Centers for Environmental Information (NCEI) (WDTB 2005).

4.7. To produce Archive Level II data, three primary filters are applied to Archive Level I data:

- **Ground Clutter suppression:** Attempts to remove returned power from objects on the surface of the Earth.
- **Range folding correction:** Attempts to correct the first of two problems introduced by using pulse-to-pulse phase shifting for computing radial velocity, which is the placement of computed velocities in the wrong range bin.
- **Velocity dealiasing:** Attempts to correct for the second of two problems introduced by using to pulse-to-pulse phase shifts, which is the calculation of non-representative radial velocities when the phase shift exceeds 180 degrees.

The first two are carried out by the RDA. The third is carried out by the processors in the RPG. All three of these are discussed in detail below.

4.7.1. **Ground Clutter suppression.** Ground Clutter occurs when returned power from stationary or nearly stationary targets is processed into the Archive Level I data. Since all higher-level products are built on these data, Ground Clutter contamination can degrade them. Precipitation estimates are very sensitive to contamination. In general, Ground Clutter is most prevalent at the lowest tilt angles, at ranges closest to the RDA. It occurs during all atmospheric conditions, and is present most of the time (WDTB 2005).

4.7.1.1. In reflectivity-based products (Figure 4.3),

- Ground targets return high power

- Reflectivity values appear somewhat randomly distributed, with significant variations from one range bin to another.

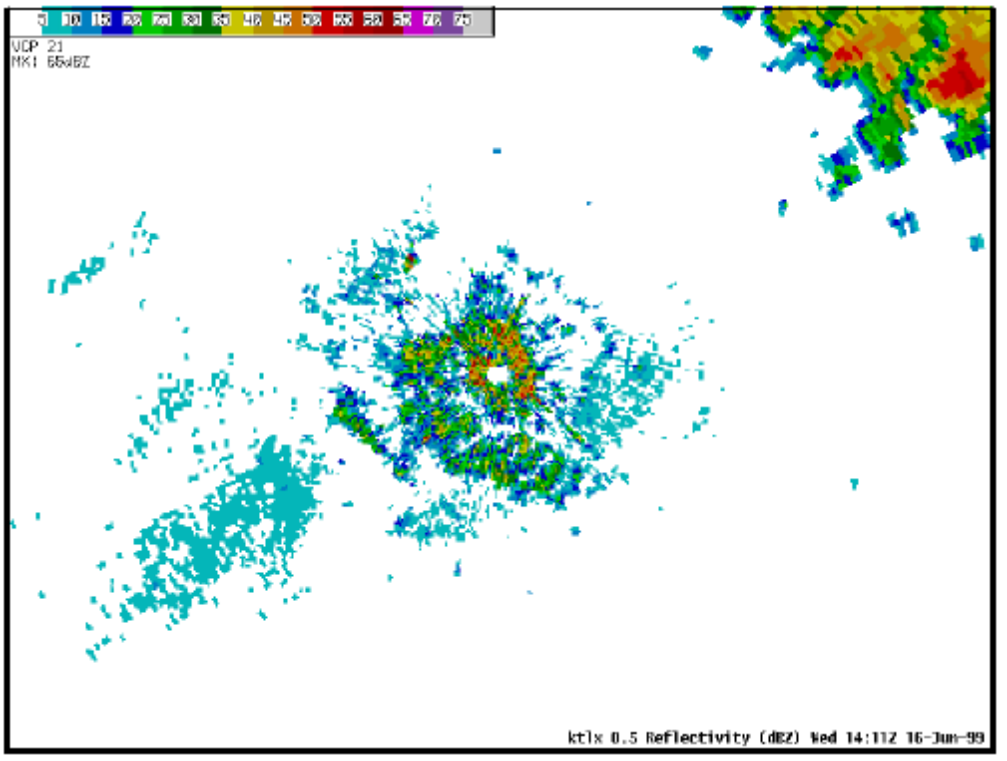


Fig. 4.3. Ground Clutter in reflectivity. Reflectivity from Ground Clutter is seen near the RDA, which is near the center of the image. Real meteorological targets are visible to the northeast. (Credit: WDTB 2005.)

In radial velocity products (Figure 4.4),

- Ground Clutter is generally stationary, therefore radial velocities are centered near zero.
- Non-zero radial velocities can occur from fluttering leaves, waves on the ocean, and vehicles.
- Large structures can produce varying radial velocities, depending on the size of the structures and the wind speed around the structure.
- Since radial velocity estimates are power weighted, the higher returned power from the stationary ground target dominates and the velocity estimate is near zero.

- Ground Clutter contamination is characterized by a general field of near-zero velocities, with embedded, isolated non-zero velocities.

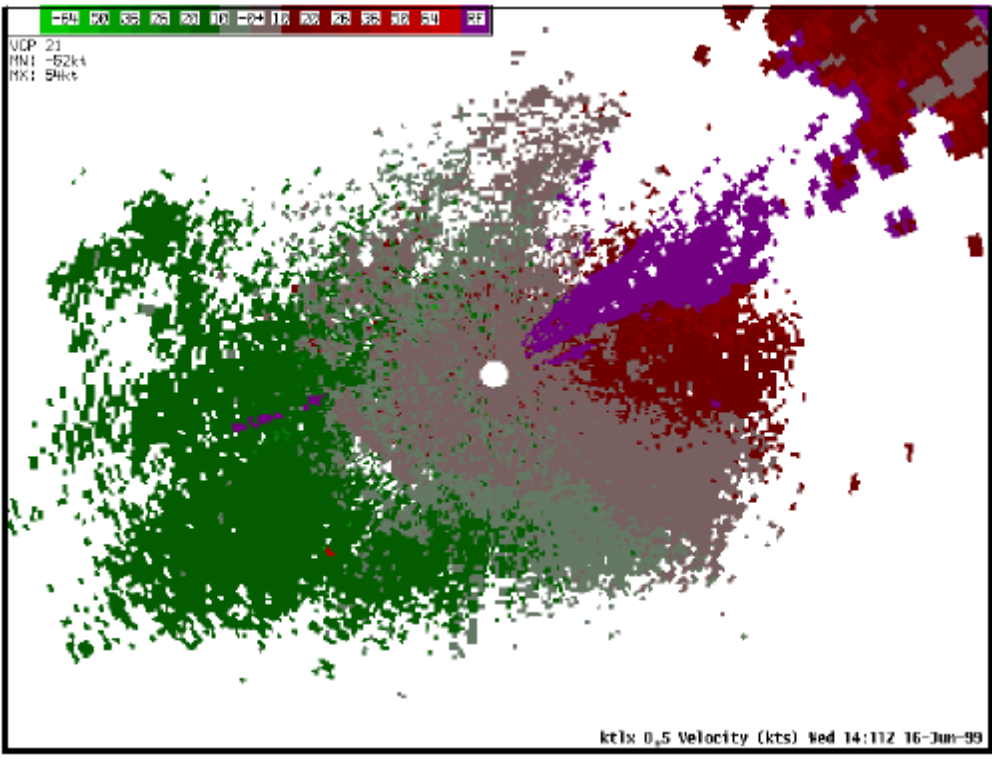


Fig. 4.4. Ground Clutter in radial velocity. (Credit: WDTB 2005.)

In spectrum width products (Figure 4.5),

- Velocity dispersion from ground targets is generally low; therefore spectrum widths are narrow.
- High spectrum widths can occur with fluttering leaves, ocean waves, or vehicles.
- Larger structures can create varying spectrum width, depending on their size relative to the size of the range bin.

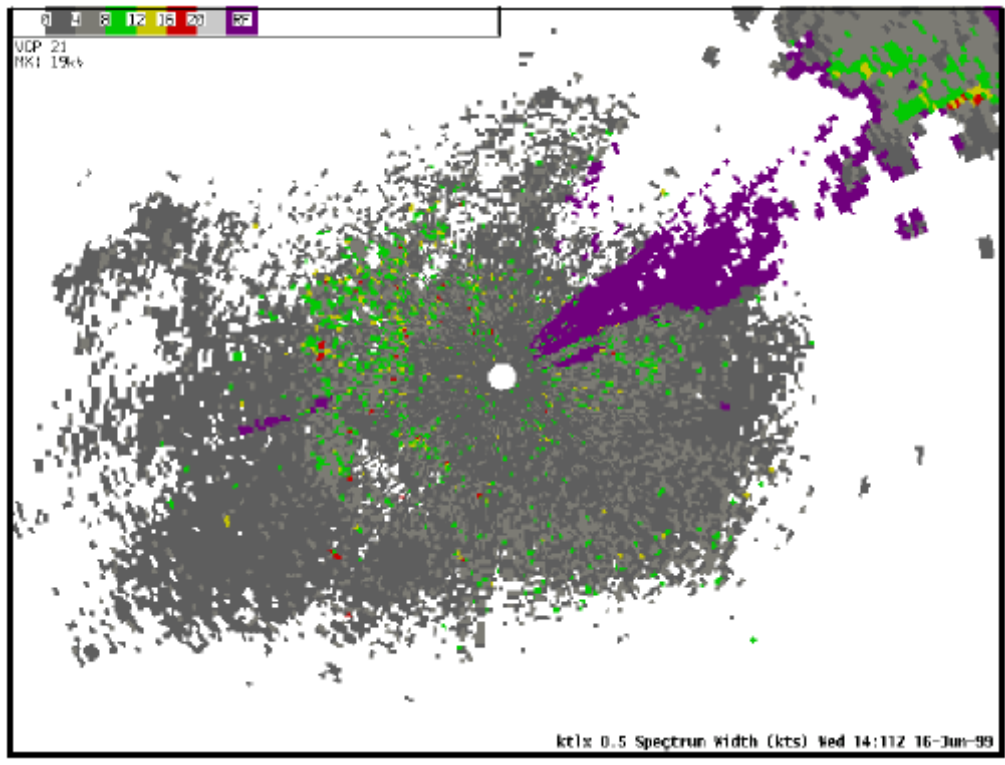


Fig. 4.5. Ground Clutter in spectrum width. (Credit: WDTB 2005.)

4.7.1.2. The Clutter Suppression Algorithm (CSA) operates by examining both the returned power and the velocity spectrum in each range bin. It assumes that clutter has high returned power, radial velocities centered near zero, and a narrow spectrum width. It also assumes that returned power from meteorological targets is highly variable, with radial velocities rarely centered at zero. Figure 4.6 shows a hypothetical scenario for the returned power in a range bin consisting of both clutter and meteorological signals.

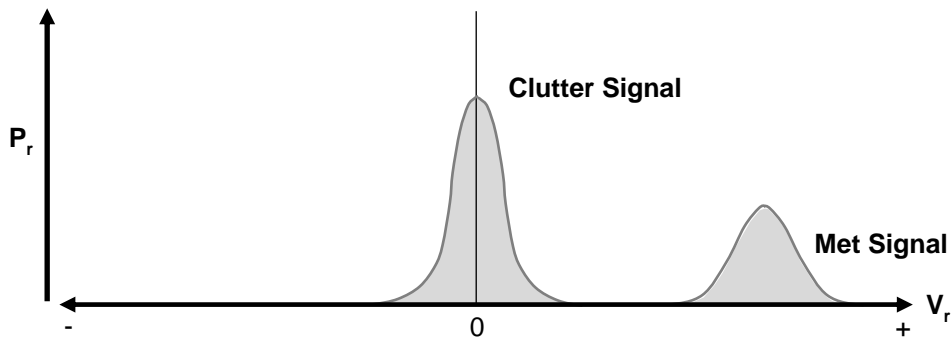


Fig. 4.6: Radial velocities recorded in a single hypothetical range bin with returned power from both Ground Clutter and a meteorological target. Horizontal axis is radial velocity, with inbounds on the left and outbounds on the right. Zero radial velocity is in the center. Vertical axis is returned power.

The CSA examines the returned power and radial velocities in each range bin. Returned power associated with radial velocities near zero is edited out. The spectrum width on either side of zero radial velocity where this filter is applied is called the notch width (Figure 4.7). Any returned power inside the notch width is removed, while returned power outside the notch is unaffected. Returned power from clutter outside the notch width is unaffected, and is called residual clutter. Ground Clutter visible in volume scans of Level II reflectivity is all residual (WDTB 2005).

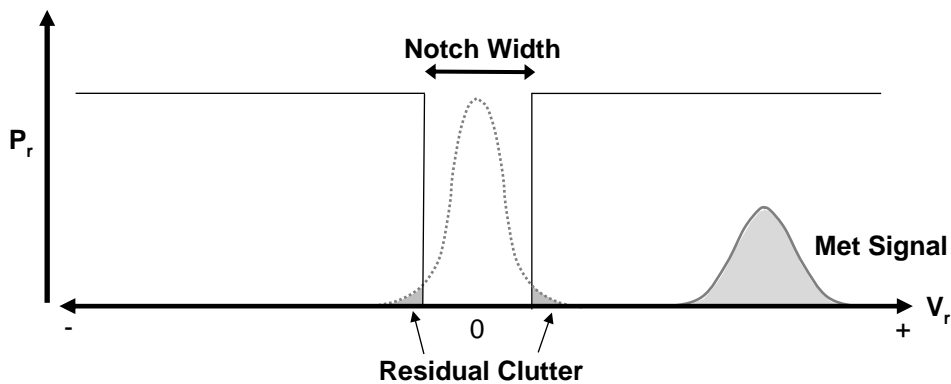


Fig. 4.7: Returned power remaining in a range bin after the Clutter Suppression Algorithm is applied. The clutter signal (with radial velocity centered near zero) is almost entirely removed, while the meteorological signal (with non-zero radial velocity) is unaffected.

This filter is highly effective, as shown in Figures 4.8 and 4.9. These images show reflectivity and radial velocity fields near and RDA with a meteorological boundary

approaching. Figure 4.8 shows the fields before application of the CSA, and Figure 4.9 shows the fields after the CSA is applied.

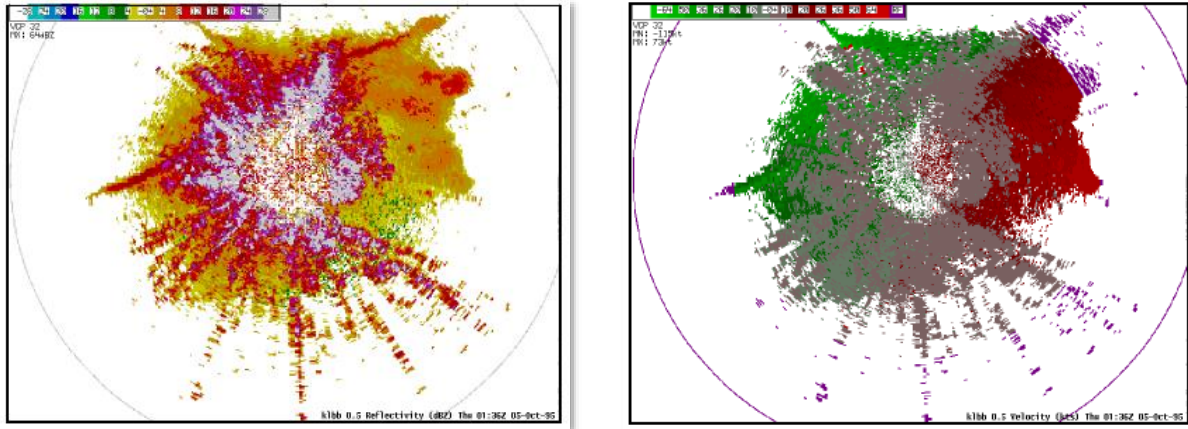


Fig. 4.8: Reflectivity and radial velocity *before* application of the Clutter Suppression Algorithm, with a meteorological boundary approaching the RDA. (Credit: WDTB 2005.)

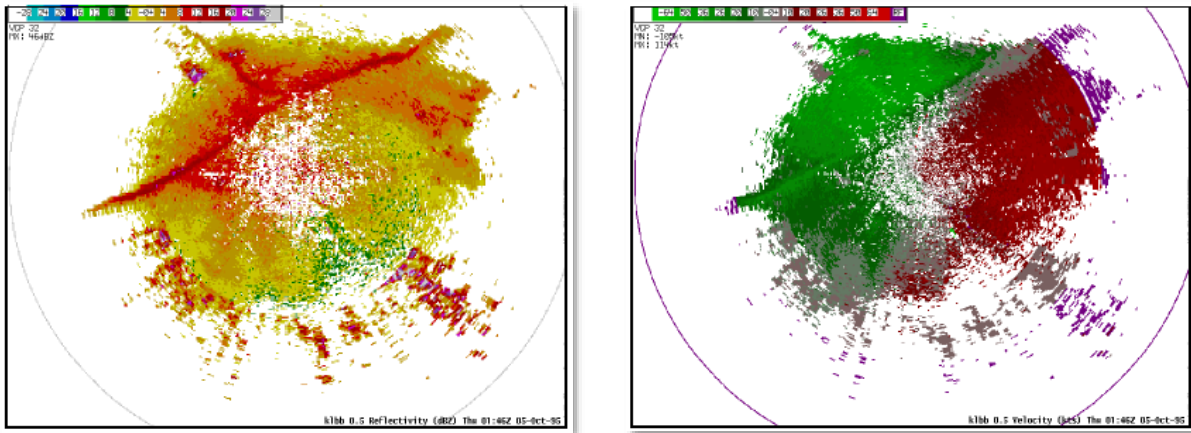


Fig. 4.9: Reflectivity and radial velocity *after* application of the Clutter Suppression Algorithm, with a meteorological boundary approaching the RDA. (Credit: WDTB 2005.)

In spite of its effectiveness, there are two ways this filter can (and does) produce erroneous results. First, as is visible in Figures 4.7 and 4.9, it doesn't remove the *entire* clutter signal. This might be improved by widening the notch width, but doing so increases the risk of editing out moving meteorological targets. Second, it doesn't provide for the possibility of meteorological targets that are not moving, such as orographic rain showers. There is no complete solution to this problem either.

There is another strength to the CSA: It's adaptable. Using an interface available in the RPG HCI, a meteorologist can (1) select which clutter suppression pattern to use, and (2) create a new pattern or edit an existing pattern. A clutter suppression pattern consists of a list of range bins to which the CSA should be applied by the RDA's processors. This is useful for helping to alleviate the second problem noted above, and it's also helpful when the next problem begins to appear (WDTB 2005).

4.7.1.3. A problem closely related to Ground Clutter is Anomalous Propagation (AP), which occurs when the outbound beam of pulses is refracted back toward the Earth's surface (Figure 4.10). Superrefraction, which causes AP, occurs in the presence of a strong vertical density gradient in the atmosphere. When the vertical density gradient is strong over a short vertical distance, the Index of Refraction varies enough between the two vertically-adjacent airmasses that it causes the light path to bend back downward. (This bending is described by Snell's Law. See Chapter 2 for details.)

The vertical density gradient is usually described in terms of the Brunt-Väisälä frequency (N), defined by:

$$N = \sqrt{\frac{g}{\theta} \frac{d\theta}{dz}} \quad (4.2)$$

where g is the effective gravity (typically about 9.81 ms^{-2}), and θ is potential temperature. Using the Ideal Gas Law (an equation of state), and assuming a fixed pressure, the potential temperature is inversely proportional to the density of air (e.g. Miller 2015). If the potential temperature *increases*, the density *decreases*. But the density of air (assuming a fixed pressure) is also a function of the water vapor mixing ratio (drier air is denser), so that (4.2) could be more correctly expressed as:

$$N = \sqrt{\frac{g}{\theta_v} \frac{d\theta_v}{dz}} \quad (4.3)$$

where θ_v is the virtual potential temperature. For Anomalous Propagation to occur, a strong vertical θ_v gradient is needed. According to (4.3), there are two ways to do this:

- A temperature inversion, wherein there is a sharp, front-like increase in temperature with height. Cooler, denser air remains below the inversion, and warmer, thinner air is above it.
- A sharp vertical variation in water vapor content, wherein there is a sharp increase in water vapor with height. Drier, denser air is below, and more humid, thinner air is above.

Figure 4.10 shows subrefraction, normal refraction, and superrefraction as a function of N . In superrefraction, backscattered energy from the surface is returned along the same path as it was transmitted, effectively creating *Ground Clutter at a distance*. Figures 4.11 – 4.13 show AP as it might appear in volume scans of the base moments.

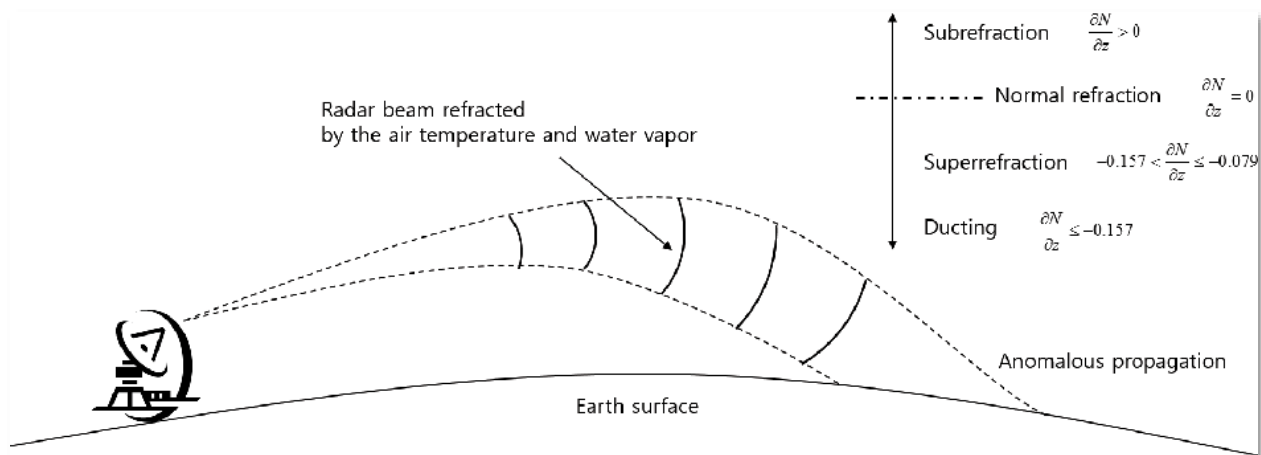


Fig. 4.10: Schematic of Anomalous Propagation in a temperature inversion. Refraction as a function of the vertical Brunt–Väisälä gradient ($\partial N/\partial z$). AP occurs under conditions of superrefraction. (Credit: Lee and Kim 2016.)

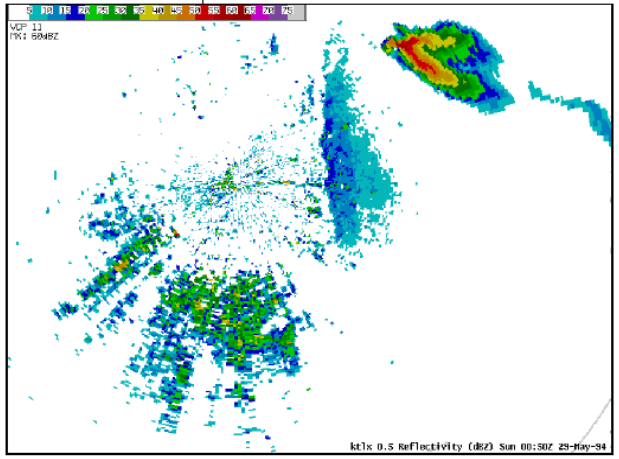


Fig. 4.11: Anomalous Propagation in reflectivity scan. (Credit: WDTB 2005.)

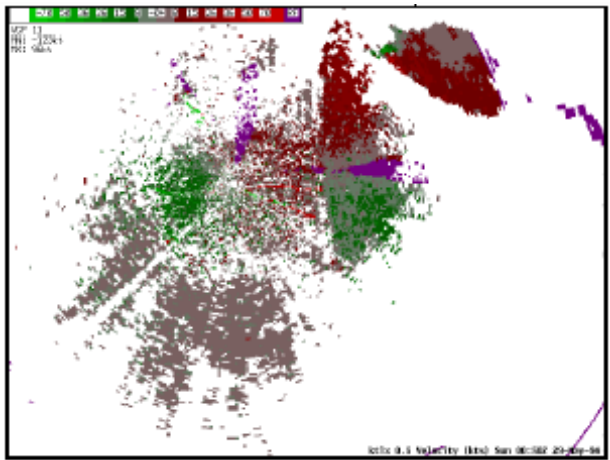


Fig. 4.12: Anomalous Propagation in radial velocity scan. (Credit: WDTB 2005.)

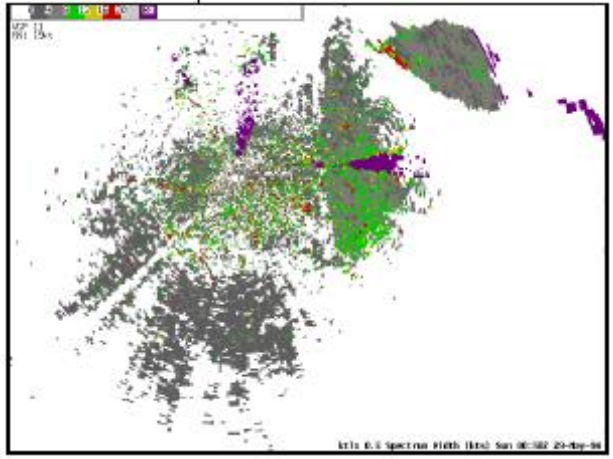


Fig. 4.13: Anomalous Propagation in spectrum width scan. (Credit: WDTB 2005.)

4.7.1.4. In extreme cases, the combination of the Earth's surface below and the temperature inversion above act as a waveguide, trapping the radar beam. Transmitted pulses are refracted back toward the surface by a temperature inversion, where they reflect back upward toward the inversion, and are once again refracted. This process, called ducting, repeats many times over (Figure 4.14), and the beam of pulses can travel many times the usual unambiguous range of the radar. Targets from extreme distances not usually detectable by the radar will appear in the volume scan and will be range folded (see below).

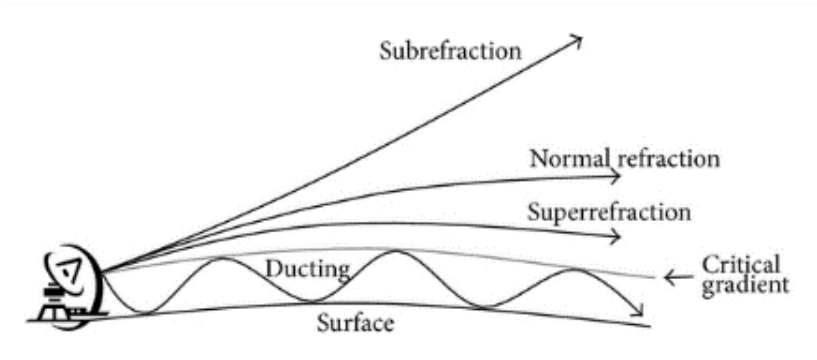


Fig. 4.14: Ducting of radar beam. The “critical gradient” is the minimum vertical Brunt–Väisälä gradient ($\partial N/\partial z$) necessary to create an atmospheric duct. (Credit: Lee, *et al.* 2016.)

4.7.2. **Range folding correction.** Range folding is the process by which returned power from beyond the radar's Maximum Unambiguous Range (R_{\max}) is mistakenly

placed at a location inside R_{\max} . The best way to explain this is with an example. Let's assume a scenario that has a meteorological target at a distance of $R_{\max} + \Delta R$, where R_{\max} is derived from the PRF in use (see Table 4.1), and ΔR is one quarter that distance. A pulse has already been fired by the RDA along a particular radial, and the system is now in listening (L) mode, waiting for backscattered energy from the pulse (Fig. 4.15) (WDTB 2005).

- In the first time step, the older ($n=2$) pulse has had time to travel to R_{\max} , and begin its trip back toward the antenna. If this is what had *really* occurred, backscattered energy from the $n=2$ pulse would be at $R_{\max} - \Delta R$ (shown as a dashed red circle in Fig. 4.15). What has *actually* happened is that the $n=2$ pulse (shown as a solid red circle in Fig. 4.15) has travelled *beyond* the Maximum Unambiguous Range and encountered a meteorological target (T) at a distance of $R_{\max} + \Delta R$.
- In the second time step, backscattered energy from the $n=2$ pulse has returned to R_{\max} , and is inbound toward the RDA. Had the $n=2$ pulse been backscattered from a target at R_{\max} , it would now be inbound at a distance of $R_{\max} - 2\Delta R$.
- In the third time step, backscattered energy from the $n=2$ pulse has reached a distance of $R_{\max} - \Delta R$ and is still inbound toward the RDA. Had the $n=2$ pulse been backscattered from a target at R_{\max} , it would now be inbound at a distance of $R_{\max} - 3\Delta R$.
- In the fourth time step, backscattered energy from the $n=2$ pulse has reached a distance of $R_{\max} - 2\Delta R$ and is still inbound. However, had the $n=2$ pulse been backscattered from a target at R_{\max} , it would have now reached the RDA. Thus, the RDA stops listening for backscattered energy from this pulse, switches to transmit (X) mode, and generates a new outbound ($n=1$) pulse. After this, the algorithm processing returned power assumes that any backscattered energy is from this newer pulse.
- In the fifth time step, backscattered energy from the $n=2$ pulse has reached a distance of $R_{\max} - 3\Delta R$, and is still inbound. At the same moment, transmitted power associated with the $n=1$ pulse is at the same point along the radial, so, in

effect, backscattered energy from the older pulse and energy from the newer pulse pass each other, going in opposite directions⁷.

- In the sixth time step, **backscattered energy from the older n=2 pulse reaches the RDA, which is listening for the energy from the newer n=1 pulse.** Meanwhile, the transmitted power of the n=1 pulse has reached a distance of $2\Delta R$ from the RDA. Put another way, the n=1 pulse has had time to travel outbound to a distance of ΔR and backscatter to the RDA. **The analog-to-digital (A2D) conversion procedure in the signal processor assumes that the returned power it's received is from the newer n=1 pulse, when it is actually from the older n=2 pulse, and it mistakenly assigns a distance to the returned power applicable to the newer pulse. The A2D convertor therefore creates a "ghost" target at a distance of ΔR from the RDA.**

This is a relatively simple scenario, involving only the most recent (n=1) pulse, and the previous (n=2) pulse. When the RDA is using a PRF with a very low R_{\max} , it is possible to have multiple pulses "in play" at the same time. In other words, there may be n=3 and n=4 pulses backscattering power from points beyond $2 \times R_{\max}$ and $3 \times R_{\max}$, respectively. **All of these will be range-folded into locations inside R_{\max} by the A2D convertor.** This is very common at high PRFs, that is, those associated with Continuous Doppler (CD) mode, as the radar collects radial velocity data.

⁷ Actually, between the time that the RDA fired off the n=2 and n=1 pulses, the antenna has rotated through a small azimuth angle, so the two pulses do not go *through* each other.

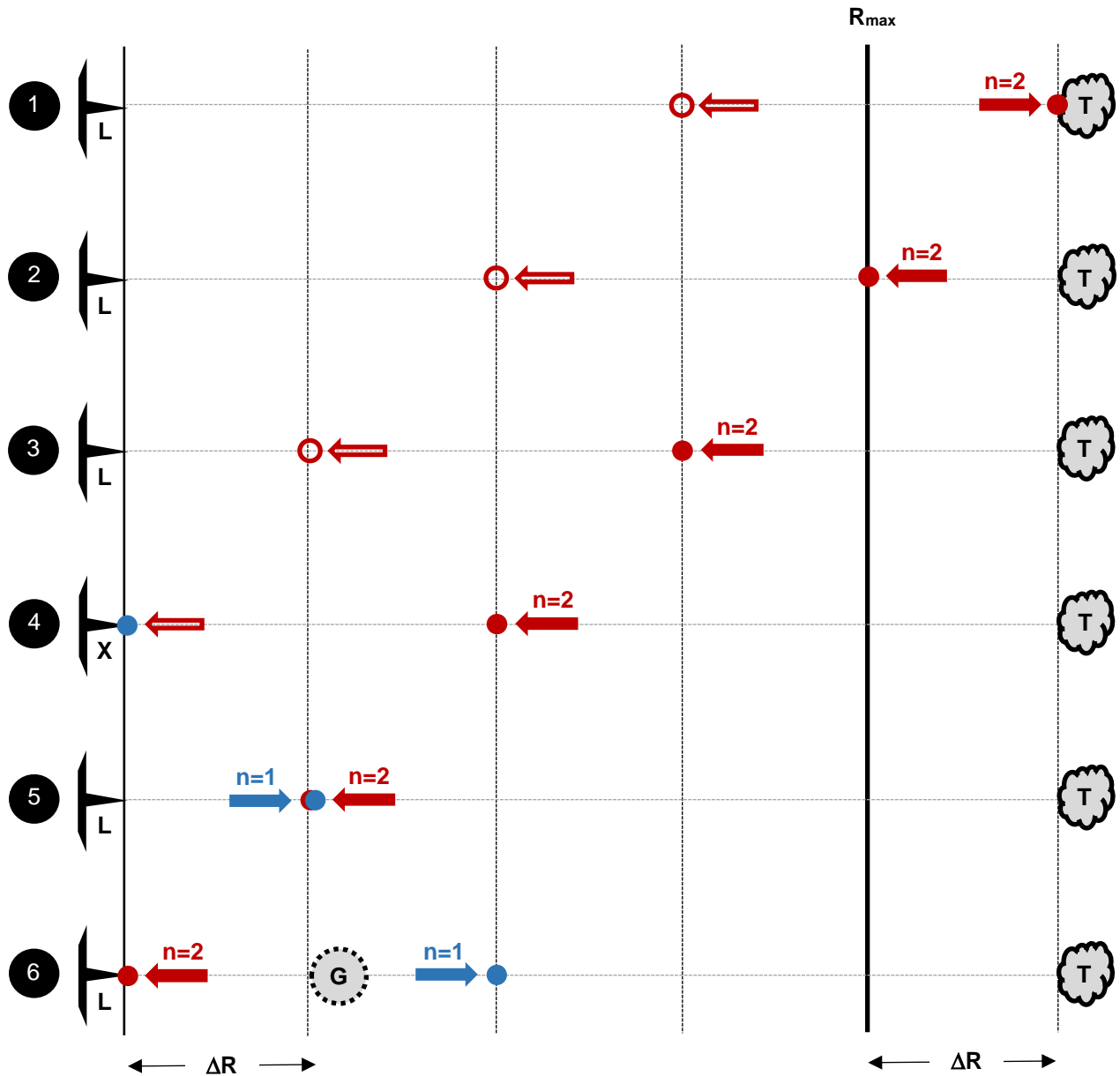


Fig. 4.15: Range folding. Time-steps are numbered 1-6 down left side of figure. The RDA is indicated with schematic symbol for antenna (as shown in Fig. 3.4). Antenna mode is indicated just below symbol, with “L” for listening, and “X” for transmit. Maximum Unambiguous Range is indicated with heavy black line, labelled as R_{max} . True location of meteorological target shown as a cloud, labelled as “T.” Induced ghost (range-folded) image of target shown as circle with dashed-border, labelled as “G.” True location of older pulse shown as red circle (filled), labelled as “n=2.” (Arrows indicates direction of pulse motion, either away from or toward antenna.) RDA’s assumed location of n=2 pulse after travel to R_{max} indicated as open red circle. Location of newer pulse shown as blue circle, labelled as “n=1.”

4.7.2.1. The **Range Unfolding Algorithm (RUA)** attempts to disentangle the mess created by range folding. It operates by making the following assumptions:

- Because of the low PRF (and corresponding distant R_{max}), *reflectivity data* (collected when the radar makes a CS scan) are rarely range folded. This is not an altogether unwarranted assumption, because power returning from beyond 252 nautical miles would normally be quite faint.
- Because of the high PRF (and corresponding close R_{max}), *radial velocity data* (collected when the radar makes a CD scan) are routinely range folded. This is a completely reasonable assumption.

The RUA then operates as follows: The RDA collects a complete scan of low-PRF reflectivity data. It then switches to CD mode and collects a scan of high-PRF data. Next, the RUA maps out the location of all *real* echoes out to R_{max} , using the reflectivity data. The RUA then computes all the locations of all possible *ghost* echoes as they will appear in the radial velocity data. Ghost echoes will appear at a distance ΔR from the RDA, where ΔR is the distance beyond an R_{max} -multiple associated with a particular pulse. R_{max} -multiples are given by:

$$R_{max}^n = (n - 1)R_{max} \quad (4.4)$$

where n is the pulse number, and R_{max} is the Maximum Unambiguous Range associated with the PRF in use (Table 4.1). Pulse numbers are integers, with $n=1$ indicating the most recent pulse (all returned power is initially assumed to come from this one), $n=2$ the second youngest (possibly returning power from beyond R_{max}), $n=3$ the third youngest (possibly returning power from beyond $2 \times R_{max}$), etc.

Range folding results in two distinct conditions. In the first, the ghost echoes are folded into a position such that they are at a unique distance from the RDA along that radial, different than the distances to the real echoes inside R_{max} as well as the other ghosts. This scenario is easier to disentangle than the second, wherein ghosts from beyond R_{max} are folded into a distance inside R_{max} that places them *on top of* real or other ghosts echoes inside R_{max} . These two scenarios are called non-overlaid and overlaid echoes, respectively. Both are illustrated in Figures 4.16 and 4.17.

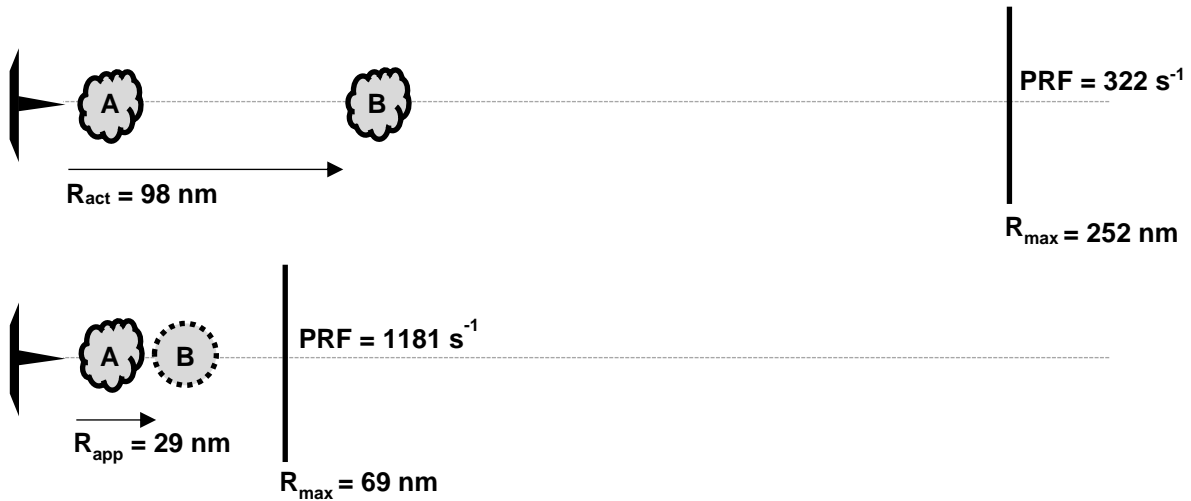


Fig. 4.16: Non-overlaid echoes. RDA shown with antenna symbol, as in previous figures. R_{act} is the actual location of target B; R_{app} is its apparent location after range folding. Upper panel shows data collected during low-PRF, high- R_{max} mode. Lower panel shows data collected during high-PRF, low- R_{max} mode. “Cloud” symbol with solid outline shows actual locations of targets. Circle with dashed outline shows range-folded (ghost) location of target. In this scenario, the range-folded location of Target B is at a different location than the real location of Target A. The radial velocity data of both targets are as correct as they can be, but the location of the radial velocity data for Target B is simply in the wrong place.

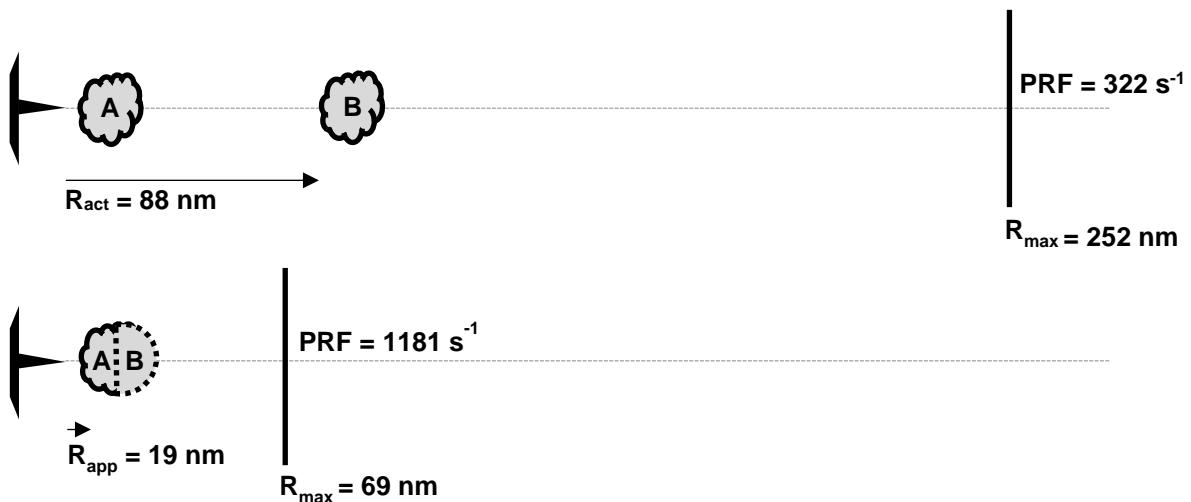


Fig. 4.17: Overlaid echoes. Symbology is the same as that used in the previous figure. In this scenario, the range-folded location of Target B is the same as the real location of Target A. The radial velocity data in the associated range bins is a hybrid of the real radial velocities of Target A and Target B.

To disentangle non-overlaid echoes, the RUA simply compares the *apparent* locations of all echoes in the high-PRF data to their (assumed) *actual* locations in the low-PRF data. The radial velocity data in the affected range bins are then relocated to the correct range bins. For overlaid echoes, an additional step is required. The *apparent* radial velocity in an overlaid bin is a hybrid of the *actual* radial velocity in that bin, and the *actual* radial velocity from the range folded target. From a strictly analytical perspective, there is no way to accurately determine the correct radial velocities for the real and ghost echoes in the bin, but it *is* possible to come up with a close approximation of one of them, under the right conditions (WDTB 2005).

The underlying idea for this approximation is based on the method used to compute radial velocities in the first place. Recall (from Chapter 3) that radial velocity is based on a power-weighted average of the phase shifts associated with 40 to 50 pulse-pairs in each range bin. High-power returns from a given target play a larger role in determining the radial velocity than low-power returns. This means that, for a range bin with a hybridized radial velocity, the high-power target is playing a larger role in the hybrid velocity than the low-power target. So, if the high-power target is sufficiently higher in returned power than the low-power target, the hybridized radial velocity should resemble the high-power target much more than the lower power target. Figure 4.18 illustrates this idea (WDTB 2005).

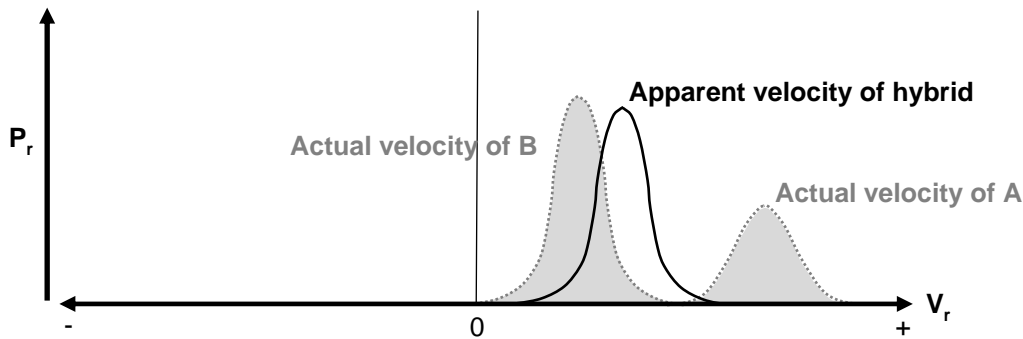


Fig. 4.18: Overlaid echoes in a single range bin. Horizontal axis is radial velocity, with inbounds on the left and outbounds on the right. Zero radial velocity is in the center. Vertical axis is returned power.

The RUA manages this by computing a power ratio (PR) for the two targets in the overlaid range bin. It uses the returned power from the low-PRF data to determine the two returned power values in the overlaid range bin, and applies them to:

$$PR = 10 \log_{10} \left(\frac{P_r^{higher}}{P_r^{lower}} \right) \quad (4.5)$$

where PR is the power ratio, which has units of decibels. The two terms inside the parenthesis are the mean returned power from the stronger and weaker targets in the range-folded range bin, respectively. If the PR exceeds 5 dB ⁸, the radial velocity and spectrum width data in the range folded bin are assigned to the higher-power target, regardless of its distance. (A 5-dB difference implies that the returned power from the more reflective target is more than three times greater than the power from the less reflective target.) The lower-power target is assigned radial velocity and spectrum width values of unknown (or “ND,” for No Data), shown as purple in both products. If the PR is 5 dB or less, then the returned power of the two targets is too similar to assign the apparent radial velocity to either, and both are “purpled out” (WDTB 2005).

4.7.3. Velocity dealiasing. Recall that the WSR uses a method used called Pulse-Pair Processing (which compares the phase shift of two successive backscattered pulses) to compute a first-guess radial velocity. In Chapter 3, phasor diagrams were introduced to illustrate this method. Phase shifts are used because the more commonly known Doppler frequency shift in EMR is too small to be detected, when applied to meteorological targets (WDTB 2005).

Figure 4.19 illustrates two possible “correct” pulse-to-pulse phase shifts ($\Delta\phi$) for the same two pulses, as well as the fundamental problem introduced by using this method. While it makes the detection of low velocity targets (relative to the speed of propagating EMR) possible, it also introduces a fundamental uncertainty. We are never sure in which direction the phase shift is occurring (clockwise or counterclockwise), and we are not even sure if the phase shift between two successive pulses resulted in more than one rotation around the phasor diagram.

⁸ This can be customized. 5 dB is the default value.

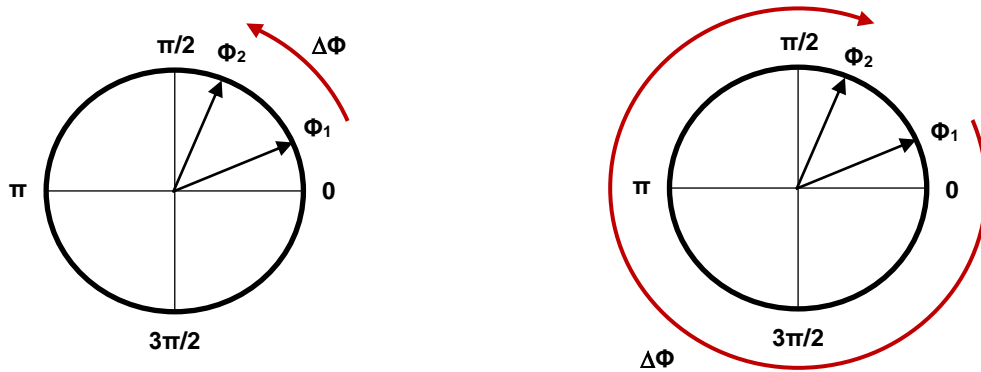


Fig. 4.19: Sample phasor diagram showing two possible phase shifts for the same two successive pulses. Curved red arrows indicates possible pulse-to-pulse phase shifts ($\Delta\phi$).

Take a look at Figure 4.19. The first-guess radial velocity is always assumed to be associated with the *smaller* of the two rotation angles – the phase shift in the left panel in this case (indicating an inbound target). But the correct answer may be the *larger* of the two angles, shown on the right (indicating an outbound target). *And there are more correct answers.* This problem is called velocity aliasing or velocity folding. For example, it may be the smaller of the two phase angles (left panel), plus one additional complete counter clockwise rotation, that is $\Delta\phi + 2\pi$ radians. It may also be the larger of the two angles (right panel), plus one additional clockwise rotation, *i.e.* $\Delta\phi - 2\pi$ radians. Additional correct answers include more multiples of the number of rotations around the diagram.

4.7.3.1. Another way of describing this problem is by stating that the first-guess radial velocity may be the incorrect velocity alias. This occurs when the actual radial velocity of the target exceeds the radial velocity associated with a 180° (π radians) phase shift. The latter is known as V_{max} , and is given by:

$$V_{max} = \frac{\lambda \times PRF}{4}$$

where λ is the wavelength, and PRF is the Pulse Repetition Frequency (see Table 4.1). Provided V_r doesn't exceed V_{max} , the former is calculated by:

$$V_r = |V_{max}| \frac{-\Delta\phi}{\pi}$$

where the vertical bars indicate the absolute value. The second expression can be elaborated by adding the alias number (m), which is an integer between $-\infty$ and $+\infty$. Each iteration of m is associated with an additional phase shift of 2π (360 degrees). Negative values of m indicate additional *clockwise* phase shifts of 2π ; positive values of m indicate additional *counterclockwise* phase shifts of 2π between pulses. The expression for radial velocity then becomes:

$$V_r = |V_{max}| \left[\frac{-\Delta\phi - (m \times 2\pi)}{\pi} \right] \quad (4.6a)$$

where $\Delta\phi$ is in radians, or,

$$V_r = |V_{max}| \left[\frac{-\Delta\phi - (m \times 360)}{180} \right] \quad (4.6b)$$

where $\Delta\phi$ is in degrees. With these two expressions in mind, we see that the first-guess radial velocity is also the zeroth-alias velocity (where $m=0$).

Let's assume we are using PRF No. 8 (1281 s^{-1}), which is associated with a V_{max} of 64 knots (Table 4.1), and we have a first-guess pulse-to-pulse phase shift ($\Delta\phi$) of -160 degrees. (This indicates an outbound target using the Right-Hand Rule, as described in Chapter 3.) Table 4.2 shows a few velocity aliases (correct values for the given value of $\Delta\phi$), and their associated alias numbers (m), computed using (4.6b).

Table 4.2: Velocity aliases for a first-guess pulse-to-pulse phase shift of -160 degrees.

Alias Number (m)	Equation (4.6b)	Velocity Alias [kts]	Direction
0	$64 \times \left[\frac{-(-160) - (0 \times 360)}{180} \right]$	+56.9	Outbound
1	$64 \times \left[\frac{-(-160) - (1 \times 360)}{180} \right]$	-71.1	Inbound
-1	$64 \times \left[\frac{-(-160) - (-1 \times 360)}{180} \right]$	+184.9	Outbound
2	$64 \times \left[\frac{-(-160) - (2 \times 360)}{180} \right]$	-199.1	Inbound
-2	$64 \times \left[\frac{-(-160) - (-2 \times 360)}{180} \right]$	+312.9	Outbound

The table indicates that if the zeroth-alias radial velocity alias is incorrect, then the $m=1$ alias is probably the right answer. At an alias number of -1, and at higher order alias numbers, the resulting velocity aliases very quickly climb into speed regions that are rare on Earth. The exceptions to *that* “rule” are radial velocities that might occur with tornadoes, or (occasionally) tropical cyclones.

Incorrectly dealiased velocities have a distinctive appearance in volume scans (Figure 4.20). The point at which V_{max} is exceeded (that is, where the first guess switches from correct to incorrect) appears as a sharp, unnatural-looking velocity gradient, usually indicating a reversal in direction between inbound and outbound. Improperly dealiased velocities often also appear as blocks of range bins that don’t make sense (from a mass continuity perspective) when compared to the surrounding range bins.

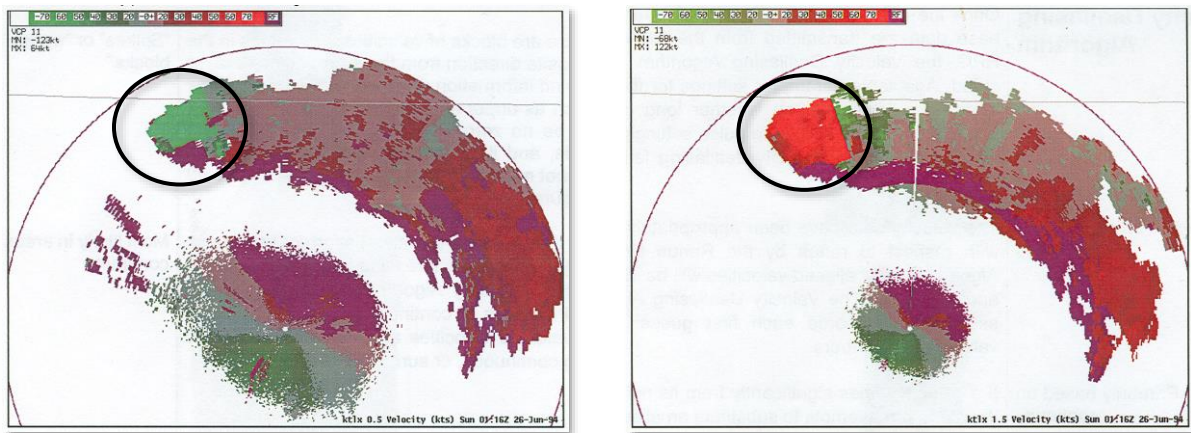


Fig. 4.20: Improperly dealiased radial velocities (circled). Example shown is from the same volume scan by the Oklahoma City (KTLX) WSR-88D. Left panel is from the 0.5° elevation angle; right panel is from the 1.5° tilt. Reds are outbounds; greens are inbounds. (Credit: WDTB 2005.)

4.7.3.2. The Velocity Dealiasing Algorithm (VDA) attempts to correct the first-guess velocity field for cases in which it exceeds V_{max} for the PRF in use. Unlike the first two filters (the CSA and RUA), which are performed by the RDA, the VDA is carried out by the processors in the RPG. The objective is to create a radial velocity field throughout the volume scan that makes physical sense from a momentum conservation perspective. The filter proceeds in steps, testing each range bin in the scan. If the first step is unsuccessful, it continues to the second step, and further if needed, until it either succeeds or exhausts all the possibilities. Throughout the execution of the VDA, error

- Five bins in the *previous* radial, beginning with the bin at the same distance from the RDA, and moving away from the RDA.

The objective of this step is to identify an alias of the first-guess velocity that is within some reasonable ΔV of the average of its neighbors.

Step 3: Expanded search. If Step 2 fails, the VDA moves to an expanded search. In this step, aliases of the velocity in the bin being checked are compared to radial velocities in:

- Up to 30 range bins in the *same* radial, back toward the RDA, and,
- Up to 15 range bins in the *previous* radial, beginning at the same distance and moving away from the RDA.

If an alias of the first-guess radial velocity is found that falls within a reasonable ΔV of the radial velocity in the comparison bin, it is substituted for the first-guess velocity in the range bin being checked.

Step 4: Compare to environmental winds from previous volume scan. One of the WSR's derived (Level III) products is a table of environmental winds above the RDA. This is produced by an algorithm called the VAD Wind Profile (VWP, where VAD means Velocity Azimuth Display), and is updated following each CD volume scan. (The VAD and VWP are described in Chapter 7.) The Environmental Winds Table (EWT) is a list of two dimensional wind vectors in 1000-foot intervals, beginning at 1000 feet ARL, and continuing up to as high as 70,000 feet ARL. As a last resort, the VDA compares aliases of the radial velocity in the range bin being checked to the EWT (for an appropriate elevation ARL) from the previous volume scan, searching for one that is within a defined ΔV .

Figure 4.22 shows the same radial velocity volume scan as in Figure 4.20, after successful dealiasing by the VDA. A tight "velocity couplet" is revealed near the center of the circled region. Comparison to the corresponding reflectivity volume scan indicates that this feature is a mesocyclone, a potentially dangerous meteorological phenomenon. However, if all four steps *fail* to produce an alias of the first-guess velocity in the range bin that makes physical sense, the VDA removes the velocity data for the bin, and enters a value of no data (ND). In the example shown, this means that the mesocyclone might have gone undetected.

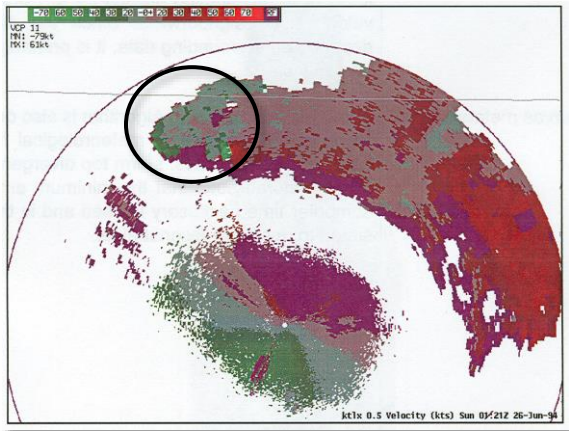


Fig. 4.22: Correctly dealiased radial velocities (circled). Example shown is the same as in Fig. 4.20, after successful dealiasing. (Credit: WDTB 2005.)

After all three filters are completed, the Level I data are fully rendered as Level II data. The RPG then gets to work computing Derived Products (Level III), based on the clean Level II data. In the next chapter, we provide a tutorial on interpreting radial velocity fields.

Summary. The Doppler Dilemma is defined as the conflict between the need to maximize both range and unambiguous velocity detection. It arises from the combination of the method used to detect radial velocity (pulse-to-pulse phase shifts rather than the direct Doppler Effect), the resulting physical relationship for V_{\max} (which is directly proportional to the Pulse Repetition Frequency), and the physical relationship for R_{\max} (which is inversely proportional to PRF). There is no solution to the Doppler Dilemma, but it can be managed, and its effects minimized, by varying the PRF. Low-PRF scans, called Continuous Surveillance scans, are used to collect reflectivity data, and have a high R_{\max} and low V_{\max} . High-PRF scans, called Continuous Doppler scans, are used to collect radial velocity data, and have a lower R_{\max} but higher V_{\max} .

After the RDA has collected the raw Level I data and performed two of the three quality-control filters used to produce Level II base moments, the data are transmitted via the broadband communication link to the RPG, which performs the third QC filter. The means used by the broadband link varies, depending on the specifics of the radar installation's architecture. There are four different methods, including direct wire, private T1 line, telco T1 line, and microwave line-of-sight.

The Radar Products Generator is usually located in the WFO (for NWS installations), or in the RDA blockhouse (for FAA and DoD installations). It completes the conversion of Level I data into Level II base moments, computes Level III (derived) products, accepts and processes One Time Requests, and distributes data to users by the narrow-band communications links. The Human Control Interface, which is part of the RPG, is a desktop computer that sits on the WFO forecast floor, and provides an interface for monitoring and controlling the entire system.

The three filters applied to Level I data are the Clutter Suppression Algorithm, the Range Unfolding Algorithm, and the Velocity Dealiasing Algorithm. The first two are run by the RDA and the third by the RPG. Ground Clutter results when returned power from objects on the ground (or sea surface) is processed into the Probert-Jones Radar Equation and rendered as reflectivity. The CSA removes Ground Clutter by subtracting returned power within a “notch” centered around zero radial velocity. A closely related problem is Anomalous Propagation, which is essentially clutter at a distance, and occurs in meteorological scenarios that include strong vertical density gradients (such as temperature inversions).

Both range folding and velocity aliasing are a result of the method used to measure radial velocity. Range folding occurs when the radar confuses returned power from an older pulse with returned power with a new pulse, and the computer erroneously places the returned power at the wrong distance from the RDA. Range folding is common in radial velocity scans, but can be disentangled by comparing returned power in radial velocity scans to returned power in ordinary reflectivity scans. Velocity aliasing (also known as velocity folding) occurs when the pulse-to-pulse phase shift exceeds 180 degrees (π radians), yielding a velocity value that may be wrong in both magnitude and sign. It can usually be corrected by comparing the radial velocity in a given range bin to different collections of neighboring range bins.

Terms and concepts:

- Alias number (m)
- Brunt-Väisälä frequency (N)
- Cellular modem
- Clutter Suppression Algorithm (CSA)
- Continuous Doppler (CD)
- Continuous Surveillance (CS)
- Doppler Dilemma
- Environmental Winds Table (EWT)

- Expanded search
- Hybrid target
- National Centers for Environmental Information (NCEI)
- National Oceanic and Atmospheric Administration (NOAA)
- Nine-point average
- Non-overlaid echoes
- Notch width
- One Time Request (OTR)
- Overlaid echoes
- Phase shift (ϕ)
- Power ratio (PR) and power ratio threshold
- Product Distribution Communications (PDC)
- Radial continuity check
- Range folding
- Range Unfolding Algorithm (RUA)
- Residual clutter
- Shannon-Hartley Theorem
- Subrefraction
- Superrefraction
- VAD Wind Profile (VWP)
- Velocity alias
- Velocity Azimuth Display (VAD)
- Velocity Dealiasing Algorithm (VDA)
- Velocity folding
- Very Small Aperture Terminal (VSAT)
- Weather and Radar Processor (WARP)

Study prompts:

1. Describe the Doppler Dilemma and explain why it occurs. How is this problem managed by the WSR-88D?
2. What are the eight PRFs available in the WSR-88D system, and how do R_{\max} and V_{\max} vary with them? How does the area scanned vary with PRF? How big is the minimum scan area compared to the maximum scan area?

3. Discuss several methods used to transmit data from the RDA to the RPG, and the circumstances under which each might be used.
4. Discuss the Shannon-Hartley Theorem.
5. What does the RPG do? How is it controlled? Where is the HCI located?
6. List and describe some radar data users.
7. What are the three basic problems addressed by the primary filters? Describe each one. Which two filters are applied by the RDA, and which is applied by the RPG?
8. Describe the cause and appearance of Ground Clutter in the three base moments, then describe the CSA. How does it function? Explain the definition and role of the notch width. What are the consequences of changing the notch width?
9. Explain the cause and appearance on Anomalous Propagation. How is this related to the vertical variation in atmospheric density? How is it related to the vertical Brunt-Väisälä gradient? What is ducting?
10. Explain range folding. What causes it? Which base moments are routinely affected, and which aren't? Explain the operation of the Range Unfolding Algorithm. What are the underlying assumptions in the RUA? What are two distinctly different scenarios that can occur with range folding, and how does the RUA deal with each?
11. What is a velocity alias? What causes them? Describe a method for (mathematically) computing velocity aliases. How does the Velocity Dealiasing Algorithm resolve this problem? List and describe four steps.

5. Velocity field interpretation.

This chapter is based on materials found in WDTB (2005).

This chapter focuses entirely on visual interpretation of radial velocity fields. Two scales of motion are discussed: Volume scan (large) and storm cell (small).

5.1. **The zero isodop.** The WSR-88D is only capable of directly detecting the radial component of the full motion vector⁹, and only when there are enough scattering particles in the correct size range to backscatter the RDA's EMR. This results in an apparent velocity field that can be confusing to the uninitiated. Figure 5.1 shows a very simple example, in which there is a consistent westerly wind (black arrows) throughout the radar's volume control area. Generally speaking, the larger the angle between the wind vector and a radial line pointing away from the RDA, the smaller the portion of the full wind vector that will be detected.

- Directly to the west of the radar, the full wind vector registers as a strong inbound wind (shown as green in the figure), while east of the radar, the full wind vector registers as a strong outbound wind (shown in red).
- To the northwest and southwest of the RDA, the radar detects an inbound wind, but not its full magnitude (since a portion of the full wind vector is perpendicular to the radial).
- To the northeast and southeast of the RDA, the radar detects an outbound wind, but not its full magnitude (for the same reason).
- To the north and south of the RDA, the radar does not detect any wind at all (since the full wind vector is perpendicular to the radial).

This then leads to another conclusion: *There are two very different reasons why the WSR might indicate a zero wind speed:*

⁹ By combining the returns from two or more Doppler-capable radars, the full velocity vector can be derived, but costs make this impractical in operational settings.

- The wind speed really is zero (rare), or,
- The wind vector is entirely perpendicular to a radial pointing away from the RDA (present in at least two places in every volume scan, or put another way, quite common).

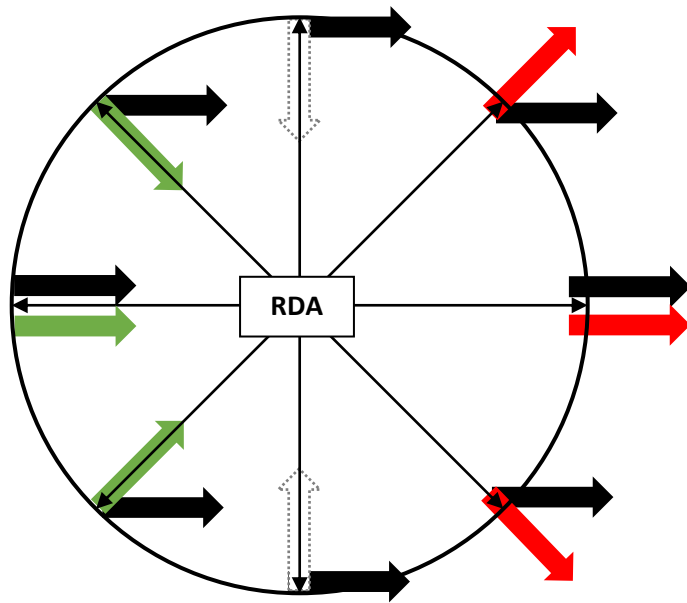


Fig. 5.1: Schematic of WSR-88D radial velocity scan in the presence of a consistent westerly wind. Ring indicates fixed radial distance from RDA (at center). Directional radials are indicated with thinner arrows, centered at the RDA. North is “up.” Heavy black arrows indicate full wind vector. Green arrows west of the RDA indicate perceived inbound winds. Red arrows east of the RDA indicate perceived outbound winds. White arrows north and south of RDA correspond to the non-existent radial component of the full wind vector perpendicular to the respective radials.

The magnitude and sign of the radial wind component are often described in terms of “isodops,” that is, lines of equal Doppler shift (even though the WSR-88D does not actually use the classical Doppler Effect). An isodop indicates a line of constant radial velocity, in both magnitude and sign. The zero isodop is the line of constant zero radial velocity. In Figure 5.1, the zero isodop (zero radial velocity line) runs from the south, through the RDA, and to the north, along which the WSR perceives no inbound or outbound wind components. Figure 5.2 illustrates the appearance of the isodops in this highly simplified scenario. Once again, the zero isodop occurs where:

- The wind speed (Doppler shift) really is zero (rare), or,
- The wind vector is entirely perpendicular to a radial (resulting in zero Doppler shift) pointing away from the RDA (common).

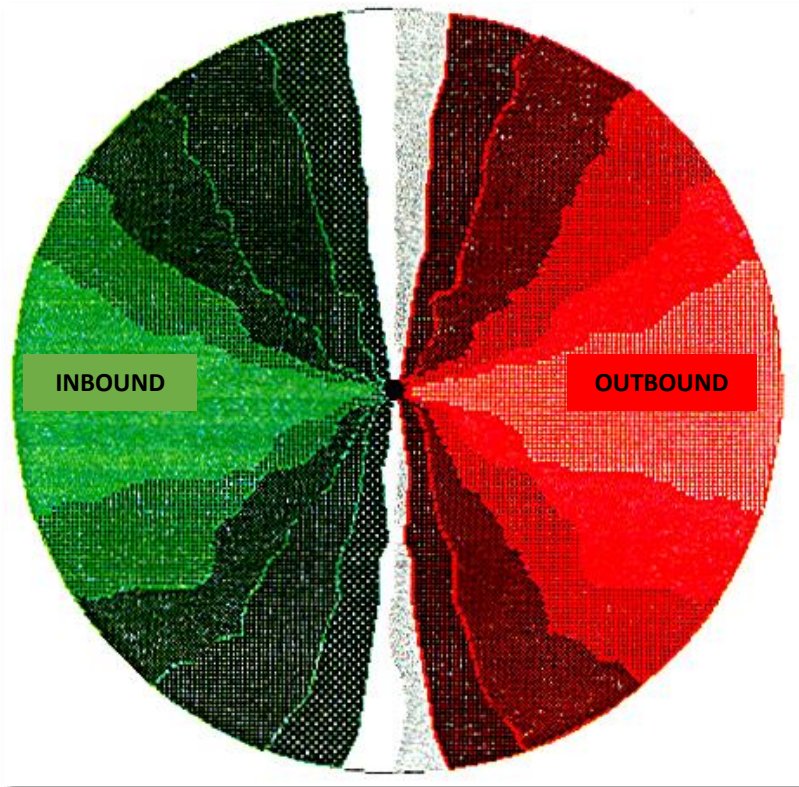


Fig. 5.2: Isodops in a westerly wind field. The RDA is located at the center of the image. The zero isodop is in white. This is a cartoon, not an image of a real velocity field. (Credit: WDTB 2005.)

In spite of its inability to directly sense the total wind vector (except when looking either directly upwind or downwind), there are two methods by which it can be inferred. The first of these, involving use of the zero isodop, will be discussed in this chapter. The second is used in a routine Level III product called the VAD Wind Profile, which will be discussed in Chapter 7.

5.2. The equivalence of range and elevation. In addition to its inability to directly detect the full wind vector (in most cases), another type of ambiguity arises from the tilted nature of the beams in volume scan. Even the lowest tilt angle isn't zero degrees, and the highest is more than 19 degrees from horizontal. This means that the *same* tilt

angle is looking at *different* elevations, depending on the distance from the RDA. Figure 5.3 illustrates this. At a range of 30 nm, the lowest tilt angle is about one quarter of a nautical mile (480 meters) ARL, and the highest tilt angle is 10 nm (18,500 meters) ARL. The region above the highest tilt angle is called the Cone of Silence, and was discussed in greater detail in Chapter 3.

In simple terms, there is a direct relationship between range (R) from the RDA and elevation ARL (H), given by:

$$H = R \sin(\phi) \tag{5.1}$$

where ϕ is the tilt angle. The farther the range bin is from the RDA, the higher above ground it's located.

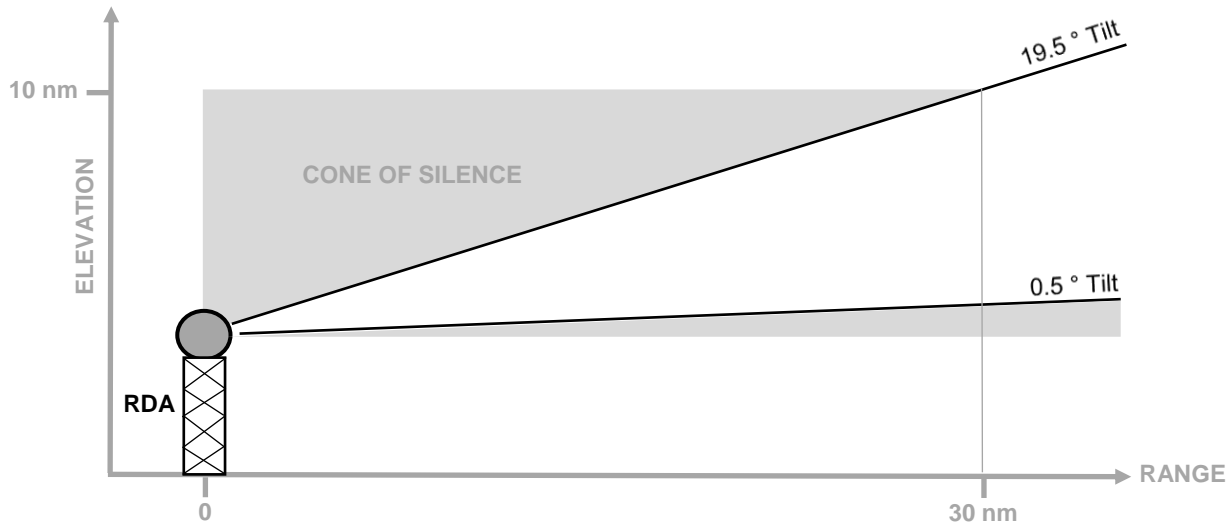


Fig. 5.3: WSR-88D Cone of Silence, and equivalence of distance from the RDA to elevation.

This is useful, because the relationship between range and height means that radar velocity fields can be used to infer information relevant to the thermal wind relationship (Holton 2004), which states that:

- If the wind direction *veers* with height (rotates clockwise in the Northern Hemisphere), then warm air advection (WAA) is indicated.
- If the wind direction *backs* with height (rotates counterclockwise in the Northern Hemisphere), then cold air advection (CAA) is indicated.

The method used to detect veering and backing in the total wind vector is discussed below.

Combining the conclusions about the zero isodop and the equivalence of range and elevation, and assuming a homogeneous wind field in the area around the RDA, a third conclusion can be drawn from this analysis: The magnitude of the full wind vector at a given elevation, that is, the *wind speed at that height*, can be found by finding the highest Doppler velocity at a given *range*, which is usually about 90 azimuth degrees on either side of the zero isodop. Figure 5.2 illustrates this pretty clearly, where the maximum inbounds and maximum outbounds both reflect the *in situ* westerly winds in the example, and capture the full wind vector where the scan radial is parallel to the wind vector, due west and due east of the RDA.

5.3. Scales of atmospheric motion relevant to meteorological radar, and interpretation of radial velocity data. Fujita (1986) defined synoptic, mesoscale, and microscale meteorological phenomena, as well as their α (large), β (medium), and γ (small) subscales. Meso- α corresponds to phenomena with a horizontal scale of 200 – 2000 km; meso- β 20 – 200 km; and meso- γ 2 – 20 km. Micro- α corresponds to a horizontal scale of 200 m – 2 km (2000 m), and so forth. With these in mind, it's apparent that the scale of a WSR-88D volume scan is either small meso- α or large meso- β , the scale of an individual range bin is micro- α , and the scale of a thunderstorm cell is micro- α or meso- γ . In the following two sections, we examine interpretation of WSR radial velocity fields on two scales.

5.3.1. Meso- β velocity field interpretation: Volume-scan scale. The basic method for velocity field interpretation at this scale is as follows:

- Draw a reference line to any point on the zero isodop.
- Draw an arrow perpendicular to this reference line, pointing from inbounds to outbounds.
- Do the previous two steps at several distances and several directions from the RDA.
- Interpret the resulting vector arrows in terms of backing (CAA) and veering (WAA).

Figure 5.4 shows an example of this method. On the left, four reference lines from the RDA are drawn in. On the right, the vector arrows are added. There are slight variations in the directions these arrows point toward, but these variations appear to depend on where – exactly – the reference lines are drawn. The example shown is the same used in Figures 5.1 and 5.2, and it’s easy to see that the method faithfully reproduces the westerly winds. It’s also clear that there is very little variation in the wind direction with elevation, so (by the thermal wind relation), there isn’t much temperature advection (CAA or WAA) occurring.

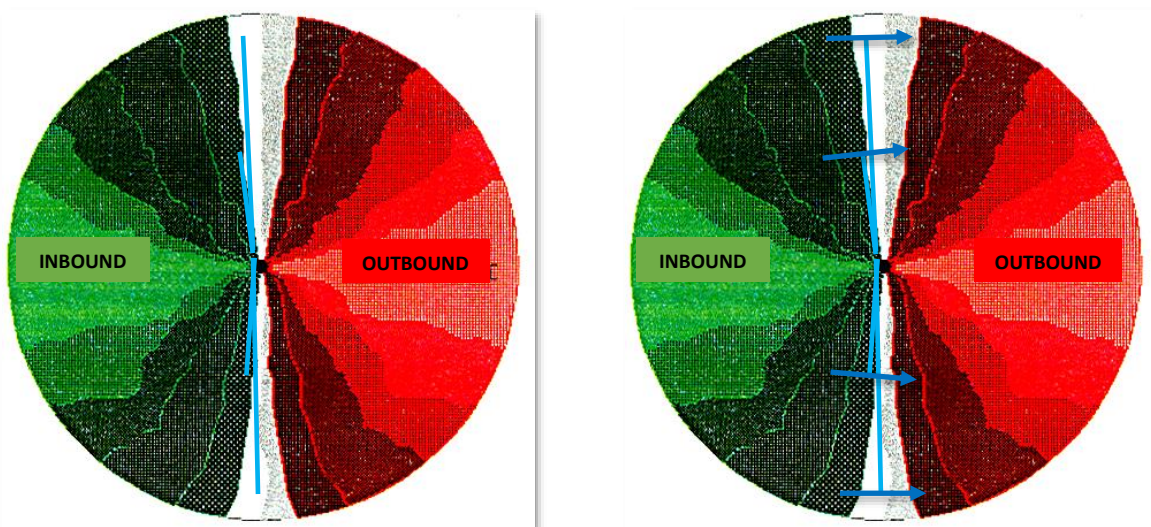


Fig. 5.4: Demonstration of basic method for interpreting radar velocity fields at meso- β scale. Inbounds are green; outbounds are red. Left: Reference lines (blue) drawn from the RDA (center) to the zero isodop (white). Right: Vector arrows indicating wind drawn at right angles to the reference lines, pointing from inbound to outbound. (Credit for underlying image: WDTB 2005.)

We now examine several examples and illustrate some basic principles.

5.3.1.1. Relatively uniform flow in the absence of strong temperature advection. In scenarios without significant temperature advection, the thermal wind relation suggests that the wind direction will remain relatively consistent with height (absent other factors – such as terrain – that may influence the wind). Figure 5.5 shows an example of northwesterly flow in the absence of strong temperature advection. Wind directions both near the RDA (lower elevation), and more distance from the RDA (higher elevation), are pretty consistent.

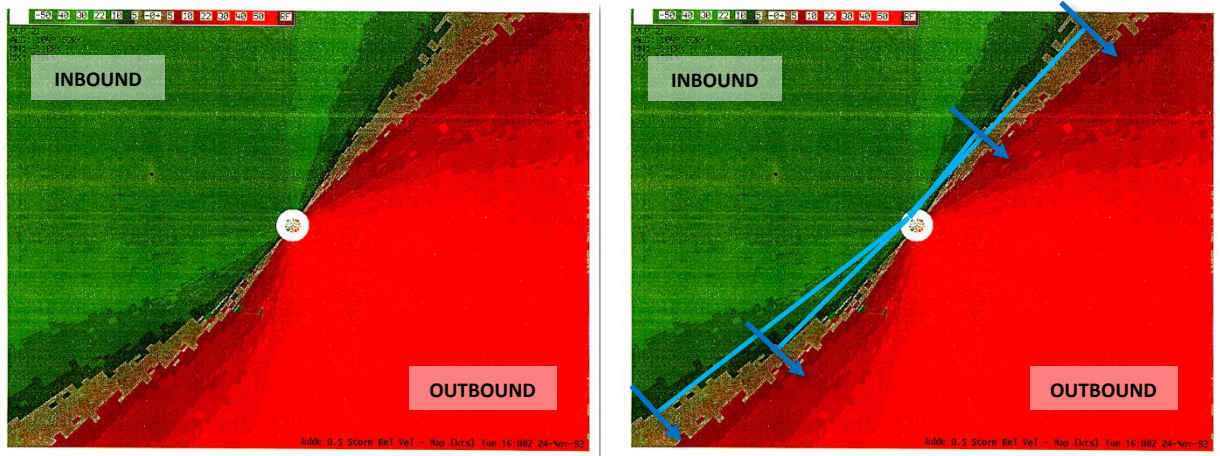


Fig. 5.5: Uniform northwesterly flow. This is a real image of a radar radial velocity field recorded by the Dodge City (KDDC) WSR, although it's been edited to make it a little clearer, and labels have been added. The velocity scale is at upper left, with inbound indicated by negative numbers (knots). The right panel shows the reference lines and vector arrows. (Credit: WDTB 2005.)

5.3.1.2. **The Forward-S zero isodop: Warm air advection.** The thermal wind relation implies that warm air advection (WAA) should cause the wind direction to rotate in a clockwise direction with height, that is, *veering*. In a WSR velocity scan, this corresponds to veering with distance from the RDA. Figure 5.6 shows a cartoon version of this scenario, with a generally westerly wind, and Figure 5.7 shows a real-world WAA scenario with a generally easterly wind. The S-shaped zero-isodop is clearly visible in both figures.

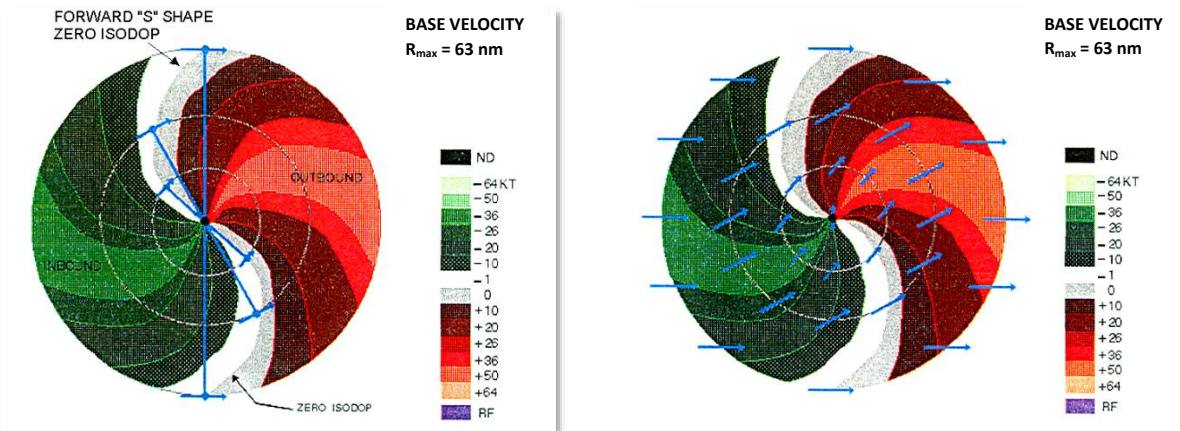


Fig. 5.6: Forward-S zero isodop. Cartoon of Forward-S zero isodop in the presence of WAA. This figure suggests that the WSR is using PRF No. 8, with 1281 pulses per second, with a corresponding R_{max} of about 63 nm. Left: Method with reference lines and vector arrows. Right: Completed velocity field, assuming uniform flow at a given altitude in the radius of the volume scan. (Credit: WDTB 2005.)

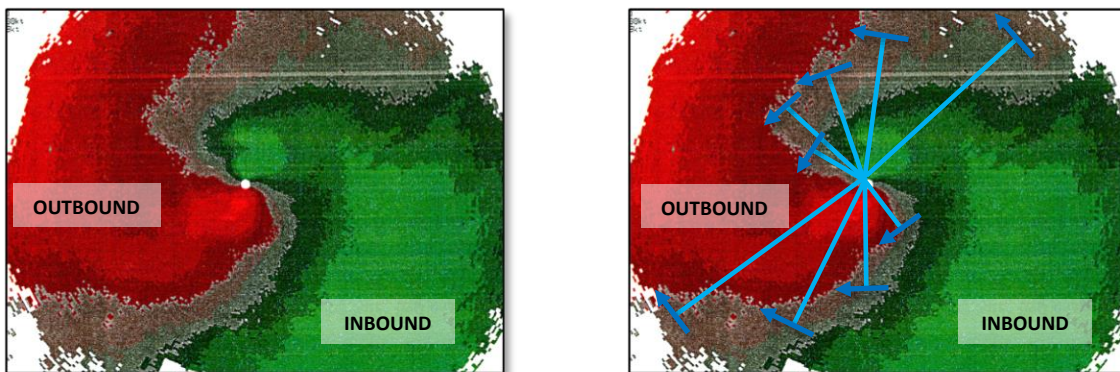


Fig. 5.7: Forward-S zero isodop: Real world example with generally easterly winds. Left: Base radial velocity. Right: Same, with reference lines and vector arrows. (Credit: WDTB 2005.)

5.3.1.3. **The Backward-S zero isodop: Cold air advection.** The thermal wind relation implies that cold air advection (CAA) should cause the wind direction to rotate in a counterclockwise direction with height, that is, *backing*. In a WSR velocity scan, this corresponds to backing with distance from the RDA. Figure 5.8 shows a cartoon version of this scenario, with a generally easterly wind. The backward S-shaped zero-isodop is clearly visible in the figure.

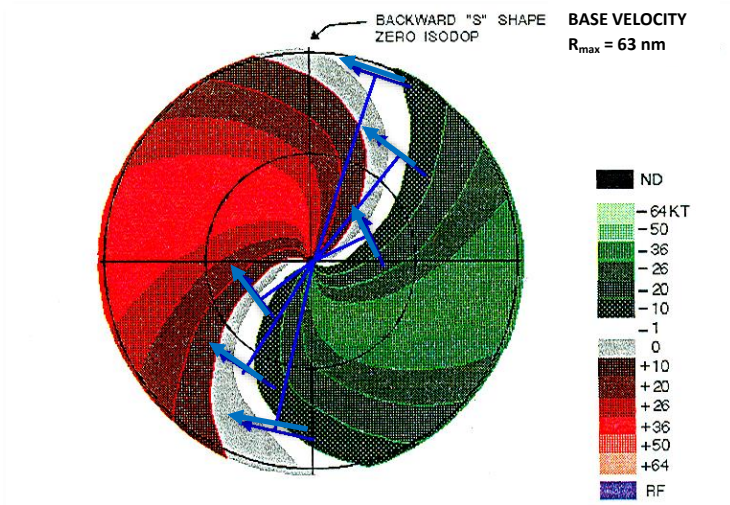


Fig. 5.8: Cartoon image of Backward-S zero isodop, with reference lines and vector arrows. As in Figure 5.6, this figure suggests that the WSR is using PRF No. 8, with 1281 pulses per second and a corresponding R_{max} of about 63 nm. Range rings are shown at 20 and 40 nm. (Credit: WDTB 2005.)

5.3.1.4. **Difluence and confluence.** In these two cases, the zero-isodop forms a U-shape. Figure 5.9 shows two examples with westerly winds. In the presence of diffluent winds, the U is open to the inbound flow (to the west in the example shown), and in the presence of confluent winds, the U is open to the outbound flow (east in the example shown). Let's assume these two cartoon examples are associated with the 0.5° tilt scan, with a PRF of 1281 pulses per second, and a corresponding R_{max} of 63 nm. This implies that the most distant point in the scan is about 0.55 nautical miles (about 1020 meters) ARL, which, in synoptic meteorology, is within the lower troposphere. In the presence of westerly winds,

- With *difluence* in the lower troposphere, one would expect *downward* vertical motion, so that the U open to the upwind direction (left panel in Figure 5.9) implies *subsidence*, a generally *stable* condition.
- With *confluence* in the lower troposphere, one would expect *upward* vertical motion, so that the U open to the downwind direction (right panel in Figure 5.9) implies *convection*, a generally *unstable* condition.

BASE VELOCITY
 $R_{max} = 63 \text{ nm}$

BASE VELOCITY
 $R_{max} = 63 \text{ nm}$

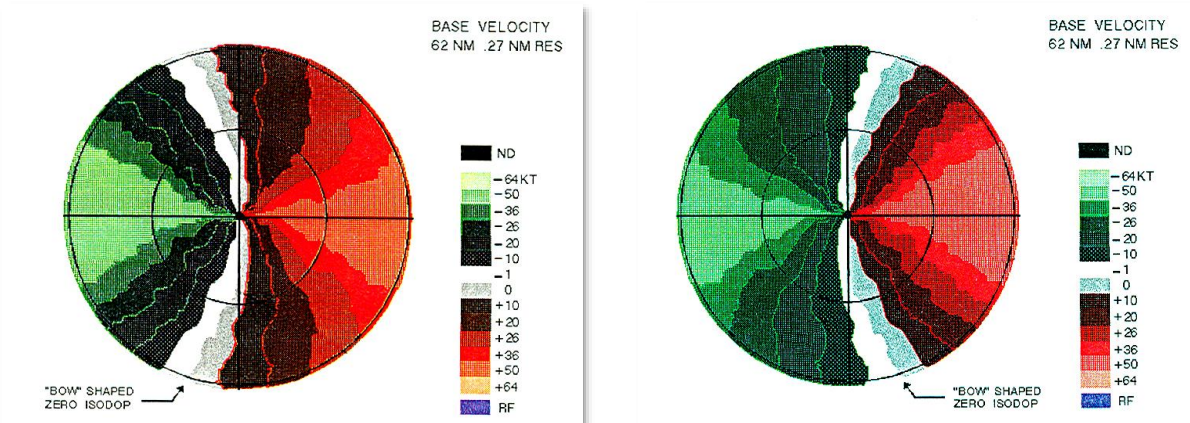


Fig. 5.9: Diffluent zero-isodop (left) and confluent zero-isodop (right). (Credit: WDTB 2005.)

5.3.1.5. **Mid-level wind maxima and sloping wind maxima.** A mid-level wind max (Figure 5.10, left) is identified by closed isodops surrounding a maximum wind velocity value at a middle distance from the RDA. Isodops greater than zero converge at the RDA, and wind speeds decrease again at the outer edges of the volume scan display. Since distance from the RDA corresponds to elevation, this means that wind speeds are lower at the higher elevations near the edge than at middle elevations above the RDA. With a sloping wind maximum, either the outbound maximum is farther from the RDA than the inbound maximum, or the reverse (Figure 5.10, right). Figure 5.11 shows a real-world example of a sloping mid-level wind max in the presence of northeasterly winds and warm air advection.

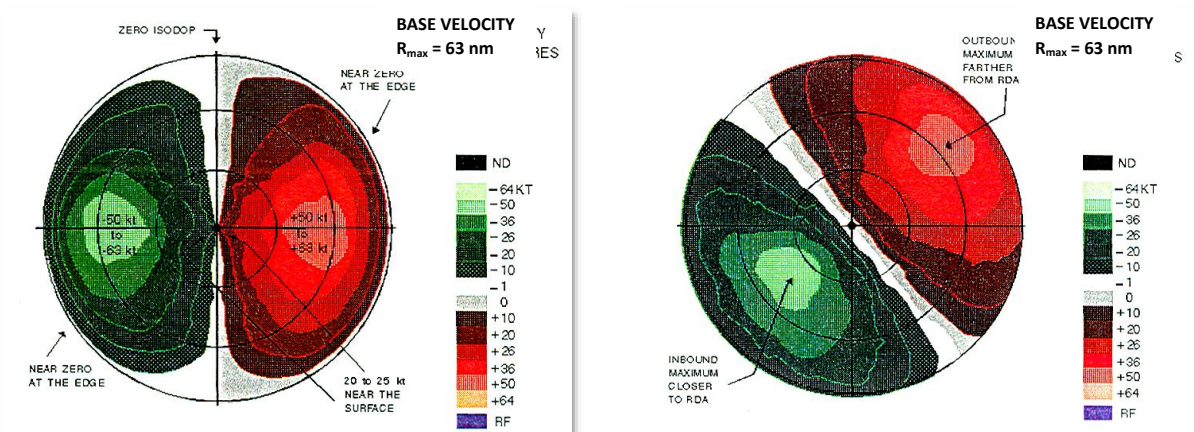


Fig. 5.10: Cartoons of mid-level wind maximum (left), and sloping mid-level wind maximum (right). Left: Velocities are lower near RDA and at the outer edge of the display (highest elevations visible). The highest wind speeds are visible at a middle distance from the RDA. Right: Sloping wind maximum,

increasing in height from southwest (where the highest speeds are nearer the RDA) to northeast (where the highest speeds are farther from the RDA). (Credit: WDTB 2005.)

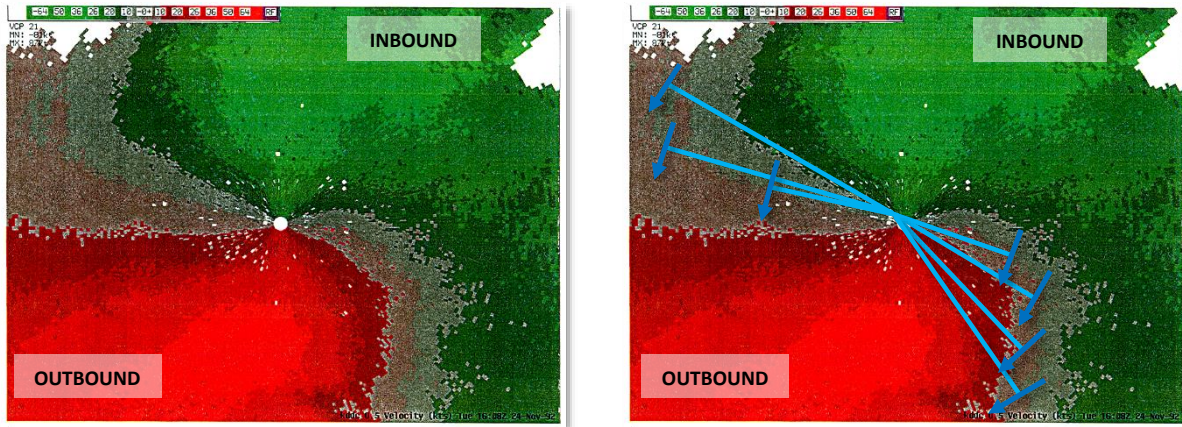


Fig. 5.11: Observed sloping mid-level wind maximum with WAA. Left: Base image. Right: Analysis with reference lines and vector arrows. The Forward-S zero isodop and veering with height are clearly visible. (Credit: WDTB 2005.)

5.3.1.6. Cold front approaching the RDA. In a scenario with a cold front moving into the volume scan area, there will be a portion of the velocity field that reflects the vertical wind variation one expects with warm air advection (veering with height), and there will be another portion (behind the cold front) where the velocity field reflects the vertical variation one expects with cold air advection (backing with height). This results in a rather complicated zero-isodop pattern that includes both Forward-S and Backward-S sections.

An example of this scenario is shown in Figure 5.12, in which a cold front is approaching the RDA from the northwest. The left panel shows a cartoon of the radial velocity field, and two things are immediately evident:

- There are two inbound maxima – one in the southwest, and one in the northwest. *Inbounds cover more than half the overall volume scan.* The inbound max in the southwest corresponds to the outbound max to the northeast, but the inbound max in the northwest has no corresponding outbound max.
- The zero isodop takes on the Forward-S configuration in the southeastern two thirds of the display (indicating WAA in the warm sector), but becomes part of a

Backward-S in the northwestern one third of the display (indicating CAA behind the cold front).

The zero isodop analysis shown in the right panel of Figure 5.12 indicates that the wind is veering with height near the RDA, and in the southeast. But, beyond the sharp bend seen in the zero isodop about 25 nm northwest of the RDA, the wind switches to backing with height.

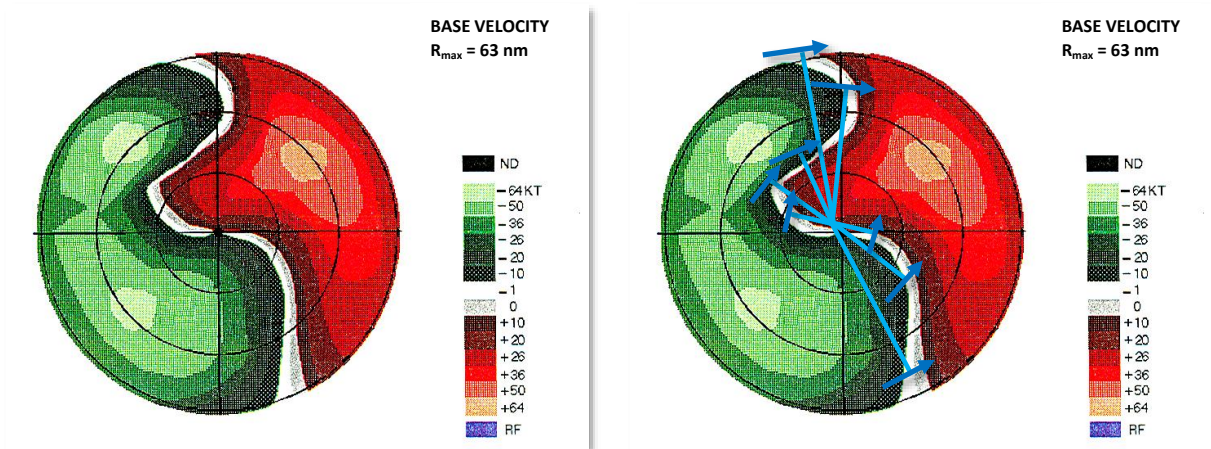


Fig. 5.12: Cartoon of the radial velocity field extant with a cold front approaching the RDA from the northwest. Left: Base image. Right: Analysis of the zero isodop with reference lines and vectors arrows. (Credit: WDTB 2005.)

Figure 5.13 shows a real world example of this scenario. Without a pretty good idea of what is happening synoptically, it would probably be fairly difficult to interpret. But it does show a great deal of similarity to the cartoons in Figure 5.12. Inbounds cover more than half the volume scan, and the inbound max to the southwest is matched by outbounds to the northeast. A confounding factor is the large amount of “purpled out” range bins. Purple is assigned to a given range bin’s velocity when the data in the bin are range folded (RF in the figure’s legend), that is, the data from a real echo in the bin are overlaid by data from a range folded bin beyond R_{max} (see Chapter 4 for more details). Another reason a given bin might be purpled out is that the Velocity Dealiasing Algorithm was unable to identify an alias of the first-guess radial velocity that was consistent with the velocities in the neighboring bins.

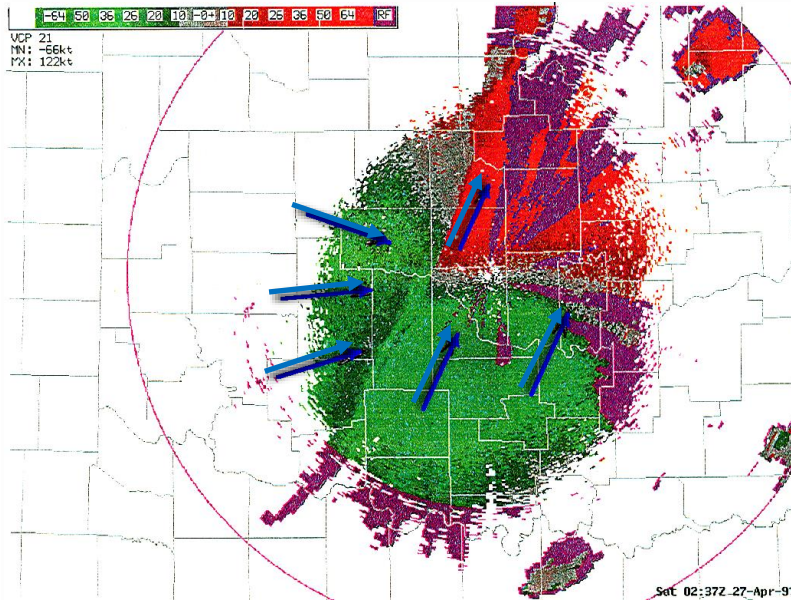


Fig. 5.13: Observed radial velocity field with approaching cold front, with a rough wind vector analysis. “Purpled out” range bins indicate No Data (ND), the result of either range folder or velocity aliasing (velocity folding). The zero isodop is rather difficult to identify. (Credit: WDTB 2005.)

A short time later, the cold front reaches the RDA. Figure 5.14 shows cartoons of this, and Figure 5.15 shows a real world example. The cartoons are relatively straightforward to analyze, using the standard technique with reference lines and vector arrows, but the real world example is fairly challenging. Inbounds now cover about $\frac{3}{4}$ of the display, and the zero isodop has taken on the appearance of the Greek letter tau (τ) (Figure 5.14). Using reference lines and vector arrows, veering with height (WAA) is visible in the southeastern half of the display, with the northwest half indicating slightly diffluent flow. The real world example (Figure 5.15) shows the dominance of inbound radial velocities, while range folding in the northeast section has made the outbound southwesterly flow almost impossible to identify. The zero isodop is equally difficult to identify.

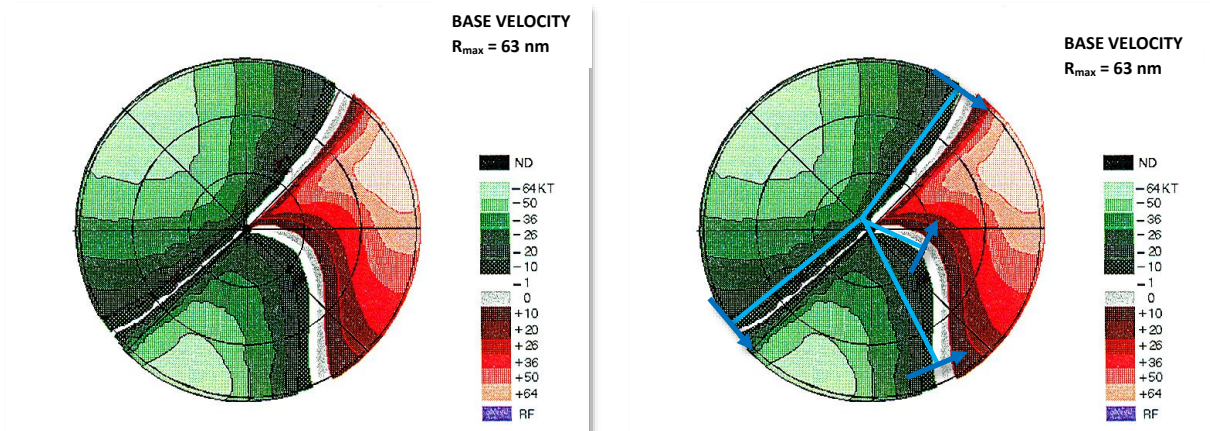


Fig. 5.14: Cartoon of the radial velocity field extant with a cold front on top of the RDA. Left: Base image. Right: Analysis of the zero isodop with reference lines and vectors arrows. (Credit: WDTB 2005.)

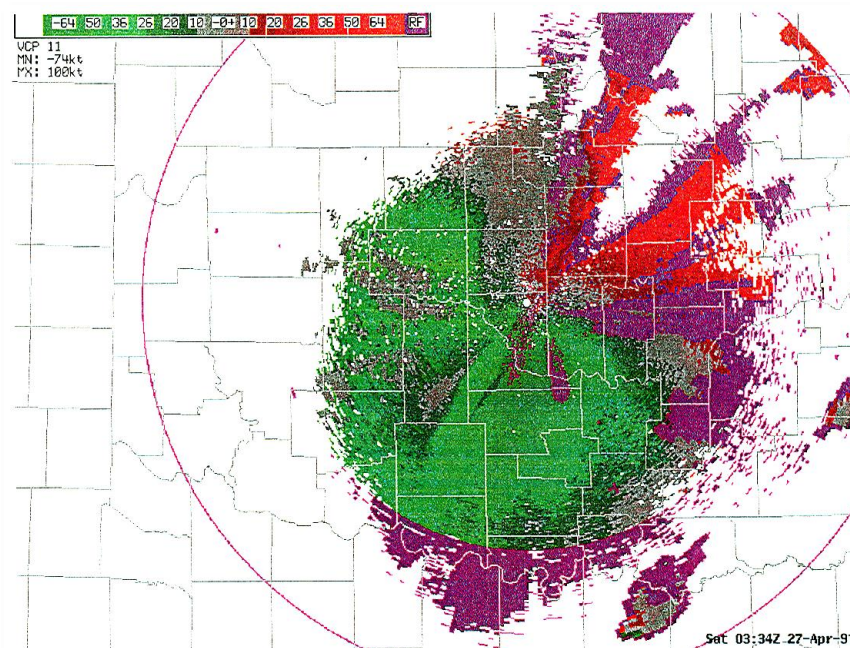


Fig. 5.15: Observed radial velocity field with cold front on top of the RDA. "Purpled out" range bins indicate No Data (ND), the result of either range folder or velocity aliasing (velocity folding). The zero isodop is rather difficult to identify. (Credit: WDTB 2005.)

5.3.2. Micro- α velocity field interpretation: Storm-scale. In this section we'll examine velocity fields on a much smaller scale, starting with cartoon depictions to keep it simple. After that we'll look at a real world example. Wood and Brown (1983)

developed complete derivations for these patterns and cataloged them in an atlas¹⁰. Here, we will keep it as straightforward and descriptive as possible.

Figure 5.16 shows a real world scenario with two scales of motion. The meso- β , Forward S zero isodop is evident inside the closest three range rings to the RDA, as is the generally southerly wind field. The micro- α velocity feature, corresponding to a thunderstorm mesocyclone, is near the top of the display (near the 160 km range ring). Notice the velocity couplet of red outbounds in close proximity to the green inbounds.

At the scale of a range bin, or of several range bins, variations in wind direction are driven by storm-scale processes such as rotation from the conservation of angular momentum (as in a mesocyclone), convergence, and divergence. And at this scale, Coriolis is not a strong force, so low-level convergence is not always associated with counterclockwise rotation (as one would expect in larger mesoscale and synoptic cyclones), but may also be associated with clockwise rotation.

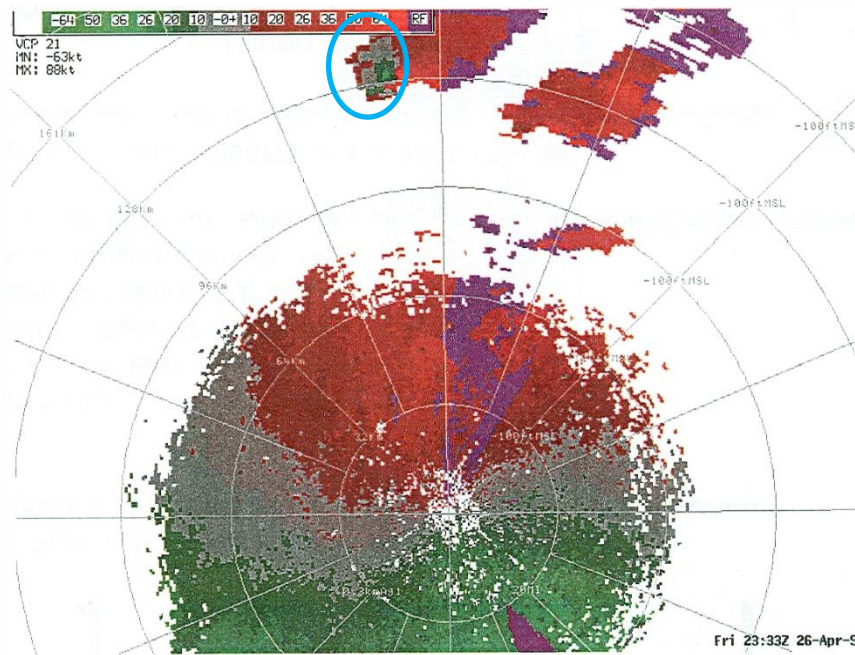


Fig. 5.16: Velocity field showing two scales of radial velocity. The meso- β Forward S zero isodop is visible near the RDA, and a micro- α mesocyclone can be seen to the north, circled in blue. (Credit: WDTB 2005.)

¹⁰ Also see Atlas (1990), Chapter 30a.

5.3.2.1. **Pure convergence and divergence.** When interpreting radial velocities at this scale, the forecaster often zooms in on a feature much smaller than the full volume scan, often leaving the RDA somewhere off the display. It's important to know where it is relative to the velocity features being interpreted. In this and all the following cartoon illustrations, the RDA is below the lower edge of the display, and north is "up."

Figure 5.17 illustrates pure convergence (left) and pure divergence (right) due north of the RDA. In the left panel, a center of outbound radial velocities (red) is closer to the RDA than a center of inbound radial velocities (green). Both are along the same radial, in this case, pointing north of the RDA. This implies convergence *toward* a point between the two centers. Since the radar cannot detect velocity components perpendicular to the radial, velocities converging on this center from the east or west are invisible. In the right panel, a center of outbound radial velocities is farther from the RDA than a center of inbound velocities, along the same radial. This implies divergence *from* a point between the two centers.

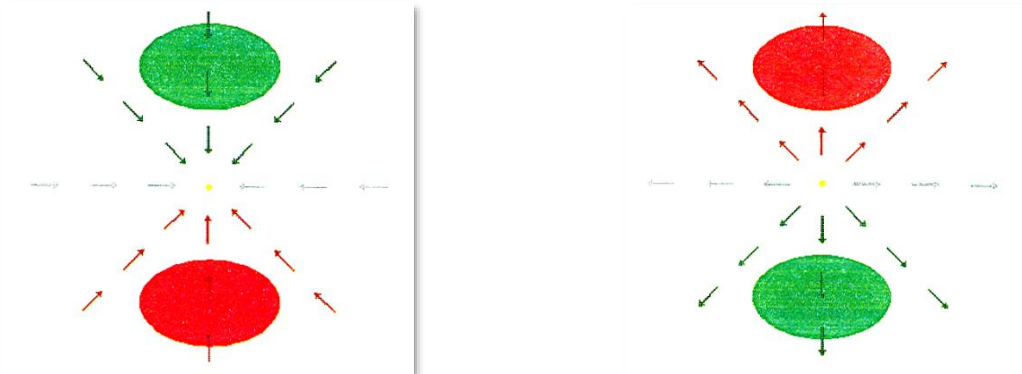


Fig. 5.17: Pure convergence (left) and divergence (right), along a radial north of the RDA. North is "up." The RDA is below (south of) the displayed area, to the south. (Credit: WDTB 2005.)

5.3.2.2. **Pure rotation.** Figure 5.18 illustrates cyclonic rotation (left) and anticyclonic rotation (right) due north of the RDA. In the left panel, a center of outbound radial velocities (red) is to the *right* of a center of inbound radial velocities (green) at the same distance from the RDA. This implies counterclockwise rotation around a point between the two centers. Since the radar cannot detect velocity components perpendicular to the radial, the westerly velocities south of this center and easterly velocities to its north are invisible. In the right panel, a center of outbound radial velocities (red) is to the *left* of a center of inbound radial velocities (green) at the

same distance from the RDA. This implies clockwise rotation around a point between the two centers.

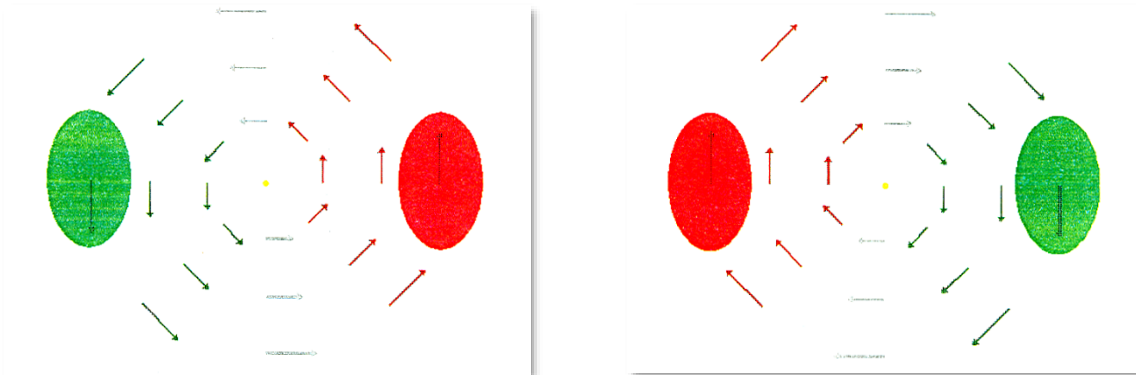


Fig. 5.18: Pure cyclonic rotation (left) and anticyclonic rotation (right), north of the RDA. North is “up.” The RDA is below (south of) the displayed area, to the south. (Credit: WDTB 2005.)

5.3.2.3. **Combined rotation, divergence and convergence.** Figure 5.19 illustrates four possible combinations of rotation, convergence, and divergence.

- To the upper left is cyclonic convergence, with the outbound max (red) closer to the RDA than the inbound max (green), indicating convergence. The outbound max is also to the right of the inbound max, indicating cyclonic (counterclockwise) rotation.
- The panel on the upper right shows anticyclonic convergence. The outbound max (red) is closer to the RDA than the inbound max (green), indicating convergence, but the outbound max is to the left of the inbound max, indicating anticyclonic (clockwise) rotation.
- On the lower left is cyclonic divergence, with the outbound max (red) farther from the RDA than the inbound max (green), indicating divergence. The outbound max is also to the right of the inbound max, indicating cyclonic (counterclockwise) rotation.
- On the lower right is anticyclonic divergence, with the outbound max (red) farther from the RDA than the inbound max (green), indicating divergence. The

outbound max is also to the left of the inbound max, indicating anticyclonic (clockwise) rotation.

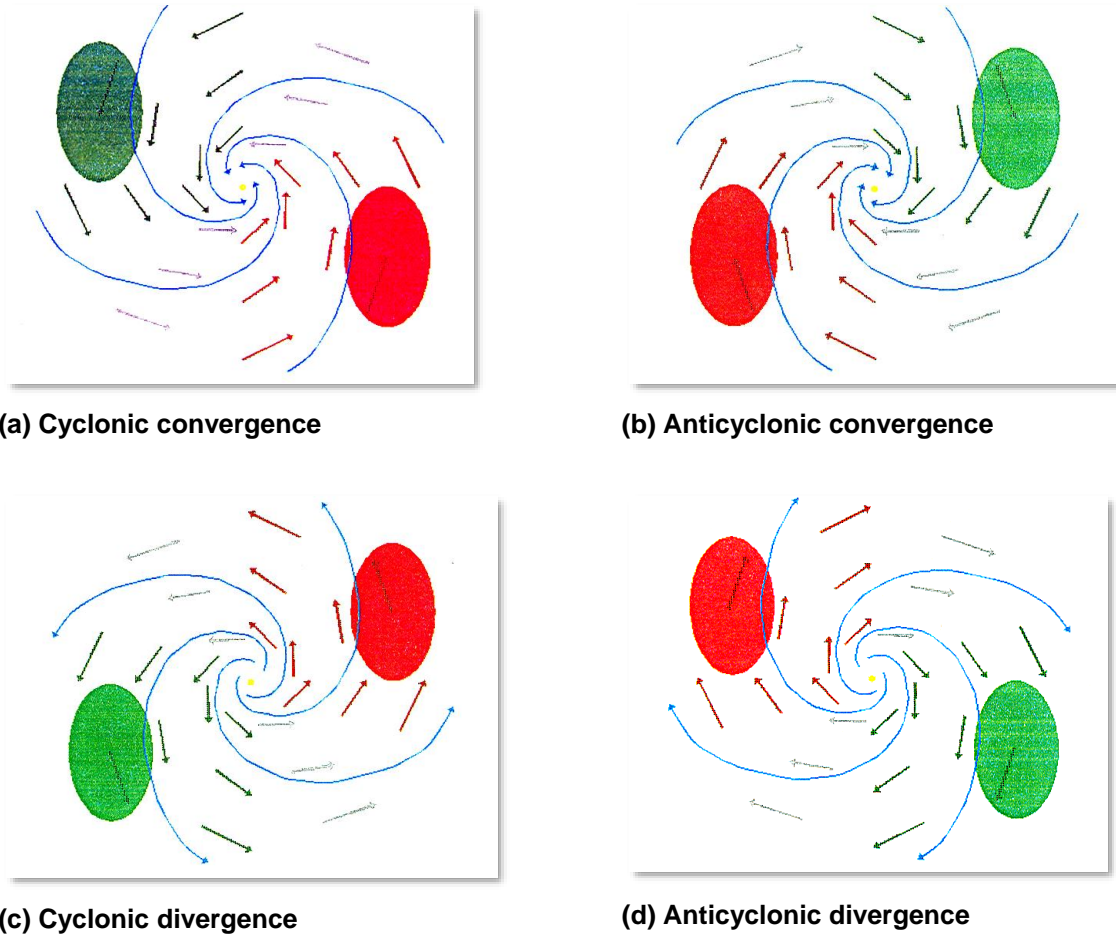


Fig. 5.19: Examples of combined rotation and convergence or divergence. North is “up.” The RDA is below (south of) the displayed area, to the south. (Credit: WDTB 2005.)

5.3.2.4. **Real world example: Supercell thunderstorm.** Figure 5.20 shows four radial velocity scans through a supercell, taken by the Oklahoma City (KTLX) RDA in April, 1991¹¹. The RDA is south-southeast of the radial velocity feature, and the 128 km range ring runs through the center of the feature. From upper left to lower right,

¹¹ Note that the figure shows Storm-Relative Mean Radial Velocity (SRM), not base radial velocity. SRM is a derived (Level III) product described in greater detail in Chapter 7. It attempts to reveal the radial velocity of a storm cell from within a coordinate system centered on the moving core of the cell.

the scans shown in the figure are from the 0.5°, 1.5°, 2.4°, and 6.0° tilt angles. Assuming $R = 128$ km with these tilts, (5.1) yields the following corresponding elevations ARL:

- 0.5°: 1.13 km (~890 hPa)
- 1.5°: 3.35 km (~670 hPa)
- 2.4°: 5.36 km (~520 hPa)
- 6.0°: 13.38 km (~150 hPa)

where the estimated pressures are from the U.S. Standard Atmosphere (e.g. Miller 2015). From this it's obvious that the four panels in Figure 5.20 represent scans through the storm from just above the Earth's surface, to a point near or somewhat above the tropopause.

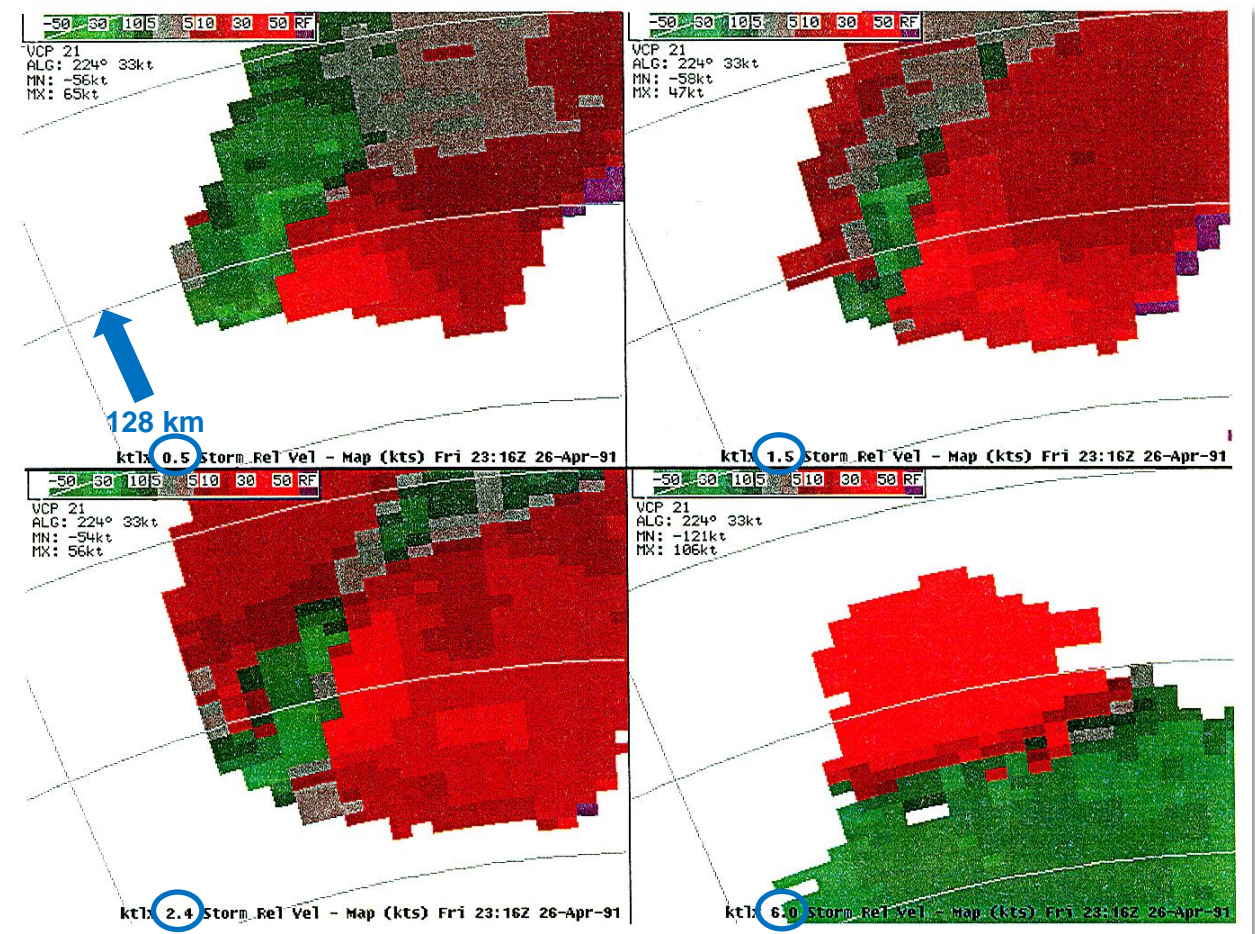


Fig. 5.20: Volume scan of Storm-Relative Mean Radial Velocity (SRM) associated with a supercell from the KTLX RDA, April, 1991. Tilt angles (degrees above horizon) are circled; the 128 km range ring is indicated with an arrow. (Credit: WDTB 2005.)

Figures 5.21 – 5.24 show the interpretation of the velocity fields in Figure 5.20. In each case, the cartoon storm-scale velocity model is on the left, and the observed radial velocity field with the supercell is on the right. Red (outbound) and green (inbound) arrows have been added to the right panels to show the approximate locations of the outbound and inbound maxima.

Beginning with the 0.5° tilt data shown in Figure 5.21, the cyclonic convergence near the base of the supercell is clearly visible. In Figures 5.22 and 5.23, corresponding to the 1.5° and 2.4° tilts, respectively, pure (or nearly pure) cyclonic rotation is visible in the middle troposphere. In Figure 5.24, corresponding to the 6.0° tilt, pure divergence near the tropopause can be seen.

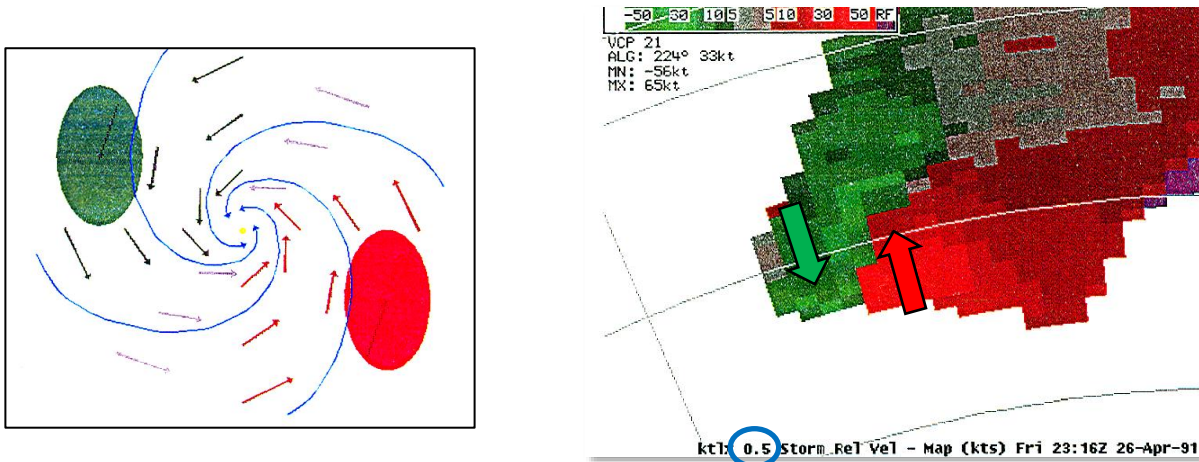


Fig. 5.21: Cyclonic convergence near the base of the supercell, at 1.13 km ARL (~890 hPa).
(Credit: WDTB 2005.)

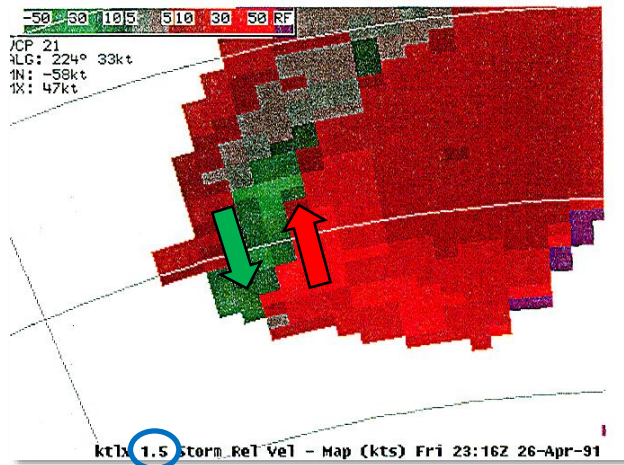
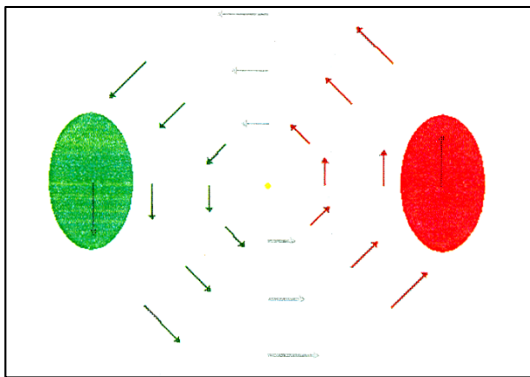


Fig. 5.22: Pure cyclonic rotation in the mid-troposphere, at 3.35 km (~670 hPa). (Credit: WDTB 2005.)

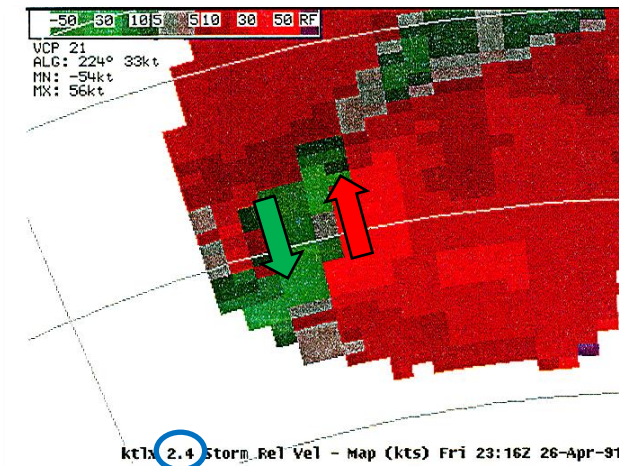
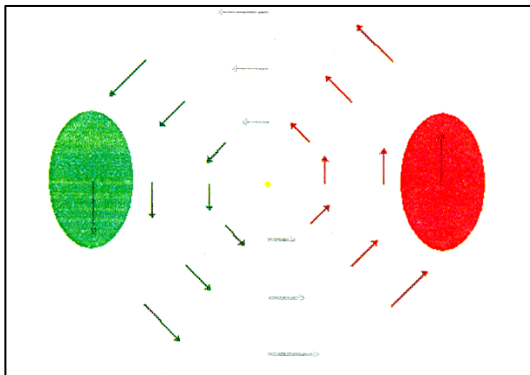


Fig. 5.23: Pure cyclonic rotation in the mid-troposphere, at 5.36 km (~520 hPa). (Credit: WDTB 2005.)

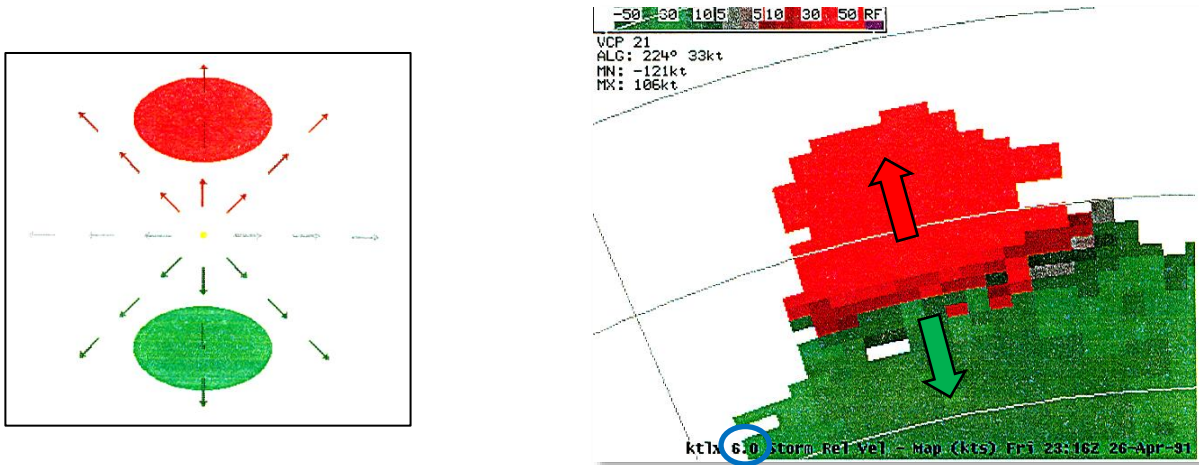


Fig. 5.24: Pure divergence at the top of the supercell, near the tropopause, at 13.38 km (~150 hPa). (Credit: WDTB 2005.)

This concludes the brief lesson in interpreting radial velocity fields. In the next chapter, we discuss several products created from Level II dual-polarization data.

Summary. The WSR-88D is incapable of directly measuring the full wind vector, except when the wind is blowing directly toward or away from the RDA. When the wind is parallel to the beam of pulses emitted by the antenna, the perceived wind corresponds to the full wind vector. As the angle between the wind and the radar beam increases, the perceived wind increases, reaching zero when the two are perpendicular to each other.

Isodops are lines of equal Doppler shift, or, equal wind speed. The zero isodop corresponds to zero perceived wind speed, and occurs where (1) the wind speed is actually zero, and (2) the wind vector is perpendicular to the radar beam. Since, at points sufficiently far above Earth's surface the wind speed is rarely zero, the zero isodop can be used to identify the point at which the wind vector is perpendicular to the radar beam. This assumption leads to the method used to estimate the full wind vector at volume-scan scale.

Because all radar beams tilt upward, there is a relationship between distance from the RDA and height above Earth's surface in all volume scans. More distance objects are higher, given a fixed tilt angle. This, and the thermal wind relation, result in distinctive zero isodop patterns in the presence of temperature advection at the volume scan scale. The Forward S corresponds to warm air advection, and the Backwards S corresponds to cold air advection. These two patterns, and the patterns corresponding

to diffluence and confluence, when events such as frontal passages occur within the volume scan area.

A different type of analysis is applied to storm-scale velocity scans, which includes identifying distinctive patterns for divergence, convergence, clockwise (anticyclonic) rotation, and counter-clockwise (cyclonic) rotation. These patterns often occur in combinations, such as cyclonic convergence and anticyclonic divergence. A vertical scan through a rotating severe thunderstorm may include several such velocity patterns, depending on where in the storm the analyst is looking.

Terms and concepts:

- Anticyclonic
- Backing
- Backward-S
- Cold air advection (CAA)
- Confluence
- Convergence
- Cyclonic
- Diffluence
- Divergence
- Equivalence of range and elevation
- Forward-S
- Isodop
- Meso- α
- Meso- β
- Meso- γ
- Micro- α
- Veering
- Velocity couplet
- Warm Air Advection (WAA)
- Zero isodop

Study prompts:

1. Explain the meaning and significance of the zero isodop.

2. What is the relationship between range and elevation, and how is this useful when interpreting radial velocity fields?
3. How are variations in wind direction with height related to the sign of the temperature advection?
4. Explain the method used for graphically interpreting radial velocity at the volume-scan scale, and illustrate with a basic example.
5. Explain the physical significance of Forward-S and Backward-S zero isodops.
6. Sketch examples of zero isodops associated with confluence and diffluence.
7. Explain how you would recognize the presence of a sloping mid-level wind maximum in the radial velocity data.
8. Why do some range bins receive the purple color designation in some radial velocity scans?
9. Summarize the appearances of pure convergence, divergence, cyclonic rotation, and anticyclonic rotation at storm scale in radial velocity scans.
10. Describe the appearance of cyclonic convergence and anticyclonic divergence at storm scale in radial velocity scans.

6. Dual-wavelength and dual-polarization variables and products.

With contributions from Dan St. Jean.

This chapter begins with a discussion of dual-wavelength radar, and describes the Hail Signal. From there it moves into a detailed description of how the recent dual-polarization retrofit to the WSR-88D network can be used to diagnose storm-scale phenomena such as hail, mixed-phase precipitation, and tornadic activity. Many examples of each are included.

6.1. In addition to base reflectivity, radial velocity, and spectrum width, many modern weather radar systems produce data by using more than one wavelength of radar energy, or by controlling and utilizing the polarity of the EMR pulses. In this chapter we'll review the types of information that can be derived from these advanced datatypes.

6.2. **Dual-wavelength radar.** Operational radar of this kind are rare; they are more often used for research purposes. Rinehart (2004) discusses several of them in his Appendix D, such as the American CP2 and the Russian MRL-5M. There are a number of technical reasons why this method hasn't been widely adopted, among them (1) it usually requires two radar antennae, which, in turn, makes it much more expensive; and (2) it requires imaging the same volumes of space (range bins) in a nearly identical way, using EMR pulses that behave differently because of their different wavelengths, which is quite difficult.

One use of dual-wavelength radar installations is hail detection, which is based on the difference between the radar reflectivity of particles with different radii. Radar reflectivity is closely related to backscattering, and in Chapter 2, we reviewed Rayleigh and Mie scattering. The first occurs when the circumference of the scattering particle is much smaller than the wavelength of the EMR; that is:

$$2\pi r \ll \lambda \tag{6.1}$$

where r is the radius of the particle, and λ is the wavelength of the EMR. Mie scattering occurs when the circumference of the scattering particle is of a similar size order as the EMR, so that:

$$2\pi r \approx \lambda \quad (6.2)$$

where the approximation is fairly broad. In general, backscattered EMR from Rayleigh scattering is much brighter than backscattered EMR from Mie scattering.

Hail-detecting dual-wavelength radar uses 10 cm (S-band) and 3 cm (X-band) microwaves. Most raindrops in the atmosphere are less than 2 to 4 mm in diameter. The largest physically possible are 6 to 8 mm, but these then break up into smaller drops.

- Raindrops of 2 to 4 mm radius are small enough to put them into the Rayleigh scattering (bright) region of both the S- and X- bands.
- When large hailstones (> 5 mm in radius) are present, they are large enough to be pushed into the Mie scattering (dimmer) region of the X-band radar.

Therefore, when large hailstones are present, the S-band (10 cm) radar still sees particles in the Rayleigh scattering region, while the X-band (3 cm) radar sees particles in the Mie scattering region.

The quantitative parameter used for this is called the Hail Signal (H), which is defined by:

$$H = 10 \log_{10} \left(\frac{Z_s}{Z_x} \right) \quad (6.3)$$

and has units of decibels (dB). Z_s is the linear reflectivity recorded by the S-band radar, and Z_x is the linear reflectivity recorded by the X-band in the same range bin [mm^6m^{-3}]. When no large hail are present, $Z_s \approx Z_x$, and H is about 0 dB. When meteorologically significant hail are in a given range bin, the Hail Signal is usually at least 3 dB, and may approach 20 dB, implying that the Z_s is *100 times greater* than Z_x (Rinehart 2004).

6.3. Dual-polarization radar. Polarization is one of the fundamental characteristics of EMR, in addition to its wavelength and amplitude. The polarization usually refers to the orientation of the plane of the electrical component of the EMR wave. The E-wave is chosen because its amplitude is 3×10^8 times greater than the amplitude of the B-wave. (All of this is discussed in greater detail in Chapter 2.) Most natural radiation is

randomly polarized (creating “glare” in visible light), while most anthropogenic radiation has a preferred polarization orientation.

6.3.1. There are two basic types of EMR polarization: Circular and linear. Circularly-polarized radiation can be either right- or left-handed, such that the E-wave plane rotates in either a clockwise or counterclockwise sense as the EMR propagates, respectively. Linearly-polarized radiation may be horizontal, vertical, or diagonal. The WSR-88D weather radars were originally installed with linear, horizontal polarization. Thus when the decision was made to retrofit the entire network with dual-polarization (commonly called “dual-pol”) capability (to increase its capabilities, and improve rainfall-rate estimates), there were several possible choices.

Dual circular polarization requires two antennae, which doubles the cost, and given the vagaries of government funding, this was (accurately) judged to be out of reach. The alternative is then linear polarization, possibly with alternation between horizontally- and vertically-polarized pulses. But this too would require additional hardware, in the form of a switch (a second duplexer) that alternates the radar between the two modes. The final alternative is then a diagonally-polarized beam, with basic trigonometry applied to analyze the differences between the transmitted and returned power in the horizontal and vertical planes. While limited in comparison to what might have been possible with either of the first two possibilities, this is still an improvement over the original horizontal polarization.

6.3.2. In 2013, the project to retrofit the entire WSR-88D network for dual-pol was completed. (More about this project from the NOAA Radar Operations Center is available here: <https://www.roc.noaa.gov/WSR88D/PublicDocs/DualPol/DPstatus.pdf>) Dual-polarization radar data are useful in meteorology because most hydrometeors are not perfect spheres. This includes both liquid and solid hydrometeors, such as hailstones and ice crystals. For example, raindrops change shape as they increase in size (Figure 6.1). (The image of a raindrop as shaped like a teardrop is in inaccurate popularization.) Small falling raindrops are nearly spherical because of their surface tension, and (because of the drag force from the surrounding air) they become progressively more flattened as their size increases. Beyond about five millimeters, they tend to break into two smaller drops.

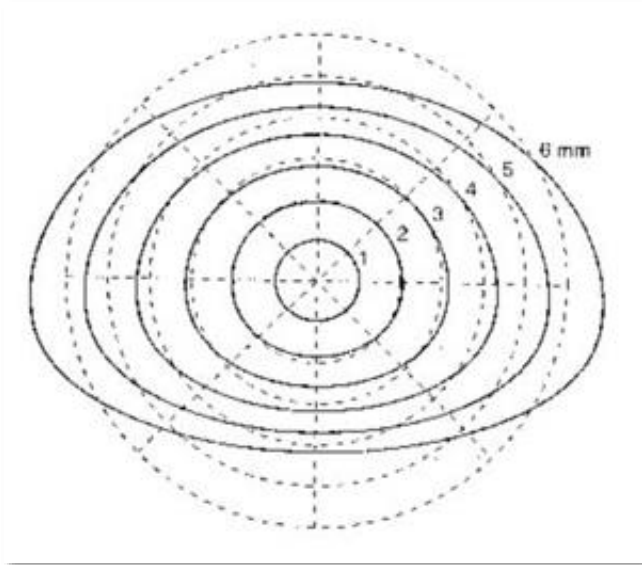


Fig. 6.1: Variation in raindrops shape with diameter. Raindrops with a diameter of 1 mm are spherical; as they get larger the horizontal diameter increases more than the vertical diameter. (Image credit: <https://pmm.nasa.gov/resources/students-and-educators/the-shape-of-a-raindrop>)

A weather radar with vertically- and horizontally-polarized beams is able to detect the mean shape of the droplets in a given range bin. It does this by comparing the backscattered EMR in the two linear planes. Figure 6.2 shows a highly simplified schematic of this scenario. On the left, the vertical and horizontal beams backscatter the same amount of EMR from a small raindrop. An algorithm in the radar compares the two and concludes that the mean raindrop shape is close to a millimeter, using the relationship shown in Figure 6.1. On the right, the vertical beam backscatters a smaller amount of EMR than the horizontal beam from a large raindrop. The radar algorithm compares the two and concludes that the mean raindrop is several millimeters, using the same relationship in Figure 6.1.

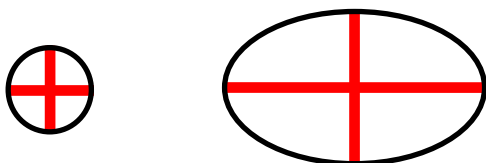


Fig 6.2: Highly schematic view of vertical and horizontal radar beams interacting with small (left) and large (right) raindrops. Vertical and horizontal radar reflectivity are shown in red.

This is useful because it provides key information needed for computing the rainfall rate, which could only be guessed at prior to the dual-pol refit. Recall the relationship in (3.6), which stated that the rainfall rate (R) is given by:

$$R \equiv \frac{\pi}{6} \int_0^{\infty} N(D) D^3 w_t(D) dD$$

where $N(D)$ is the dropsize distribution [m^{-3}], D is the drop diameter [mm], and $w_t(D)$ is the terminal fall speed for spherical raindrops, as a function of their diameters [ms^{-1}]. R has units of $mm s^{-1}$. The difference between the vertically- and horizontally-polarized reflectivity provides an estimate of the mean dropsize distribution in each range bin, allowing (in theory, at least) a somewhat better estimate of rainfall rate.

There are at least three complicating factors. The first is that the “horizontally-polarized” beam is not really horizontal, because of the tilt angle(s) of the antenna. The second is that the dropsize distribution estimated by the means described above is only an average value in each range bin, and it is still heavily weighted toward larger raindrops because of their much higher reflectivity. (See Chapter 3.) The third is that, because of the way that larger raindrops fall, the vertically- and horizontally-polarized beams are not really measuring the largest dimension of the raindrops. This is illustrated in Figure 6.3. Large rain drops don’t usually fall with their widest dimension perfectly horizontal, but are often tilted at what is called the Cant Angle (β). The greater the cant, the more the raindrop’s wide dimension is tilted out of the horizontal plane. This, in turn, means that the horizontally-polarized beam is measuring somewhat *less* than the full size of the large dimension, and the vertically-polarized beam is measuring somewhat *more* than the real size of the small dimension. The result is that the radar algorithm using the two reflectivities to estimate dropsize is producing an underestimation, which in turn affects the rainfall rate (Rinehart 2004).

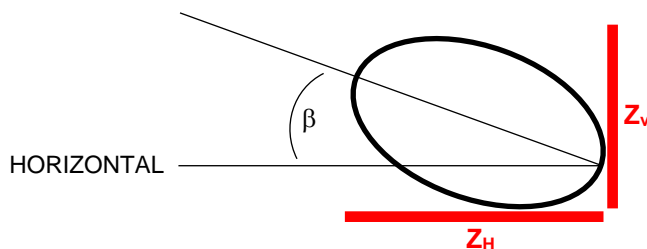


Fig 6.3: Cant Angle (β) of a large raindrop.

6.3.3. Another example of two types of hydrometeor that can be differentiated using dual-pol data are ice crystals and hailstones. Ice crystals can come in many shapes, but for the purposes of this demonstration let's consider cone-shaped needles, falling with the heavier side down. Figure 6.4 illustrates this comparison. Prior to the WSR's dual-pol retrofit, these two frozen hydrometeors were simply highly reflective, and it was often difficult to distinguish between them. With dual-pol, the conic ice crystal (left) backscatters more EMR in the vertical plane than it does in the horizontal plane, while the large hailstone (right), which tumbles as it falls, backscatters roughly equal amounts of EMR in both planes. Once again, the WSR algorithm that compares the vertically- and horizontally-polarized backscattered energy in each range bin can distinguish the difference between the two types (Rinehart 2004).

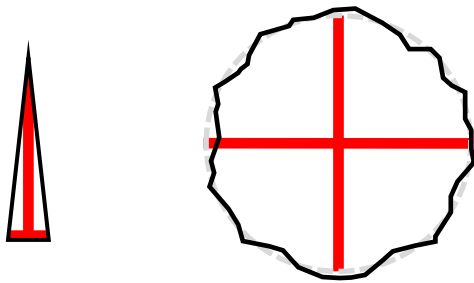


Fig 6.4: Highly schematic view of vertical and horizontal radar beams interacting with conical ice crystals (left) and large tumbling hailstones (right). The large hailstone may be irregularly shaped because of its formation process, but because it tumbles as it falls, its mean shape as perceived by the radar is spherical (dashed gray line). Vertical and horizontal radar reflectivity are shown in red.

6.4. Since the dual-pol retrofit, which required additional on-site engineering at each of the approximately 160 WSR-88D RDA locations, a great deal of work has been done to incorporate dual-pol data into existing algorithms, and to create new parameters based on the dual-pol data. In the following sections, we'll discuss some of the new datatypes.

6.4.1. Differential Reflectivity (Z_{DR}). This is a parameter built around the use of linearly-polarized reflectivity. It is generated at the RDA, then sent to the RPG for quality control and conversion into a base product. The retrofitted WSRs transmit diagonally-polarized EMR, with equal amounts of energy in the horizontal and vertical

planes. The pulses interact with hydrometeors in each range bin, and backscatter differing amounts of energy in the two planes depending on the types of hydrometeors present. The Probert-Jones Radar Equation (3.4) is then applied to the returned power in the horizontal and vertical planes, resulting in separate values of horizontal reflectivity (Z_H) and vertical reflectivity (Z_V). To compute the Z_{DR} , the two reflectivities are placed into the relation:

$$Z_{DR} \equiv 10 \log_{10} \left(\frac{Z_H}{Z_V} \right) \quad (6.4a)$$

where Z_{DR} has units of decibels, and typically varies between about -8 dB and +8 dB (St. Jean 2012). To use the form in (6.4a), both Z_H and Z_V must be linear reflectivity, with the usual base units of $\text{mm}^6 \text{m}^{-3}$. If Z_H is *greater* than Z_V , the ratio inside the parenthesis has a value of greater than one, the log of which is greater than zero, and the Z_{DR} is a positive number. If Z_H is *less* than Z_V , the ratio inside the parenthesis is less than one, the log of which is less than zero, and the Z_{DR} is a negative number. If the two base reflectivities are in decibels, Z_{DR} can be computed by:

$$Z_{DR} \equiv dZ_H - dZ_V \quad (6.4b)$$

which can be found from (6.4a) using a simple logarithmic identity (Rinehart 2004).

Table 6.1 shows a simplified set of values one would expect from different types of hydrometeors in a given range bin. Column 1 lists the type: Small (spherical) raindrops, large (oblate) raindrops, tumbling hailstones, or conical ice crystals. (These are all described in the previous section.) Column 2 of the table lists the relative values of unpolarized reflectivity one would expect with each of these precipitation types. Large raindrops, tumbling hailstones, and conical ice crystals all produce high reflectivity values and would have been difficult to differentiate prior to the dual-pol refit. The remaining three columns show how the dual-pol data allow differentiation.

- Small raindrops produce low unpolarized reflectivity and Z_{DR} values near zero.
- Large raindrops produce high unpolarized reflectivity and Z_{DR} values of greater than zero.
- Tumbling hailstones produce high unpolarized reflectivity and Z_{DR} values near zero.
- Conical ice crystals produce high unpolarized reflectivity and Z_{DR} values of less than zero.

Table 6.1: Relative values of Z_{DR} and related parameters for different hydrometeor types.

Type	Unpolarized Z	Z_H	Z_V	Z_{DR}
Small raindrops	Low	Low	Low	~ 0
Large raindrops	High	High	Low	> 0
Hail	High	High	High	~ 0
Ice crystals	High	Low	High	< 0

Figure 6.5 shows a more detailed scheme of Z_{DR} values for different types of targets in a range bin. For example, rain and drizzle produce values between about 0.25 dB and 5 dB; hailstones range from about -2 to about 6 dB; and graupel (small hail) ranges from about -1 to about 2 dB. Expected values with biological targets (birds and insects), Ground Clutter and AP, chaff (strips of foil distributed by aircraft to confuse radar), and debris (such as a tornado debris ball) are also shown. Figure 6.6 shows a sample of side-by-side AWIPS images of conventional reflectivity and Z_{DR} for the same scene, just to provide an idea of how the two differ in appearance.

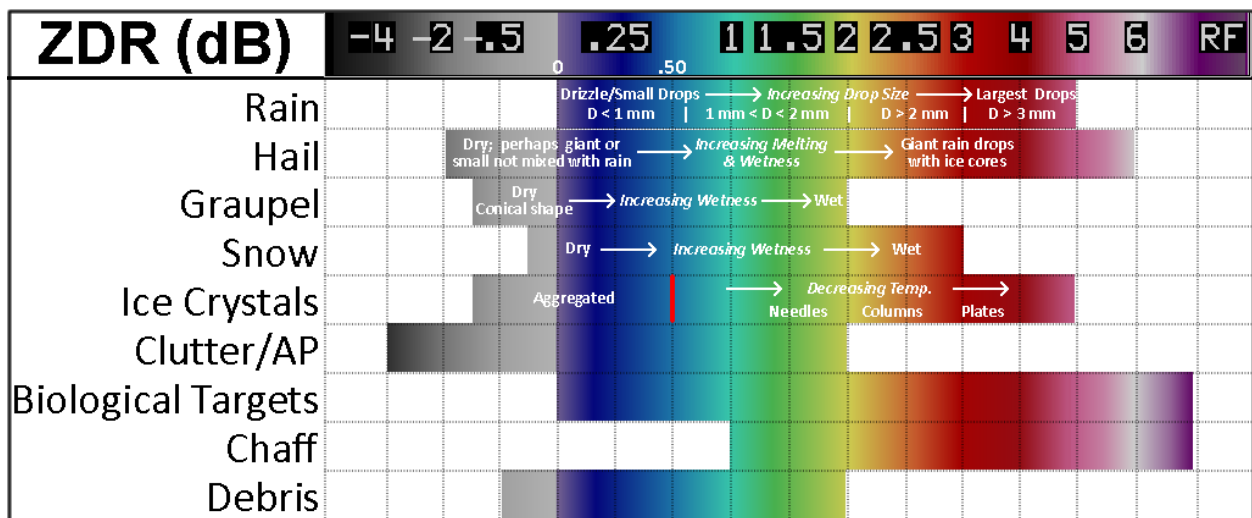


Fig. 6.5: Typical Z_{DR} values associated with different types of targets. (Credit: St. Jean 2012; WDTD 2019.)

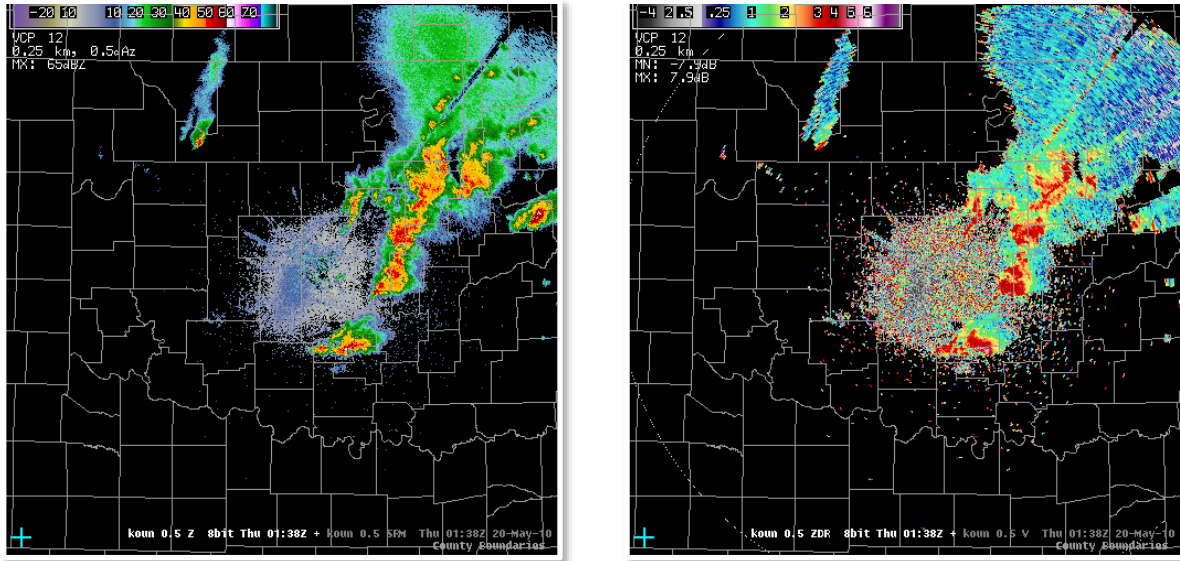


Fig. 6.6: Sample of conventional reflectivity (left) and Z_{DR} (right) visualized using AWIPS. Z_{DR} products are available for all elevation angles. (Credit: St. Jean 2012; WDTD 2019.)

Next, we'll review a few examples of how Z_{DR} can be used to identify:

- Hail
- The melting layer in stratiform precipitation scenarios
- Thunderstorm updrafts
- Tornadic debris
- Non-meteorological echoes, such as birds and insects

6.4.1.1. Hail identification. The hail core in a thunderstorm consisting of tumbling hailstones, and the surrounding portion of the storm, populated by large, liquid rain drops, are both areas of high conventional reflectivity. But large droplets should generate high values of Z_{DR} (because their horizontal dimensions are larger than their vertical dimensions), while large hailstones should generate Z_{DR} values that are near zero (because they tumble, making their mean horizontal and vertical dimensions the same size). Figure 6.7 shows an example of a thunderstorm hail core, using side-by-side displays of conventional reflectivity and Z_{DR} (St. Jean 2012; WDTD 2019).

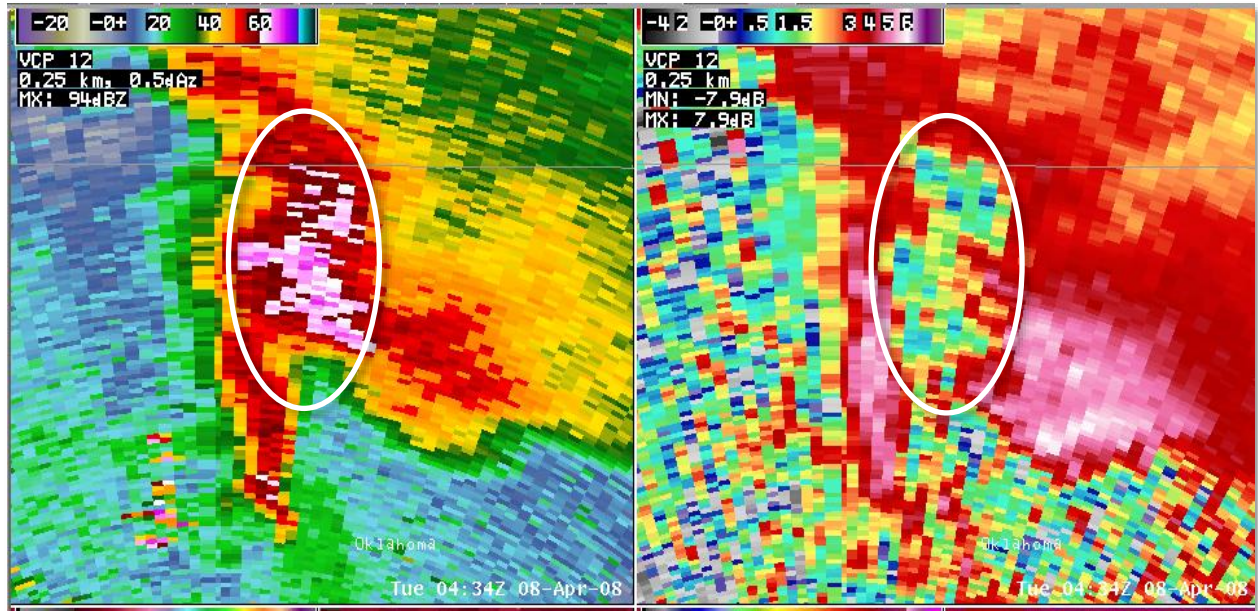


Fig. 6.7: Example of hail identification using Z_{DR} . Conventional reflectivity is shown on the left; Z_{DR} is on the right. The reflectivity core (noted by the white oval) shows values greater than 60 dBZ, indicating the likely presence of hail. The Z_{DR} product on the right provides more evidence, with values less than 1 dB, much lower relative than surrounding areas. High reflectivity with low Z_{DR} (near 0 dB and at times even slightly negative) is a classic hail signature. (Credit: St. Jean 2012; WDTD 2019.)

6.4.1.2. Melting layer identification. The melting layer is a region just below the 0 °C isotherm, where solid precipitation (snow) begins to melt as it falls into a warmer layer. From the point that it begins to melt, to the point lower in the atmosphere where it has completely melted, there is often a region of high radar reflectivity. (Wet snowflakes are usually highly reflective.) In a tilted radar beam, it should appear as a ring of high reflectivities around the RDA, at a distance where the beam encounters the melting precipitation particles. But this is not always the case, particularly in very light precipitation scenarios. Figure 6.8 shows an example of using the Z_{DR} to identify the melting layer, when it doesn't show clearly in conventional reflectivity (St. Jean 2012; WDTD 2019).

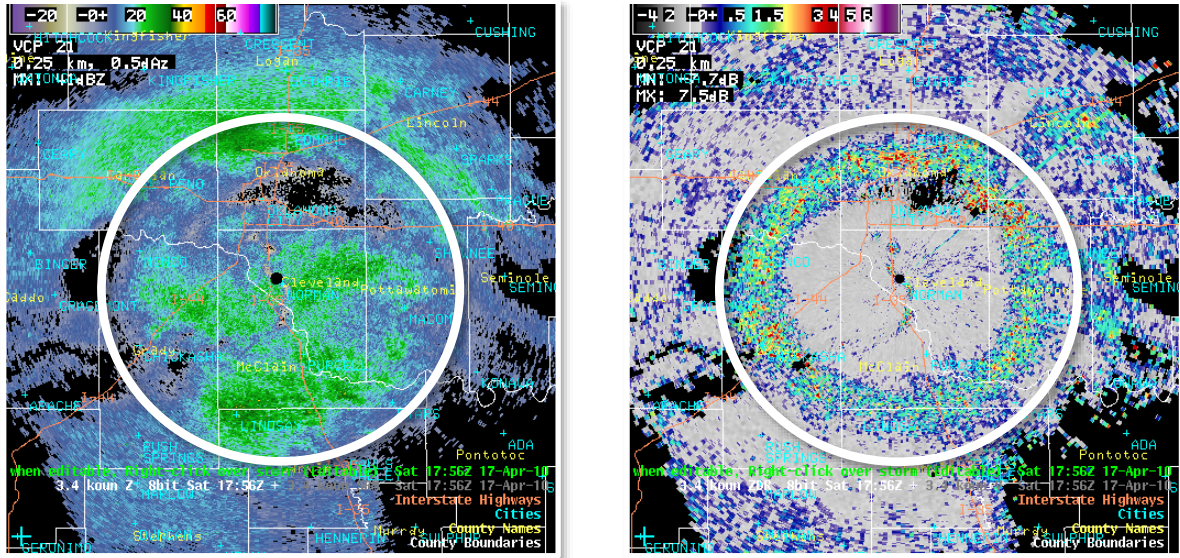


Fig. 6.8: Identifying melting layer using Z_{DR} . This example is from the 3.4 degree tilt angle of the Kegelman Field, Oklahoma (KOUN) WSR-88D dual-pol radar during a stratiform rain event. Note that the reflectivity image (left) does not show a pronounced ring of high reflectivity (the bright band typically associated the melting layer), but the Z_{DR} (right) shows a ring of higher (and noisier) Z_{DR} . As snow and ice crystals begin to melt, they increase in density and also grow in the horizontal dimension, both of which leads to an increase in Z_{DR} . (Credit: St. Jean 2012; WDTD 2019.)

6.4.1.3. Identifying thunderstorm updrafts. When intense updrafts develop, and enough liquid water is present within them, the liquid water can be lofted well above the environmental 0° Celsius level. This results in an area of locally enhanced Z_{DR} within an updraft. Figure 6.9 shows an example where Z_{DR} clearly indicates liquid water in a supercell updraft, well above the freezing level (St. Jean 2012; WDTD 2019).

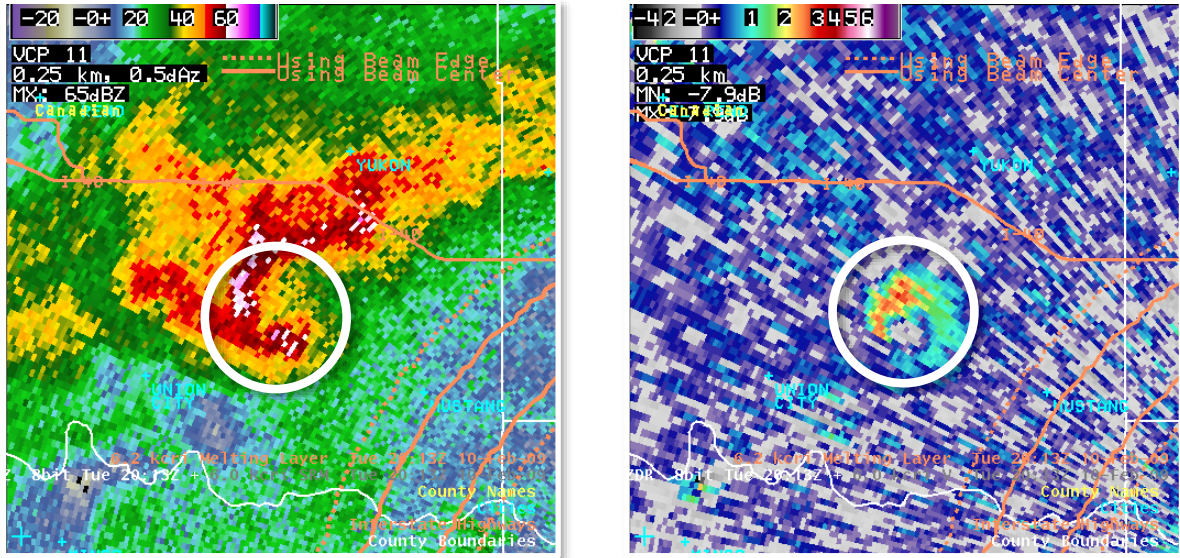


Fig. 6.9: Updraft creating a Z_{DR} column, or, a localized area of enhanced Z_{DR} well above 0°C . Example from 10 February 2009 at 2013 UTC in Central Oklahoma. The melting layer height was roughly 10,500 feet AGL; image is for 15,700 feet AGL. Reflectivity (left) indicates a supercell with an inflow notch and hook echo denoted by the white circle. *The location of the inflow notch should be roughly the location of the updraft.* Z_{DR} (right) indicates a localized area of enhanced Z_{DR} (> 2 dB) in the inflow notch, or inferred updraft region. This is likely where the updraft is located in this storm; hail production is also likely given the presence of liquid several thousand feet above 0° Celsius level. (Credit: St. Jean 2012; WDTD 2019.)

6.4.1.4. Identifying tornadic debris balls . Tornadoes often loft a tremendous amount of material from the Earth's surface, including dust and soil, and parts of trees and structures, such as building construction elements (like lumber or roofing shingles). These objects are usually randomly shaped, and tumble in the rotational circulation around the tornadic vortex. The random orientation of objects in the tornadic debris ball will produce Z_{DR} values lower than the surrounding regions of large raindrops (which should register with high Z_{DR} values). Figure 6.10 shows an example of a tornadic debris ball, using a radial velocity field and a Z_{DR} field (St. Jean 2012; WDTD 2019).

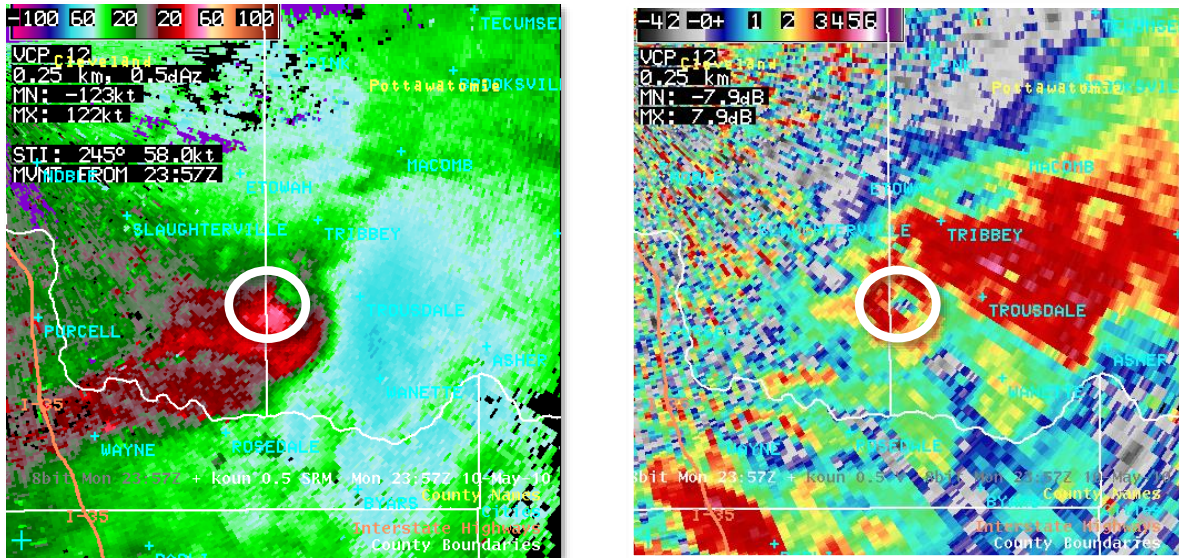


Fig. 6.10: Tornadoic debris. This example shows how Z_{DR} can be used to detect debris being lofted by a tornado. On the left is a Storm-Relative Mean Radial Velocity (SRM)¹² image, indicating the Gate-to-Gate Shear associated with the tornadoic vortex. In Z_{DR} , shown on the right, there is a localized area of depressed Z_{DR} values collocated with the velocity couplet, which is near the tip of the hook echo (not shown). These depressed Z_{DR} values are caused by lofted debris from a tornado causing damage. (Credit: St. Jean 2012; WDTD 2019.)

6.4.1.5. **Identifying biological targets.** Birds produce Z_{DR} values that are slightly lower than those produced by insects. Values for birds can be anywhere from slightly negative (-2 to -3 dB) to substantially positive (+6 or +7 dB), depending on the viewing angle and Mie scattering effects. For insects, Z_{DR} values are typically positive and range from +1 to greater than +7.9 dB, depending on viewing angle, but *not* strongly on Mie scattering, because they are smaller than most birds. Additionally, birds are most prominent at night, while insects are most prominent during the day, even though both may be present quite often. Knowing the local bird/insect population and habits will help in interpretation.

Figure 6.11 shows two examples, one of birds (left) and one of insects (right). The reflectivity images (not shown) appear very similar, but the Z_{DR} images show distinct differences. In the bird image, the Z_{DR} has a corridor of large, positive Z_{DR} from the south to the north/northwest of the radar, following the ambient low-level wind flow. The radar is most likely viewing the birds head-on. The negative values to the west and east of the radar are most likely a result of viewing angle of the birds and Mie scattering. In contrast, the insect image shows very high Z_{DR} in all directions from the

¹² SRM is a Level III derived product.

radar, revealing little information on the orientation of the insects (St. Jean 2012; WDTD 2019).

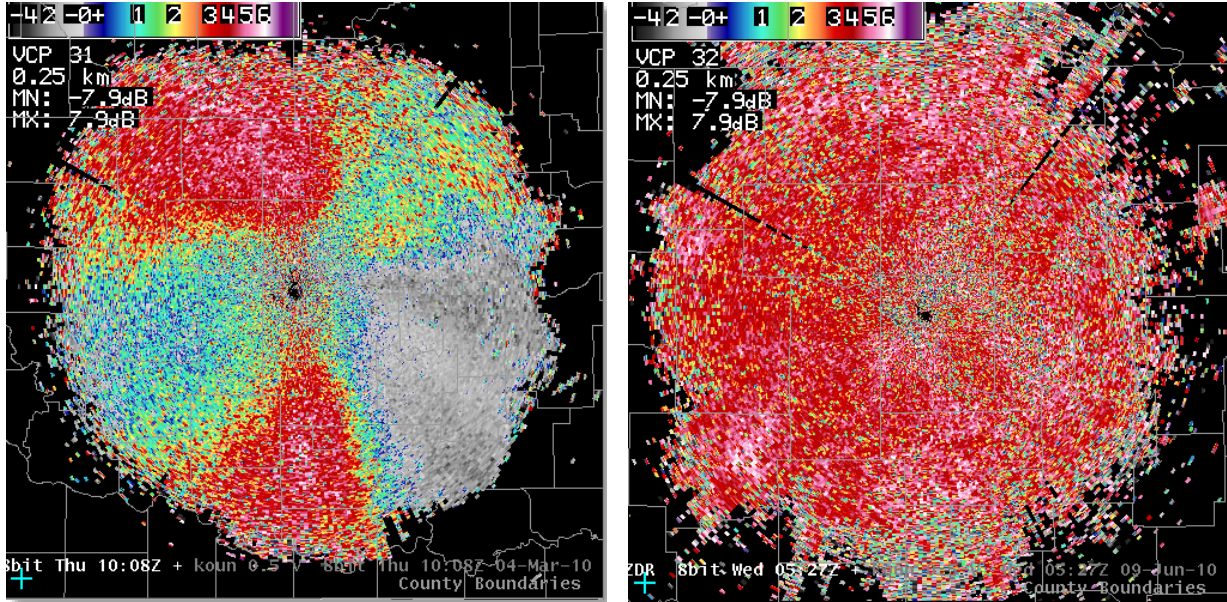


Fig. 6.11: ZDR signatures of birds (left) and insects (right). (Credit: St. Jean 2012; WDTD 2019.)

6.4.2. Differential Propagation Phase (ϕ_{DP}) and Specific Differential Phase (K_{DP}). The propagation speed of EMR slows down as it passes through various media, which is quantified by the Index of Refraction (see Chapter 2). In air, the Index of Refraction (n) is on the order a few one hundredths of one percent, so the propagation speed of the EMR is pretty close to c (the speed of light in a vacuum). However, through water, it slows down by about a quarter. For liquid water, n is about 1.33, and for ice, it is about 1.31. In other words, by (2.2), in liquid water,

$$v_c = \frac{c}{n} = \frac{3 \times 10^8 \frac{m}{s}}{1.33} = 2.26 \times 10^8 \frac{m}{s}$$

The more water the EMR encounters, the greater its cumulative delay (relative to EMR in a vacuum) will be. One way to measure this slowing is by the phase shift (ϕ) measured in the two components of the diagonally-polarized radar beam. The Differential Propagation Phase (ϕ_{DP}) is a measure of the difference in the phase shifts of the two components. It is generated at the RDA. It assesses separately the phase shift

in the horizontal and vertical components of the beam, then takes the difference between the two, using:

$$\phi_{DP} \equiv \phi_{HH} - \phi_{VV} \quad (6.5)$$

which has units of radians or degrees. The subscripts in the terms on the right-hand side of (6.5) indicate (first subscript) the plane of the *transmitted* power, and (second subscript) the *returned* power, so that, for example, ϕ_{HH} is the cumulative phase shift observed in the *backscattered* horizontally-polarized power as compared to the *transmitted* horizontally-polarized power (Rinehart 2004).

To interpret ϕ_{DP} , consider the shapes of the hydrometeors in a given range bin. If the precipitation particles are wider than they are tall, ϕ_{HH} will be greater than ϕ_{VV} , and ϕ_{DP} will be *positive* in that range bin. If the precipitation particles are taller than they are wide, ϕ_{HH} will be less than ϕ_{VV} , and ϕ_{DP} will be *negative* in that range bin. Further, since the amount of phase shifting in each range bin depends of the *total* amount of water, ϕ_{DP} depends on the number density of droplets as well as their median shape. So, higher number densities of short, wide (oblate) droplets will result in greater ϕ_{HH} than lower number densities of the droplets with the same shape (Rinehart 2004)

ϕ_{DP} is cumulative, so that the phase shift in range bins is not only a function of what has occurred in that range bin, but also in all other range bins closer to the RDA. This makes it somewhat difficult to interpret. For this reason, the Specific Differential Phase (K_{DP}) is also available, and shows the amount of differential phase shifting in each range bin. K_{DP} is generated from ϕ_{DP} at the RPG. It is defined by:

$$K_{DP} \equiv \frac{\phi_{DP}(r_2) - \phi_{DP}(r_1)}{2(r_2 - r_1)} \quad (6.6)$$

which has units of deg km^{-1} . It compares the values of ϕ_{DP} on each end of a range bin in the radial direction, where r_2 (the range, or distance, in km) is further from the RDA than r_1 . It is divided by *twice* the difference between r_2 and r_1 , because any EMR returning to the RDA from r_2 (the more distant point) has traversed the range bin twice (once outbound, and once inbound). (See Figure 6.12.)

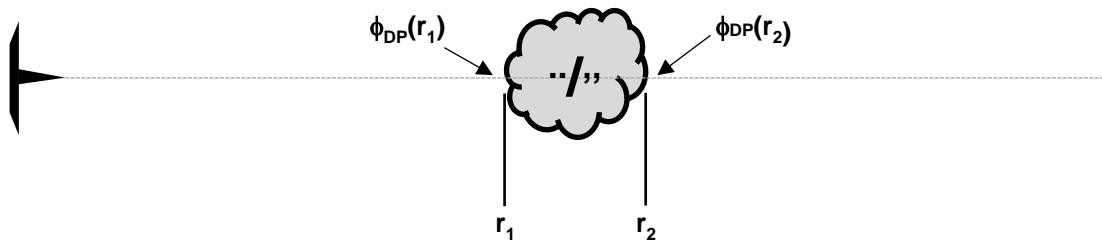


Fig. 6.12: Interpretation of K_{DP} . ϕ_{DP} from r_1 (the point nearer the RDA) represents the phase shift of EMR that has traversed clear air between the RDA and r_1 . ϕ_{DP} from r_2 (the point farther from the RDA) represents the phase shift of EMR that has traversed the rain (or drizzle) particles inside the range bin with the precipitation *twice* (once *outbound* to r_2 , and once *inbound* from r_2).

K_{DP} normally varies between about -2 and 7. Table 6.2 shows general guidelines for interpreting K_{DP} , and Figure 6.13 shows a more detailed scheme of K_{DP} values for different types of targets in a range bin. For example, rain produces values between about 0 deg km⁻¹ (spherical droplets) and 6 deg km⁻¹ (wide, or *oblate* droplets); hailstones and graupel range from about -0.5 to about +1 deg km⁻¹; and ice crystals range from about -1 to about +1 deg km⁻¹, depending on their orientation. Figure 6.14 shows a sample of side-by-side AWIPS images of conventional reflectivity and K_{DP} for the same scene, just to provide an idea of how the two differ in appearance (St. Jean 2012).

Table 6.2: Hypothetical values of ϕ and K_{DP} .

Target Character	Comparison of ϕ_{HH} and ϕ_{VV}	Value of ϕ_{DP} in the range bin	Difference between ϕ_{DP} at r_2 and r_1	Sign of resulting value of K_{DP} in the range bin
Targets randomly distributed or spherical (e.g. small raindrops or tumbling hailstones)	$\phi_{HH} \sim \phi_{VV}$	$\phi_{DP} \sim 0$	$\phi_{DP}(r_2) \sim \phi_{DP}(r_1)$ (Remains the same through range bin)	$K_{DP} \sim 0$
Targets wider than tall (e.g. large raindrops)	$\phi_{HH} > \phi_{VV}$	$\phi_{DP} > 0$	$\phi_{DP}(r_2) > \phi_{DP}(r_1)$ (Increases through range bin)	$K_{DP} > 0$
Targets taller than wide (e.g. conical ice crystals)	$\phi_{HH} < \phi_{VV}$	$\phi_{DP} < 0$	$\phi_{DP}(r_2) < \phi_{DP}(r_1)$ (Decreases through range bin)	$K_{DP} < 0$

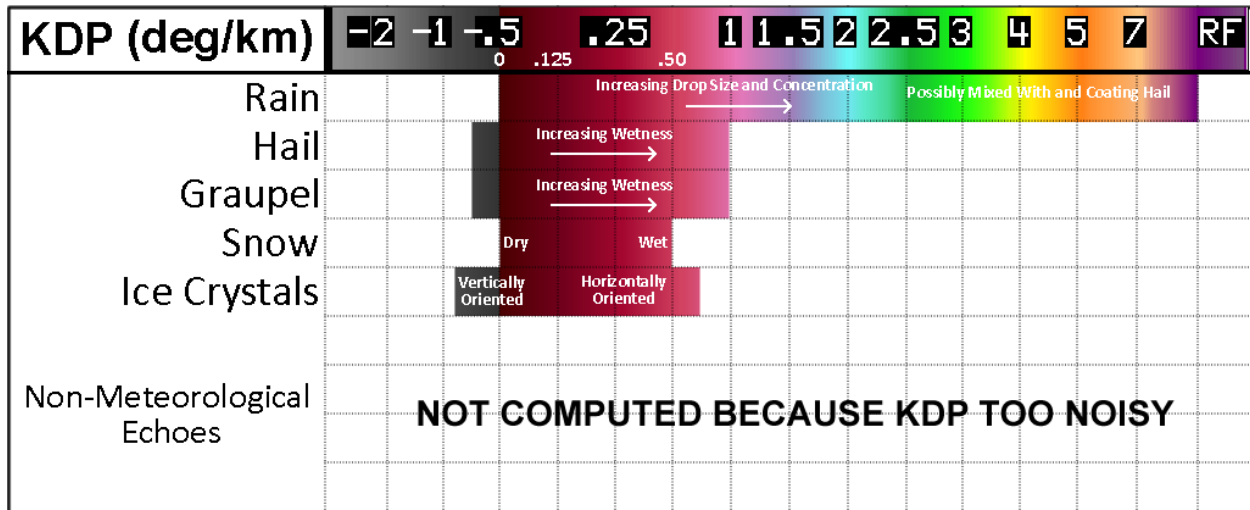


Fig. 6.13: Typical values of K_{DP} for different types of meteorological targets. For non-meteorological targets, K_{DP} is too noisy and is not usually computed. (Credit: St. Jean 2012; WDTD 2019.)

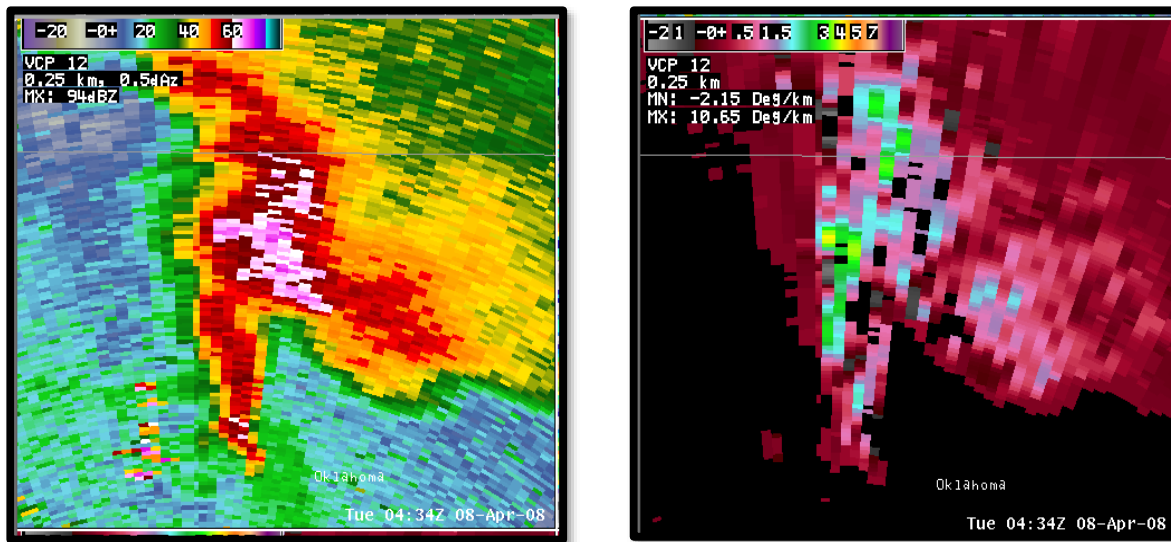


Fig. 6.14: Conventional reflectivity (left) and the corresponding K_{DP} field (right). K_{DP} products are available on all elevation angles. (Credit: St. Jean 2012; WDTD 2019.)

Next, we'll review a few examples of how K_{DP} can be used to differentiate:

- Heavy rain without hail or other hydrometeors
- Heavy rain mixed with hail
- Cold vs. warm rain processes

6.4.2.1. **Heavy rain only.** One of the main advantages of K_{DP} is its ability to identify heavy rain scenarios. Figure 6.15 shows an example of an area (big white polygon) of conventional reflectivity (left) with values greater than 40 dBZ and fairly uniform in intensity. K_{DP} (right) shows higher values to the north (top white oval), and lower values to the south (bottom white oval), despite reflectivity values being almost identical. Heavy rain is falling where the K_{DP} values are higher, but is much lighter where K_{DP} is lower (St. Jean 2012; WDTD 2019).

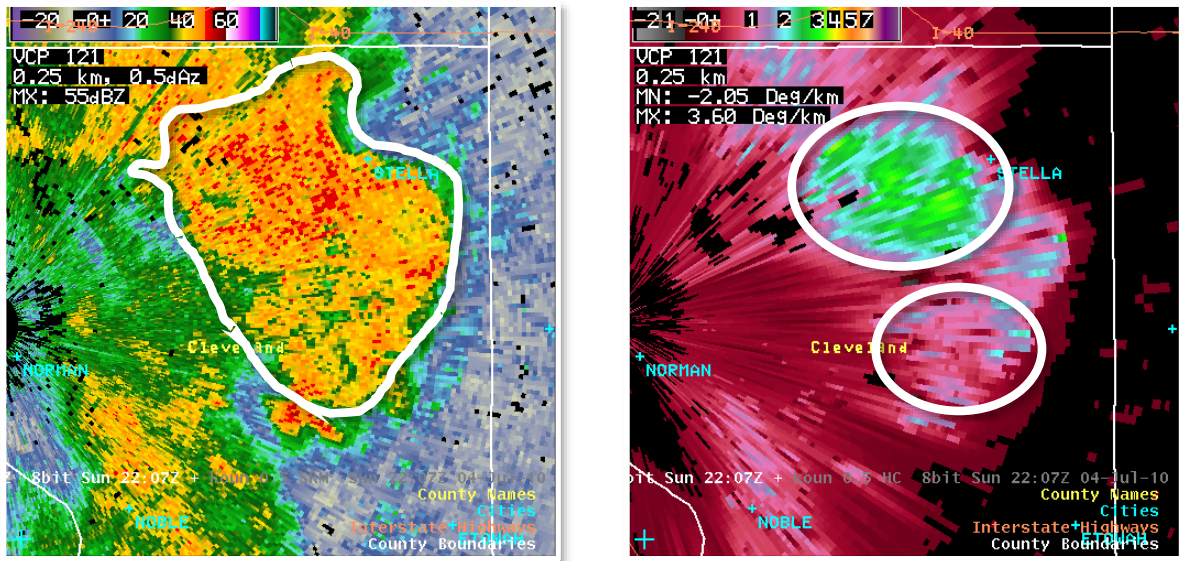


Fig. 6.15: Conventional reflectivity (left) and K_{DP} (right) for heavy rain scenario. (Credit: St. Jean 2012; WDTD 2019.)

6.4.2.2. **Identifying rain, hail, or rain-hail mix.** Another advantage of K_{DP} is the identification of liquid water whether hail is present or not. Figure 6.16 shows an example with a mature supercell that developed over southern Oklahoma, and passed east of I-35. Conventional reflectivity (not shown) indicates a forward flank region with an area of greater than 60 dBZ near the inflow region. It also has a well-defined hook echo.

Let's focus on three areas. The first area is out toward the edge of the forward flank (far right white circle). Reflectivity (not shown) is near 50 dBZ, and Z_{DR} (left panel of Figure 6.16) is around 3 to 4 dB. This indicates large, oblate hydrometeors falling in this region. Looking at K_{DP} (right panel), the values are near 1 to 1.5 deg km^{-1} . There is most likely no hail in this region and the drops that are falling are most likely large and low in concentration.

Moving a bit closer to the core (middle white circle), conventional reflectivities (not shown) are once again near 50 dBZ. However, Z_{DRS} in the region are near 0.5 dB and K_{DP} are near 0 deg km⁻¹. This tells us that there is mostly (spherical, in the mean) hail in this region with little or no liquid water falling to the surface.

The third area is just to the northwest of the second area (and is indicated by far left circle). Conventional reflectivities (not shown) are near 60 dBZ, and Z_{DRS} are back to around 3 to 4 dB. However, now K_{DP} is on the order of 5 deg km⁻¹. This indicates two possible things: (1) There is melting hail (given the 60 dBZ), or (2) there is a substantial amount of liquid water falling along with the possible hail in this region. Either way, there is substantial liquid water in this region as compared with the other two (St. Jean 2012; WDTD 2019).

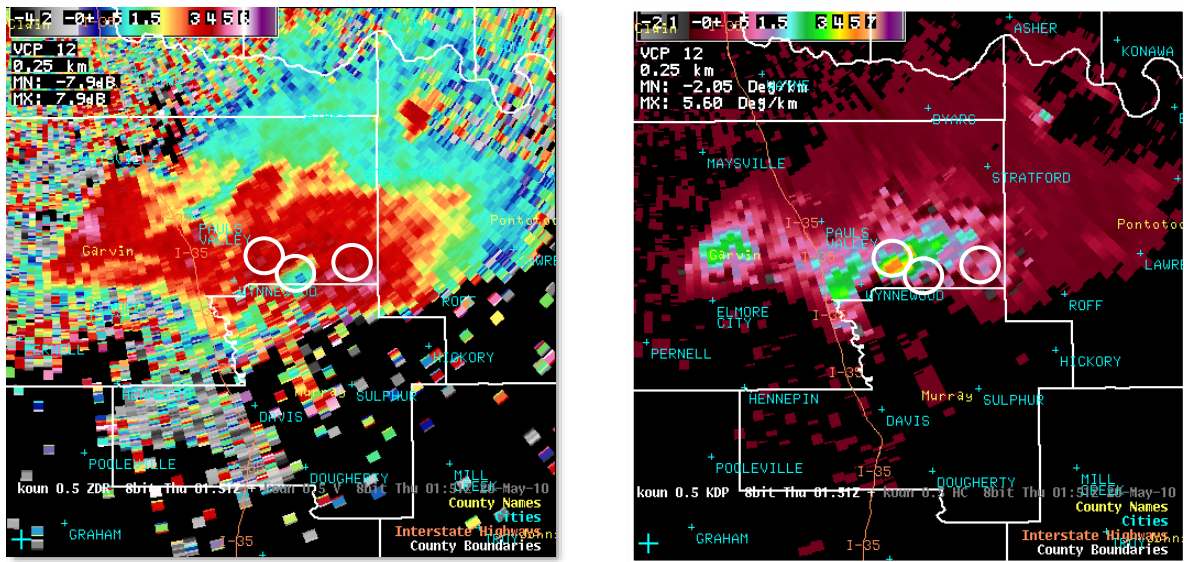


Fig. 6.16: Supercell in scans of Z_{DR} (left) and K_{DP} (right). (Credit: St. Jean 2012; WDTD 2019.)

6.4.2.3. Cold vs. warm rain processes. Let's take a deeper look at the example used in 6.4.2.1 (Figure 6.15). Recall that there was heavy rain occurring to the north and not as much rain occurring to the south (based on the K_{DP} values), despite there being similar conventional reflectivity values. The two areas to examine here are defined by two white ovals in Figure 6.17. In Z_{DR} (left panel), the northern area has Z_{DR} values around 1.5 to 2.5 dB. Down south, the Z_{DR} values are approaching 3 dB. This indicates that the drops to the south are larger in size than the drops to the north. However, K_{DP} (right) values are higher to the north. How does this make sense? How can smaller drops be producing a higher rain rate than larger drops?

The answer is in the concentration of the two types of drops. K_{DP} is dependent not only on the shape of the particle, but on their number density. So, if the raindrops to the north are smaller in size (associated with a lower Z_{DR}) but have higher K_{DP} , it is because the concentration per unit volume of the drops to the north is higher than the drops to the south. The reason for that is the type of process by which the drops formed. The drops to the north most likely formed via a warm rain process (producing smaller drops with a higher number density) whereas the drops to the south formed via a cold rain process (producing larger drops with a lower number density (St. Jean 2012; WDTD 2019)).

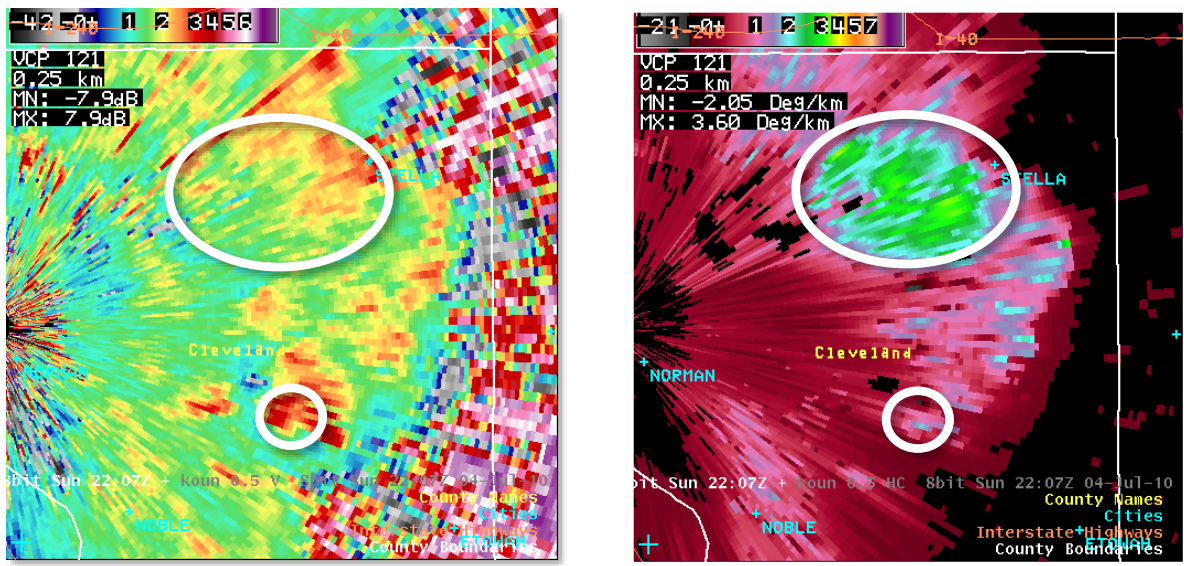


Fig. 6.17: Z_{DR} (left) and K_{DP} (right). (Credit: St. Jean 2012; WDTD 2019.)

6.4.3. **Co-Polar Cross-Correlation Coefficient (ρ_{HV} or CC).** This datatype is initially generated at the RDA, then sent to the RPG for quality control, and conversion into a base product. It is based on signal strength (think returned power), and is defined by:

$$\rho_{HV} \equiv \frac{\langle S_{VV}S_{HH}^* \rangle}{\langle |S_{HH}|^2 \rangle^{1/2} \langle |S_{VV}|^2 \rangle^{1/2}} \quad (6.7)$$

where S_{VV} and S_{HH} are power transmitted in the vertical plane that is backscattered in the vertical plane, and power transmitted in the horizontal plane this is backscattered in

the horizontal plane, respectively. The triangular brackets indicate averaging over all particles contributing to the signal strength, and vertical bars indicate absolute value. ρ_{HV} has no physical units and varies between 0 and 1 (Rinehart 2004).

S_{HH}^* is the complex conjugate of S_{HH} . A little background on complex numbers will help explain this. Figure 6.18 shows the familiar real number line in the horizontal dimension, and the imaginary number line in the vertical dimension. Imaginary numbers are like real numbers, except they are all multiplied by the square-root of -1, that is, i .

All numbers are a combination of real and imaginary parts. The general form is $Z = a + bi$, where a and b are the components of Z along the real and imaginary number lines, respectively. The complex conjugate of Z is Z^* , and is simply defined as $Z^* = a - bi$. In the context of S_{HH} , the “imaginary” part is that component of the returned signal strength that has been phase shifted by 90 degrees, or $\pi/2$ radians. The complex conjugate of S_{HH} is then simply the same horizontally-polarized signal strength, with the rotational angle of the phase shifted portion simply reversed in sign.

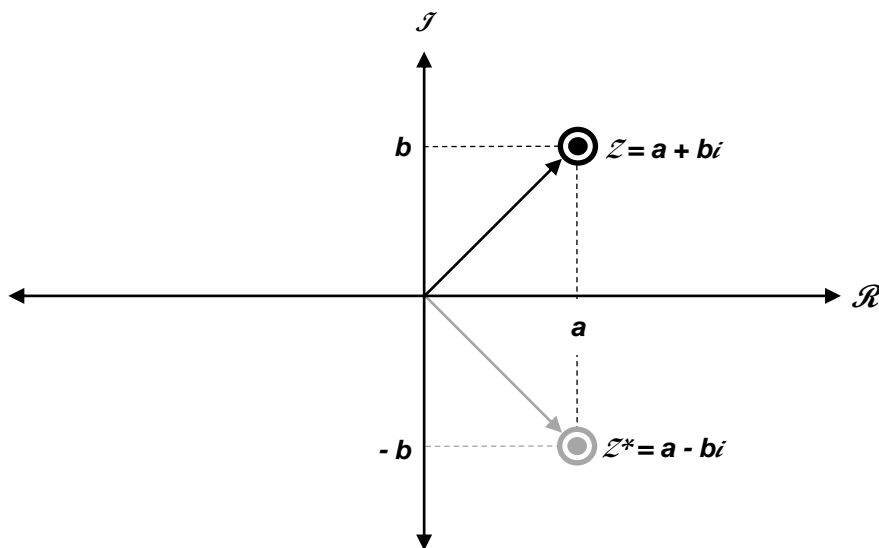


Fig. 6.18: Real and imaginary number lines, and the complex conjugate of a number. All numbers (Z) have a real (a) and an imaginary component (b), The complex conjugate of a number (Z^*) has the same real component, but the sign of the imaginary component is reversed.

Since this is a correlation coefficient, the more similar the particles in the range bin, the closer it is to 1. Non-meteorological targets, particularly those with complex

and highly variable shapes, are associated with correlation coefficients of less than 0.9. Meteorological targets with mixed shapes, or of mixed phase, are associated with correlation coefficients between 0.85 and 0.95. When the types of hydrometeors are generally uniform in a range bin, correlation coefficients of 0.95 or greater often result. Figure 6.19 shows a more detailed list of values that occur with different kinds of particles, and Figure 6.20 shows a side-by-side example of conventional reflectivity and the correlation coefficient (St. Jean 2012; WDTD 2019).

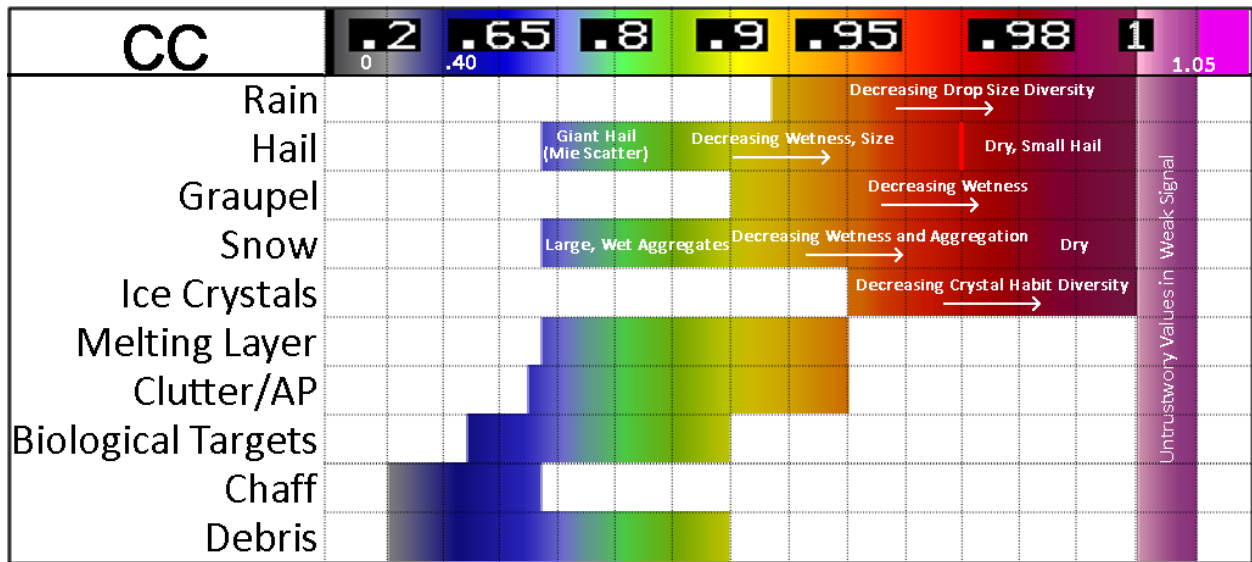


Fig. 6.19: Typical CC (ρ_{HV}) values associated with different types of targets. (Credit: St. Jean 2012; WDTD 2019.)

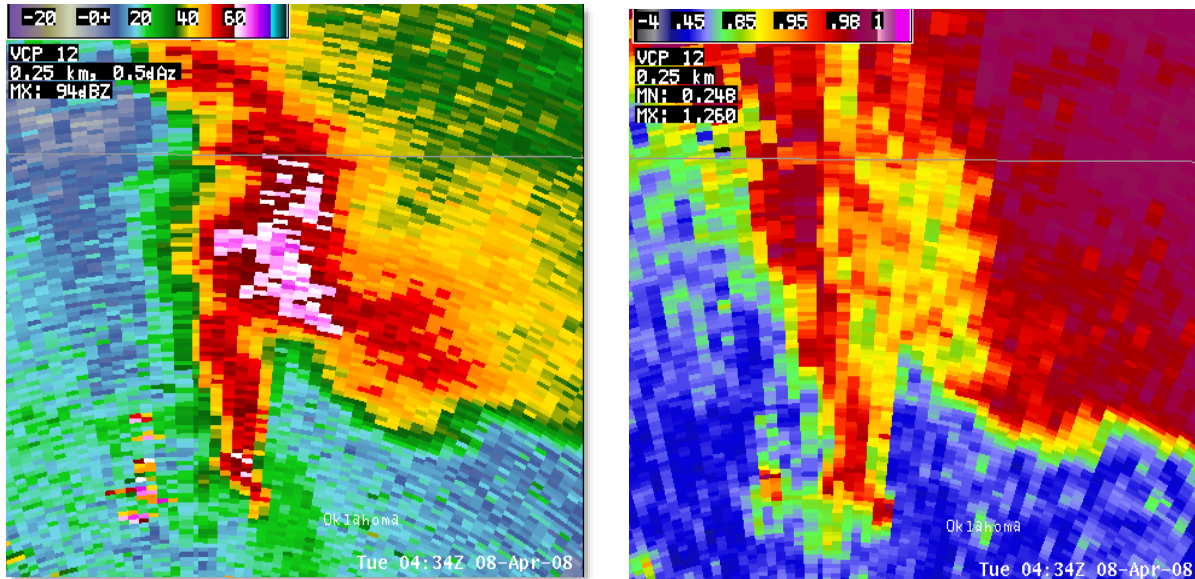


Fig. 6.20: Conventional reflectivity (left) and the corresponding CC field (right). CC products are available on all elevation angles. (Credit: St. Jean 2012; WDTD 2019..)

Next, we'll review a few examples of how the correlation coefficient can be used to differentiate:

- Meteorological vs non-meteorological echoes
- Melting layer
- Rain vs. snow
- Giant hail
- Tornadoic debris

6.4.3.1. Meteorological vs non-meteorological echoes. A major advantage of the correlation coefficient is its ability to discriminate between meteorological and non-meteorological echoes. Figure 6.21 shows an example. In conventional reflectivity (left), a line of storms is visible, oriented SW to NE, just south and east of the RDA. Behind this line (north and west of the RDA) there are more high-reflectivity echoes that aren't part of the line. If we were to loop it, or look at radial velocity, we could tell instantly that it is Anomalous Propagation (AP). The AP extends right into the line of precipitation, and there we can't tell from the reflectivity display that it is AP. Using the correlation coefficient (right panel), the AP shows up instantly as low values of CC whether it is by itself or embedded in precipitation. As shown in the typical values image (Figure 6.19), the majority of meteorological echoes have CC values above 0.9, while non-meteorological echoes are below 0.85. In practice, look for smooth fields of CC greater than 0.9, which show up as yellow and maroon, to identify

areas of precipitation. Areas of noisy CC less than 0.85, which show up as greens and blues, most likely indicate the presence of non-precipitation targets, such as chaff, volcanic ash, smoke, insects, bats, and birds (St. Jean 2012; WDTD 2019).

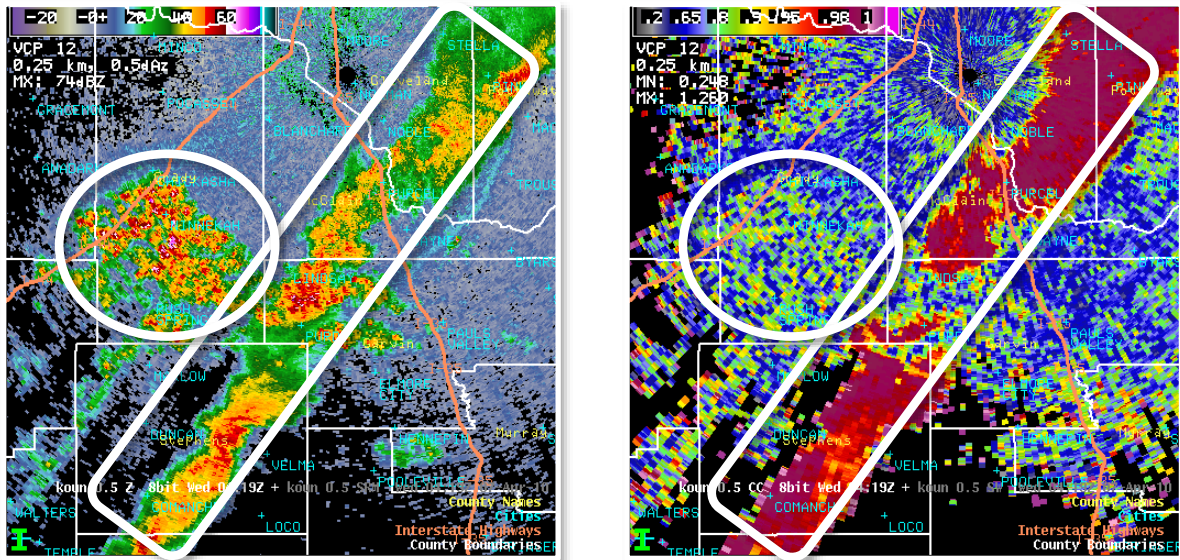


Fig. 6.21: Conventional reflectivity (left) and correlation coefficient (right). A line of showers is indicated with a rectangle; Anomalous Propagation, with an oval. The precipitation targets are highly correlated, while the AP targets are not. (Credit: St. Jean 2012; WDTD 2019.)

6.4.3.2. Melting layer. Another advantage of the correlation coefficient is identification of the melting layer. Figure 6.22 shows an example. In reflectivity (left) the melting layer is sometimes, but not always, identifiable as a bright band. In this case, it is not. With correlation coefficient (right), it almost always is much more easily identified. It is characterized by a ring of low correlation coefficient (~ 0.85) surrounded by higher correlation coefficient (~ 0.98). This signature is due to the presence of mixed-phase hydrometeors which decrease CC below 0.95 (St. Jean 2012; WDTD 2019).

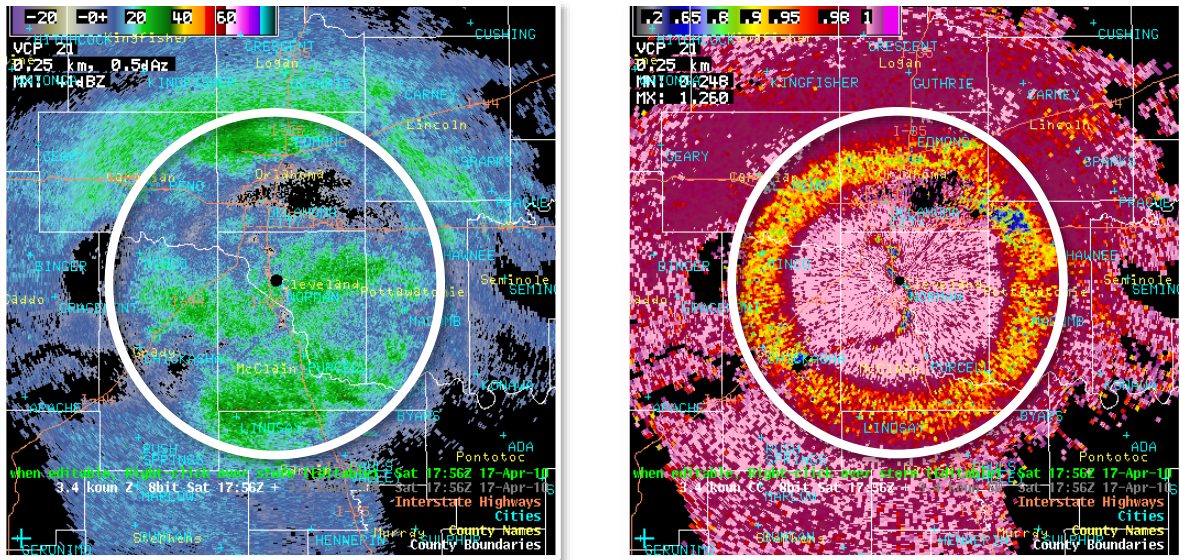


Fig. 6.22: Conventional reflectivity (left) and CC (right). Ovals indicate location of the melting layer, which is clearly visible in the correlation coefficient, but not in the reflectivity image. (Credit: St. Jean 2012; WDTD 2019.)

6.4.3.3. Rain vs. snow. During the seasonal transition period, when precipitation reaching the ground may be either rain or snow, the CC can help a forecaster better locate where the transition from snow to rain is occurring. It is simply the manifestation of the melting layer signature near the ground. Therefore, look for a drop in CC associated with the melting of snow to rain near the surface. It's also helpful to overlay surface observations (if available) when trying to identify this feature and to look at other polarimetric variables (such as Z_{DR} , discussed above) to help in identifying the rain-snow line.

Figure 6.23 shows an example from 20 March 2010 at 1407 UTC. East of the radar there are strong echoes and surface temperatures near freezing (32°F). However, reflectivity (left) doesn't show any clear-cut evidence that there is snow, or rain, or a mixture occurring at the ground. However, if we look at CC (right), it becomes readily apparent where the transition from rain to snow is occurring. This transition area is noted by the white line. East of the white line, CC values are between 0.9 and 0.95, where surface temperatures are just above freezing, and METAR (METeoro logical Aerodrome Reports) data in these areas indicated rain. To the west of the white line, we see CC of 0.99 where surface temperatures are below freezing. METAR data in these regions were reporting snow. Therefore, the white line separating the lower CC from the higher CC is a good indication where the rain/snow line was occurring (St. Jean 2012; WDTD 2019).

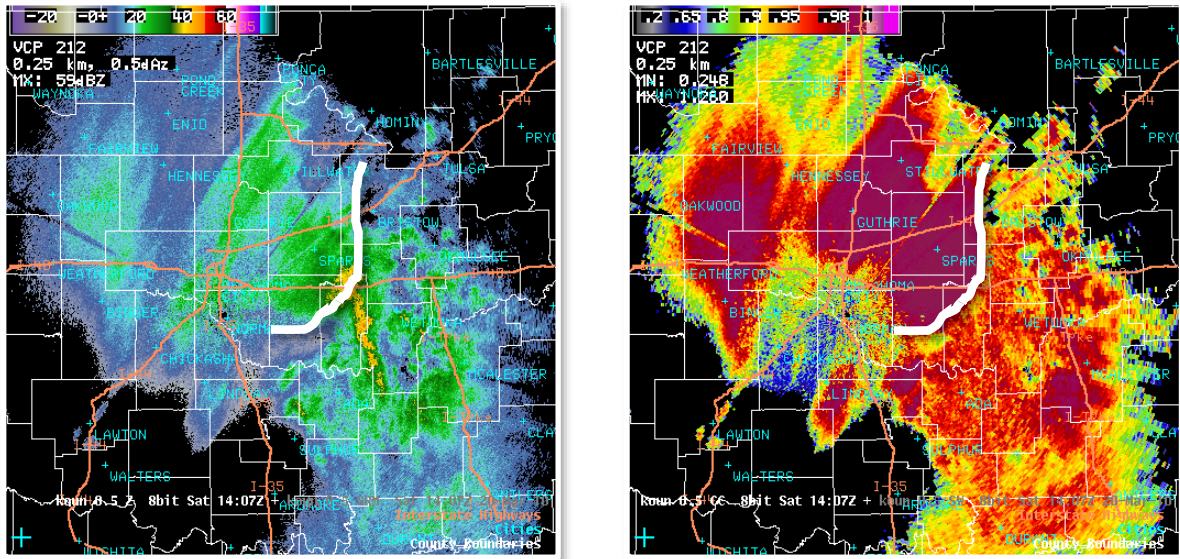


Fig. 6.23: Conventional reflectivity (left) and correlation coefficient (right). White line indicates rain-snow line. (Credit: St. Jean 2012; WDTD 2019.)

6.4.3.4. **Giant hail**, which we define as larger than approximately two inches in diameter, will have noticeably reduced correlation coefficient due to Mie scattering effects. Typical values will start out around 0.93 and decrease to as low as 0.8 as the hail becomes significantly large (> 3.5 inches in diameter). Some cases have had CC as low as 0.7, though this isn't common. Figure 6.24 shows conventional reflectivity (left) and correlation coefficient (right) from a supercell thunderstorm over Oklahoma City. The white circle indicates where 2.5 inch hail was reported at the ground. Note the high reflectivity and low CC (St. Jean 2012; WDTD 2019).

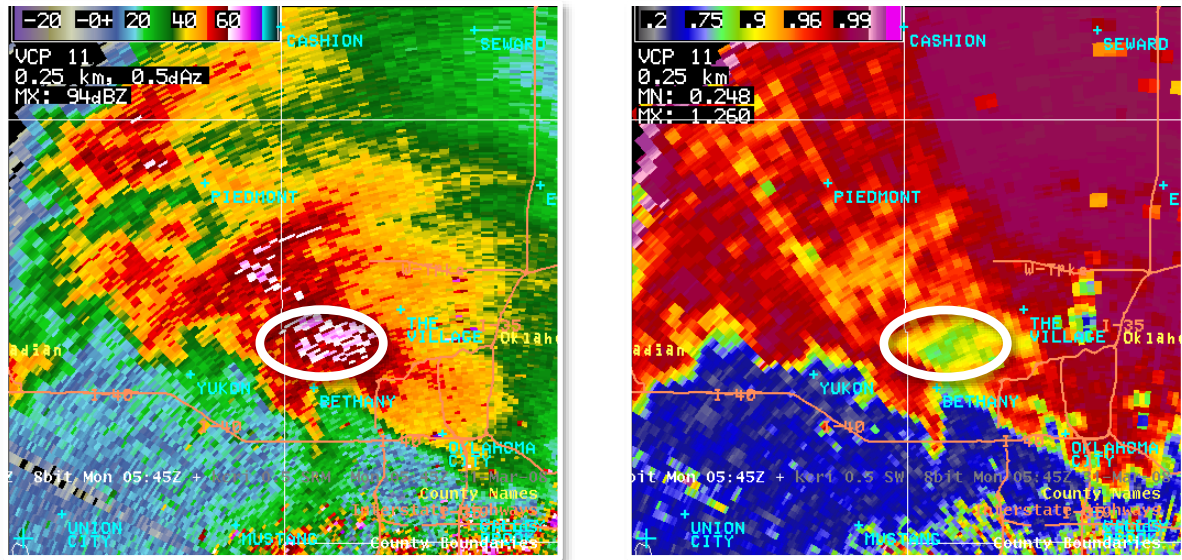


Fig. 6.24: Conventional reflectivity (left) and correlation coefficient (right), with white oval indicating location of giant hail. (Credit: St. Jean 2012; WDTD 2019.)

6.4.3.5. **Tornadic debris.** When a tornado is within 75 km of a WSR-88D RDA, and lofts debris high enough for the radar to be able to sample it, a very distinct debris signature can be generated using dual-pol data. A tornadic debris ball is marked by a significant drop in correlation coefficient due to complex scattering by the debris field. It must be collocated with a velocity couplet in either base radial velocity or Storm-Relative Mean Radial Velocity (SRM).

Figure 6.25 shows an example from 10 May 2010, where there were *four* tornadoes occurring simultaneously. One is located in SE Oklahoma County and two in Eastern Cleveland County. However, the one to note here is located in far Western Pottawatomie County. In the conventional reflectivity image for this storm (not shown), there is no well-defined hook or debris ball. In SRM (left panel of Figure 6.25), there is a noticeable couplet which prompted a tornado warning. No spotter report was available to indicate whether the circulation was on the ground. However, in CC (right panel), there is a localized region of low correlation coefficient collocated with the SRM couplet. This signature indicates that there is a tornado that is already doing damage, and is *not* a precursor to a tornado. This is especially useful for nighttime or rain wrapped tornadoes where spotter reports are very difficult to obtain (St. Jean 2012; WDTD 2019).

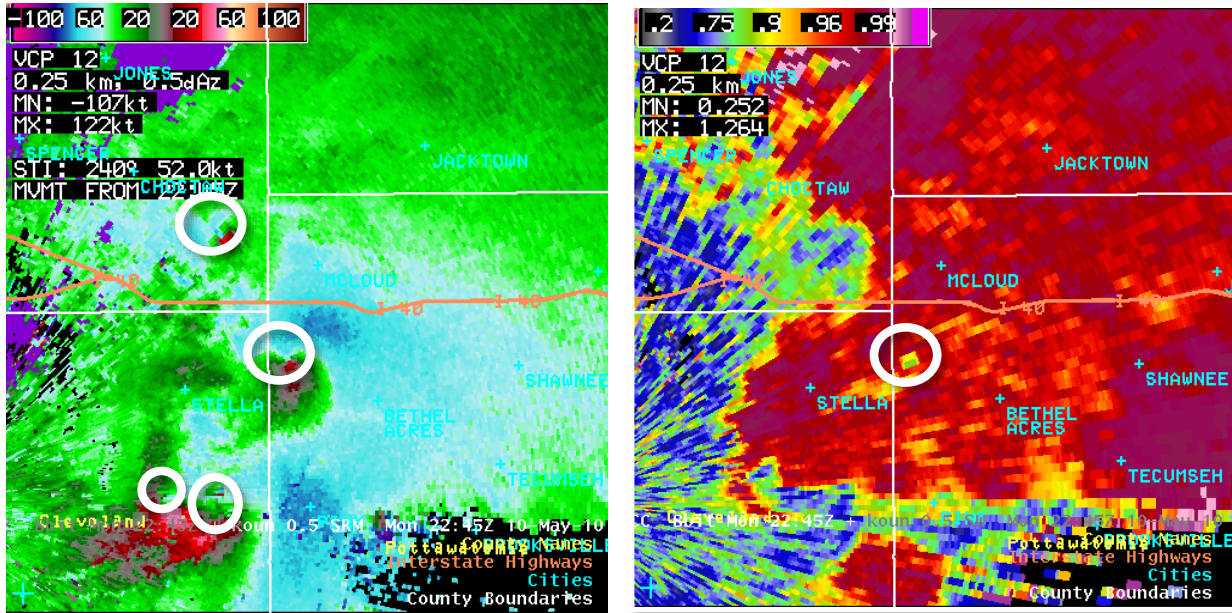


Fig. 6.25: SRM (left) and CC (right). Ovals in SRM indicate locations of four velocity couplets associated with tornadic vortices. Oval in CC indicates debris ball associated with one of them. (Credit: St. Jean 2012; WDTD 2019.)

This concludes the brief lesson in interpreting dual-polarization data. In the next chapter, we discuss several Level III derived products.

Summary. Many modern weather radar systems utilize dual-wavelength or dual-polarization techniques to increase the analytical capability of radar data users. Dual-wavelength systems have been used to develop a Hail Signal. Dual-pol techniques are more frequently utilized because of the lower costs involved, and have been used to develop many different parameters that aid in identifying precipitation type and intensity. Dual-pol techniques can also be used to differentiate hydrometeors from other types of small objects (such as insects) in the atmosphere.

The WSR-88D systems are linearly, diagonally-polarized. The amount of back-scattered EMR in the horizontal and vertical planes is determined using a simple trigonometric relationship. The Probert-Jones Radar Equation is then applied to compute the vertical and horizontal components of reflectivity. The phase shifts and the reflectivities in each plane are a function of the mean shape of the particles in a given range bin, as well as their number density. These basic concepts are combined in several different ways to produce dual-pol products that can be displayed as volume scans or vertical cross-sections.

Differential Reflectivity (Z_{DR}) is a parameter based on the ratio of the horizontal- and vertical-components of reflectivity. When combined with ordinary reflectivity, Z_{DR} can be used to differentiate small raindrops, large raindrops, (tumbling) hailstones, and conical ice crystals. Specific examples of its use discussed in this chapter are identifying (1) hail, (2) melting layers in stratiform, winter-time scenarios, (3) thunderstorm updrafts, (4) tornadic debris balls, and (5) non-meteorological targets (such as birds and insects).

Differential Propagation Phase (ϕ_{DP}) and Specific Differential Phase (K_{DP}) are both based on the difference between the phase shifts of the vertically- and horizontally-polarized EMR. ϕ_{DP} is cumulative along a radial, while K_{DP} is a function of the target character in each individual range bin. K_{DP} can be used to differentiate spherical, vertically-extended, or horizontally-extended particles. Specific examples of its use discussed in this chapter are identifying (1) heavy rain (with or without other hydrometeors), (2) heavy rain mixed with hail, and (3) cold rain vs. warm rain process.

The Co-Polar Cross-Correlation Coefficient (ρ_{HV} or CC) is based on signal strength (returned power) in the two linear planes. High CC values correspond to highly-correlated (homogenous) targets in the range bin, while low CC values correspond to highly-diverse targets in the range bin. CC is often used to differentiate precipitation type, and to differentiate precipitation particles from non-precipitation particles, such as biologicals (birds and insects), chaff, and debris. Specific examples of its use discussed in this chapter are identifying (1) meteorological vs. non-meteorological targets, (2) melting layer (winter-time stratiform scenarios), (3) rain vs. snow, (4) giant hail, and (5) tornadic debris.

Terms and concepts:

- Biological targets
- Cant Angle
- Cold rain process
- Complex conjugate
- Conical ice crystal
- Co-Polar Cross-Correlation Coefficient (ρ_{HV} or CC)
- CP2 (radar)
- Differential Propagation Phase (ϕ_{DP})
- Differential Reflectivity (Z_{DR})
- Dual-polarization radar
- Dual-wavelength radar

- Giant hail
- Graupel
- Hail Signal (H)
- Horizontal reflectivity (Z_H)
- Imaginary number line
- Melting layer
- METAR (METeorological Aerodrome Reports)
- MRL-5M (radar)
- NOAA Radar Operations Center (ROC)
- Number density
- Real number line
- Signal strength
- Specific Differential Phase (K_{DP})
- Tornadic debris ball
- Vertical reflectivity (Z_V)
- Warm rain process

Study prompts:

1. Describe the theoretical basis for the dual-wavelength Hail Signal. How does this parameter behave when hail is indicated in the data.
2. What is the physical reason that dual-polarization radar is useful when measuring hydrometeors?
3. How does the Cant Angle affect estimation of droplet size?
4. What is the mathematical formulation of Differential Reflectivity? Create a table and describe how Z_{DR} behaves in the presence of small raindrops, large raindrops, ice crystals, and giant hail.
5. Discuss identification of hail, the melting layer, thunderstorm updrafts, tornadic debris balls, and biological targets (birds and insects) using Z_{DR} .
6. What are the mathematical formulations of Differential Propagation Phase and Specific Differential Phase? How are these two related to each other? Create a

table and describe how K_{DP} behaves in the presence of randomly-shaped or spherical hydrometeors, wide hydrometeors, and tall hydrometeors.

7. Discuss identification of heavy rain without hail or other hydrometeors, heavy rain mixed with hail, and cold vs. warm rain processes using K_{DP} , possibly combined with other radar datatypes.
8. What is the mathematical formulation of Co-Polar Cross-Correlation Coefficient? How does it behave as the hydrometeors (and other targets) in a range bin become more dissimilar? What are typical values for scans of the melting layer, Ground Clutter (and Anomalous Propagation), biological targets, chaff, and debris?
9. Discuss identification of the melting layer, giant hail, and tornadic debris using CC, possibly combined with other radar datatypes.
10. Discuss differentiating meteorological from non-meteorological targets, and rain from snow using CC, possibly combined with other radar datatypes.

7. Level III derived products.

With contributions from Alex Jacques.

In this chapter we will describe a broad array of Level III products, including those computed for each storm cell, such as Vertically-Integrated Liquid and Maximum Expected Hail Size. Some derived products are based on unpolarized reflectivity, some on radial velocity, and some on both.

We will conclude with the Mesocyclone Detection Algorithm and the Tornado Detection Algorithm.

7.1. Level III products fall into four major categories:

- Storm-cell products
- Other reflectivity-based products
- Velocity-based products and products utilizing both Z and V_r .
- Precipitation products

This chapter will discuss some of the products in the first three categories. The next chapter will go into precipitation products.

7.2. **Storm-cell products.** There are two major components in this category: The Storm-Cell Information and Tracking (SCIT) system, and the Hail Detection Algorithm (HDA).

7.2.1. The **Storm-Cell Information and Tracking** system identifies, tracks and forecasts the future positions of up to one hundred individual convective cells. It also computes several parameters for each cell, such as its base and height, and tracks the trends in these parameters. It does all this fully automatically. Arguably, this is one of the most important and valuable functions of the WSR-88D system. Data developed by the SCIT are used extensively as input for other derived products, such as the Hail Detection System (HDS), Storm-Relative Mean Radial Velocity (SRM), and the Tornadic Detection Algorithm (TDA), as well as applications such as the System for Convective Analysis and Nowcasting (SCAN). It also generates a table of attributes and a graphical

depiction of past and future (predicted) positions of each storm cell it is actively tracking.

The SCIT system consists of four major components:

- Storm-Cell Segment Subfunction
- Storm-Cell Centroid Subfunction
- Storm-Cell Tracking Subfunction
- Storm Position Forecasting Subfunction

7.2.1.1 Storm-Cell Segment Subfunction (SCSS). A segment is defined as a run of contiguous range bins along a radial with reflectivity values greater than or equal to a specified threshold. (Recall that reflectivity range bins are 1 km long in the radial direction, and consist of four of the smaller 250-meter range bins in the Level I data.) The SCSS searches for segments along each radial, for up to seven different reflectivity thresholds, that meet several different conditions. These are:

- Minimum reflectivity thresholds: 30, 35, 40, 45, 50, 55, and 60 dBZ.
- Minimum segment length: There must be at least two contiguous range bins meeting or exceeding the reflectivity threshold. (Two range bins is 2 km in the radial direction, consisting of eight of the original 250-meter range bins in the Level I data.)
- Maximum dropout number: Within a segment corresponding to a given reflectivity threshold, there may be up to two range bins that are *below* the reflectivity threshold value, provided they are not more than the dropout reflectivity difference below the threshold value.
- Dropout reflectivity difference: 5 dBZ.
- Overall limit of segments along a given radial: To limit processor time, each radial is limited to a maximum of 15 segments for each reflectivity threshold, making a total of 105 segments per radial. With 360 radials, that's 37,800 possible segments per tilt angle. And for a VCP with 14 tilt angles, that's 529,200 possible segments per volume scan.

Figures 7.1 – 7.3 show examples of segment identification along a single radial. Once all segments in the volume reflectivity scan are identified, the SCSS hands the results off to the next section.

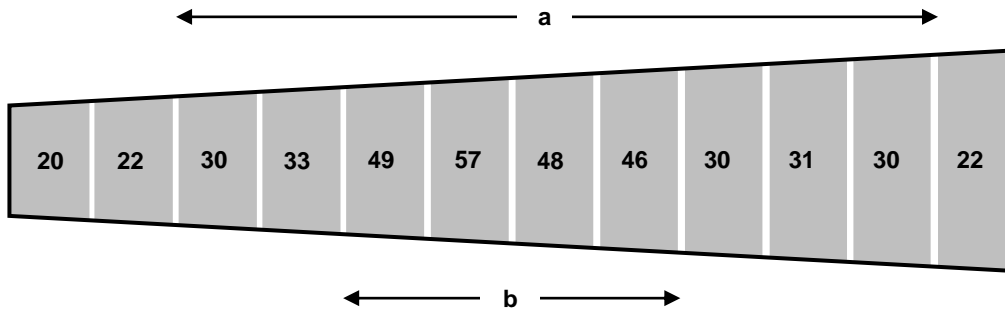


Fig. 7.1: Storm-cell segments example. In this example, segment **a** includes range bins that meet or exceed the 30 dBZ threshold. Segment **b** includes range bins for the 35, 40, and 45 dBZ thresholds. There are therefore a total of *four* segments in this example.

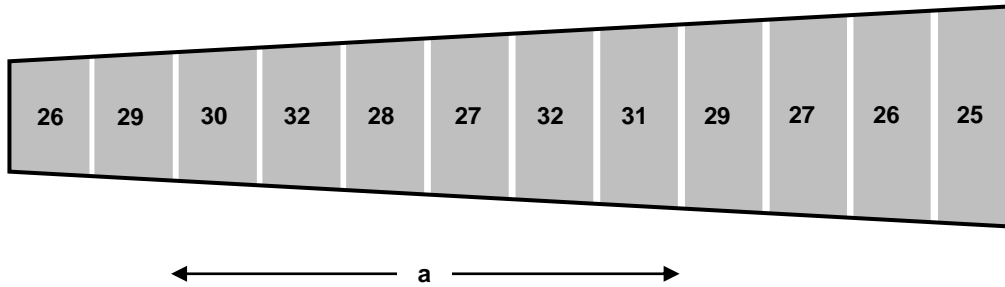


Fig. 7.2: Storm-cell segments example. In this example, segment **a** includes range bins that meet or exceed the 30 dBZ threshold. Two bins in the segment have reflectivities 28 and 27 dBZ, but are included in the 30 dBZ segment, because (1) they are interior to the contiguous segment; (2) there are only two adjacent bins with reflectivities below 30 dBZ (within the maximum dropout number); and (3) both of these bins have reflectivities that are within the 5 dBZ (the dropout reflectivity difference) of the 30 dBZ threshold. There is a total of *one* segment in this example.

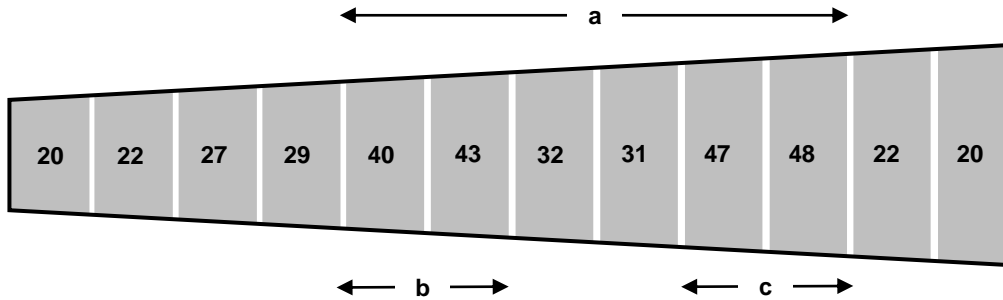


Fig. 7.3: Storm-cell segments example. In this example, segment **a** includes range bins that meet or exceed the 30 and 35 dBZ thresholds. Two bins in the segment have reflectivities 32 and 31 dBZ. These are still included in the 35 dBZ segment, because (1) they are interior to the contiguous segment; (2) there are only two adjacent bins with reflectivities below 35 dBZ (within the maximum dropout number); and (3) both of these bins have reflectivities that are within 5 dBZ (the dropout reflectivity difference) of the 35 dBZ threshold. Segment **b** includes range bins meeting or exceeding the 40 dBZ threshold, and segment **c** includes range bins meeting or exceeding the 40 and 45 dBZ thresholds. The two bins between **b** and **c**, with reflectivities of 32 and 31, break the 40 dBZ segment into two parts, because both are more than 5 dBZ less than 40 dBZ. There are a total of *five* segments in this example.

7.2.1.2. **Storm-Cell Centroid Subfunction (SCCS).** This part of the SCIT ingests the output of the SCSS, takes two additional steps to identify complete storm cells and computes several parameters for each cell.

Some basic vocabulary is needed before we continue:

- **Component:** A *two-dimensional* area of segments, on adjacent radials, within the same elevation scan.
- **Centroid:** The *three-dimensional* location of a cell's center of mass, represented by the center of highest reflectivity.

At each elevation angle, the SCCS groups adjacent one-dimensional segments into two-dimensional components. If components corresponding to different reflectivity thresholds overlap, the component with the higher reflectivity is saved, and the other is dropped. Two-dimensional components of high reflectivity are then vertically correlated into three-dimensional cells. It takes at least two vertically-correlated components to create a cell. *Up to 100 cells can be identified.*

Once a cell is identified, the SCCS computes the following parameters:

- The cell's centroid of highest reflectivity, in polar-cylindrical coordinates (radial, range, and elevation ARL).
- Maximum reflectivity averaged over three range bins.
- Height of averaged maximum reflectivity.
- Cell base and top, defined as the vertical threshold of 30 dBZ.
- Number of two-dimensional components in the cell.
- Cell-based Vertically-Integrated Liquid (VIL).

Originally developed by researchers Greene and Clark in 1972, VIL is a rough estimate of the total amount of liquid water suspended in the atmosphere by the cell, per unit area of the Earth's surface (Burgess and Lemon 1990). Cell-based VIL is computed by using the maximum reflectivity from each of the cell's individual 2-D components so usually does not have a perfectly vertical central axis (Figure 7.4). It assumes that all back-scattered EMR is from liquid water. Reflectivities below 18 dBZ are removed, and any reflectivities of more than 56 dBZ are reduced to 50 dBZ. (The latter is an attempt to remove any reflectivity data that may have resulted from a hail core, which is usually highly reflective.) Mathematically, it is defined by the relationship:

$$VIL \equiv k_1 \sum_{n=1}^N (Z_n)^{k_2} \Delta H \quad (7.1)$$

where VIL has units of kg m⁻². Z_n is the maximum linear reflectivity [mm⁶ m⁻³] in component n , k_1 is a constant equal to 3.44×10^{-6} and k_2 is another constant equal to $4/7$. N is the total number of 2-D components in the cell, and ΔH is the difference in the height between two adjacent components. Cell-based VIL is only one of three types in common use. The other two are discussed in greater detail below.

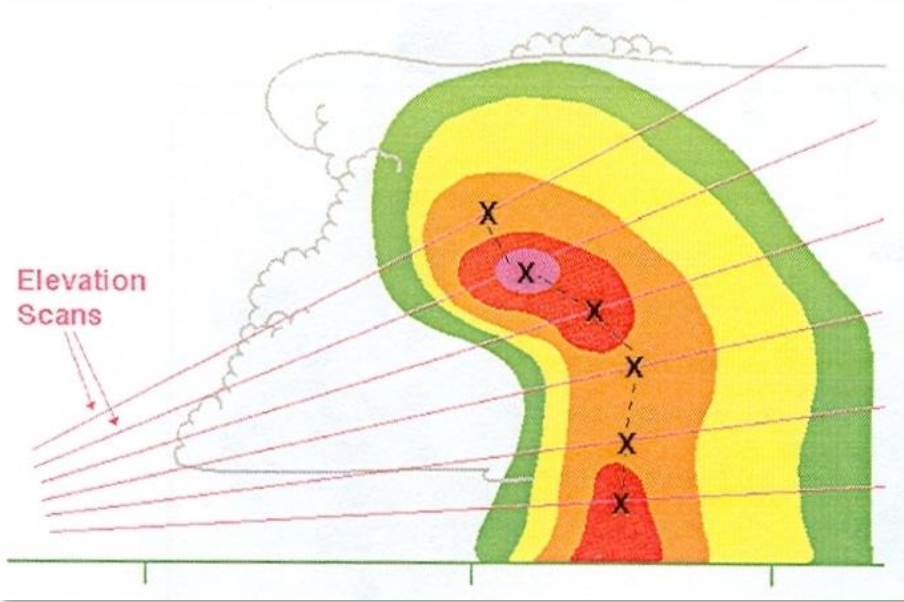


Fig. 7.4: Cell-based VIL, computed through the vertical core of a cell, following the maximum reflectivity center on each of the cell's 2-D components. The vertical core is often not perpendicular to Earth's surface. (Credit: WDTB 2005.)

Once cell-based VIL has been computed by the SCCS, the top 100 cells are ranked by VIL, and can be displayed in AWIPS using several different applications, such as the System for Convection Analysis and Nowcasting (SCAN). SCIT output of these attributes can also be overlain as a table on a display of a volume scan in AWIPS.

7.2.1.3. Storm-Cell Tracking Subfunction (SCTS). This part of the SCIT system monitors the movement of storm cells by matching the positions of cells found in the *current* volume scan with the projected positions of cells identified in *previous* volume scans. Beginning with the cell in the current volume scan with the highest VIL, the SCTS compares its centroid location with the projected centroid positions of cells from the previous volume scan (Figure 7.5).

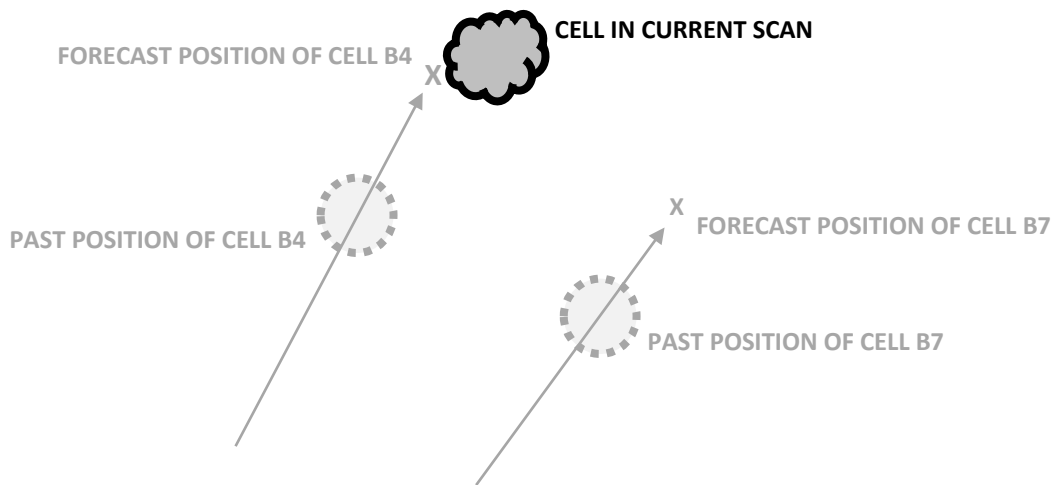


Fig. 7.5: Matching cell identified in current volume scan with forecast positions of cells from previous volume scans. Arrows indicate forecast tracks of previously identified cells. X's identify their forecast positions for the current volume scan.

If it finds a “match” (a current centroid coinciding with a projected centroid, within a defined threshold), the two are considered to be the same cell, and the cell inherits the name of the matching cell from the previous volume scan. If no match is made, the cell is given a new name. Cell names consist of a letter-number combination, in the following format, and are assigned sequentially:

A0, A1, A2, A3 ... A9
 B0, B1, B2, B3 ... B9
 C0, C1, C2, C3 ... C9
 .
 .
 .
 Z0, Z1, Z2, Z3 ... Z9

The list resets to A0 when the RPG is rebooted (rare), or when a sufficient amount of time has passed without any cells in the volume scan area.

7.2.1.4. Storm Position Forecast Subfunction (SPFS). This part of the SCIT system uses the current and past positions of a cell centroid to predict its future positions. If a cell is new, the forecast position are based either the average movement

of all other cells in the volume scan, or, if there are no other cells present, a default speed and direction set using the RPG Human Control Interface.

For known cells, future positions are predicted using a least-squares fit to its past and present positions (Figure 7.6). Future positions are computed for 15-minute intervals. The better the least-squares fit to the previous and current positions, the more future positions are predicted, out to 60 minutes (four forecast positions) in the future. A graphical representation of the past and future positions, similar to that shown in Figure 7.6, can be overlain on a display of a volume scan in AWIPS.

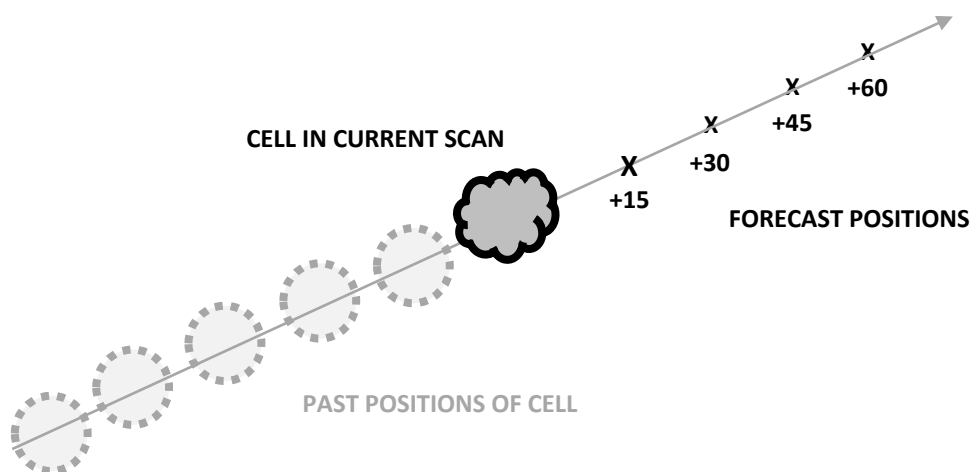


Fig. 7.6: Least-squares fit to past (gray circles) and current cell positions (black cloud), and forecast positions (X's), in 15-min intervals.

7.2.1.5. Summing up the SCIT. The storm-cell system automatically tracks and computes short-term forecasts for storm cells, carrying out the task that was one of the primary motivations for building the WSR-88D system in the first place. It is one of the most important jobs performed by the radar system. It functions best with well-defined, widely-separated cells. The output it generates is fed into to the Hail Detection Algorithm (discussed next), as well as other Level III products, such as Storm-Relative Mean Radial Velocity (SRM). Its graphical and tabular products are useful overlays on volume scans. That said, it struggles with a number of limitations.

Large errors in cell attributes may occur when the cell is so close to the RDA (within about 30 nautical miles) that its upper portion falls within the Cone of Silence. For example, it may miss the highest reflectivity values in the cell, which could be

above the beam associated with the highest tilt angle. This would also degrade the cell's computed VIL value. The SCIT also delivers unreliable information about storm cell movement in scenarios when cells are in close proximity to one another, such as in a Mesoscale Convective System (MCS), or when there are multiple, rapidly-evolving reflectivity centers within a single cell, which is often the case with supercell thunderstorms. Finally, real storm cells often move in curved paths (see "right movers" and "left movers"), yet the SCIT uses a least-squares *linear* fit to compute future storm positions.

7.2.2. The **Hail Detection Algorithm (HDA)** computes three parameters for each cell in the volume scan area: The Probability of Hail, Probably of Severe Hail, and the Maximum Expected Hail Size. "Severe" hail is defined by the U.S. National Weather Service as any hailstone with a diameter of one inch or more. The HDA requires accurate, recent measurements of the heights of the 0 °C and -20 °C isotherms to carry out its calculations (which are described in detail below).

7.2.2.1. **Computing the Probability of Hail (POH).** In the first step, the HDA estimates the probability that a given cell is producing hail of *any* size, using a function cited by Witt *et al.* (1998), and derived from Waldvogel *et al.* (1979). Figure 7.7 reproduces the figure given in Witt *et al.* (1998). The method is based on observations of reflectivity in hail-producing thunderstorms over the U.S. Great Plains. Probabilities are in increments of 10 percent, and use the elevation difference between the height of the 45 dBZ reflectivity [km ARL] (H_{45}) and the height of the freezing level (H_0).

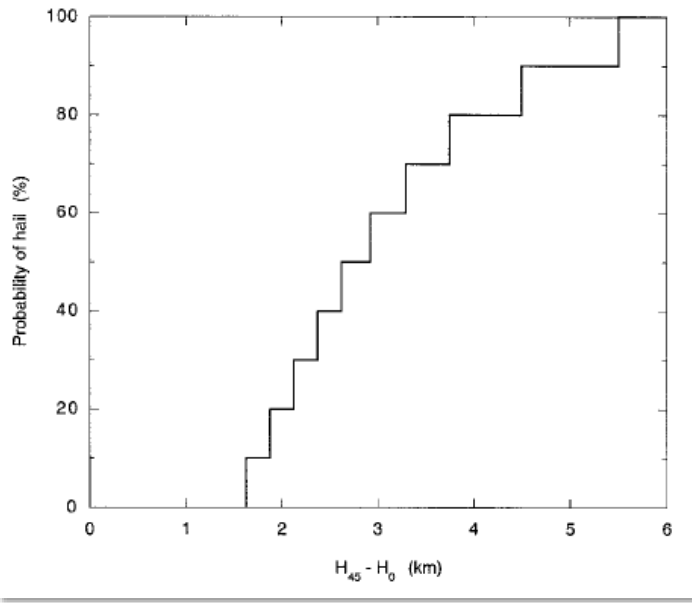


Fig. 7.7. Probability of hail at the ground as a function of $H_{45} - H_0$. (Credit: Witt *et al.* 1998.)

7.2.2.2. Computing Maximum Expected Hail Size (MEHS). In the next step, the HDA starts by computing the Severe Hail Index (SHI), which uses a process similar to that used for computing VIL. Instead of estimating the liquid water content of a cell, an equation is used to estimate Hail Kinetic Energy (\dot{E}):

$$\dot{E} \equiv c_1 10^{0.084Z} W(Z) \quad (7.2)$$

where c_1 is a constant equal to 5×10^{-6} , Z is the maximum reflectivity in the cell [dBZ], and $W(Z)$ is a reflectivity weighting function (Witt *et al.* 1998). The weighting function is defined by:

$$W(Z) = \begin{cases} 0 & \text{if } Z \leq Z_L \\ \left(\frac{Z - Z_L}{Z_U - Z_L}\right) & \text{if } Z_L < Z < Z_U \\ 1 & \text{if } Z \geq Z_U \end{cases} \quad (7.3)$$

where Z_L and Z_U are 40 and 50 dBZ, respectively. These choices are made because most observed reflectivities below 40 dBZ are not associated with hail, while those above 50

dBZ often contain hail (Witt *et al.* 1998)¹³. These values are among the HDA's adaptable parameters, and can be adjusted as necessary for local conditions.

Given these two relations, Witt *et al.* (1998) defined the SHI by:

$$SHI \equiv 0.1 \int_{H_0}^{H_T} W_T(H) \dot{E} dH \quad (7.4)$$

where H_0 is the height of the freezing layer [m ARL], H_T is the height of the top of the storm cell [m ARL], $W_T(H)$ is the weighting function for hail growth based on temperature, and \dot{E} is the Hail Kinetic Energy computed by (7.2). SHI has units of $J m^{-1} s^{-1}$, and typically varies between 0 and $2000 J m^{-1} s^{-1}$ (Witt *et al.* 1998). The weighting function $W_T(H)$ is required because hail growth becomes enhanced at temperatures below $-20^\circ C$, and is defined by:

$$W_T(H) = \begin{cases} 0 & \text{if } H \leq H_0 \\ \left(\frac{H - H_0}{H_{m20} - 0} \right) & \text{if } H_0 < H < H_{m20} \\ 1 & \text{if } H \geq H_{m20} \end{cases} \quad (7.5)$$

where H_0 is the height of the freezing level [m ARL], H_{m20} is the height of the $-20^\circ C$ isotherm [m ARL], and H is the height [m ARL] at which the weighting function is being computed (Rasmussen and Heymsfield 1987).

Using the SHI, Witt *et al.* (1998) define a function for MEHS, given by:

$$MEHS \equiv c_2 (SHI)^{0.5} \quad (7.6)$$

where c_2 is a constant equal to 2.54. Computed values of MEHS are in millimeters, and are usually converted to inches, in increments of $\frac{1}{4}$ inch.

7.2.2.3. Computing the Probability of Severe Hail (POSH). In this step, the HDA computes the Warning Threshold (WT), developed by Witt *et al.* (1998) using data from the Norman, Oklahoma County Warning Area, and are, therefore, representative of Great Plains thunderstorms. Lenning *et al.* (1998) concluded that modifying the WT function can improve results for other geographic regions. The WT function is defined by:

¹³ A study conducted by Dye and Martner (1978) concluded that reflectivities as high as 65 dBZ may not be associated with hail.

$$WT \equiv c_3 H_0 + c_4 \quad (7.7)$$

where c_3 is a constant equal to 57.5, c_4 is another constant equal to -121, and H_0 is the height of the freezing level [km ARL].

With both the SHI and WT computed, the final step is to compute the POSH, using:

$$POSH \equiv c_5 \ln\left(\frac{SHI}{WT}\right) + c_6 \quad (7.8)$$

where c_5 is a constant equal to 29, and c_6 is equal to 50 (Witt *et al.* 1998). POSH has units of percent, and is rounded to the nearest 10 percent before being reported by the HDS.

7.2.2.4. Summing up the HDA. The hail system has a very high Probability of Detection (POD) for severe hail¹⁴. A computed POSH of 50 percent or higher has very good skill as a warning threshold. The HDA is handicapped by its need for accurate information about the heights of the 0 °C and -20 °C isotherms, and POSH and MEHS tend to overestimate the chances and size of hail in weak wind environments, as well as in tropical and mountainous areas. (This is because it was built around data taken in the U.S. Great Plains region.) Its maximum range is 124 nautical miles (230 km) – considerably shorter than the Maximum Unambiguous Range associated with the 322 pulse-per-second PRF. And, all three of its output parameters – POH, MEHS, and POSH – fluctuate at both very close ranges and very long ranges, due to the limited number of tilts intersecting the cell.

7.3. Other reflectivity-based Level III products. There are several pieces in this category, consisting of:

- Gridded and Digital VIL
- Reflectivity Cross-Sections
- Composite Reflectivity
- User-Selectable Layer Reflectivity Maximum
- Enhanced Echo Tops

¹⁴ POD, FAR, and CSI are discussed in Appendix 2.

7.3.1. Gridded and Digital VIL (GVIL and DVIL). Vertically-Integrated Liquid (VIL) was defined in the previous section as an approximation of the amount of liquid water suspended in the atmosphere by a storm cell, per unit area of the Earth's surface. (Put another way, it assumes that all reflectivity is from liquid water droplets.) It is computed from unpolarized linear reflectivity using the relationship shown in (7.1).

Conventional VIL comes in two forms: (1) cell-based, which is automatically computed by the SCIT system, and (2) Gridded, which is computed as a separate product. In both types, reflectivities of less than 18 dBZ are truncated, and reflectivities of more than 56 dBZ are reduced to 50 dBZ (to remove possible contamination from hail reflectivity). Cell-based VIL cannot be shown in a Plan Position Indicator (PPI)¹⁵ presentation like reflectivity or radial velocity, because it is computed as a single number for each cell being tracked by the SCIT system.

Gridded VIL is a product originally created for the FAA, as an overlay to the Air Traffic Control (ATC) radar systems they use. It is computed on a rectangular coordinate system, as opposed to the polar-cylindrical coordinate system native to the WSR-88D. This Cartesian coordinate system takes the reflectivity in each 2.2×2.2 nautical mile (4×4 km) rectangular box and integrates it vertically along a z-axis perpendicular to Earth's surface (Figures 7.8 and 7.9).

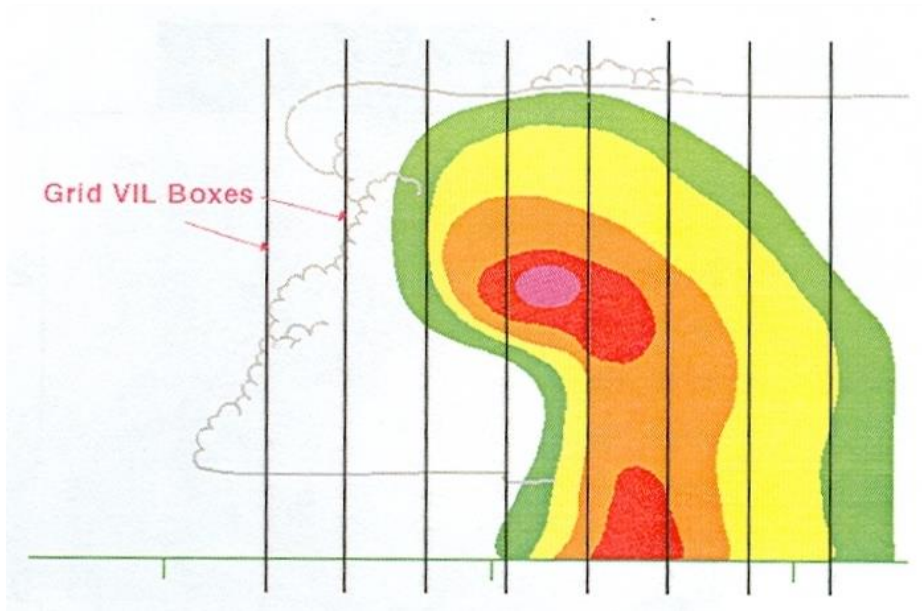


Fig. 7.8: Vertical integration axis of Gridded VIL. (Credit: WDTB 2005.)

¹⁵ This is a “plan” view display, using terminology associated with older radar systems. The alternative is **Range Height Indicator (RHI)**, today referred to as a **Vertical Cross-Section (VCS)**.

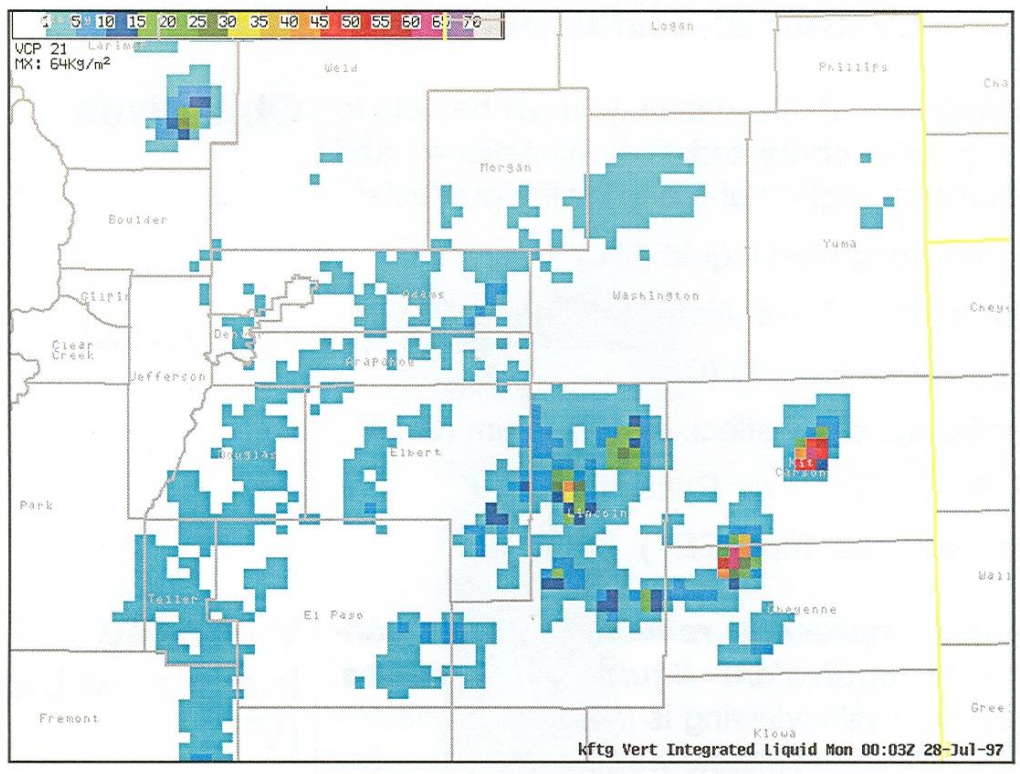


Fig. 7.9: Typical Gridded VIL display, showing rectangular grid coordinate system. (Credit: WDTB 2005.)

Like cell-based VIL, GVIL is compromised by dropsize distribution assumptions. Its values may differ from cell-based VIL because its vertical axis of integration is different: Cell-based VIL integrates through the (possibly tilted) vertical axis of a storm cell, while GVIL integrates along a line perpendicular to Earth's surface. Like cell-based VIL, it is degraded at distances very close to the RDA because of the *Cone of Silence*, as well as very great distances because of the *Wedge of Silence* (Chapter 3). Its greatest weakness is probably its assumption that all returned power is from liquid water droplets, while in fact some may be from highly reflective hailstones.

High VIL values are associated with deep regions of high reflectivity, which are in turn usually a result of strong updrafts. Persistent high VIL values are associated with supercell thunderstorms. A rapid *decrease* in VIL may indicate the onset of powerful downdrafts in a storm cell, such as a microburst, and has been used as a technique to forecast wind damage.

A quantity closely related to VIL is VIL Density (VILD), defined by:

$$VILD \equiv \frac{VIL}{EET} \quad (7.9)$$

where VIL is either the cell-based VIL (computed by the SCIT) or GVIL (computed separately). EET is Enhanced Echo Tops, which is discussed in greater detail below, but for now: It is the point near the top of a storm cell where the reflectivity drops below 18 dBZ, making it distinct from the *Cell Top* computed by the SCIT, which is defined as that point near the top of the cell where the reflectivity drops below 30 dBZ. Since EET has units of mARL, VILD, therefore, has units of kg m⁻³, a density. Sudden changes in VILD have also been used as a technique for forecasting wind damage from thunderstorm downdrafts (*e.g.* Loconto 2005).

Digital VIL (DVIL), also known as High-Resolution VIL, uses the same equation (7.1) to convert reflectivity to kilograms of liquid water per square meter. It differs from both cell-based VIL and GVIL in that it neither truncates reflectivities below 18 dBZ nor reduces reflectivities above 56 dBZ to 50 dBZ. All reflectivity values are used. Another way it differs is that it is computed in the polar-cylindrical coordinate system (with a z-coordinate perpendicular to Earth's surface) used for other reflectivity products, that is, 1° wide in the circumferential direction and 1 km in the radial direction. Figure 7.10 shows an example of DVIL. Values are represented at 256 data levels, varying from 0 to 80 kg m⁻².

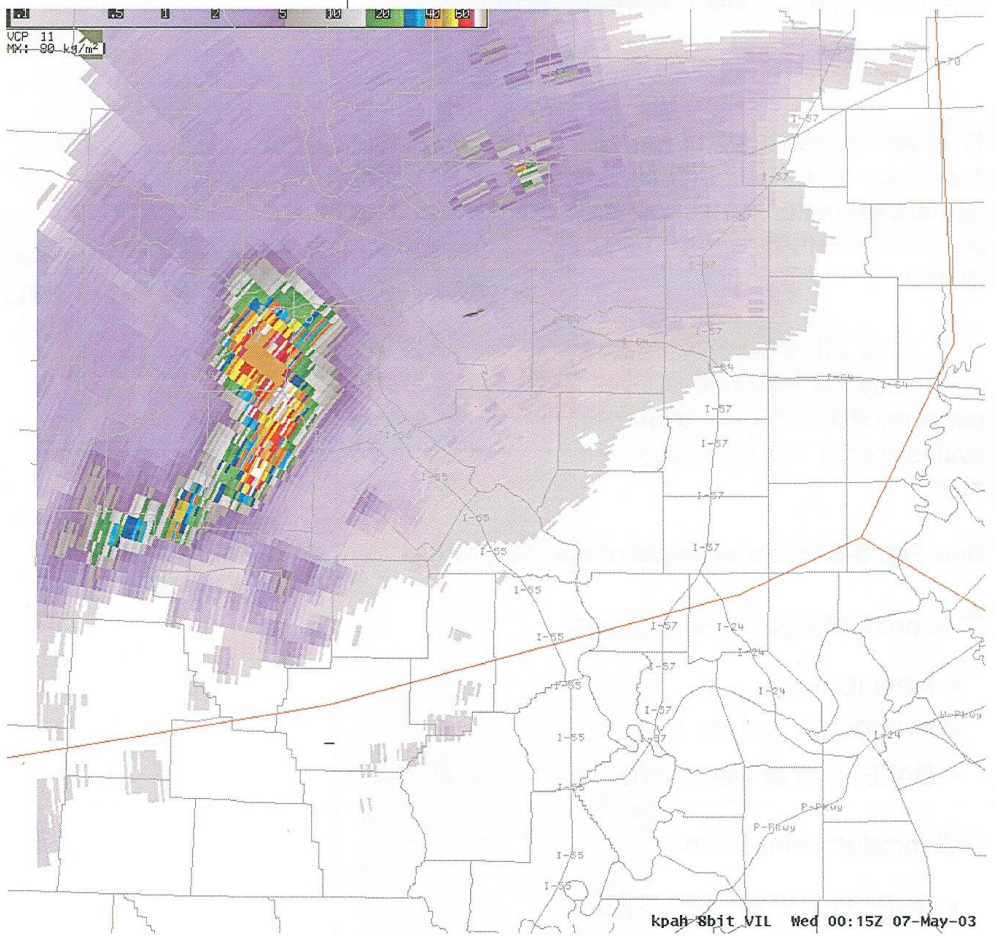


Fig. 7.10: Sample Digital VIL display. (Credit: WDTB 2005.)

Digital VIL, because it doesn't truncate very low or very high reflectivities, produces different values than both cell-based VIL and GVIL. Because of its relatively fine spatial resolution (especially when compared to GVIL), fast moving or highly vertically tilted storm cells may be "smeared out" across several range bins and be represented by relatively low values of VIL. The highest VIL values possible (80 kg m^{-2}) are often reached because of the lack of high-end truncation. But DVIL has a number of useful features, among them its ability to enhance the visibility of very low-reflectivity features, such as snow bands, gust fronts, and smoke plumes.

7.3.2. Reflectivity Cross-Sections (RCS). Before describing this product, let's look back on a little bit of history. Older, manually-operated weather radar systems had one capability that the WSR-88D does not have: The ability to scan up-and-down

along a fixed azimuth, creating a vertical cross-section through a storm cell (or some other meteorological phenomena).

One example is the old U.S. Air Force's AN/FPS-77 radar system (see Chapter 1). To take a radar observation, the operator would sit down at the control console and set the antenna to rotate horizontally while transmitting. There was a single tilt angle. The radar would paint an image of the surrounding weather echoes on the main screen. Once a sufficiently high-resolution image was painted, the operator switched off the automatic rotation mode. After identifying highly reflective storm cells, he (or she) could then use a small wheel and manually rotate the antenna to a particular azimuth. There were then two options for *vertically* examining the cell of interest: An automatic, repeating up-and-down scan that painted a vertical reflectivity cross-section on a different screen, or a manual mode, where the operator could point the antenna at a given tilt to examine some feature in the target, using another manual rotation wheel. The first of these options was called a Range Height Indicator (RHI) scan.

Figure 7.11 shows an example of an RHI scan from a modern radar with dual-polarization capability. In this case, the user was diagnosing the melting level along a particular radial, which is visible as a bright band in both conventional reflectivity and Z_{DR} . The bright band occurs just below the height of the 0 °C isotherm, where solid precipitation is melting, becoming very bright in conventional reflectivity, and resulting in precipitation particles of mixed phase, resulting in high Z_{DR} values.

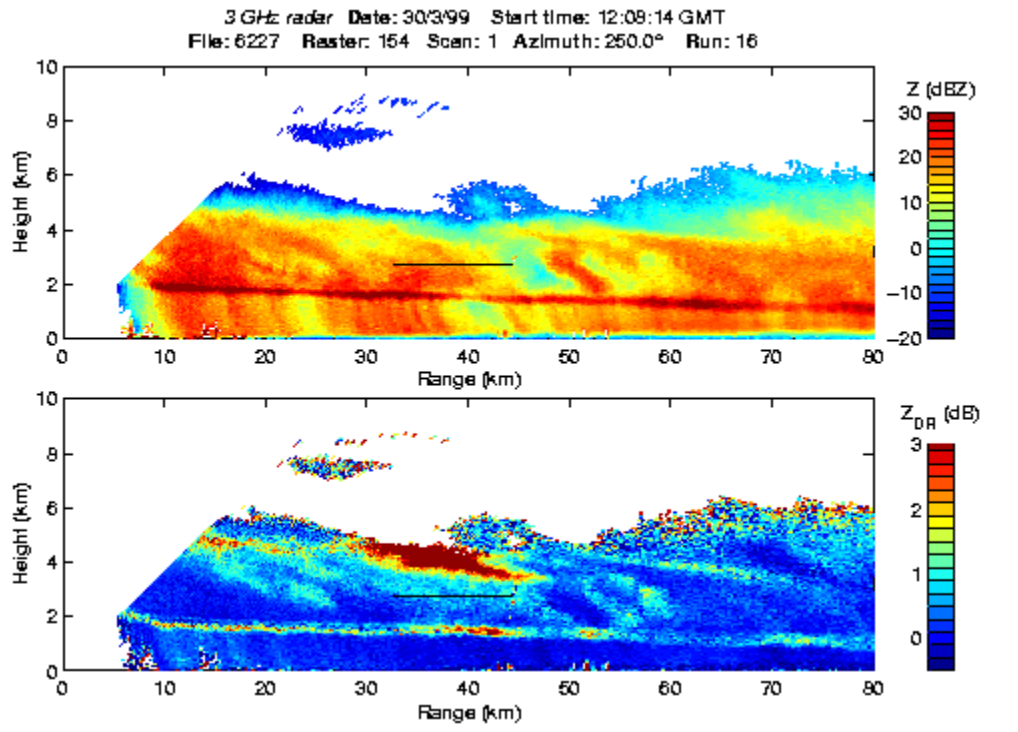


Fig. 7.11: Reflectivity Cross-Section and Z_{DR} Cross-Section showing melting layer. Conventional reflectivity is shown in the upper panel; Z_{DR} is in the lower panel. The bright band associated with the melting layer is clearly visible as a nearly horizontal line in both. (Credit: University of Reading, Department of Meteorology, 2019.)

The WSR-88D does not have the native capability to create RHI scans, because of the constant, automated surveillance it carries out under computer control. But taking a vertical scan through a storm cell or some other meteorological phenomenon is a pretty important capability, so the WSR-88D RPG is loaded with two separate algorithms that attempt to reproduce the same information as an RHI scan. The first of these is the Reflectivity Cross-Section (RCS), and the second is the Velocity Cross-Section (VCS), which will be discussed later.

To create an RCS, the user engages the drawing tool in AWIPS and draws a line through a reflectivity volume scan display (Figure 7.12). The line indicates the location of the RCS the user wants. The first end point is the left end of the line, and the second end point is the right end of the line. Both end points must both be within 124 nautical miles (230 km) of the RDA, and within 124 nautical miles of each other. The line is then submitted through the AWIPS One Time Request (OTR) menu to the RPG, which creates the RCS and sends it back to AWIPS. This process normally takes only few

seconds. When the completed RCS arrives back at AWIPS, a small pop-up box is triggered on the AWIPS display notifying the user.

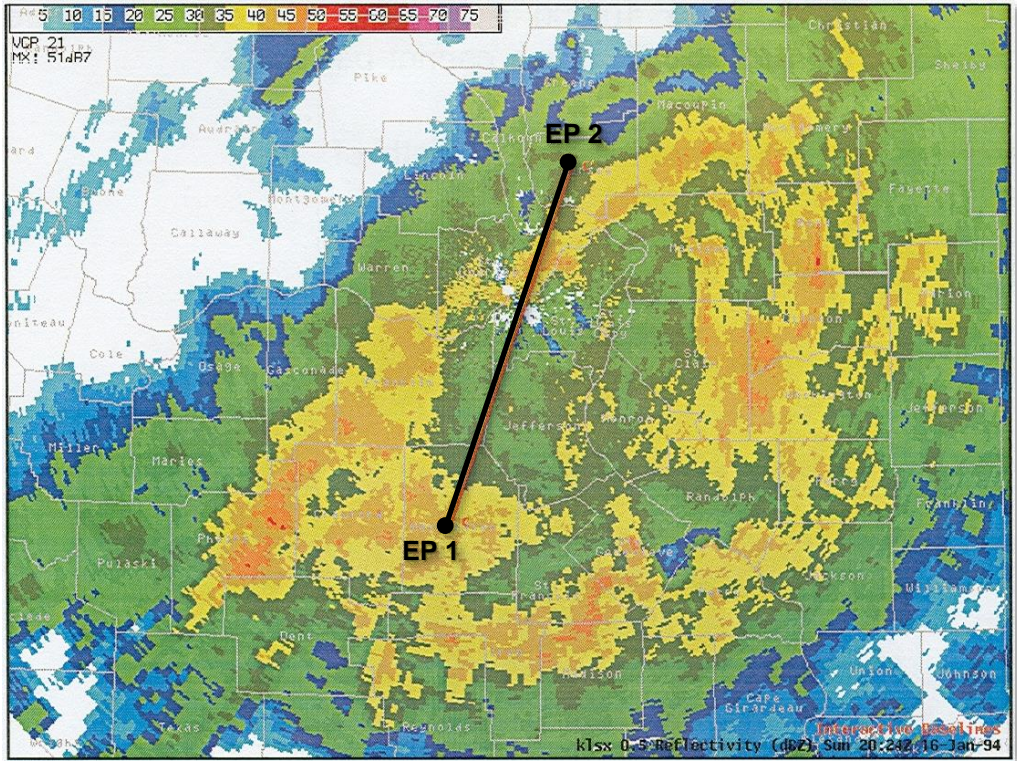


Fig. 7.12: Use of the AWIPS drawing tool to create an RCS. EP1 and EP2 are the user-defined endpoints of the RCS line. (Credit: WDTB 2005.)

The RPG creates the RCS by linking all elevation scans using the $1^{\circ} \times 1.00$ km Level II reflectivity data in the most recent volume scan. Values of reflectivity in between elevation angles are *interpolated* at a resolution of 500 meters. There is no *extrapolation* above the highest tilt or below the lowest tilt. The vertical scale of the resulting RCS is fixed at 70,000 feet ARL (21,340 meters), but the horizontal scale varies, depending on the length of the line drawn for the OTR. Figure 7.13 shows an example.

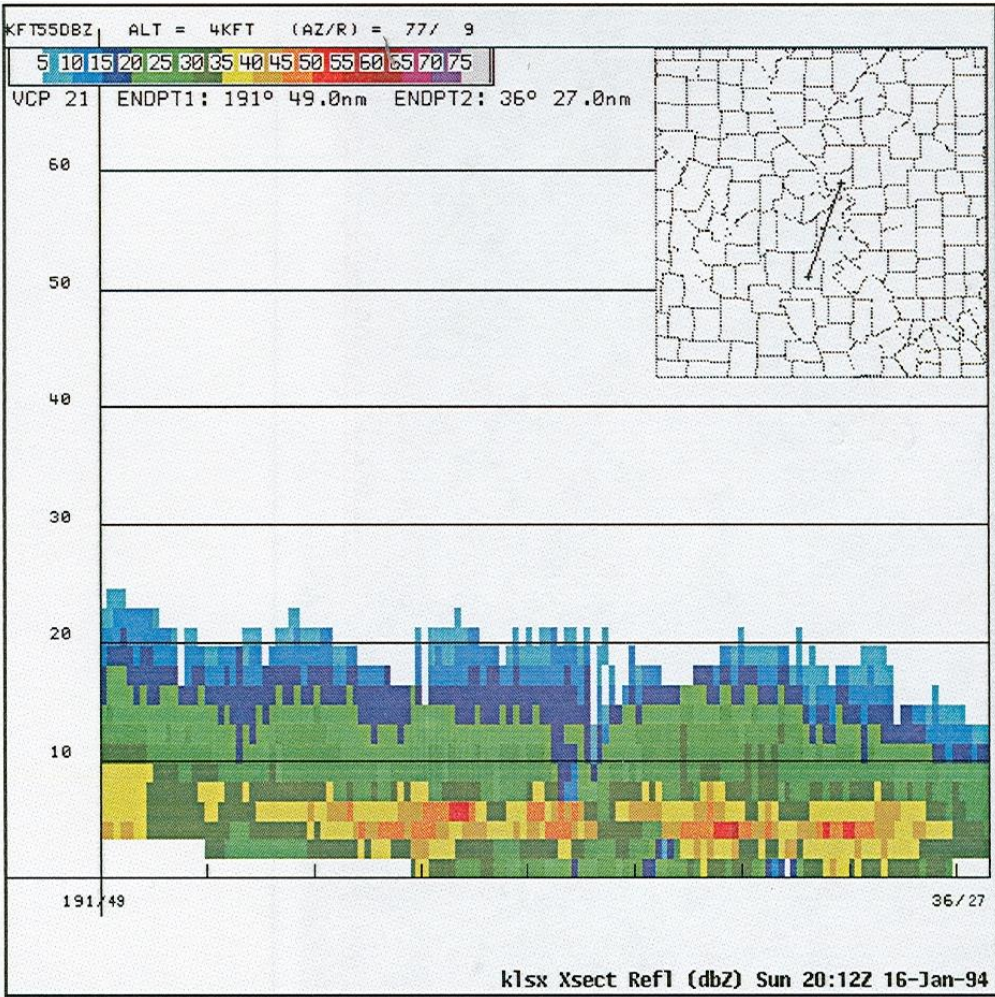


Fig. 7.13: Completed RCS corresponding to line in Fig. 7.12. (Credit: WDTB 2005.)

The RCS product is subject to a number of limitations. Small features may be either enlarged or wiped out by the interpolation between elevation angles. The echo tops and bases may be truncated, because of the lack of extrapolation above or below. The aspect (height-to-length) ratio may be misleading because of the fixed vertical scale and variable horizontal scale. And fast-moving storms may appear overly tilted, because of the delay in collecting the base reflectivity data at successive tilt angles.

Despite these issues, the RCS can be used for several purposes, among them the evaluation of a storm cell's structure. (This was the most frequent purpose for which RHI scans were used in the old AN/FPS-77.) Important storm structure features often evaluated are its base, top, and any Bounded Weak Echo Regions (BWER), also known as an Echo Free Vaults. Figure 7.14 shows an example. A BWER is caused by an

intense updraft above the portion of a thunderstorm where warm, moist air flows into the core of the storm. It isn't visible to the eye.

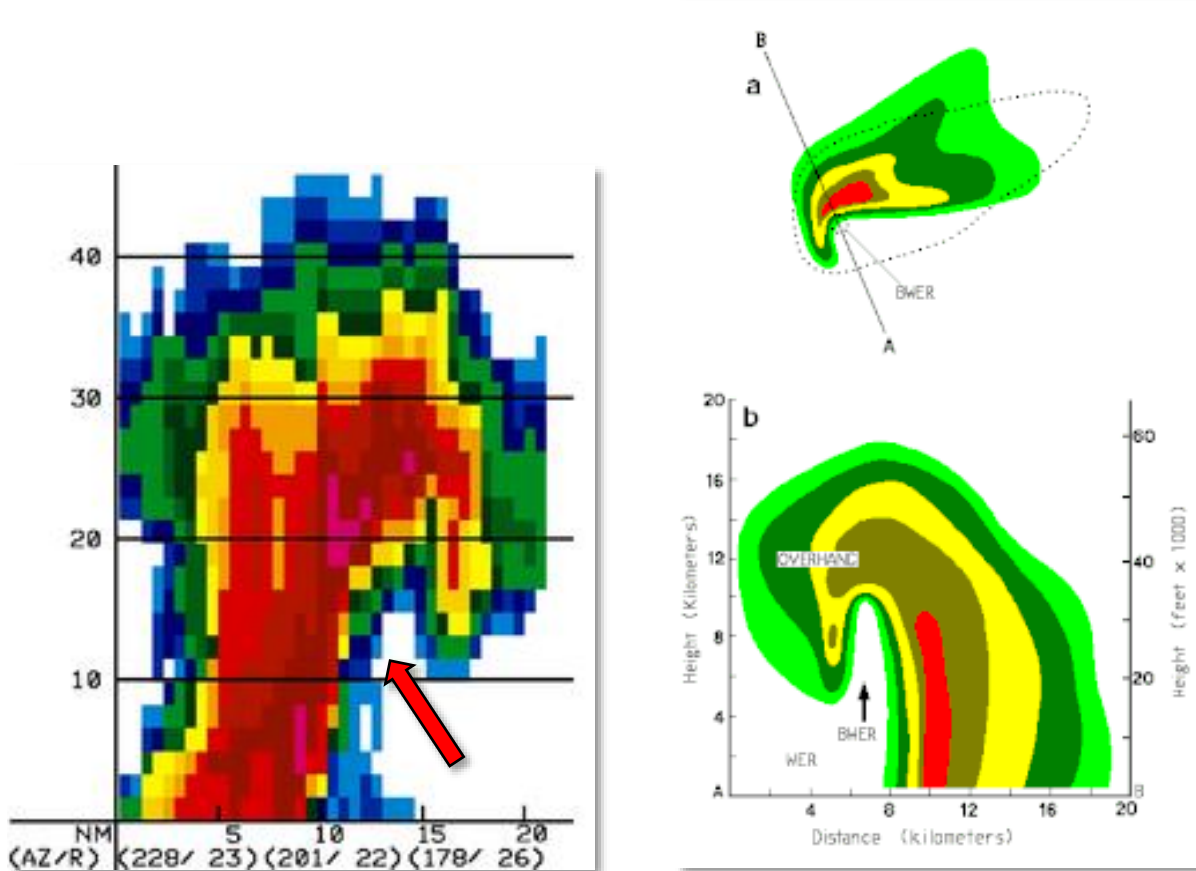


Fig. 7.14: Bounded Weak Echo Region (BWER) in an RCS display. Left: The BWER is the part of the storm with light reflectivity, surrounded by heavier reflectivity, indicated by the red arrow. (Credit: U.S. National Weather Service, Rapid City, South Dakota 2019.) Right: Relationship between the BWER in the RCS display (b), and a developing hook in a plan-view reflectivity volume scan (a). (Credit: U.S. National Weather Service, Southern Regional Headquarters.)

7.3.3. Composite Reflectivity (CZ). This is another product originally created for the Federal Aviation Administration for use as an overlay in Air Traffic Control radar displays. CZ is defined, in this context, as the highest reflectivity in the vertical column above a certain rectangular grid box on Earth's surface. This means that CZ has a rectangular grid coordinate system similar to GVIL, making it possible to easily combine the output from several WSR-88D RDAs in a single display. It differs from the GVIL coordinate system slightly:

- From the RDA to 124 nautical miles (230 km): Grid boxes are 1 km x 1 km
- From 124 nautical miles (230 km) to 248 nautical miles (460 km): Grid boxes are 4 km x 4 km (same as GVIL)

Composite Reflectivity suffers from a number of relatively minor limitations. These include the inability to tell whether a particular precipitation echo is on the lowest tilt angle, rather than farther aloft. Another way of stating this is that it's hard to tell the difference between virga and precipitation reaching the ground using Composite Reflectivity. Since only the highest reflectivity value is shown in each box, the user (1) doesn't know the height of the reflectivity being displayed, and (2) is unable to see lower reflectivity values that might be closer to the ground than the value being displayed. But CZ is very useful to meteorologists in stratiform precipitation scenarios, when the distribution of reflectivity is often more vertically uniform. And the CZ algorithm also generates a table, call the Combined Attributes Table (CAT), that's useful as an overlay on volume displays.

Figure 7.15 shows a sample of the CAT. It combines information about storm cells output by several Level III derived products, including the SCIT, which identifies each cell's location (azimuth and range), computes its VIL, forecasts its movement, computes the height of its maximum reflectivity center, and tags it with a letter-number designator. The CAT also includes output from the Hail Detection Algorithm, the Tornado Detection Algorithm (TDA), and the Mesocyclone Detection Algorithm (MDA, formerly MESO). The order of the cells in the CAT is determined by whether it is associated with a Tornadic Vortex Signature (TVS) or a mesocyclone, its Probability of Severe Hail, its probability of any hail, and its cell-based VIL.

STORM/ID	AZ/RAN	TVS	MESO	POSH/POH/MX SIZE	VIL	DBZM	HT	TOP	FCST	MVMT
SO	357/ 62	NO	YES	70/100/ 1.25	46	59	18.5	32.7	238/	29
AO	181/ 90	NO	NO	100/100/ 2.50	62	66	20.0	37.7	257/	33
C3	160/107	NO	NO	80/100/ 1.25	53	61	13.7	35.2	234/	39
F3	326/ 16	NO	NO	70/100/ 1.25	37	62	15.8	>34.0		NEW

Fig. 7.15: Sample CZ Combined Attributes Table (CAT). (Credit: WDTB 2005.)

A closely related product is the **Layer Composite Reflectivity Maximum (LRM)**, which displays the highest reflectivity above a rectangular grid box on Earth's surface, in three different vertical layers. LRM was also developed for the FAA as an overlay in Air Traffic Control radar displays. In this case, all grid boxes are 4 km x 4 km, out to a maximum range of 248 nautical miles from the RDA. The three vertical layers are:

- **Low:** Just above radar level to 24,000 feet (about 7,300 meters).
- **Mid:** 24,000 feet to 33,000 feet (7,300 meters to about 10,000 meters).
- **High:** 33,000 feet to 60,000 feet (10,000 meters to about 18,300 meters).

7.3.4. **User-Selectable Layer Reflectivity Maximum (ULR).** This product is similar to Composite Reflectivity, except (1) it uses the same polar cylindrical grid system as conventional reflectivity ($1^\circ \times 1$ km), and (2) the user can specify the upper and lower vertical limits of the layer through which the reflectivity maximum is computed, using the One Time Request (OTR) menu in AWIPS. Layer thicknesses are selectable in 1,000-foot increments, varying from 1,000 feet to 70,000 feet. Selecting the latter value would result in CZ values similar to those in the conventional CZ product.

The advantages of this product over the other iterations of CZ are that it has a finer horizontal resolution, and the user can customize the vertical region through which the composite is computed. One important use is investigating the presence of high reflectivity centers near the height of the -20°C isotherm, which is a good indication of hail. Another is identifying the bright band immediately below the melting level. If the feature under interrogation is sufficiently narrow in the vertical dimension, the ULR may produce an apparent structure of concentric rings from a single bright-band, such as the example illustrated in Figure 7.16. An explanation of the ring structure is provided in the figure caption.

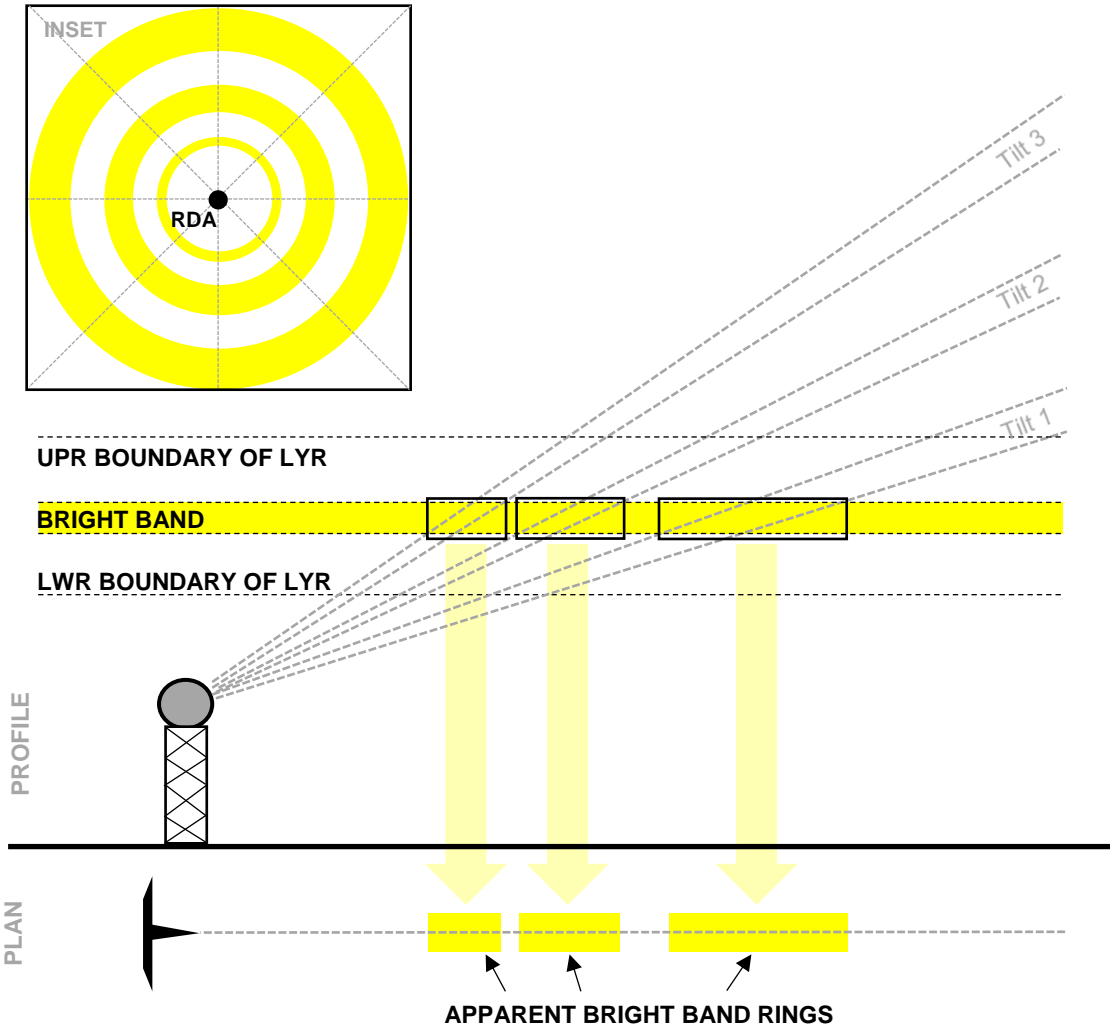


Fig. 7.16: Creation of an apparent ring-like structure from a single bright band. Inset (upper left): Plan view of reflectivity with RDA in center (black dot), surrounded by three concentric bright rings, caused by a single bright band. Top (main diagram): Vertical profile showing beams on three separate tilts. All three pass through the bright band, but at different distances from the RDA. The gaps between the locations where they pass through the bright band show up as relatively dark areas in a reflectivity scan. Bottom (main diagram): Plan view of reflectivity bright bands created by the scenario shown in the upper panel, showing short sections of the rings in the inset.

7.3.5. Enhanced Echo Tops (EET). This product identifies the highest elevation angle in a given range bin where the reflectivity is at least 18 dBZ. (Recall that the cell top and base were defined as corresponding to 30 dBZ in the SCIT.) It uses the same $1^\circ \times 1$ km polar cylindrical coordinate system as Level II base reflectivity. If needed, interpolation is performed between tilt angles to estimate the height of the 18 dBZ upper limit, but there is no extrapolation either above the highest tilt or below the lowest tilt. In areas where the reflectivity is at least 18 dBZ on the highest tilt angle, the

height is indicated as “topped,” and shown in black in a display of the product. A sample is shown in Figure 7.17.

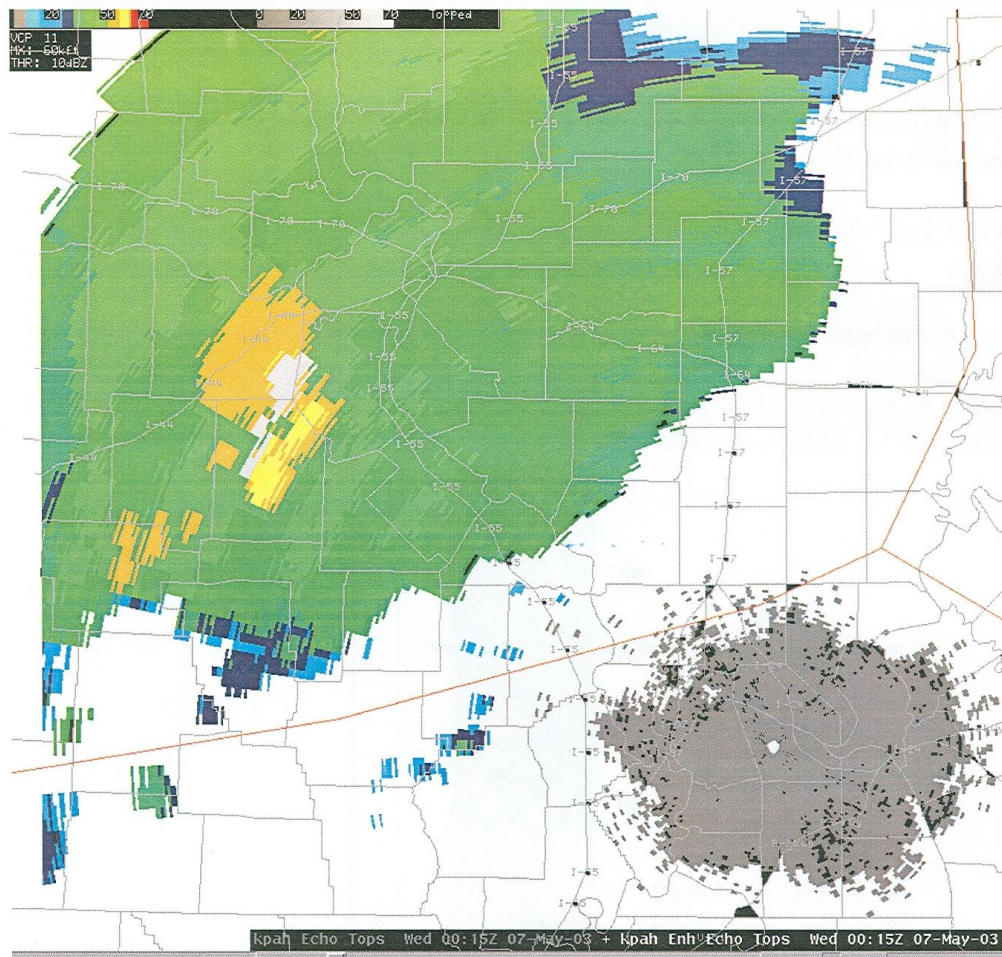


Fig. 7.17: Typical display of Enhanced Echo Tops (EET). (Credit: WDTB 2005.)

The EET is useful for identifying details of a storm cell’s structure, such as its tilt, the presence of updrafts, and the maximum height of a cell top over a strong low-level reflectivity center.

One problem this product suffers from is an erroneous “stair-stepped” appearance, because of the use of interpolation between tilt angles. A sample of this is shown in Figure 7.18. Another error that sometimes occurs with EET displays is caused by contamination from radar side lobes. Figure 7.19 reproduces the left panel of Figure 3.5, illustrating the presence of microwave side lobes near the RDA antenna. While side lobes usually return very low power (compared to the main lobe), the EET algorithm

uses such a low reflectivity threshold that it may mistake returned power from a side lobe (perhaps backscattered from the ground near the RDA) for a target in the main lobe. If this happens, it may paint a “ghost echo” at a distance, azimuth, and tilt angle at which the returned power would be if the main lobe were responsible for the echo. The main lobe would be pointing toward a higher elevation angle.

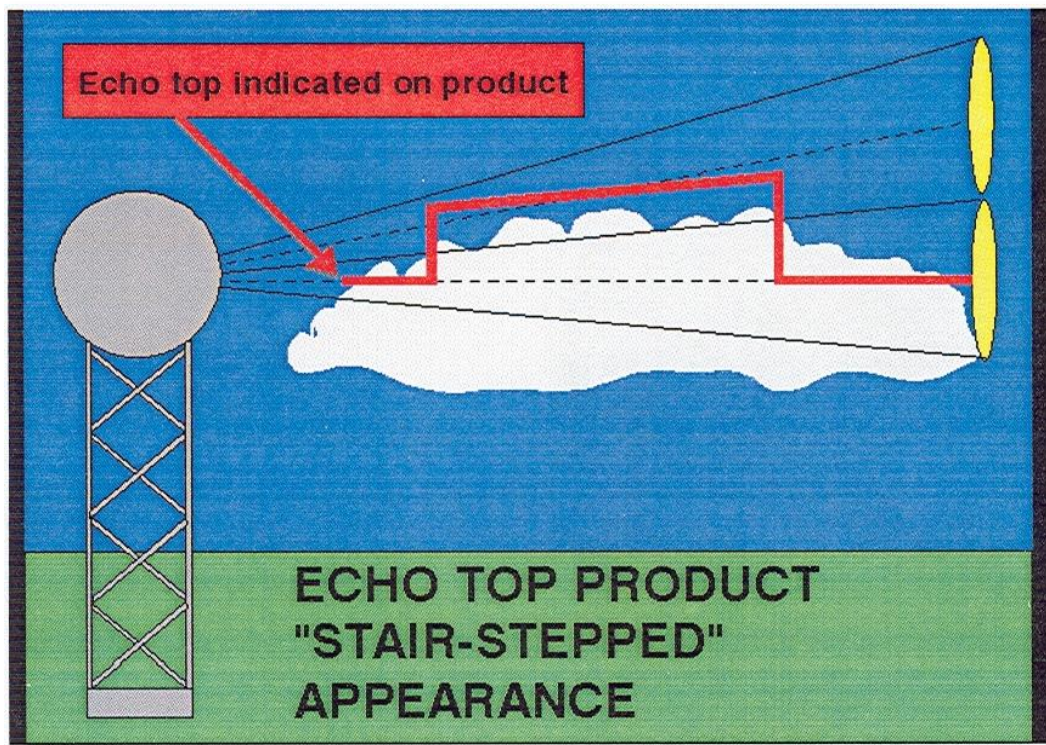


Fig. 7.18: Cause of stair-stepped appearance in EET product. (Credit: WDTB 2005.)

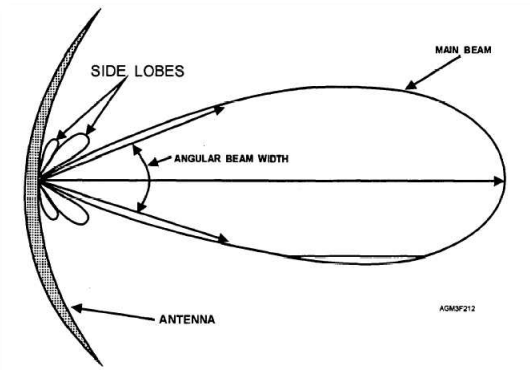


Fig. 7.19: Main and side lobes of a transmitted microwave beam. (Image credit: http://meteorologytraining.tpub.com/14271/css/14271_61.htm)

7.4. Velocity-based products, and products using both reflectivity and radial velocity.

There are several pieces in this category, including:

- Storm-Relative Mean Radial Velocity
- Velocity Cross-Sections
- Velocity Azimuth Display
- VAD Wind Profile
- Mesocyclone Detection Algorithm
- Tornado Detection Algorithm

7.4.1. Storm-Relative Mean Radial Velocity (SRM). The algorithm that creates this product attempts to compute the portion of the radial velocity in each range bin that would be observed if the origin of the coordinate system was centered on, and moving with, a given storm cell. Put another way, it is the component of radial velocity that remains once a storm cell's translational velocity across the landscape is subtracted. The objective is to clearly identify rotating cells. SRM is available in the region between the RDA and 124 nautical miles (230 kilometers) out in all directions.

To compute SRM, the algorithm takes (as its default setting) the average of all storm cell motions computed by the STIC, and subtracts this velocity from the radial velocity in every range bin. If most of the storm cells are moving in the same direction and at the same speed, what remains in each range bin should be the rotational component of the velocity. A user can force the SRM algorithm to recompute the storm-relative velocity by subtracting a *different* translational component, by invoking a One Time Request (OTR) through AWIPS. While SRM is subject to all the same sources of

error as Level II radial velocity, when it functions correctly, it can provide improved detection of tornadic vortex signatures, mesocyclones, microbursts, outflow boundaries, and regions of upper-level divergence.

7.4.2. Velocity Cross-Sections (VCS). This product is very similar to the Reflectivity Cross-Section (RCS), discussed above. It is created using a similar process, involving the AWIPS drawing tool and an OTR. Both end points must be within 124 nautical miles (230 km) of each other, and the RDA. The algorithm carries out interpolation at a 500-meter vertical resolution between tilts, but there is no extrapolation above the highest tilt, or below the lowest tilt.

In this case, the base data used are Level II radial velocity data, which are on a 1° x 250m polar cylindrical coordinate system (finer in the radial direction than the Level II reflectivity data). A carefully selected VCS aids in evaluating storm structure, such as inferring regions of updrafts and downdrafts (by evaluating convergence and divergence), and the depth of a mesocyclone. VCS's are best used in one of two ways:

- *Parallel* to a radial, with one endpoint near the RDA and another farther away. This can be used to diagnose convergence or divergence.
- Over a short distance *perpendicular* to a radial, with one endpoint to the left of the radial, and another to the right of the radial. Both endpoints are the same distance from the RDA. This can be used to diagnose rotation. If inbounds are on the left and outbounds are on the right, counter-clockwise (cyclonic) rotation is indicated. Figure 7.20 shows an example of this.

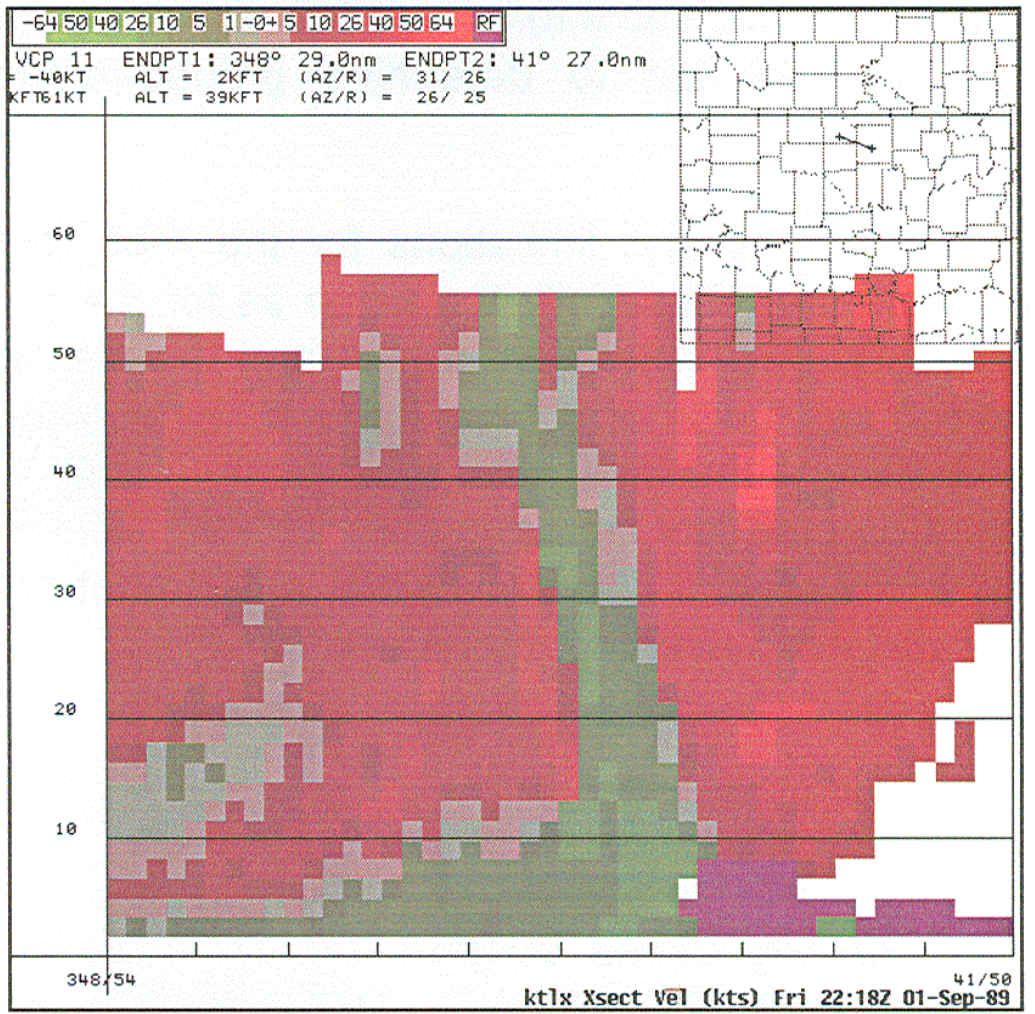


Fig. 7.20: Velocity Cross-Section. Outbounds (red) are to the right of the inbounds (left), indicating counter-clockwise (cyclonic) rotation. (Credit: WDTB 2005.)

As with an RCS, the aspect ratio may be misleading. The vertical height is fixed at 70,000 feet (21,340 meters), while the horizontal length varies, depending on choices made by the user. Interpolation may either obscure or exaggerate features in between tilt angles. And the product is subject to limitations arising from the Cone of Silence near the RDA. Another important limitation is that Vertical Cross-Sections are available only for Level II radial velocity, not SRM.

7.4.3. Velocity Azimuth Display (VAD). This product is not commonly used as a stand-alone display, but feeds data into two other Level III products: The VAD Wind Profile (VWP), and the Environmental Winds Table (EWT). The VAD algorithm attempts to infer the *full* wind vector, not just its radial component, by using wind data

(at a fixed elevation) from all radial directions around the RDA, at a fixed distance. The zero isodop (see Chapter 5) is implicitly involved in the calculation.

For each altitude requested by the VAD, the algorithm selects the tilt angle that most closely intersects the requested altitude at the VAD Slant Range, defined as an optimum distance of 16.2 nautical miles (30 km). (The *actual* slant range may vary, depending on the altitude requested by the VAD.) Level II radial velocity data in the corresponding range bins at the selected tilt are collected for all 360 one-degree radials, creating a ring of radial velocity data around the RDA. (See Figures 7.21 and 7.22.)

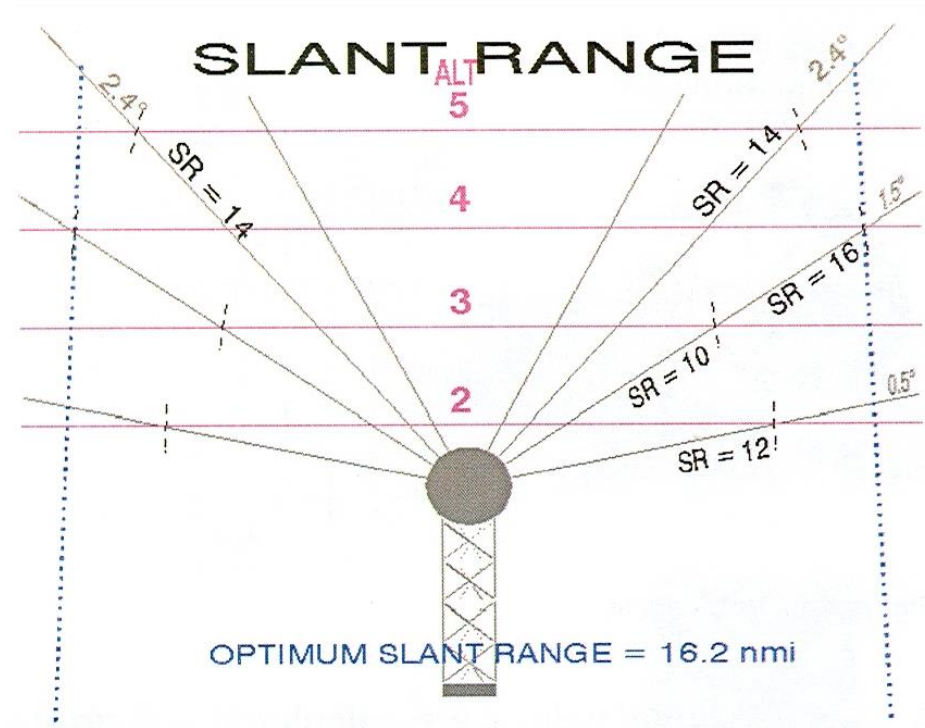


Fig. 7.21: Level II radial velocity data are collected in a 360-degree circle around the RDA from the range bins in the tilt angle that most closely intersects the requested altitude at the VAD Slant Range. (Credit: WDTB 2005.)

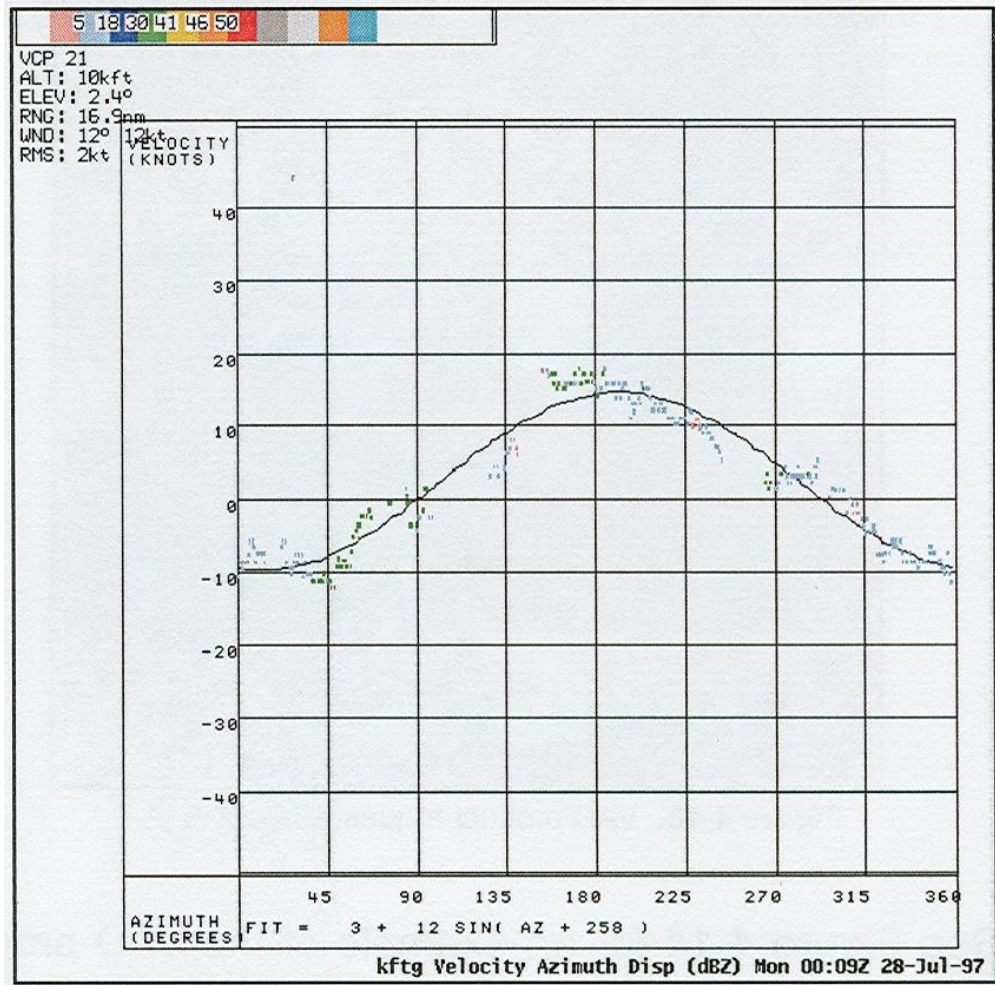


Fig. 7.22: Radial velocity data in the range bins most closely corresponding to the selected elevation, in a 360-degree circle around the RDA. Horizontal axis is azimuth; vertical axis is Level II radial velocity in the corresponding bin. (Positive velocities are outbound; negatives are inbound.) Discrete datapoints are shown as dots; curve fit is a solid line in the form of a sine wave. (Credit: WDTB 2005.)

If there are 25 radial velocity datapoints (of 360 possible) in the ring around the RDA, a sine wave is fitted to the data. This is an attempt at further noise reduction. *The VAD wind is computed using the sine wave, not the raw data.*

- The half-amplitude of the sine wave is the estimated wind speed
- The point on the sine wave associated with the greatest negative (inbound) wind speed is taken as the wind direction.

Notice that this method implicitly assumes a homogenous wind field within the VAD Slant Range.

Two additional parameters are then computed. The first is Symmetry (Sym), defined as the difference between the zero radial velocity line (V_0), and the median line of the sine wave curve (V_{med}):

$$Sym \equiv V_{med} - V_0 \quad (7.9)$$

If $Sym < 0$, then V_{med} is also < 0 , and inbound velocities are greater than outbound velocities. This implies *convergence* over the RDA. If $Sym > 0$, then V_{med} is also > 0 , and inbound velocities are less than outbound velocities. This implies *divergence* over the RDA. The second is the Root-Mean Square Error (RMSE) for the sine wave fit to the radial velocity data. This is an indicator of the reliability of the wind estimate.

Thresholds are then tested for these two parameters. If the absolute value of the Symmetry exceeds 13.6 kts (7 ms^{-1} , implying convergence or divergence in excess of 0.42 kts per nautical mile, or 0.12 ms^{-1} per km), or RMSE exceeds 9.7 kts (5 ms^{-1}), the VAD will *not* output a value to either the VAD Wind Profile or the Environmental Winds Table.

To operate, the VAD requires only 25 datapoints in the 360-degree ring around the RDA. (This could be considered both a strength *and* a weakness.) This condition is sometimes not met, particularly in clear, cold, clean conditions, when an air mass has few scatterers in the correct size range. Notice that these datapoints need *not* be evenly distributed around the full azimuth circle, but may be clustered into a single narrow sector, reducing the representativeness of the derived wind.

The algorithm also may not produce reliable results in scenarios where the underlying assumption – that the wind field is homogenous in a 30-km radius around the RDA – is invalid. Some examples where this assumption may fail are when there is a sea breeze or some other mesoscale boundary present in the volume scan area. These types of mesoscale boundaries often trigger the algorithm's threshold failure for either Symmetry, RMSE, or both. Finally, large flocks of migrating birds may produce anomalous radial velocity datapoints that can cause the algorithm to fail.

7.4.4. VAD Wind Profile (VWP). The VWP is a vertical profile of VAD-derived winds at several levels above the WSR-88D RDA, in time steps corresponding to the CD volume scans. As many as 11 profiles can be displayed at one time. Figures 7.23 and 7.24 show examples.

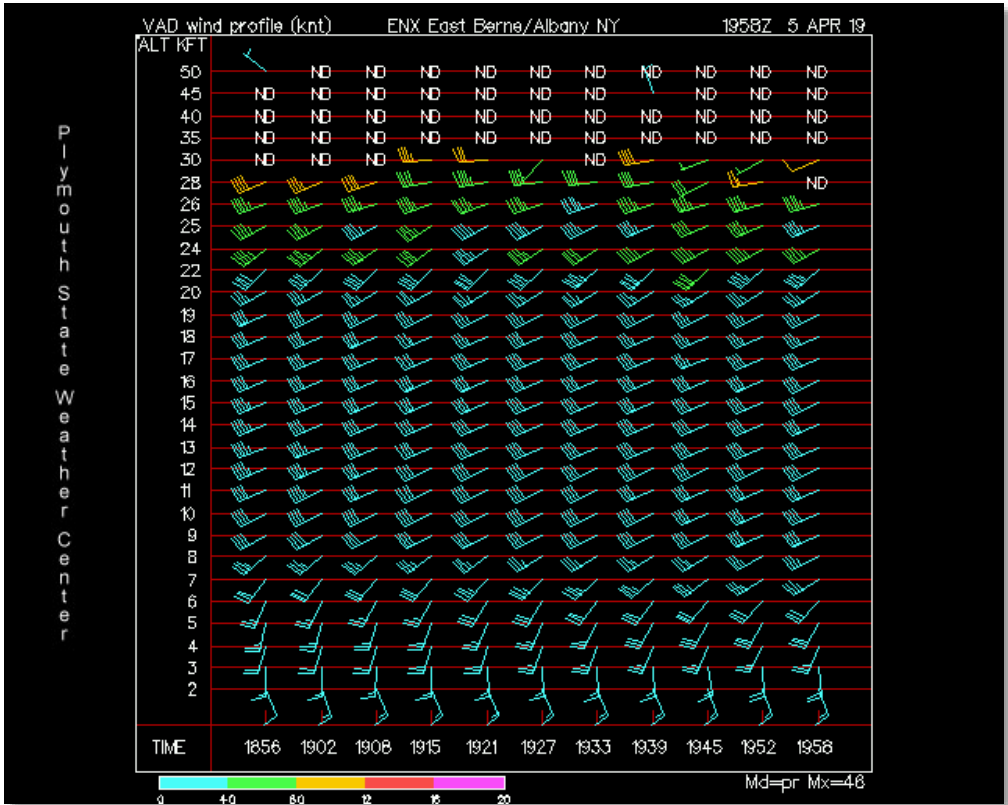


Fig. 7.23: Sample VWP, when plenty of scattering particles are present. (Credit: PSU 2019.)

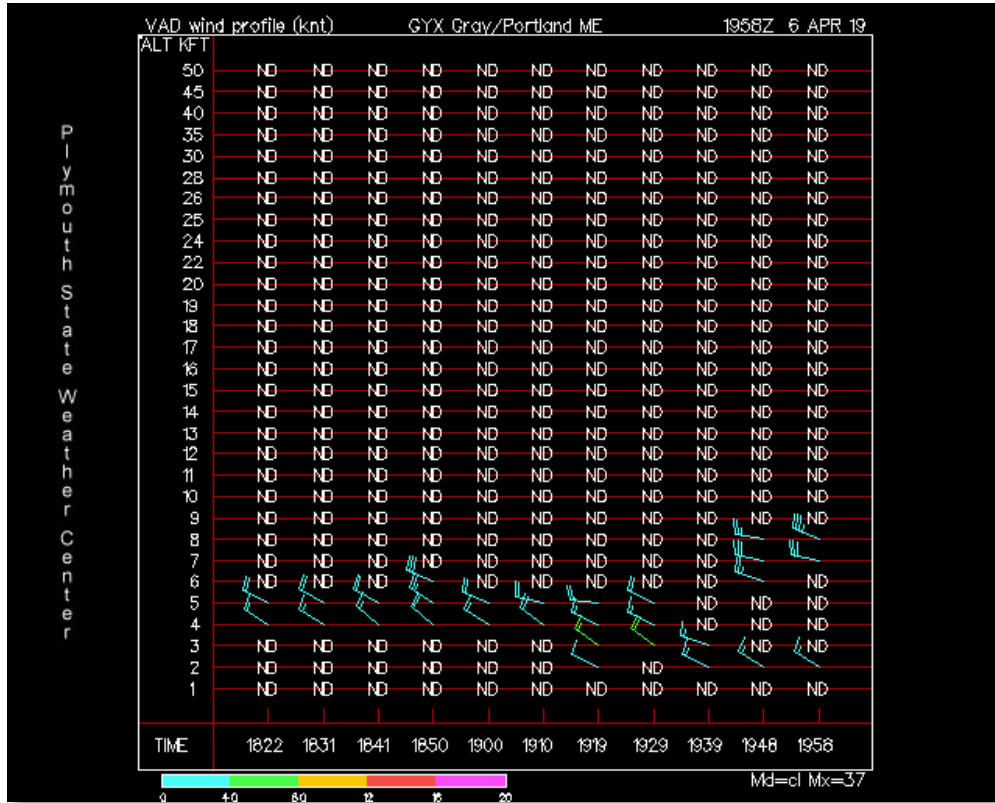


Fig. 7.24: Sample VWP, when few scattering particles are present. (Credit: PSU 2019.)

A maximum of 30 different altitudes can be displayed from each volume scan, although the number actually shown is usually smaller than that. Wind data can be displayed for altitudes as high as 70,000 feet ARL (about 21,340 meters), but it is uncommon to accurately derive winds above 45,000 feet ARL (about 13,720 meters), because of the lack of scattering particles in the stratosphere. Winds are usually displayed in 1,000-foot intervals in the low levels, switching to 2,000-foot, then 5,000-foot intervals at higher elevations.

The data are coded using standard meteorological wind barbs, with a short feather indicating 5 knots, and a long feather indicating 10 knots. The wind barbs are also color-coded to indicate the quality of the sine-wave fit in the corresponding VAD. The first data level corresponds to an RMSE < 4 kts; the second data level to an RMSE of 4 - 7 kts; and, the third data level to an RMSE of 8 - 12 kts. "ND" is encoded in cases where the corresponding VAD had fewer than 25 datapoints, the RMSE exceeds 9.7 kts, or the Symmetry exceeds 13.6 kts.

The VWP should be understood as representing the mean wind above the RDA, for an area 16.2 nautical mile (30 km) in radius around the radar installation. It may

sometimes be difficult to read, such as when the winds aloft are all either from the north or the south, causing the plotted wind barbs to overlap each other. And, the data can be distorted by all the limitations affecting radial velocity, such as range folding, velocity aliasing, and erroneous data resulting from the presence of birds, insects, or bats. Nonetheless, the VWP can be very useful for assessing backing or veering of the wind (and therefore, of severe weather potential), helicity, and regions of wind shear.

7.4.5. Identifying tornadic thunderstorms. Prior to the advent of Doppler-enabled radar, potentially tornadic storms could only be identified in radar data by the “hook echo” that appeared in ordinary reflectivity (Figure 7.25). Hook echoes were first noted in 1945 (shortly after WWII), but their significance was not fully realized until a hook echo was observed in association with a tornado in 1958. By 1965, these echoes were explained as resulting from the redistribution of precipitation within a storm cell by the intense winds circulating around the tornado and its parent mesocyclone.

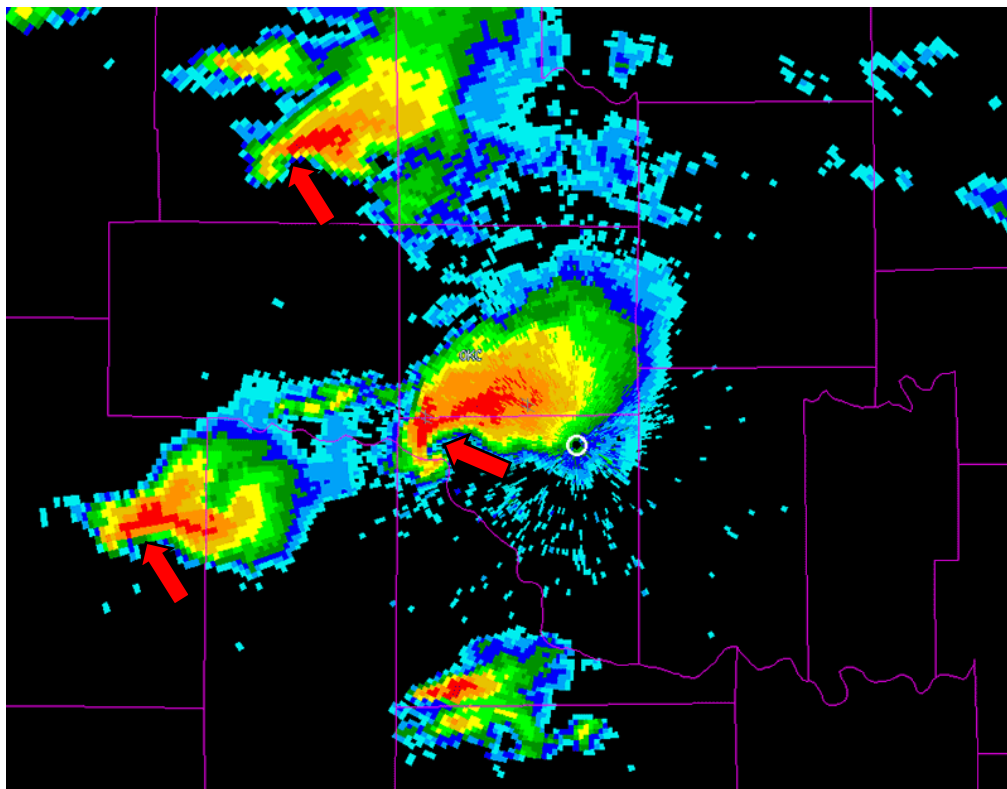


Fig. 7.25: Hook echoes produced by scanning tornadic thunderstorms. Potential tornado locations are indicated by arrows. (Image: NOAA National Severe Storms Laboratory 2019.)

Hook echoes alone were not completely reliable indicators of tornadic storms. Using data from a large outbreak of tornadoes in the spring of 1974, Forbes (1981) found that not all tornadic storm cells produced either a hook or any other distinctive reflectivity echo. However, he *did* find that 65 percent of these distinctive echoes *were* associated with tornadoes, and that these echoes accounted for 81 percent of the tornadoes in the outbreak. Unfortunately, he also found that the appearance of distinctive echoes did *not* provide sufficient lead time for tornado warnings, and when they *did* appear, they often produced a high False Alarm Rate (FAR) for the warnings subsequently issued. From this, he suggested that Doppler-enabled meteorological radar was the best hope for greater reliability and longer warning lead times (Mitchell *et al.* 1998). The last two velocity-based WSR-88D Level III products we will discuss are specifically designed to locate and track potentially tornadic thunderstorms.

7.4.6. Mesocyclone Detection Algorithm (MDA). This Level III product is designed to locate and track storm-scale cyclonic circulations (with diameters between one and five nautical miles), compute their relative strength (assigning a Strength Rank), and forecast their future positions (Lee and White 1998). It is similar to the SCIT system, differing in that it relies primarily on radial velocity data rather than reflectivity data. While only about half of mesocyclones produce tornadoes, detecting the former is an important ability for meteorologists because most tornadoes are produced by mesocyclones (Lee and White 1998; Stumpf *et al.* 1998). To protect life and property, it is better to detect as many mesocyclones as possible (yielding a high POD), and accept that not all of them will actually produce a tornado (FAR)¹⁶.

The National Severe Storms Laboratory (NSSL) established the following criteria for identifying mesocyclones with weather radar:

- A mesocyclone must persist for the elapsed time of at least two volume scans.
- Its vertical extent must be at least 10,000 feet (about 3050 meters).
- Its horizontal extent (distance between the associated inbound and outbound wind maxima) of the velocity couplet must be less than or equal to five nautical miles (about 9.3 kilometers).
- The velocities detected in the feature must meet certain threshold values, depending on their distance from the RDA.

¹⁶ See Appendix 2 for a discussion of POD and FAR.

The MDA sequentially processes data at one, two, and three dimensions. One-dimensional radial velocity patterns are referred to as Shear Segments and Convergence Vectors. Two-dimensional patterns are called Shear Features, and three-dimensional patterns are called Features.

7.4.6.1. **Processing for a single tilt angle.** The MDA first examines radial velocity data for collocated Shear Segments and Convergence Vectors.

- A Shear Segment is defined as a string of base radial velocity range bins ($1^\circ \times 250\text{m}$) at a fixed range, with values increasing in the clockwise direction. This may mean (1) inbound radial velocities on the left end of a circumferential arc, gradually diminishing to zero, then reversing and become increasingly outbound radial velocities on the right end of the arc (as shown in Figure 7.26, which is the same as condition described in Chapter 5, Figure 5.18, left panel); (2) increasing outbound radial velocities along the arc; or (3) decreasing inbound radial velocities along the arc.

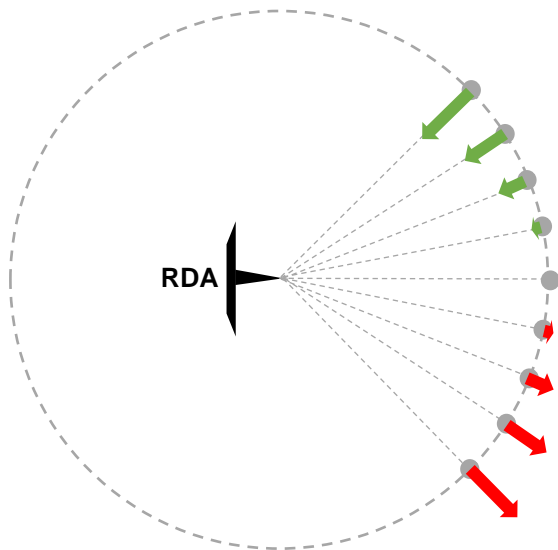


Fig. 7.26: Shear Segment showing increasing radial velocities in a clockwise arc (plan view).

- A Convergence Vector is defined as a string of base radial velocity range bins ($1^\circ \times 250\text{m}$) in a fixed direction, with values *decreasing* as distance from the RDA

increases. This matches the condition described in Chapter 5, Figure 5.17 (left panel). This may imply actual inbounds farther from the RDA than outbounds closer in, or it may merely be weaker outbounds further away from the RDA.

Candidates for Shear Segments and Convergence Vectors are also tested for reflectivity exceeding a minimum threshold value. This is one of the MDA's adaptable parameters. By default, it's set to 0 dBZ. In locations where terrain-induced circulations may cause a high FAR by the algorithm, the user can adjust the Minimum Reflectivity Threshold as needed.

7.4.6.2. Computing Strength Rank (SR). For each Shear Segment identified by the MDA, three attributes are computed.

- The first is the Velocity Difference (ΔV), defined as the difference between the maximum inbound velocity (V_{IN}) and the maximum outbound velocity (V_{OUT}):

$$\Delta V \equiv |V_{IN}| - |V_{OUT}| \quad (7.10)$$

- The second is the Shear (S), defined as the Velocity Difference divided by the length (L) of the Shear Segment. The length is defined as the distance between the inbound and outbound maxima. Shear is defined by:

$$S \equiv \frac{|V_{IN}| - |V_{OUT}|}{L} \quad (7.11)$$

- The last is the maximum Gate-To-Gate Velocity Difference (GTGVD), defined as the greatest *difference* between two adjacent radial velocity range bins within the Shear Segment.

Strength Rank is then computed from these three attributes, using a set of distance-dependent thresholds for each. SR is a non-dimensional number varying from one to 25. Table 7.1 shows sample values applicable within 100 km of the RDA, and the caption describes the method used to compute additional values. The SR of a Shear Segment is the *higher* SR-value computed for (1) the GTGDV and (2) the smaller of the two Strength Ranks computed for both ΔV and S . An SR value of one corresponds to the weakest mesocyclone recognized by the MDA (Stumpf *et al.* 1998). For more details about computing SR, please see Stumpf *et al.* (1998).

Table 7.1: NSSL MDA 2-D Strength Rank Thresholds. These values are applied for Shear Segments within 100 km of the RDA. Between 100 and 200 km, the thresholds decrease linearly for ΔV and GTGVD, and 50 percent for shear. Beyond 200 km, the thresholds remains constant at the decreased value for an additional 200 km. Only the first nine of the 25 Strength Ranks are shown. (Reproduced from Stumpf *et al.* 1998.)

Strength Rank	Velocity Difference (ΔV) and GTGVD [ms ⁻¹]	Shear [ms ⁻¹ /km]
1	10.0	3.00
2	15.0	3.75
3	20.0	4.50
4	25.0	5.25
5	30.0	6.00
6	35.0	6.75
7	40.0	7.50
8	45.0	8.25
9	50.0	9.00

Those Shear Segments that overlap in azimuth, and are separated by one kilometer or less, are combined into a common 2-D Shear Feature. If there are fewer than four Shear Segments in the 2-D Feature, or if the feature extends less than one km in the radial direction (to force a 1-km minimum diameter), the feature is dropped. Features more than 12 km ARL, or whose two-dimensional aspect ratio (radius divided by circumference) is greater than two are also discarded. If a feature is kept, the SR's for all segments in the 2-D Feature are compared, and an overall SR for the feature is computed (Stumpf *et al.* 1998).

Next, several attributes are computed for each 2-D Shear Feature, including:

- Number of 1-D Shear Segments
- Centroid location
- Centroid elevation above radar level
- Diameter
- Shear
- Maximum GTGDV for all Shear Segments
- Aspect ratio (as described above)
- 2-D Strength Rank
- Minimum and maximum azimuth
- Minimum and maximum range

- Tilt angle, and
- Rotational velocity (V_{ROT}), defined by:

$$V_{ROT} \equiv \frac{|V_{max}| + |V_{min}|}{2} \quad (7.13)$$

where V_{max} and V_{min} are the maximum outbound velocity and the maximum inbound velocity, respectively (Stumpf *et al.* 1998).

The azimuth and range of the 2-D Feature's centroid are defined as the point midway between the velocity range bins containing V_{max} and V_{min} . The diameter (D) of the feature is defined as the distance between V_{max} and V_{min} . The shear for the feature is calculated using $S = V_{ROT} / D$, and the GTGVD of the feature is the largest GTGVD for all the Shear Segments in the 2-D Feature. These values, and the method for SR described above, are then used to compute a 2-D SR for the Feature (Stumpf *et al.* 1998).

7.4.6.3. Processing for multiple elevation angles. The next step is to correlate 2-D Features into 3-D Features. The MDA goes through a complex process of vertically matching 2-D Shear Features, sorting them by strength, and allowing for variations in beam propagation with distance from the RDA. A 3-D Feature is identified when two or more 2-D Features are vertically correlated on adjacent tilt angles. At distances of more than 175 km from the RDA, a single 2-D Shear Feature can be identified as a 3-D Feature, under the right conditions. Stumpf *et al.* (1998) spells out this process in detail.

Once a 3-D Feature is identified, the MDA computes its attributes, including:

- Center location, using an average of all 2-D centroids below 6 km.
- Center location of the 2-D Feature on the lowest tilt angle.
- Two diameters: One for lowest-altitude 2-D Feature, and the maximum diameter of all 2-D Features below 12 km.
- Two values of V_{ROT} : Lowest-altitude and maximum.
- Two values of shear: Lowest-altitude and maximum.
- Two values of GTGVD: Lowest altitude and maximum.
- Heights of the maximum diameter, maximum rotational velocity, maximum shear, and maximum GTGVD.
- Base: Height ARL of lowest-altitude 2-D Feature.
- Top: Height ARL of highest-altitude 2-D Feature.

- Depth: Calculated by adding the half-power beamwidth to both the top and the base of the 3-D Feature¹⁷.
- Storm relative depth: Defined as the percentage of the depth of the storm *cell*, as provided by either the SCIT¹⁸ or sounding data.

Values of low-level (0–2 km ARL) and mid-level (2–4 km ARL) convergence are also calculated for each 3-D Feature, by averaging the Convergence Vector velocity differences for all the 2-D Shear Features within the two layers (Stumpf *et al.* 1998).

Another Strength Rank, called the Mesocyclone Strength Index (MSI) is assigned to each 3-D Feature, by vertically-integrating the Strength Ranks of its constituent 2-D Shear Features (weighted by air density), and multiplying by 1000. The integration is computed from the base of the 3-D Feature to its top (or 8 km, whichever is lower). The MSI is then divided by the total depth of the 3-D Feature. Like the Strength Ranks of the individual 2-D Shear Features, the scale of the MSI varies from one to 25.

7.4.6.4. Classification of 3-D Features. Once the MSI is computed, all 3-D Features in the volume scan are tested and classified using the following set of rules (Stumpf *et al.* 1998):

1. 3-D Feature has a continuous half-beamwidth depth of at least three km.
2. 3-D Feature has base at or below five km ARL.
3. All 2-D Shear Features within the 3-D Feature meet the strength thresholds listed in Table 7.1.
4. 3-D Feature is detected during at least two consecutive volume scans (usually at five or six minute intervals).

The first three conditions are satisfied only if the 3-D Strength Rank is greater than or equal to five. Based on these, the following naming conventions are applied:

- If a 3-D Feature has a 3-D Strength Rank ≥ 5 , and it *can* be correlated with a 3-D Feature from the previous volume scan (process described below) scan, then it is classified as a mesocyclone (MESO).
- If a 3-D Feature has a 3-D Strength Rank ≥ 5 , but it *cannot* be correlated with any 3-D Feature from the previous volume scan, it is classified as a couplet (CPLT).

¹⁷ See Chapter 3, Figure 3.5.

¹⁸ See Storm Cell Centroid Subfunction, and definition of Cell Top and Base, above.

- If the 3-D Strength Rank of the 3-D Feature is < 5 , then it is classified as a circulation (CIRC).

7.4.6.5. Feature Tracking. In a manner similar to the SCIT, the MDA attempts to track 3-D Features from one volume scan to the next, and project future positions. At the end of volume scan, all 3-D Features are assigned an extrapolated position for later scans. This is done by a least-squares linear fit to up to 10 of its previously known positions, or by a default motion vector (if the feature is new)¹⁹. The MDA searches the database of 3-D Features from the current scan for a match to the projected position of a known 3-D Feature from previous volume scans. The search continues until the height of the beam centerline is three km above the previously identified base of the feature.

If *no* match is found, the feature is dropped. If there *is* a match, its new position is added to the list of its previously known positions. The total number of known positions is also saved for future diagnostic purposes. The latest ten positions are then used to recompute up to six future extrapolated positions, in five-minute intervals (for a total forecast period of up to 30 minutes). There may be fewer than ten past position fixes for a given feature. In this case, the total number of projected future positions will be smaller. The number of projected positions will never exceed the number of past known positions.

7.4.6.6. MDA Output. The algorithm creates two basic types of output product, both of which can be used as an overlay on volume scan displays. The stats on each 3-D Feature tracked by the algorithm are also fed into SCAN.

The first type of output is tabular, which includes information on the top 15 features tracked by the algorithm. The second type is graphical, which includes a symbol to indicate the current location of the feature and indications of its past and predicted future positions. Figure 7.27 shows an example. The three types of icons used to indicate the present position of the feature are:

- Thin yellow circle, used for features with an MSI of less than five.
- Thick yellow circle, used for features with an MSI of five or more.

¹⁹ The default motion is an average of all the motion vectors from other mesocyclones identified by the MDA. If there are no other mesocyclones, a user-defined value is used.

- Thick yellow circle with spikes, if the feature has an MSI of 5 or more at the lowest elevation angle, or has a base below 1 km ARL.

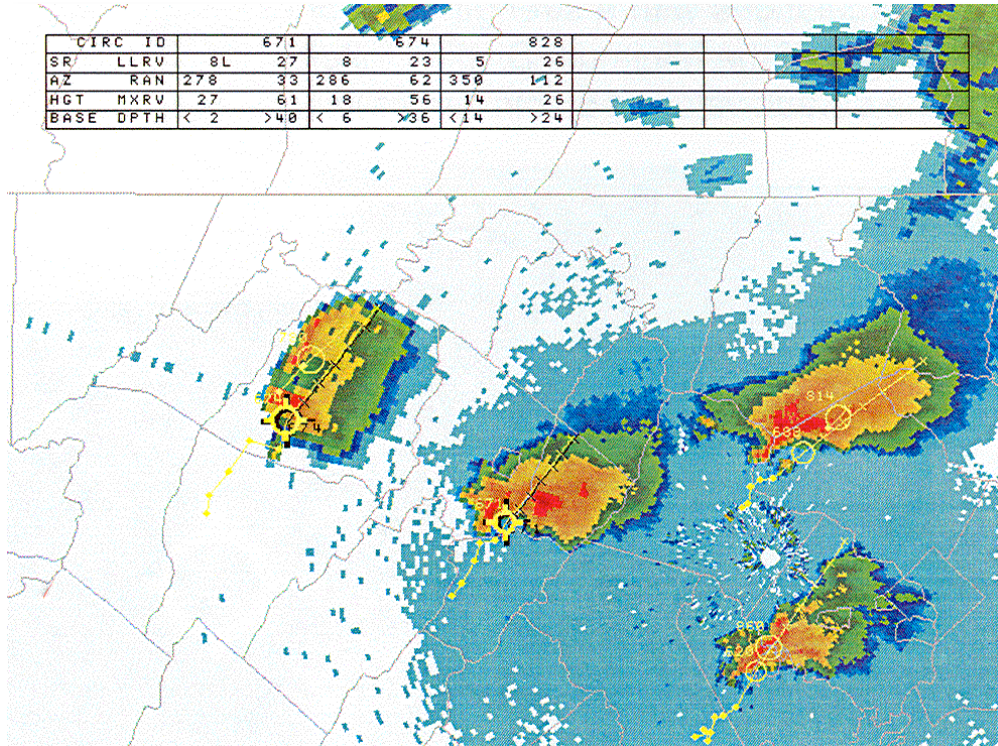


Fig. 7.27: MDA graphical output with attributes table. (Credit: WDTB 2005.)

7.4.6.7. Summing up the MDA. The algorithm is biased to search only for cyclonic rotation. It is known that about five percent of tornadic thunderstorms in the United States rotate in the opposite direction²⁰, and the algorithm will not identify these. It is also subject to errors imposed by range folding and incorrect velocity dealiasing, as are all other products based on radial velocity. Finally, the entire point of the algorithm is to detect the rotating mesocyclones that ultimately give rise to tornado-scale rotations, but not all tornadoes are associated with pre-existing mesocyclones, and not all mesocyclones cause tornadoes.

Despite these limitations, the MDA is extremely useful in provisionally identifying and tracking potentially-dangerous thunderstorms. It has some adaptable parameters that can be adjusted for local variations. There is also a “rapid update”

²⁰ This is because of the relative weakness of the Coriolis force at the scale of a storm cell.

feature, called the MDA Rapid Update (MRU)²¹, that provisionally updates features after each tilt angle. While it's never a good idea to let a computer algorithm do one's thinking, forecasters should carefully examine 3-D Features flagged by the algorithm before making any decisions about issuing a warning.

7.4.7. Tornado Detection Algorithm (TDA). In 1973, Brown, Lemon, and Burgess at NOAA analyzed radar information recorded when a tornado struck Union City, Oklahoma. They noted the presence of what has come to be called a “velocity couplet,” that is, very strong inbound and outbound radial velocities in close proximity, which they recognized as the signature of a tornadic vortex (Lubchenco and Hayes 2012). The TDA is designed to identify these intense micro-scale vortices associated with tornadoes. It operates independently from the MDA. When the TDA replaced an older (“legacy”) algorithm that performed the same task, it was initially tested with a dataset consisting of 31 tornadoes, and scored a POD of 43 percent, a FAR of 48 percent, and a Critical Success Index (CSI) of 31 percent²². These values are relatively low (although they represent a significant improvement over the legacy TVS-detection algorithm) because of the very small scale of a typical tornadic vortex, relative to the width of a radar beam. The inbound and outbound maxima associated with the tornado may be as close as one half a degree of azimuth apart, making the vortex narrower than the 1.4°-wide²³ radar beam (Brown and Wood 2012; Mitchell *et al.* 1998).

The NSSL describes a tornadic vortex as “an intense Gate-to-Gate Shear,” and has established the following criteria for identifying them with weather radar:

- There is a velocity couplet apparent in Level II base radial velocity data, consisting of a strong inbound and a strong outbound max in close proximity. Figure 7.28 shows a velocity couplet (using SRM for clarity), associated with a tornado near Dickens, Texas, in the spring of 2016.

²¹ See U.S. National Weather Service sources, such as the periodic “Build Training” documents, issued when updates WSR-88D software updates are brought on-line. These are easily found with a quick internet search.

²² See Appendix 2 for a discussion of POD, FAR, and CSI.

²³ This is the angular distance between the 50-percent power points.

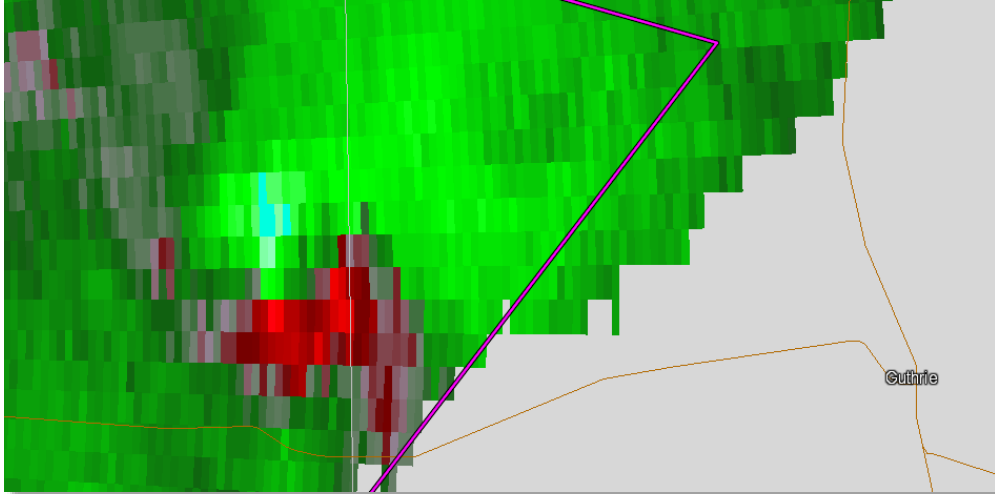


Fig. 7.28: Velocity couplet associated with a tornado, observed by the Lubbock, Texas WSR-88D, in April of 2016. Inbounds are in bright green; outbounds in dark red. The Lubbock RDA is beyond the left margin of the display. (Credit: NWS 2016.)

- Its associated Gate-to-Gate Shear (defined below) is ≥ 90 knots (about 46 ms^{-1}) if the couplet is within 30 nautical miles (about 56 km) of the RDA, and ≥ 70 knots (about 36 ms^{-1}) if the couplet is between 30 and 55 nautical miles (about 102 km) of the RDA. The lower threshold is defined for greater distances because of the loss of resolution as the beam spreads. By default, the TDA does not operate beyond 55 nautical miles.
- Gate-to-Gate Shear is defined by:

$$V_{GTG} \equiv |V_{IN}| + |V_{OUT}| \quad (7.14)$$

where V_{IN} is the inbound max, and V_{OUT} is the outbound max in the couplet.

7.4.7.1. Processing for one, two, and three dimensions. Like the MDA, the TDA sequentially processes data for single and multiple tilts. It searches for one-dimensional Shear Segments, two-dimensional Features, and three-dimensional Features.

- One-dimensional Shear Segments are identified by locating range bins at the *same* distance and at *immediately adjacent* azimuths that have *increasing* radial velocity, indicating cyclonic (counterclockwise) rotation at a scale smaller than a

mesocyclone. Gate-to-Gate Shear (V_{GTG}) is computed for each pair of adjacent velocity bins.

- Two-dimensional Features are created by combining a minimum of three adjacent 1-D Shear Segments. A symmetry test is applied to the 2-D Feature, that examines the length-to-width aspect ratio. (The default ratio threshold is 4, but can be adjusted.) This is to eliminate other possible causes of intense shear, such as gust fronts, which are usually linear rather than circular. Features that do not pass this test are discarded.
- Three-dimensional Features are located by vertically-correlating at least three 2-D Features (Figure 7.29). In an ideal case, there are no tilt angles without a circulation in between vertically-correlated 2-D circulations. However, a gap of one tilt angle is permitted by the algorithm because of possible errors in base radial velocity, such as improper velocity dealiasing. At the very high velocities associated with tornadoes, velocity dealiasing is often problematic.

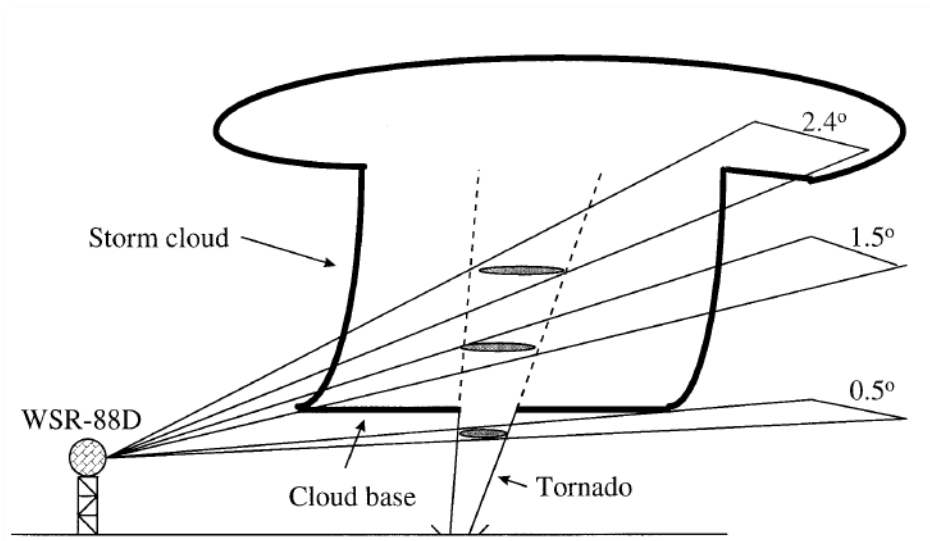


Fig. 7.29: Schematic of a 3-D Feature (dashed and solid cone) composed of three 2-D features. (Reproduced from Mitchell *et al.* 1998.)

7.4.7.2. Classifying 3-D Features. Once a 3-D Feature is identified, and if it meets the threshold values listed in Table 7.2, the TDA classifies it as either a Tornadic Vortex Signature (TVS) or an Elevated TVS (ETVS).

- The feature is classified as a TVS if the base of its rotation is located on the $\frac{1}{2}^\circ$ elevation angle, *or* it is below 600 meters ARL. A TVS is displayed on the TDA's graphical output as a *solid* red, inverted triangle.
- The feature is classified as an ETVS if the base of its rotation is both above the $\frac{1}{2}^\circ$ elevation angle, and it is higher than 600 meters ARL. An ETVS is displayed on the TDA's graphical output as an *open* red, inverted triangle.

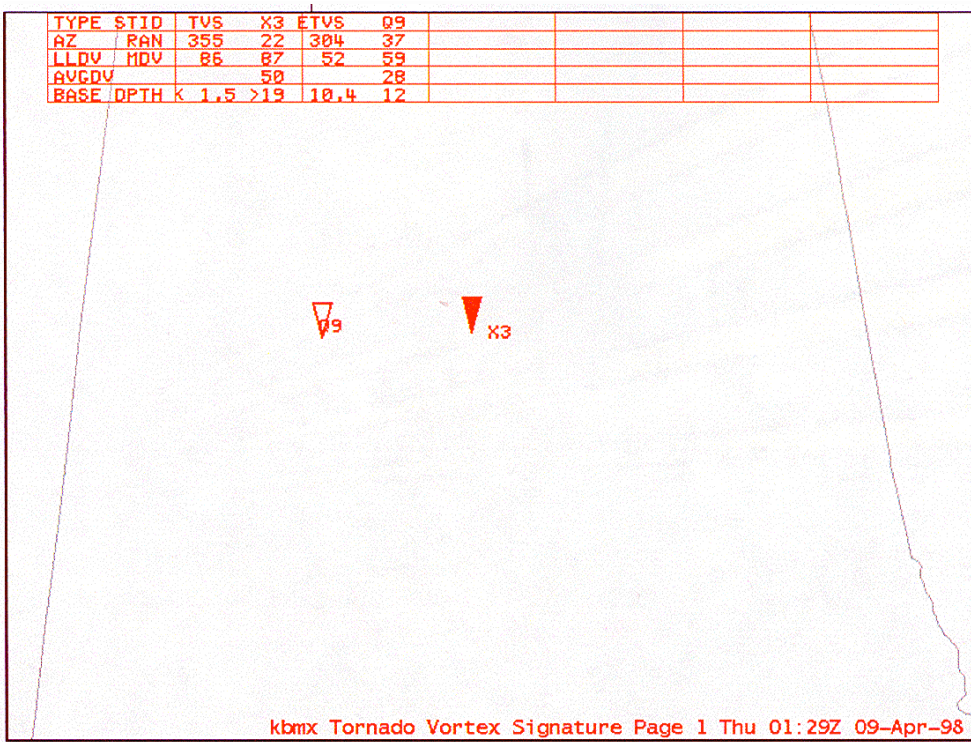


Fig. 7.30: TDA Graphical Output with Attributes Table. TVS features are shown as filled, red triangles; ETVS features are shown as open, red triangles. (Credit: WDTB 2005.)

7.4.7.3. Adaptable parameters. Several of the threshold values the TDA uses to identify a TVS can be adjusted. The default settings are chosen for consistency with Midwestern/Great Plains tornadoes produced by classic supercell thunderstorms, or to ensure the highest possible POD, but can be adjusted to suit local conditions. Table 7.2 summarizes the TDA's adaptable parameters and their associated default settings.

Table 7.2: TDA Adaptable Parameters and Default Settings. (Source: WDTB 2005.)

Parameter	Default Setting
Minimum 3-D Feature depth	1.5 km
Minimum low-level V_{GTG}	25 ms^{-1}
Minimum TVS ²⁴ V_{GTG}	36 ms^{-1}
Minimum reflectivity	0 dBZ
Maximum pattern vector range	55 nautical miles (~100 km)
Maximum number of Elevated TVS (ETVS) displayed	0

In addition to these parameters (also called attributes), a Tornado Strength Index (TSI, analogous to the MSI described above) is computed for each TVS and ETVS in the volume scan, by vertically integrating the altitude-weighted maximum V_{GTG} of each 2-D Feature in the 3-D Feature. Mitchell *et al.* (1998) describe the details of the integration procedure.

7.4.7.4. Output. The TDA outputs a graphical product that can be used as an overlay on a volume display, as well as an attributes table. Figure 7.30 shows an example.

7.4.7.5. Summing up the TDA. The WSR-88D's tornado detection system has an important built in bias, similar to the bias in the MDA: It searches only for cyclonically-rotating TVS's. This is usually, but not always, a reasonable bias. There are a small number of tornadoes that rotate in the opposite direction, and these will not be detected by the algorithm. The TDA also has a relatively high FAR, especially near thunderstorm squall lines. And because the TDA was designed to function in the conditions found in the American Midwest and Great Plains, there is also a high FAR in tropical regions, where its underlying assumptions aren't valid.

Like the MDA, the TDA has a rapid update system called the TDA Rapid Update (TRU), which also includes logic for tracking TVSs and ETVSs and estimating trends in their strength.

- The TRU algorithm generates a provisional update of the location of a feature after each tilt angle, rather than waiting until the entire CD volume scan is complete. This provides an update as often as once every 30 seconds.

²⁴ Somewhere in the 3-D Feature this threshold must be met.

- The TRU uses the average motion of all features identified by the MDA in the previous scan to project future positions of TVSs and ETVSs identified by the TDA (in 5-min intervals).

It attempts to match features in the present scan to previously identified features, as data from each tilt angle arrives, searching along a widening radius from a forecast position for the feature (beginning with 1-km radius from the forecast position). If no match is found, the feature is dropped. If a match is found, the current feature initially inherits the attributes of the previous feature, including its ID (a letter-number combination); type (TVS or ETVS); low-level V_{GTG} , maximum V_{GTG} , and average V_{GTG} ; maximum shear; depth; and the heights of its base and top.

A feature in the present CD volume scan matched to a previously known feature is then trend-tested, by comparing the current values of its strength attributes to their past values. These include the feature type (TVS or ETVS), low-level V_{GTG} , and its depth. If it changes from an ETVS to a TVS²⁵, or either of the other two strength attributes increase, it is marked as “increasing” in the attributes table. If none of them change, it’s marked as “persistent.” Sometimes apparent changes in the attributes of a given feature are not the result of real physical changes in the feature in question, but of sampling issues as the feature moves closer to or farther away from the RDA (Mitchell *et al.* 1998). And additional errors may occur because range folding, improper velocity dealiasing, or erroneous data passed on by the MDA.

This concludes our overview of Level III storm-cell, reflectivity, and radial velocity products. In the next chapter, we discuss radar estimates of precipitation.

Summary. Level III products are derived from Level II base moments, and fall into four basic classes: Storm-cell products, other reflectivity-based products, velocity-based products (and products utilizing both Z and V_r), and precipitation products. This chapter discusses derived products in the first three classes.

Storm-cell products include the output of the Storm-Cell Information and Tracking (SCIT) system, and the Hail Detection Algorithm (HDA). The first automatically identifies, characterizes, and tracks up to 100 convective cells at the same

²⁵ The circulation associated with tornadoes often develops in the middle altitudes of a storm cell, well before the appearance of a tornado or funnel cloud visible from the ground, then descends downward (Mitchell *et al.* 1998). Thus, an ETVS evolving into a TVS would indicate intensification.

time. It computes several parameters describing each, including cell-based Vertically-Integrated Liquid (VIL). It also forecasts the future positions of each cell, in 15-minute intervals, out to one hour in the future. The HDA computes three parameters for each cell identified by the SCIT: The Probability of Hail (POH), Probability of Severe Hail (POSH), and the Maximum Expected Hail Size (MEHS). POH is an estimate of the cell's probability of producing hail of any size, in increments of 10 percent. The POSH is an estimate of the probability that a given cell will produce hailstones one inch or more in diameter, in increments of 10 percent. The MEHS is an estimate of the diameter of the largest hailstone a cell is capable of producing, in increments of ¼ inch.

Other reflectivity-based products include Gridded VIL (GVIL), Digital VIL (DVIL), Reflectivity Cross-Sections (RCS), Composite Reflectivity (CZ), User-Selectable Layer Reflectivity Maximum (ULR), and Enhanced Echo Tops (EET). GVIL and DVIL both use the same equation as cell-based VIL to convert base reflectivity to an estimated amount of liquid water above a unit area of Earth's surface. GVIL was originally created for use by the FAA, as an overlay on air traffic radar displays. It uses a rectangular grid, with a grid-size of 4 x 4 km. DVIL is similar, but uses the same polar-coordinate system as Level II reflectivity, and thus has a finer spatial resolution. Reflectivity Cross-Sections attempt to recreate the functionality in older, manually-operated radar systems that permitted the user to scan vertically along a fixed radial and study storm structure or locate bright bands. The RPG constructs an RCS by accepting a requested cross-section location, drawn in AWIPS, and vertically interpolating (in 500-meter intervals) between the reflectivity recorded in tilts from the most recent volume scan.

CZ is also on a rectangular grid coordinate system, although its spatial resolution varies with distance from the RDA, and is populated with the highest reflectivity above a given grid box on Earth's surface. The user does not know *a priori* how high above the surface the displayed reflectivity was recorded. The Layer Composite Reflectivity Maximum (LRM) is the same as CZ, except that it is divided up into three vertical regions corresponding to different aircraft flight regimes. ULR is also similar to CZ, except that it is on the polar-coordinate system used by Level II reflectivity, and the user can select the upper and lower limits of the product (in 1000-foot intervals) via the AWIPS One Time Request (OTR) process. The EET product identifies the altitude ARL that the reflectivity associated with a given cell (tagged by the SCIT) drops below 18 dBZ, and differs from the "cell top" (output by the SCIT) in that the latter is the height at which the reflectivity drops below 30 dBZ.

Velocity-based products include Storm-Relative Mean Radial Velocity (SRM), Velocity Cross-Sections (VCS), Velocity Azimuth Display (VAD), the VAD Wind Profile

(VWP), and the outputs of the Mesocyclone Detection Algorithm (MDA) and Tornado Detection Algorithm (TDA). SRM subtracts the average translational movement of all cells tagged by the SCIT from the observed radial velocity in each range bin and attempts to compute storm-relative velocities. This tool is useful for identifying rotating thunderstorms. VCSs are similar to RCSs, but are based on Level II base radial velocity rather than base reflectivity. VAD uses up to 360 radial velocities recorded in bins in a circle around the RDA, at a fixed distance (from the RDA) and a fixed elevation, and estimates the full wind vector at that elevation. It assumes the wind field is homogenous within about a 30 km radius around the RDA. VWP combines the VAD products from several different elevations and produces a vertical wind profile. VAD output is also used to produce the Environmental Winds Table.

The MDA and TDA both evaluate radial velocity volume scans and attempt to locate regions of rotation on two different scales. The MDA operates at storm scale, and the TDA operates on a much smaller scale. Both attempt to identify three-dimensional rotational features, and assign Strength Ranks that are dependent on many different variables. Both output a graphical overlay for use with volume scans, as well as tabular output. The MDA tracks 3-D Features from scan to scan, and predicts future positions of mesocyclones in 5-min intervals, out to 30 minutes. Both the MDA and TDA have rapid-update capability. The rapid-update capability associated with the TDA also tracks tornado-scale features, and estimates whether they are increasing in strength or persistent.

Terms and concepts:

- Adaptable parameters
- Air Traffic Control (ATC)
- Bounded Weak Echo Region (BWER)
- Centroid
- Circulation (CIRC)
- Combined Attributes Table (CAT)
- Component
- Composite Reflectivity (CZ)
- Convergence Vector
- Couplet (CPLT)
- Critical Success Index (CSI)
- Elevated Tornadoic Vortex Signature (ETVS)
- Enhanced Echo Tops (EET)

- Environmental Winds Table (EWT)
- False Alarm Rate (FAR)
- Feature (3-D)
- Feature tracking
- Feature type
- Gate-To-Gate Shear
- Gate-To-Gate Velocity Difference (GTGVD)
- Hail Detection Algorithm (HDA)
- Hail Kinetic Energy (\dot{E})
- High-Resolution VIL
- Layer Composite Reflectivity Maximum (LRM)
- Maximum Expected Hail Size (MEHS)
- MDA Rapid Update (MRU)
- Mesocyclone (MESO)
- Mesocyclone Detection Algorithm (MDA)
- Mesocyclone Strength Index (MSI)
- Mesoscale Convective System (MCS)
- Minimum Reflectivity Threshold
- National Severe Storms Laboratory (NSSL)
- Probability of Detection (POD)
- Probability of Hail (POH)
- Probability of Severe Hail (POSH)
- Reflectivity Cross-Section (RCS)
- Root-Mean Square Error (RMSE)
- Segment
- Severe Hail
- Severe Hail Index (SHI)
- Shear Feature (2-D)
- Shear Segment
- Storm-Cell Centroid Subfunction (SCCS)
- Storm-Cell Information and Tracking system (SCIT)
- Storm-Cell Segment Subfunction (SCSS)
- Storm-Cell Tracking Subfunction (SCTS)
- Storm Position Forecast Subfunction (SPFS)
- Storm-Relative Mean Relative Velocity (SRM)
- Strength attributes

- Strength Rank (SR)
- Symmetry (Sym)
- TDA Rapid Update (TRU)
- Tornado Detection Algorithm (TDA)
- Tornadic Vortex Signature (TVS)
- User-Selectable Layer Reflectivity Maximum (ULR)
- VAD Slant Range
- VAD Wind Profile (VWP)
- Velocity Azimuth Display (VAD)
- Velocity Cross-Section (VCS)
- Velocity Difference (ΔV)
- Vertically-Integrated Liquid (VIL); Cell-based, gridded (GVIL), and digital (DVIL)
- VIL Density (VILD)
- Warning Threshold (WT)

Study prompts:

1. List the names and describe the functions performed by the SCIT's four subcomponents. Include definitions of *segment*, *component*, and *centroid*. What is VIL, and which subcomponent computes cell-based VIL? How many cells can be identified and tracked?
2. Describe the Hail Detection System, including the names and meanings of the three products it creates.
3. Compare and contrast the three different types of VIL. Include discussion of the appropriate grid coordinate system, if any. What is VIL Density? What are Enhanced Echo Tops?
4. Describe the process for creating a Reflectivity Cross-Section, along with at least two possible uses. Do the same for a Velocity Cross-Section. Why is it necessary to use this process with the WSR-88D, when it was not necessary with older weather radars?
5. Compare and contrast three variations on the Composite Reflectivity product.

6. What is SRM, and how is it generated? What option does the user have for adjusting the output of this algorithm?
7. Describe the process by which the WSR-88D computes VAD and VWP. Be sure to define two parameters computed by VAD, and their physical significance.
8. The WSR-88D has two independently-operating algorithms for identifying tornadic thunderstorms. What are they? What NSSL guidelines do they use? How do the two algorithms differ? How are they similar? What are their respective outputs? If you could improve these using newer radar technology, what would you do?

8. Radar estimates of precipitation.

With contributions from Phil Poyner and Bryan Rand.

This chapter describes WSR-88D precipitation estimates, using both unpolarized and polarized radar data. Both methods are still in place and are being run in parallel. Sources of error are also discussed.

8.1. Level III products fall into four major categories:

- Storm-cell products
- Other reflectivity-based products
- Velocity-based products
- Precipitation products

The previous chapter discussed some of the products in the first three categories. This chapter will go into precipitation products.

8.2. In Chapter 3, we introduced the base moments collected by the WSR-88D, as well as the theoretical bases for reflectivity and rainfall rate. It was demonstrated that the two are both functions of dropsize distribution, but are *different* functions of dropsize distribution, and that there is no one-to-one relationship between them.

We also introduced the idea of a statistically-based Z-R Relationship, which attempts to square this circle by correlating long records of observed reflectivity in a given range bin to the rainfall measured by a precipitation can, located somewhere on the ground in the same range bin. From Chapter 3, we saw that these Z-R Relationships take the general form:

$$Z = \alpha R^\beta$$

where Z is the linear reflectivity (computed from the Probert-Jones Radar Equation), R is the rainfall rate [mm hr⁻¹], and α and β are coefficients to be determined by a least-squares fit. To compute rainfall from a Z-R Relationship, the equation is inverted and solved for R :

$$R = \left(\frac{Z}{\alpha}\right)^{\frac{1}{\beta}} \quad (8.1)$$

This is the form for unpolarized reflectivity, and it produces large errors in rainfall rate estimates. These large errors were the primary motivation for retrofitting the WSR-88D radar network with dual-pol capability.

Since dual-polarization is a relatively recent addition to the WSR-88D network, we will begin by discussing the older Z-R Relationships that were based on ordinary reflectivity. After that we will move on to some of the newer relationships that take advantage of the dual-pol datatypes discussed in Chapter 6.

8.3. Legacy Z-R Relationships based on ordinary reflectivity. In the early days of weather radar, Marshall *et al.* (1947) found a serviceable correlation between radar reflectivity (Z) and rainfall rate (R), in spite of the fact that these two parameters are very different functions. In 1948, Marshall and his colleague Palmer, both of McGill University in Montreal, Quebec, published another paper relating the mass of liquid water in a range bin to its radar reflectivity. From these data, the Marshall-Palmer relationship was developed, stating that:

$$Z = 200R^{1.6} \quad (8.2)$$

where Z and R are in the units discussed above. This relationship was used throughout the earlier WSR-57 network that predated the WSR-88Ds now deployed throughout the United States. While it is no longer the default Z-R Relationship in use, it is retained as one of several options for use during any warm-season stratiform precipitation event (Fournier 1999).

When the WSR-88D system was brought on-line during the 1980s and 1990s, a new Z-R Relationship was put into place with it. The new relationship is given by:

$$Z = 300R^{1.4} \quad (8.3)$$

This was promulgated because of errors inherent in the Marshall-Palmer relationship, which *overestimated* rainfall rates during light precipitation events, and *underestimated* rainfall rates during heavy precipitation events. Research by the U.S. National Weather Service has shown that (8.3) provides improved results over most of the eastern two thirds of the CONUS (Fournier 1999), and Jorgensen and Willis (1982) found that a nearly identical Z-R Relationship worked well for hurricanes. But this relationship is

only one of many available in the WSR-88D system, which can be selected using the RPG Human Control Interface. It is most often used for summer-time deep convection (such as one would expect with large Midwestern and Great Plains thunderstorms) or any non-tropical convection (WDTB 2005).

During tropical and sub-tropical precipitation events, which are associated with large numbers of smaller precipitation droplets, (8.3) underestimates rainfall rates. In this situation, the Rosenfeld (1993) Z-R Relationship can be selected for use in individual WSR-88D installations:

$$Z = 250R^{1.2} \tag{8.4}$$

which has been shown to be more accurate when measured against measurements from precipitation cans (Fournier 1999; Rauber and Nesbitt 2918).

All three of the relationships noted so far are meant for use during liquid precipitation events. During wintertime events with solid precipitation particles, there is a different relationship between the particles (because of the varying shapes and densities of ice crystals) and radar pulses, which in turn alters the relationship between reflectivity and the precipitation *mass* originally specified by Marshall and Palmer (1948). This indicates that different Z-R Relationships are needed when ice crystals are present to relate reflectivity and liquid precipitation equivalent (LPE), also known as snow-water equivalent (SWE). These are often called Z-S relationships (*e.g.* Vasiloff 2001; Rasmussen *et al.* 2003; Campbell *et al.* 2016).

One of these (called “East Cool Season”) takes the form:

$$Z = 130R^{2.0} \tag{8.5}$$

which is used for winter stratiform precipitation east of the Continental Divide (WDTB 2005). Another is:

$$Z = 180R^{2.0} \tag{8.6}$$

which is used by the U.S. National Weather Service in the Great Lakes Region (Campbell *et al.* 2016). For RDAs in the Rockies and west of the Continental Divide, the relation developed by Vasiloff (2001) (sometimes called “West Cool Season”) is given by:

$$Z = 75R^{2.0} \tag{8.7}$$

8.4. Z-R Relationships using dual-pol datatypes. In 2013, the project to retrofit the entire WSR-88D network with dual-polarization capability was completed. The primary motivation for this work was to improve rainfall rate estimates in the CONUS, which were routinely contaminated by bright-banding over most of the volume control area of a given RDA, even in the summertime. (Bright banding occurs when ice crystals fall below the melting level and become coated with an outer layer of liquid water. The resulting highly-reflective particles cause erroneously high rainfall rates to be computed in the legacy Z-R Relationships.)

A paper by Giangrande and Ryzhkov (2008) discusses a method for estimating precipitation rates based on distance from the RDA and a classification of precipitation type, called Polarimetric Echo Classification (PEC). This system spells out several precipitation types to be identified using dual-pol parameters, as well as a few dual-pol-based rainfall rate estimates, based on parameters such as Z_{DR} and K_{DP} . (These datatypes are discussed detail in Chapter 6.)

Radar echoes are classified into several types (Table 8.1) using ordinary reflectivity (Z), Z_{DR} , the Co-Polar Cross-Correlation Coefficient (ρ_{HV}), and a texture parameter $SD(Z)$.

Table 8.1: Radar echo classes (Giangrande and Ryzhkov 2008).

Ground Clutter and Anomalous Propagation	GC/AP
Biological scatterers	BS
Light to moderate rain	RA
Heavy rain	HR
Combined rain and hail	RH
Big drops*	BD
Graupel	GR
Wet snow	WS
Dry snow	DS
Ice crystals	CR

* Commonly observed in updraft areas where sorting of raindrops by size occurs.

Giangrande and Ryzhkov (2008) tested the following rainfall rate relations:

$$R(Z) = (1.7 \times 10^{-2})Z^{0.714} \quad (8.8)$$

$$R(K_{DP}) = (44.0)|K_{DP}|^{0.822} \text{sign}(K_{DP}) \quad (8.9)$$

$$R(Z, Z_{DR}) = (1.42 \times 10^{-2})Z^{0.770}Z_{DR}^{-1.67} \quad (8.10)$$

where Z is ordinary reflectivity [$\text{mm}^6 \text{m}^{-3}$], K_{DP} has units of degrees km^{-1} , Z_{DR} has *linear* (as opposed to logarithmic) units, and R has units of mm hr^{-1} . The first (8.8) is the same as (8.3), which is the standard Z-R Relationship for the WSR-88D, solved for R rather than Z . The second (8.9) depends entirely on K_{DP} . Strong positive values of K_{DP} are associated with larger raindrops that have horizontal dimensions greater than their vertical dimensions. Negative K_{DP} values are associated with hydrometeors larger in the vertical dimension than in the horizontal dimension, such as ice crystals. The vertical bars in (8.9) indicate absolute value. (The function $\text{sign}(K_{DP})$ allows for negative values.) The third (8.10) is similar to a conventional Z-R Relationship, but is weighted to Z_{DR} , which is near zero with small raindrops, and positive with large raindrops. The negative exponent in the Z_{DR} term has the effect of reducing the estimated rainfall rate as Z_{DR} increases – that is, as dropsize increases – which is consistent with the comparison of Z to R shown in Chapter 3. (Given a constant Z , as dropsize increases, R decreases.)

For light and moderate rain (RA), there is no significant difference in the rainfall rates predicted by all three relationships. All three produce similar errors when compared to a tight network of rain gauges. The lowest biases were associated with (8.10), with bias defined as $R_{\text{radar}} - R_{\text{gauge}}$. However, Giangrande and Ryzhkov (2008) report a clear benefit for HR, RH, and BD precipitation events. Both (8.9) and (8.10) showed a clear and comparable reduction in bias, and were both less susceptible to hail contamination than (8.8), which significantly *over*-estimated rainfall rates in the presence of hail. At closer distances, (8.9) produced slightly higher biases and RMS errors than (8.10), but the opposite was true at greater distances from the RDA.

When applied in wet snow (WS) scenarios, (8.8) significantly overestimated rainfall rates, because of the higher reflectivity that occurs when ice crystals are coated with an outer layer of liquid water. A *slight* improvement relative to precipitation gauges occurs when (8.9) and (8.10) are used, but not to the degree that occurs when liquid rain is falling at the surface. Giangrande and Ryzhkov (2008) suggest using a simple linear correction, rather than either of the two polarimetric relationships in this case:

$$R(Z) = (0.6)(1.7 \times 10^{-2})Z^{0.714} \quad (8.11)$$

Five types of precipitation may occur above the melting layer: DS, CR, GR, BD, and RH. DS and CR represent the majority of precipitation types associated with low

reflectivity. Discrimination between these two types can be made using the magnitudes of Z and Z_{DR} . GR and RH are relatively highly reflective, and can be differentiated using ρ_{HV} . BD represents most of the remaining liquid precipitation above the melting level, and is associated with ρ_{HV} values of more than 0.97.

To compute the rainfall (SWE) rate when DS or CR are present above the melting layer, Giangrande and Ryzhkov (2008) recommend the relation:

$$R(Z) = (2.8)(1.7 \times 10^{-2})Z^{0.714} \quad (8.12)$$

and for GR:

$$R(Z) = (0.8)(1.7 \times 10^{-2})Z^{0.714} \quad (8.13)$$

Defining R_t as the minimal slant range for which the entire volume scan is above the local freezing level, and using the functions for rainfall rate (R) discussed above, Giangrande and Ryzhkov (2008) recommend the methods shown in Table 8.2 for computing R in the RDA's volume scan.

Table 8.2: Recommended methods for computing R (Giangrande and Ryzhkov 2008).

$R = 0$	Non-meteorological targets in range bin
$R = f(8.10)$	Light or moderate rain detected
$R = f(8.10)$	Heavy rain or big drops detected
$R = f(8.9)$	Rain-hail at range $< R_t$
$R = f(8.11)$	Wet snow detected
$R = f(8.13)$	Graupel or rain hail at range $\geq R_t$
$R = f(8.8)$	Dry snow at range $< R_t$
$R = f(8.12)$	Dry snow or ice crystals at $\geq R_t$

8.5. Sources of error in radar estimates of rainfall and SWE. Errors fall into three broad categories: Z -estimate errors, Z - R Relationship errors, and below-beam effects. We will review each of these in somewhat more detail.

8.5.1. Z -estimate errors. Recall that reflectivity is not directly measured, since the dropsize distribution is unknown, but is estimated from returned power (P_r) using the Probert-Jones Radar Equation (3.4). An accurate estimate of reflectivity is, therefore, dependent on an accurate measurement of returned power, the character of the targets

in the range bin, the range of the targets, and other factors. (See Chapter 3.) Errors of this type result from the following causes:

8.5.1.1. **Ground Clutter**, or, power returned from targets on the ground. Some returned power from Ground Clutter usually slips through the Clutter Suppression Algorithm (CSA), which is then mistaken for returned power from meteorological targets. This results in an *over*-estimation of the precipitation rate in the affected range bins.

8.5.1.2. **Anomalous Propagation (AP)**, which results in Ground Clutter at a distance. AP occurs when atmospheric conditions create strong vertical gradients in density, such as when a temperature inversion or a significant vertical variation in atmospheric water vapor content are present. The resulting variation in the Index of Refraction causes the radar beam to bend (refract) in undesirable ways, illuminating targets on the ground at a much greater distance than is usually associated with ordinary Ground Clutter. In extreme cases, “ducting” can occur, wherein the radar beam alternately (and repeatedly) refracts off a temperature inversion and the ground, causing it to travel much greater distances than it normally does. The WSR-88D cannot completely filter out AP-induced returned power, resulting in erroneously high reflectivity values in the affected range bins. Like Ground Clutter, AP results in an *over*-estimation of the rainfall rate in the affected range bins.

8.5.1.3. **Partial beam filling** is a problem that occurs when there are meteorological targets at a great distance from the RDA. At a distance of 100 nautical miles (about 185 kilometers), a one-degree wide beam is 1.745 nautical miles (3.23 kilometers) across. A small rain shower may not fill the entire range bin. The edge of a larger range rain shower may bisect the range bin, filling only part of it. Since the WSR-88D can only process a *single* mean reflectivity value for each range bin, the reflectivity from the precipitation filling part of the range bin will be averaged together with the near-zero reflectivity in the clear part of the bin. This results in a lower overall average reflectivity in the range bin, which produces rainfall rate values that are *too low* in some parts of the bin, and *too high* in other parts.

8.5.1.4. **A wet radome**, during heavy rainfall or when there is partially frozen precipitation covering the outside, can attenuate the transmitted power on the way out from the RDA and the returned power on the way back from a distant target. This means that the radar pulse is reduced in power *twice* as it passes through the

dome. The result is that the distant meteorological target returns less power than it would have if the radome had not been wet, and the rainfall rate of the target is *under-estimated*.

8.5.1.5. **Incorrect hardware calibration.** When originally deployed, the prescribed uncertainty in the reflectivity estimate was set to 1.0 dBZ, which was judged the level of accuracy needed to obtain an operationally acceptable rainfall rate accuracy. The Operational Support Facility (OSF) Engineering Branch developed a method for reflectivity calibration, based on a software tool that compared the reflectivities from neighboring WSR-88D installations that identified specific units requiring attention (Ice *et al.* 2013). Each RDA calibrated itself once each volume scan. If the error estimate reached 1.0 dBZ, a message would be sent indicating that the threshold had been reached. If the error reached 2.0 dBZ, the WSR-88D would send a message stating that maintenance was required.

With dual-pol capability and the new Quantitative Precipitation Estimator (QPE) algorithm in place, Z_{DR} must be estimated to within a much closer accuracy of 0.1 to 0.2 dB (Ryzhkov 2005). For light to moderate rain, the 0.1 dB accuracy limit keeps errors in rainfall rates to 10 percent or less. For heavier rain, the more forgiving 0.2 dB limit is sufficient. If the calibration error exceeds 0.3 dB, the new dual-pol Z-R Relationships do not perform substantially better than the relationships based on ordinary reflectivity (Ice *et al.* 2013).

The primary source of error in Z_{DR} estimates is uncertainty in the contribution to the overall power ratio coming from the radar hardware itself. Research (non-operational) radars are often calibrated using a method that rotates the radar antenna through 360 degrees as it is pointed vertically, and light precipitation is falling (Gorgucci, 1999). Theory assumes that light precipitation droplets falling towards the antenna is spherical (see Chapter 6), so the mean Z_{DR} in a vertical scan should be zero. Any non-zero value of Z_{DR} obtained in this manner would be the result of the radar system's internal bias (Ice *et al.* 2013). Unfortunately the WSR-88D cannot be pointed vertically during normal operations, so this method for operationally calibrating it is not available.

Instead, a procedure for conducting an "engineering method" of determining the bias has been developed by a government contractor, and is used to obtain the bias and update the calibration at each WSR-88D RDA. During operations, the transmitter, antenna, and receiver are tested for bias and recalibrated at different intervals. The receiver bias and overall system bias is recomputed at the end of each volume scan. The transmitter is recalibrated once every eight hours (a procedure requiring about two

minutes), and the antenna is updated about once a month. The objective is to calibrate the dual-pol reflectivity to within the 0.1 dB accuracy limit discussed above (Ice *et al.* 2013).

In 2013, the dual-pol upgrade to the entire WSR-88D network was complete, and the Radar Operations Center (ROC) implemented a process for monitoring the calibration of each installation. It appears that the calibration process is not producing consistent results. Personnel at the ROC have noted that up to 40 percent of the sites have estimated system bias errors exceeding 0.2 dB (Cunningham 2013). This level of error significantly reduces rainfall rate estimate accuracies, and errors in the 0.3 and more range reduce the accuracy to that of the legacy Z-R Relationships. Calibration is an ongoing challenge, and alternative methods are also being tested (Ice *et al.* 2013).

8.5.2. Z-R Relationship errors.

8.5.2.1. Variations in dropsize distribution. While this type of error primarily affects legacy Z-R Relationships, dual-pol-based relationships are not entirely immune. This error arises from the fundamental physical difference between reflectivity and rainfall rate, the first being a function of drop diameter to the sixth power, the second being a function of drop diameter to the third power (multiplied by fall rate). This type of error can result in both *over-* and *under-*estimates of rainfall rate.

8.5.2.2. Mixed precipitation (bright banding). This type of error also has a stronger effect on legacy Z-R Relationships, but, once again, dual-pol relationships are not immune. As ice crystals fall through the melting level, their outer surfaces become coated with liquid water. Partially-melted ice crystals are much more reflective than both (entirely) liquid droplets and frozen ice crystals. The higher reflectivity in the bright band results in misleadingly high precipitation rates (that is, the result is an *over-*estimate).

8.5.3. Below-beam effects.

8.5.3.1. Strong horizontal winds. An implicit assumption in all Z-R Relationships is that precipitation reaching the ground is directly proportional to the precipitation in the volume of space directly above the same point on Earth's surface. In other words, the algorithm assumes that precipitation falls straight down.

This is often untrue in high wind conditions. Precipitation particles imaged by the radar in a range bin above a given place on the surface may be blown into an

entirely different range bin by the wind. This problem can result in both *under-* and *over-*estimates of the rainfall rate, depending on where the radar detects precipitation particles aloft, which way the wind is blowing and how strong it is, and where the rainfall is actually reaching the ground. The errors are greatest with convective showers, separated by areas of open space.

8.5.3.2. Evaporation below radar beam, also known as virga. In this scenario, the radar images precipitation particles aloft, but as the particles fall, they pass through a region of the atmosphere with very low humidity and partially or completely evaporate before reaching the ground. This type of error results in an *over-*estimate of rainfall rate by the radar.

8.5.3.3. Coalescence below radar beam. At large distances from the RDA, the beam on the lowest tilt may be passing through portions of a given storm cell that are well above the highest reflectivity center. This means that non-representative reflectivities and dual-pol products are used to estimate the rainfall rate associated with the storm cell, resulting in an *under-*estimate of the precipitation. While this is most likely to occur in the Tropics, it also occurs in many areas of the CONUS, especially in the summertime.

8.6. WSR-88D rainfall algorithms. There are two separate rainfall rate algorithms currently running in parallel in the WSR-88D system (Figure 8.1). The first of these is the “legacy” system, called the Precipitation Processing System (PPS), which is based on conventional reflectivity and the other base moments. The second is based on dual-pol variables as well as the base moments, and includes the Quantitative Precipitation Estimator (QPE). This parallel condition will continue until the dual-pol has advanced to the point where its estimates are consistently and unambiguously better than the PPS. The two systems are discussed next.

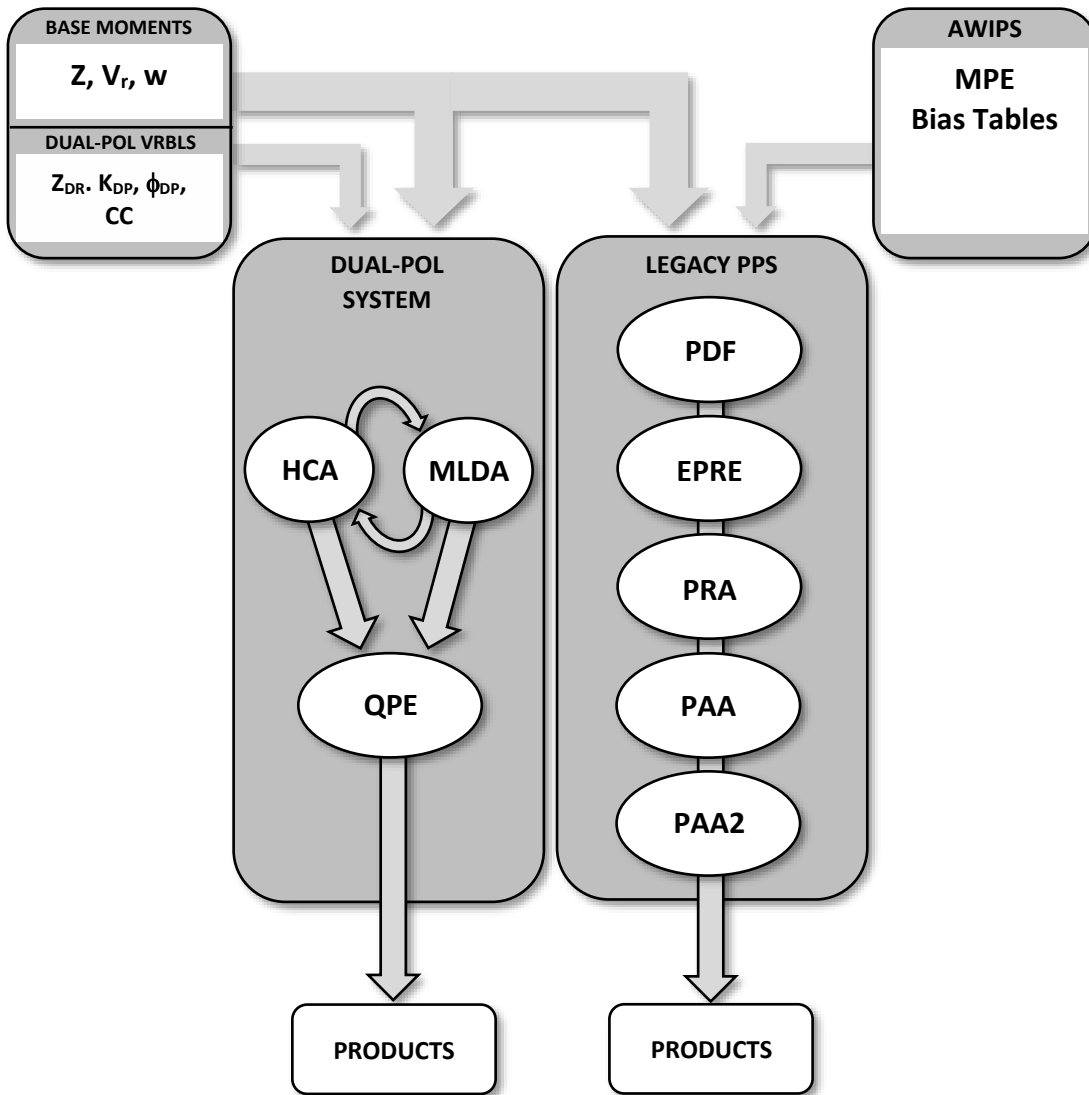


Fig. 8.1: Parallel operation of the PPS (legacy) and dual-pol precipitation systems. Inputs are shown near the top of the diagram; outputs near the bottom. The two systems will continue to operate in parallel for the foreseeable future.

8.6.1. The **Precipitation Processing System (PPS)** is based on ordinary reflectivity, and was last updated in 2004. Rainfall estimates are computed out to a range of 124 nautical miles (239 kilometers), after more than 99 percent of the data have been collected. Rainfall rates are not generated beyond this range because of rapidly increasing errors, resulting from increasing elevation of the lowest tilts above ground level and beam spreading (Fulton *et al.* 1998; WDTB 2005).

8.6.1.1. The **Precipitation Detection Function (PDF)** determines when the WSR-88D automatically switches from clear-air mode to precipitation mode or when the operator may change it from precipitation mode back to clear-air mode. The reason for wanting to do the latter is that there are fewer tilt angles, and the rotation rate of the antenna turntable is slowed, reducing wear and tear on the mechanical components of the system. Clear-air mode consists of VCPs 31 and 32, while precipitation mode uses the remaining Volume Control Patterns. See Chapter 3, Figure 3.6 for details about the available WSR-88D VCPs.

During each volume scan, the PDF compares base reflectivity (Z) on the lowest four tilt angles, within a 124 nautical mile (239-km) radius of the radar, against reflectivity and minimum area thresholds. These are:

- Reflectivity threshold: 20 dBZ, equivalent to rainfall rate of 0.5 mm hr^{-1} , assuming the legacy default Z-R Relationship of $Z = 300R^{1.4}$ (8.3).
- Area threshold: The Minimum Reflectivity Threshold must be met in a minimum area of 80 km^2 .

The PDF then assigns a precipitation category, based on the outcome of this check and the following criteria:

- Category 0: No precipitation exceeding the threshold values.
- Category 1: Significant precipitation, corresponding to at least 30 dBZ, in an area at least as large as the area threshold.
- Category 2: Light precipitation, corresponding to at least 20 dBZ (but less than 30 dBZ), in an area at least as large as the area threshold.

If Category 0 or 2 occurs for at least one hour, and the radar is in precipitation mode, the operator *may* switch the system into clear-air mode. If Category 1 is detected, and the system is in clear-air mode, it *automatically* switches itself into precipitation mode (WDTB 2005).

8.6.1.2. The **Enhanced Precipitation Preprocessor (EPRe)** uses the Radar Echo Classifier (REC) to identify residual clutter or returns from AP, performs the Hybrid Scan, and determines when rainfall accumulations begin and end. The EPRe

also includes a function to define exclusion zones, where a user can define a set of range bins in which residual Ground Clutter or returns from Anomalous Propagation are likely to appear.

The REC uses all three base moments (Z , V_r , and w) and assigns a percentage likelihood that the returns in a given range bin are clutter or AP. Then, starting with the $\frac{1}{2}^\circ$ elevation angle, the Hybrid Scan examines the reflectivity in each range bin and accepts it for precipitation processing if (a) the clutter likelihood (from the REC) is 50 percent or less; (b) the range bin does not fall within an exclusion zone; and (c) the radar beam in the range bin is 50 percent or less beam-blocked (based on a U.S. Geological Survey digital terrain model). Reflectivity in a given range bin that does not meet all three conditions is removed before processing into precipitation data, and the Hybrid Scan checks the corresponding range bin at the next higher elevation. Additional corrections are made for isolated, high-reflectivity, small-area targets, which are deemed to be previously undetected non-meteorological targets (*i.e.* residual clutter), and for Anomalous Propagation. For this reason, a display of reflectivity from the Hybrid Scan is likely to differ from a display of the corresponding Level II base reflectivity (Fulton *et al.* 1998; WDTB 2005).

The output of the Hybrid Scan is then used to determine whether to begin (or continue), or end rainfall accumulations in the volume control area. Rainfall accumulations begin (or continue) when *either* a minimum hybrid reflectivity threshold or minimum area threshold are met. The former is 20 dBZ (corresponding to 0.5 mm hr⁻¹, using the default Z-R Relationship), and the latter is 80 km². After a full hour of *neither* being met, precipitation accumulations end, and are reset to zero in each precipitation range bin (WDTB 2005).

8.6.1.3. The **Precipitation Rate Algorithm (PRA)** accepts reflectivity from the Hybrid Scan, and converts it into rainfall rates using the Z-R Relationship currently active²⁶. Initially, a rainfall rate is computed for each $1^\circ \times 1$ km reflectivity range bin (and recall that these are derived from average returned power in four successive 250 meter range bins). Then, the average rainfall rates in two successive reflectivity bins are averaged together, creating a precipitation range bin, which is $1^\circ \times 2$ km (Figure 8.2). The PRA then applies the Maximum Precipitation Rate Allowed (MPRA) parameter, which caps the maximum rate to 4.09 in hr⁻¹ (103.8 mm hr⁻¹, corresponding to 53 dBZ). The PRA can sometimes initially produce rainfall rates exceeding the MPRA, if hail or bright band contamination is present in the reflectivity volume scan. An additional test

²⁶ The default relationship, shown in (8.3) is usually used. Some tropical locations use the Z-R Relationship shown in (8.4).

is applied that compares the rainfall rate in the current volume scan to the derived rainfall rate from the previous volume scan, in each range bin. If there is a scan-to-scan change in the rainfall rate that exceeds a given threshold, the rainfall rate for the current volume scan is discarded (Fulton *et al.* 1998; WDTB 2005).

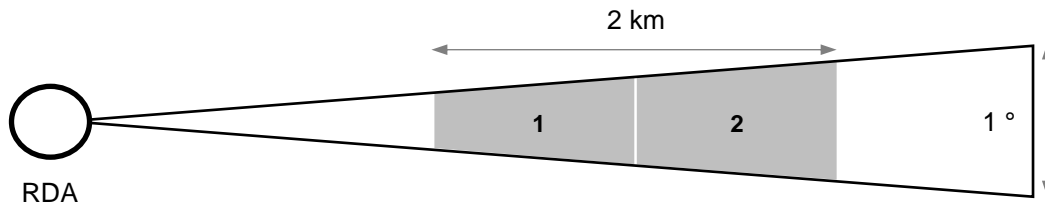


Fig. 8.2: Two successive 1-km reflectivity range bins (along a 1°-wide radial) are combined into a 2-km deep precipitation range bin (plan view).

8.6.1.4. The **Precipitation Accumulation Algorithm (PAA)** takes output from the PRA, and produces scan-to-scan and top-of-the-hour accumulations in each 1° x 2 km range bin as described below. The PAA also performs a quality-control step to remove hourly outliers, removing any hourly accumulation exceeding 400 mm in a given range bin, and replacing it with an average of the hourly accumulations in the eight nearest neighboring range bins (Fulton *et al.* 1998).

- Scan-to-scan accumulations are used to produce the One Hour Precipitation (OHP) and Storm Total Precipitation (STP) products (Figures 8.3 and 8.4). The OHP uses a one-hour wide sliding window to produce an updated product after each volume scan and is available after the first volume scan in which precipitation is detected. It *will not* be created in the event of an outage exceeding 30 minutes in length during the relevant period. The STP represents accumulations in each range since the reflectivity or area thresholds were met in the Hybrid Scan, and *will* be created (but will also be degraded) if there is an outage exceeding 30 minutes. STP is reset to zero after one full hour when no precipitation is detected (WDTB 2005).
- Top-of-the-hour accumulations are used to produce the Three Hour Precipitation (THP) (Figure 8.4) and User Selectable Precipitation (USP) products. The USP shows accumulations in a user-specified series of hours, and is created via a One Time Request in AWIPS. (It can be created using the most recent 30 hours of data, for a total duration of up to 24 hours.) Two thirds of the top-of-the-hour

accumulation totals in the relevant periods are required to produce both the THP and USP products (WDTB 2005).

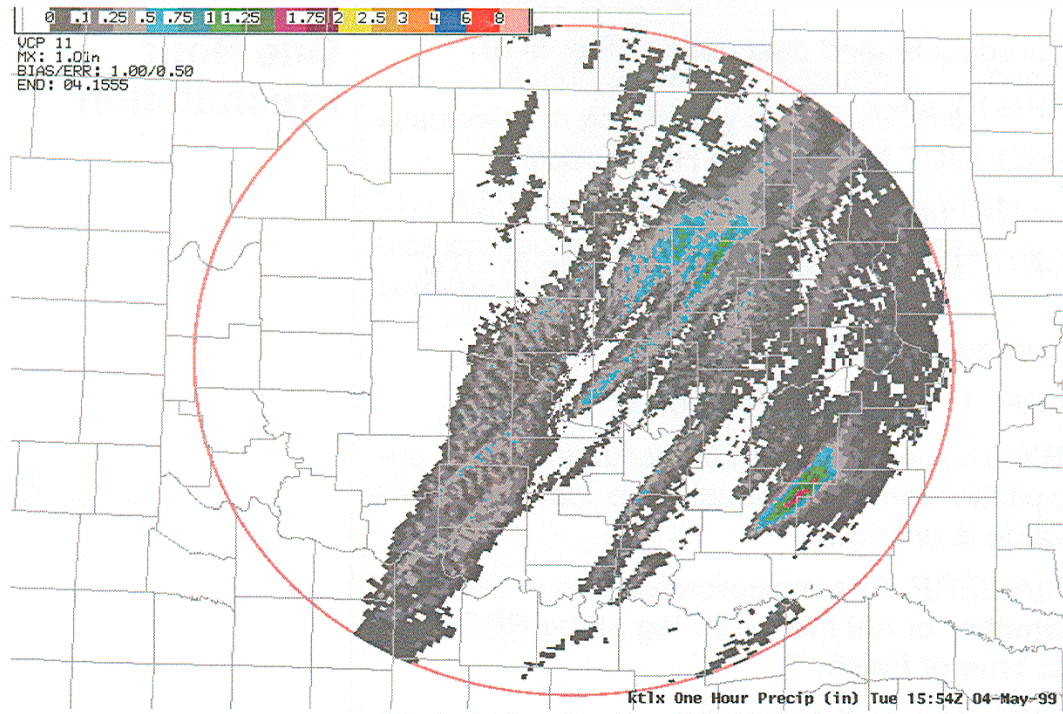


Figure 8.3. One Hour Precipitation. (Credit: WDTB 2005.)

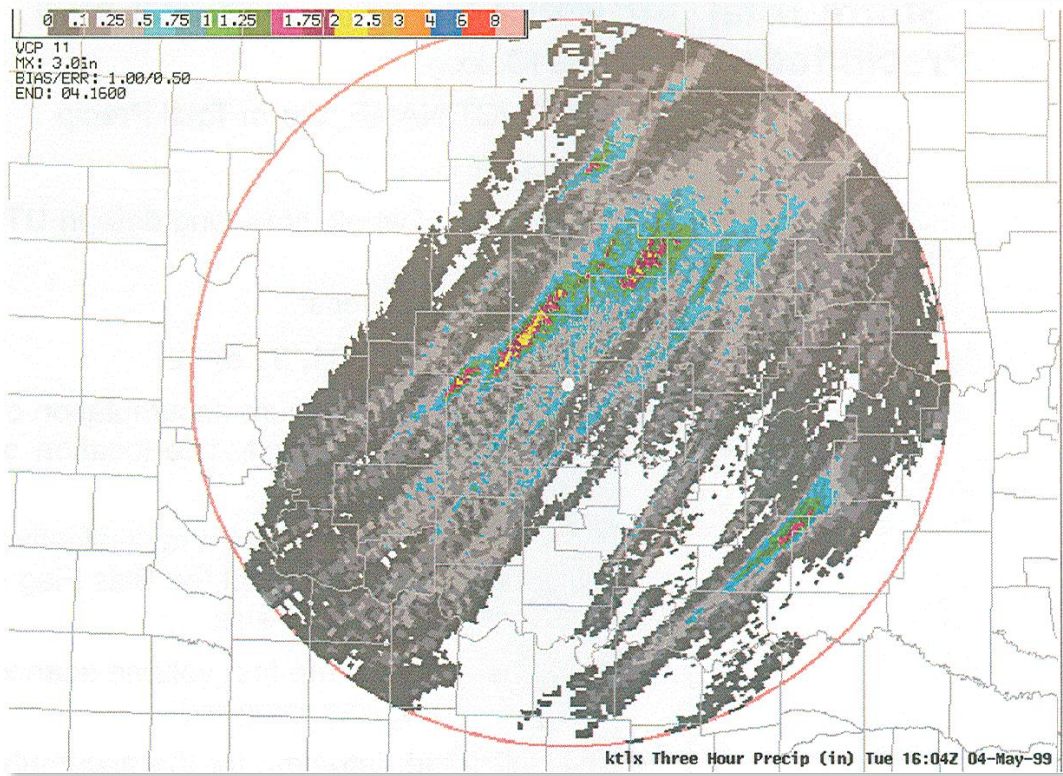


Figure 8.4. Three Hour Precipitation. (Credit: WDTB 2005.)

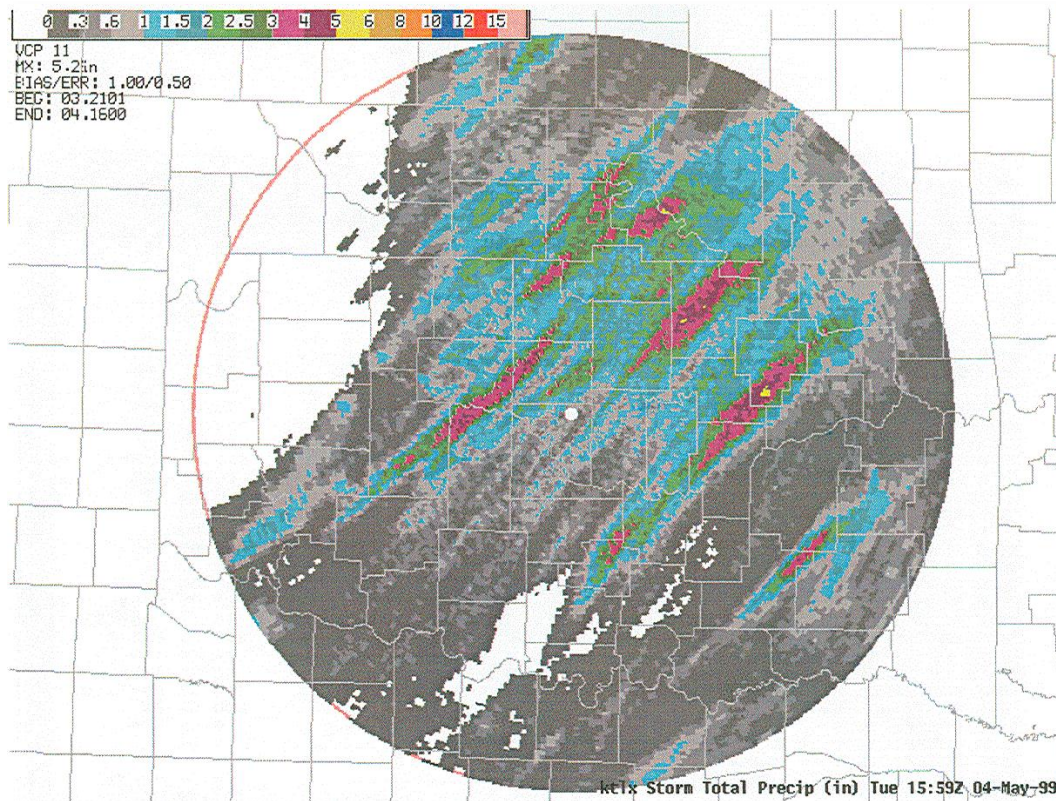


Figure 8.5. Storm Total Precipitation. (Credit: WDTB 2005.)

8.6.1.5. The **Precipitation Adjustment Algorithm (PAA2)** attempts to correct for two errors that have proven difficult: (a) Non-representative Z-R Relationships, and (b) incorrect hardware calibration.

AWIPS generates Bias Tables using an algorithm called the Multisensor Precipitation Estimator (MPE). The MPE ingests rain gauge precipitation measurements from the Automated Surface Observing Systems (ASOS) and Automated Weather Observing Systems (AWOS) within a given WFO's Area of Responsibility (AOR). It then compares the precipitation estimates for a given WSR-88D precipitation range bin to the measurements from the corresponding ASOS/AWOS precipitation rain gauge, and generates a bias number, defined as the difference between the radar estimate and the gauge measurement, converted to an appropriate multiplier. The Bias Table is sent to the WSR-88D RPG at the top of the hour, and can be applied to accumulation totals produced by the PAA. The default setting for the PAA2 is "off," but can be activated at the RPG HCI by a user (WDTB 2005).

8.6.1.7. **Outages** fall into two classes: Those 30 minutes or less in length and those exceeding 30 minutes. The WSR-88D PPS responds to them differently:

- **Radar outages totaling 30 minutes or less:** The PPS uses the average of the derived rainfall rates in a given bin before and after the outage to *interpolate* the rainfall rate during the outage. All precipitation products are created as described above (WDTB 2005).
- **Radar outages total more than 30 minutes:** For the 15 minutes after the beginning of the outage, the last rainfall rate in a given bin is *extrapolated forward*. For the 15 minutes before the end of the outage, the first available rainfall rate in a given bin is *extrapolated backward*. If the “gap” between the 15-minute forward extrapolation and the 15-minute backward extrapolation does *not* exceed six minutes, all precipitation products will be created as already described. If the gap *does* exceed six minutes, the OHP product will not be created, and the THP and USP will not be created until two thirds of the top-of-the-hour accumulations are available. The STP will still be created, but will be degraded (WDTB 2005).

8.6.2. Dual-polarization precipitation processing.

8.6.2.1. The **Hydrometeor Classification Algorithm (HCA)** operates at each elevation angle, and classifies the probable hydrometeor type in the relevant bin into one of twelve classes, shown in Table 8.3. A quick examination of Table 8.2 will show that these types are a very close parallel to those discussed in Giangrande and Ryzhkov (2008).

Table 8.3: Hydrometeor type output by the HCA. (Credit: WDTB 2018).

Class	Hydrometeor Type	Abbreviation
1	No data	ND
2	Biological	BI
3	Ground Clutter	GC
4	Ice crystal	IC
5	Dry snow	DS
6	Wet snow	WS
7	Light or moderate rain	RA
8	Heavy rain	HR
9	Big drops	BD
10	Graupel	GR
11	Hail-rain	HA
12	Unknown	UK

The HCA uses several datatypes as input, including base reflectivity (Z) and base radial velocity (V_r), Differential Reflectivity (Z_{DR}), correlation coefficient (CC), Differential Propagation Phase (ϕ_{DP}), and Specific Differential Phase (K_{DP}). It also ingests two texture parameters, $SD(Z)$ and $SD(\phi_{DP})$, as well as signal-to-noise ratio, and the top and base of the melting layer (which are generated by the Melting Layer Detection Algorithm, discussed below) (WDTB 2018).

Two different methods are used to classify the hydrometeor type. The first involves threshold values of the input variables, and the second uses the location of the relevant range bin with respect to the top and base of the melting layer. After testing all bins using both methods, the probabilities of each hydrometeor type in the bin are assigned. Additional testing is then performed to determine the likelihood that the classification is correct, using the known reliability of each of the input variables. In the event of poor data quality, or when two competing types are equally likely, the type is labeled as unknown (UK). Otherwise, each bin is tagged with a most likely hydrometeor type, corresponding to those shown in Table 8.3 (WDTB 2018).

8.6.2.2. The **Melting Layer Detection Algorithm (MLDA)** identifies the height of the melting layer using the unique signatures of the melting layer in Differential Reflectivity (Z_{DR}) and the Co-Polar Cross-Correlation Coefficient (CC , or ρ_{HV}), which are described in Chapter 6. This height is updated once per volume scan, and can be displayed as an overlay on volume products using the algorithm's Melting Layer (ML) graphical output. Figure 8.6 shows an example (WDTB 2018).



Fig. 8.6: Melting Layer (ML) graphical output shown as an overlay on conventional reflectivity. (Credit: WDTB 2018.)

The MLDA uses several types of data from tilt angles between 4° and 10° above the horizon. These include conventional reflectivity (Z), Differential Reflectivity (Z_{DR}), the correlational coefficient (CC), signal-to-noise ratio, and the output of the Hydrometeor Classification Algorithm (HCA) from the current volume scan. It also ingests the output of the MLDA from previous volume scans²⁷ and the default height of the freezing level from *either* (a) a user-defined height (set at the RPG HCI) *or* (b) RUC-model output (which is rerun once per hour by the National Centers for Environmental Prediction) (WDTB 2018).

The MLDA conducts an automated quality-control procedure that eliminates data contaminated by Ground Clutter or biological echoes, as identified by the HCA. It also eliminates range bins flagged by the HCA with unknown precipitation types, or where the signal-to-noise ratio is less than 5 dB. Once this is completed, the MLDA computes weighted averages of the melting layer top and bottom heights from its input sources, and checks the results against the computed heights from previous volume scans. This entire process can be switched to the “off” position at the RPG HCI, and the MLDA will switch to using the user-selected or RUC-derived solution instead (WDTB 2018).

²⁷ Two previous scans when in precipitation mode, and five when in clear-air mode. For more, see WDTB (2018).

8.2.6.3. The **Quantitative Precipitation Estimator (QPE)** is the new, dual-pol version of the Precipitation Processing System. There is still a considerable amount of work to be done on the QPE, and for the foreseeable future it will run on the RPG in parallel with the PPS. It ingests the output from the MLDA and HCA, along with Z , Z_{DR} , CC and K_{DP} , and generates output products that are very similar to the output products of the PPS. One feature *not* currently available in the QPE is an analog to the gauge-bias adjustment performed by the Precipitation Adjustment Algorithm (PPA2) of the PPS (WDTB 2018).

QPE follows a similar process to the PPS for starting and stopping precipitation accumulations. It begins with the Precipitation Accumulation Initiation Function (PAIF), which is the analog of the PPS's Precipitation Detection Function (PDF). Like the PDF, it has both a minimum area threshold (80 km²) and a rainfall rate threshold (0.5 mm hr⁻¹), which is equivalent to 20 dBZ, assuming the legacy default Z-R Relationship of $Z = 300R^{1.4}$ (see (8.3), above). Both of these are adaptable, using an interface at the RPG HCI (WDTB 2018).

The QPE has definable exclusion zones, where moving Ground Clutter may occur that will not be removed because it falls outside the CSA's notch width. Examples are vehicles on roads and the rotating blades of wind turbines. Exclusion zones can be defined by azimuth, range, and tilt angle using another RPG HCI interface. Both the QPE and PPS respond to defined exclusion zones by using the lowest elevation angle above the exclusion zone to estimate rainfall rates (WDTB 2018).

When computing rainfall rates, the QPE allows data from bins that are 70 percent or less blocked (read from a local terrain file, listing the percentage of beam blockage), as opposed to the 50 percent limit set in the PPS's EPR Hybrid Scan. The higher tolerance is allowed because K_{DP} , one of the parameters used to compute dual-pol rainfall amounts, is not strongly affected by beam blockage. However, if the HCA determines that the "hydrometeor" type is "biologicals" (BI), the rainfall rate is set to zero for that bin, and all range bins that fall directly above it. If the HCA determines that the type is Ground Clutter (GC), the QPE looks at the next elevation angle at the same range and azimuth.

To compute rainfall rates, the QPE uses the three different relationships discussed in Giangrande and Ryzhkov (2008), and shown in (8.8) through (8.13), where Z is ordinary reflectivity [mm⁶ m⁻³], K_{DP} has units of degrees km⁻¹, Z_{DR} has *linear* (as opposed to logarithmic) units, and R has units of mm hr⁻¹. The $R(K_{DP})$ relation allows for negative rainfall rates, but the logic built into the QPE rejects these automatically (WDTB 2018).

The choice of which rainfall rate to use is based on the type of hydrometer identified in the relevant range bin (from the HCA) and the height of the melting layer (from the MLDA). Details of the selection process are discussed in Giangrande and Ryzhkov (2008), and above (Table 8.2). The first, (8.8), is based on ordinary reflectivity, and serves as the default Z-R Relationship in the legacy PPS, but underestimates rainfall when warm rain dominates, and overestimates rainfall for mixed precipitation (because of bright banding). The second, (8.9), based on K_{DP} , is relatively immune to beam blockage. The third, (8.10), is based on both Z and Z_{DR} , and should perform better in stratiform rain scenarios. The remaining relations, (8.11) – (8.13), are all simple adaptations of the legacy Z-R Relationship, and are applied near the melting layer or when hail is present (WDTB 2018).

The QPE is based on work performed in Norman, Oklahoma, and still requires a considerable amount of research to mitigate its known weaknesses. Among these are the impact of non-uniform beam filling, calibration (to which Z_{DR} is very sensitive, discussed in detail above), inaccuracies in the assignment of precipitation type by the HCA, and discontinuities near the top of the melting layer (the result from switching between rainfall rate functions). That said, it is a distinct improvement over the legacy system, because of its improved ability to identify non-meteorological targets (including biologicals and Ground Clutter), and adapt the rainfall rate to different environmental conditions (such as bright banding and hail contamination) (WDTB 2018).

8.2.6.4. Products. Like the PPS, the QPE generates accumulation products for use by hydrologists and other interested parties. Here, we discuss a few of them, focusing on how they are either *similar to* or *different from* the analogous PPS product.

8.2.6.4.1. “Pre-product” product. Both the PPS and the QPE generate a rainfall rate in every range bin during volume scans when the area and rate thresholds are exceeded (80 km² and 0.5 mm hr⁻¹, respectively). Figure 8.7 shows examples of each. They differ in how the rainfall rate is generated for the relevant bin (WDTB 2018).

- The PPS produces the Digital Hybrid Scan Reflectivity (DHR), which is the *reflectivity value* in each range bin (in dBZ), before it is converted to rainfall rate using the operational Z-R Relationship.

- The QPE produces the Digital Precipitation Rate (DPR), which is the *rainfall rate* in each range bin, computed by the appropriate $R(Z)$, $R(Z, Z_{DR})$, or $R(K_{DP})$ relationship (discussed above).

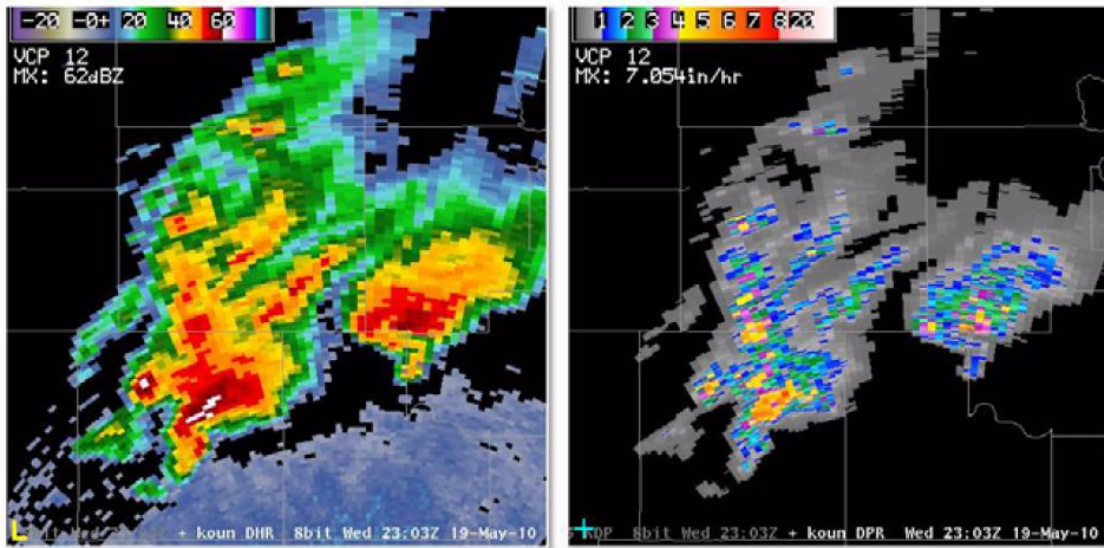


Fig. 8.7: PPS Digital Hybrid Scan Reflectivity (Left), and QPE Digital Precipitation Rate (Right). (Credit: WDTB 2018.)

8.2.6.4.2. One Hour Precipitation. Accumulation begins after the areal and rate thresholds are exceeded, and are updated following each volume scan. The one-hour product becomes available once a full hour has elapsed. In the event of an outage, the QPE’s one-hour product will be available with the second full volume scan after the return to operational status, while the PPS version will not be available for a full hour (WDTB 2018).

8.2.6.4.3. Storm Total Precipitation. Once the reflectivity returns exceed the areal and rate thresholds, accumulation begins. After the reflectivity returns have fallen below and remained below the thresholds for one full hour, accumulations stop, and storm-total accumulations are reset to zero. This is the same as the analogous PPS product (WDTB 2018).

This completes the overview of WSR-88D precipitation estimates, and the WSR-88D in general. In the next chapter, we will discuss a sample of other meteorological radar systems currently in use.

Summary. Precipitation estimates are Level III products. There are currently two sets of precipitation algorithms running in parallel on the WSR-88D RPGs. The first is the “legacy” system, called the Precipitation Processing System (PPS), which is based primarily on unpolarized reflectivity. The second includes the Quantitative Precipitation Estimator (QPE), which primarily uses reflectivity and dual-pol datatypes. Calibrating the WSR-88D hardware (now approaching 30 years of age) to the specifications required to make the QPE more accurate than the PPS has proven to be a challenge, and additional development of the QPE is required to overcome its own internal weaknesses. For these reasons, the PPS and the QPE will continue to run in parallel for the foreseeable future.

The PPS has five components. The first is the Precipitation Detection Function (PDF), which (based on reflectivity and area thresholds) makes decisions about whether the WSR-88D will operate in either precipitation or clear-air mode. Switching to clear-air mode is advantageous when there’s no important precipitation in the volume scan area, because it slows the turntable rotation rate and reduces the number of antenna tilt angles.

The second PPS component is the Enhanced Precipitation Preprocessor (EPRe), which uses the Radar Echo Classifier (REC) to identify regions of residual clutter and beam blocking. The REC uses all three unpolarized base moments. A Hybrid Scan then extracts the improved reflectivity from the volume scan, and makes the decision whether to begin (or continue) or end precipitation accumulations in each range bin. The third component is the Precipitation Rate Algorithm (PRA), which applies the active Z-R Relationship to obtain the rainfall rate in each range bin. (There are several conventional Z-R Relationships to choose from.) It also averages the rate across two reflectivity range bins, and applies a rate limiter called the Maximum Precipitation Rate Allowed (MPRA). The limiter is sometimes needed because of bright-band or hail contamination of the base reflectivity. The fourth component is the Precipitation Accumulation Algorithm (PAA), which tracks rainfall totals in each range bin, and produces output such as the One Hour Precipitation (OHP) and the User Selectable Precipitation (USP) products. The last component is the Precipitation Adjustment Algorithm (PAA2), which applies a rainfall rate correction derived by AWIPS from ASOS and AWOS precipitation cans corresponding to individual radar range bins. This

is done to correct for two errors that have proven difficult to correct: Non-representative Z-R Relationships, and incorrect hardware calibration.

The Quantitative Precipitation Estimator (QPE) is part of the dual-pol precipitation system. The QPE employs a Hydrometeor Classification Algorithm (HCA) to differentiate biological targets and Ground Clutter from precipitation particles. It also uses a complex decision process to determine the *type* of precipitation particles present in each range bin, which may include ice crystals, dry or wet snow, light or moderate rain, heavy rain, giant drops above the freezing level, or graupel. The HCA, in turn, uses the Melting Layer Detection Algorithm (MLDA) to assist with its decision making process. The MLDA is itself a complex algorithm that utilizes many sources of data, including output from the Rapid Update Cycle (RUC) model run at NCEP.

Once the precipitation type has been determined, the QPE applies one of several possible relationships to compute precipitation rate. Some of these use ordinary reflectivity only and are very similar to the Z-R Relationships employed by the PPS. Some use dual-pol variables such as Z_{DR} and K_{DP} . After the precipitation rates have been computed for each range bin, products very similar to those produced by the PPS are output by the system.

There are many sources of error affecting both precipitation estimation systems, which fall into three general classes: Z-estimate errors, Z-R Relationship errors, and below-beam effects. Z-estimate errors include Ground Clutter, Anomalous Propagation, partial beam filling, wet radomes, and incorrect hardware calibration. The latter is an ongoing challenge, and the dual-pol-based precipitation system requires a much finer degree of calibration than the legacy system to be of greater value. Z-R Relationship errors include variations in dropsize distribution (described in Chapter 3) and bright-banding. The dual-pol system was specifically built to cope with both of these sources of error. Below-beam effects include strong horizontal winds (which blows falling precipitation particles into a different range bin), as well as evaporation (producing virga) and coalescence beneath the lowest antenna tilt angle.

Terms and concepts:

- Area of Responsibility (AOR)
- Below-beam effects
- Bright banding
- Clear-air mode
- Digital Hybrid Scan Reflectivity (DHR)

- Digital Precipitation Rate (DPR)
- East Cool Season Z-R Relationship
- Enhanced Precipitation Preprocessor (EPRe)
- Exclusion zone
- Hybrid Scan
- Hydrometeor Classification Algorithm (HCA)
- Marshall-Palmer relationship
- Maximum Precipitation Rate Allowed (MPRA)
- Melting layer
- Melting Layer Detection Algorithm (MLDA)
- Multisensor Precipitation Estimator (MPE)
- One Hour Precipitation (OHP)
- Operational Support Facility (OSF)
- Partial beam filling
- Polarimetric Echo Classification (PEC)
- Precipitation Accumulation Algorithm (PAA)
- Precipitation Adjustment Algorithm (PAA2)
- Precipitation category
- Precipitation Detection Function (PDF)
- Precipitation mode
- Precipitation Processing System (PPS)
- Precipitation Rate Algorithm (PRA)
- Quantitative Precipitation Estimator (QPE)
- Radar Echo Classifier (REC)
- Radar Operations Center (ROC)
- Radar outages: 30 minutes or less; more than 30 minutes
- Rosenfeld Z-R Relationship
- Storm Total Precipitation (STP)
- Three Hour Precipitation (THP)
- User Selectable Precipitation (USP)
- Virga
- West Cool Season Z-R Relationship
- Wet radome
- Z-estimate errors

Study prompts:

1. What is the generic form of a “legacy” Z-R relationship? List and describe the terms of the equation.
2. Discuss the origins and current use of the Marshall-Palmer relationship.
3. Compare and contrast four more legacy WSR-88D Z-R relationships.
4. Describe two new Z-R relationships tested by Giangrande and Ryzhkov (2008).
5. What are three broad categories of errors in Z-R Relationships? List and describe at least two examples of each.
6. Discuss why hardware calibration is even more important to dual-pol Z-R Relationships than it is to conventional Z-R Relationships.
7. Describe the components of the PPS. What is a Hybrid Scan? What is the Radar Echo Classifier, and how does it function? What are the major components of the PPS, and which applies the Z-R Relationship? What is the MPRA? What is the MPE and how does it function?
8. Describe how the PPS copes with radar outages, for outages of 30 minutes or less, and for outages of more than 30 minutes.
9. What is the Hydrometeor Classification Algorithm, and what does it do? What are its inputs? Briefly discuss hydrometeor types output by the HCA.
10. What is the Melting Layer Detection Algorithm, and how does it function?
11. Compare and contrast the PPS and the QPE.

9. More weather radar systems.

With contributions from Jason Cordeira and Paul Johnston.

In this chapter we introduce a few other types of weather radar. Among these are scanning, mobile radar systems primarily for research purposes, upward-directed radar systems for classifying precipitation type, radars built for detecting wind shear, as well as operational networks of weather radars in countries outside the United States.

9.1. This chapter is *not* intended to be a comprehensive overview of all radar systems beyond the WSR-88D network, and *could not be* and still fit into a chapter of reasonable length. Many countries (and consortia of countries) outside the United States run operational weather radar networks²⁸. And there are several well-developed international data sharing agreements to supplement the radar systems in individual countries, many of them coordinated through the World Meteorological Organization (WMO). For example, the Mexican government's Servicio Meteorológico Nacional (SMN) has a small network of radar installations clustered around Mexico City and obtains additional coverage from an installation in Belize and from several WSR-88Ds just north of the U.S.-Mexican border. The Canadian weather service also has a growing network of weather radars.

The primary focus here will be on a few example systems found in North America and Europe. Some are used for research, and some are operational. Specifically, we will discuss:

- Snow Level Radar
- Doppler on Wheels
- Terminal Doppler Weather Radar
- Canadian weather radar
- European weather radar, including systems in Western Europe and in Turkey.

Among those *not* discussed in detail here are **Radar Wind Profilers (RWP)**, which are upwardly-directed systems specialized to derive three-dimensional wind

²⁸ For brief discussions about operational weather radar in Australia, China, Japan, New Zealand, and South Africa, see Rauber and Nesbitt (2018).

components (u, v , and w) in the region directly above the antenna. These are solid-state, phased array systems (see Chapter 10), have vertical resolutions as fine as 40 meters, and vertical ranges of several kilometers. Vaisälä, headquartered in Helsinki, Finland (www.vaisala.com), is one of several companies that manufacture wind profilers. Radar Wind Profilers are often co-located with **Radio-Acoustic Sounding Systems (RASS)**, which use a combination of radio waves and sound pulses to measure the speed of sound at different heights above the instrument. Since the speed of sound in air is related to density, the vertical virtual temperature profile can be estimated by the device via the Ideal Gas Law (*e.g.* Miller 2015). Typically, these devices have a vertical resolution of 5-10 meters, and a maximum range on the order of one km. Scintec, with headquarters in both Germany and Colorado (<http://www.scintec.com/english/web/Scintec/>), is one company that manufactures RASS devices.

A closely-related technology is **LIDAR**, which uses pulses of laser light (rather than microwave EMR) to measure aerosols in the atmosphere. One type of LIDAR is called a **Doppler Wind Lidar (DWL)**, and, like a RWP, it measures three-dimensional wind components in several range gates. DWLs may be ground- or aircraft-based, and research is currently underway into the efficacy of mounting these systems on satellites for global wind measurements beneath the satellite track (*e.g.* Tucker *et al.* 2018; Baider *et al.* 2018). Another type of LIDAR is called a **laser ceilometer**, which is used for detecting the heights of cloud bases at airport weather stations. There are several companies that manufacture LIDAR systems.

Another closely-related technology is **SODAR**, which uses pulses of *sound*, rather than EMR. SODAR systems, such as the Scintec SFAS and XFAS, measure three-dimensional wind components in up to 256 range gates above the emitter, with a resolution as fine as five meters, and a maximum height of two km.

Radar has become a mainstream technology, and is no longer confined to high-end government-funded endeavors. There are many private companies that manufacture weather radars in both C- and X-bands, although most S-band systems (larger and more expensive) are still largely built to government specifications. For example, EWR Radar Systems, in St. Louis, Missouri (www.ewradar.com), builds several models of compact C- and X-band systems with both Doppler and dual-pol capability. So does Foruno, a company based in Japan (www.foruno.com). These systems are usually highly automated and rugged enough for field operations.

9.2. NOAA Snow Level Radar (SLR). The NOAA Earth System Research Laboratory's (ESRL) mission is to study a range of physical, chemical, and biological processes over a broad range of spatial and temporal scales. To this end, the ESRL's Physical Sciences

Division (PSD) has constructed a network of portable, upward-pointing radar installations to detect the altitude at which falling snow melts, becoming rain. This parameter (the melting level) is critical to understanding runoff in mountainous areas. When the snow level is higher than most of the terrain, a storm moving through the region is likely to produce rapid runoff, producing flooding. If the snow level is lower than the tops of the terrain, the precipitation will fall as snow, increasing snowpack, and providing a valuable source of fresh water for the warm season (NOAA 2016).

A snow-level radar (SLR) is an S-band (see Chapter 2, Table 2.2), vertically pointing continuous-wave Doppler radar. It does *not* operate in the same transmit-listen mode as the WSR-88D. It transmits at a wavelength of 10 cm, which corresponds to a frequency of 2.835 GHz (White *et al.* 2000; Johnston *et al.* 2016). It detects the melting layer using an algorithm, described in White *et al.* (2002), which measures the vertical differential of the range-corrected signal-to-noise ratio and Doppler *vertical* velocity. The average transmitted power is between one and 12 Watts (depending on the model; this is much lower than the WSR-88D's average transmitted power of about one kW). Its maximum vertical range is 10.3 km (much lower than the WSR's horizontal range of more than 460 km), and its vertical resolution is 30 meters (much finer than the WSR's horizontal resolution of 250 meters).

Radar engineers at the University of Colorado's Cooperative Institute for Research in Environmental Sciences (CIRES) and ESRL's PSD constructed these low-cost, low-power vertically-pointing systems following earlier work involving lower frequency, pulsed radar installations. Since then, SLRs have been used in a number of field campaigns and studies, including Hydrometeorological Testbed - West, CalWater, CalWater 2, and Hydrometeorological Testbed - Southeast Pilot Study (HMT-SEPS), among others (White *et al.* 2013; Ralph *et al.* 2016). NOAA maintains a network of ten of these radars in California in collaboration with the California Department of Water Resources, to "provide 21st Century observing systems to help address water resource and flood control issues" and are "part of an unprecedented observing network that will provide critical information on the forcings of extreme precipitation and flooding, as well as long-term climate observations to help decision makers adapt to a changing climate" (NOAA 2016).

Following the HMT-SEPS (which ran from June 2013 to October 2014), a SLR was relocated from Hankins, North Carolina to the Plymouth State University (PSU) campus in Plymouth, New Hampshire (PMH) for an experimental deployment (Figure 9.1). It remained at Plymouth State for approximately three years, and was used to study mixed-phase precipitation, freezing rain, aspects of the Planetary Boundary Layer (PBL), and bird migrations. Some of this work is discussed below.



Fig. 9.1: SLR deployment at Plymouth State University, in Plymouth, New Hampshire. The campus is located along the Pemigewasset River in the Merrimack River watershed (shaded yellow in map at left). The SLR is accompanied by a 2-m surface meteorological observing tower (not shown). (Map created using USGS data; adapted from Karl Musser at <https://commons.wikimedia.org/wiki/File%3AMerrimackrivermap.png>, which is licensed under the Creative Commons Attribution-Share Alike 2.5 Generic license. Photo credit: Paul Johnston.)

9.2.1. Observations of mixed-phase precipitation using the SLR. Mixed-phase precipitation events over New England often occur with winter storms, as advancing warm air aloft changes the characteristics of the temperature profile and the precipitation type of hydrometeors reaching the ground. The reflectivity with these hydrometeors increases as ice crystals become rimed and/or begin to melt, forming a bright band before accelerating toward the ground as raindrops²⁹. Observations and theoretical estimates indicate that expected hydrometeor fall speeds (depending on size) for ice crystals are 0.5–1.0 m s⁻¹, rain drops are generally between 4.0 and 9.0 m s⁻¹, and mixed-phase precipitation (*e.g.*, wet snow, sleet or rimed ice crystals) are generally between the two latter values (Gunn and Kinzer 1949; Foote and DeToit 1969; Morsi and Alexander 1972; Beard 1976; Bohm 1989)³⁰.

The first mixed-phase precipitation event observed by the PMH SLR occurred on 9 – 10 December 2014. A weak surface low pressure system over the mid-Atlantic (Figure 9.2a) and warm air advection over central New England resulted in precipitation (Figure 9.2b) in the form of light snow, snow mixed with sleet (ice pellets),

²⁹ Bright banding is discussed in much greater detail in Chapters 6, 7 and 8.

³⁰ See also Chapter 3, Table 3.3.

and rain from 0700 UTC 9 December 2014 to 1100 UTC 10 December 2014. These times were recorded by the AWOS located at the Plymouth Municipal Airport (K1P1; elevation 153 m MSL, and about 8 km from the location of the SLR).

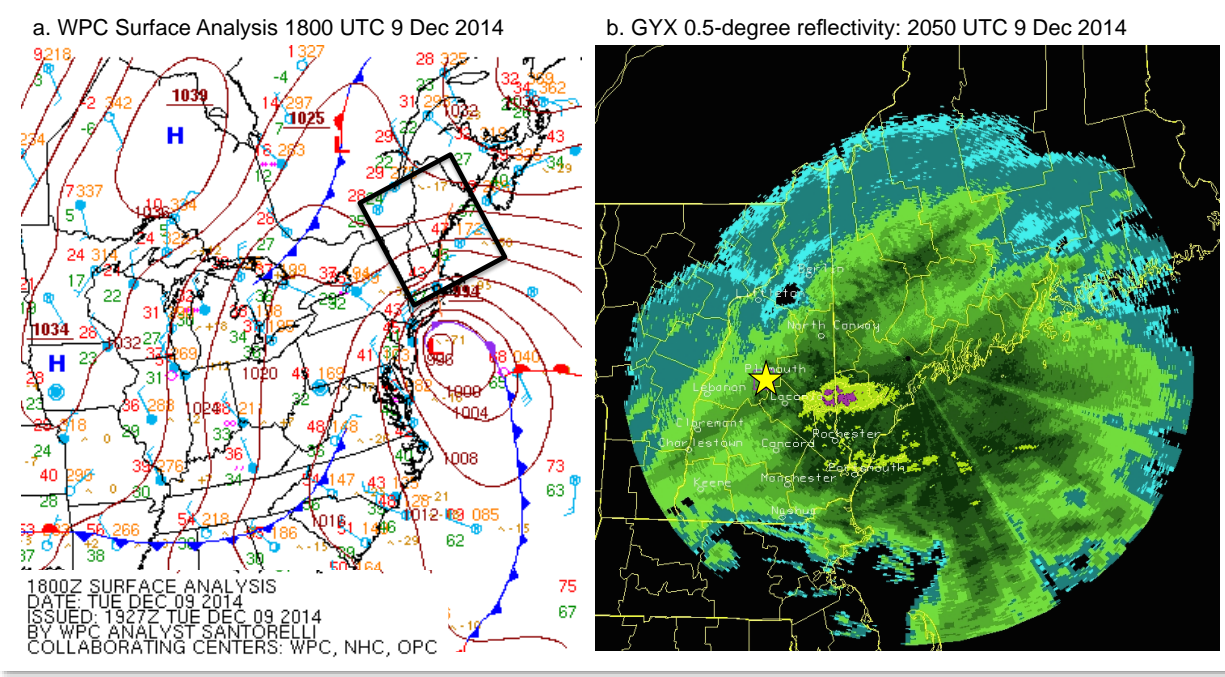


Fig. 9.2: (a) Surface observations and frontal analysis valid at 1800 UTC 9 December 2014 adapted from imagery provided by the Weather Prediction Center, and (b) 0.5-degree reflectivity (dBZ; shaded) from the WSR-88D in Gray, Maine (KGYX; image provided by <http://vortex.plymouth.edu>.) The black square in (a) represents the domain in (b).

Initial precipitation occurred as light snow and snow mixed with sleet, falling from a cloud layer below ~2 km AGL between 0700 and 1100 UTC 9 December 2014, per the K1P1 AWPS and the 1200 UTC KGYX radiosonde observations (not shown). These light snow observations were confirmed by PMH SLR precipitation fall velocities of ~1 m s⁻¹ below 2 km AGL (Figure 9.3) and accompanying surface temperature observations between -3°C and -5°C (not shown). Precipitation resumed from a deeper cloud layer (>6 km) and progressed from light snow and sleet to rain during 1300–2000 UTC 9 December 2014 (per K1P1), as surface air temperatures warmed above 0°C between 1615 and 1715 UTC (Figure 9.3). The PMH SLR detected precipitation fall velocities that increased over time, and with decreasing altitude, from ~1 m s⁻¹ to >4–5 m s⁻¹, confirming the presence of mixed-phase precipitation trending toward rain.

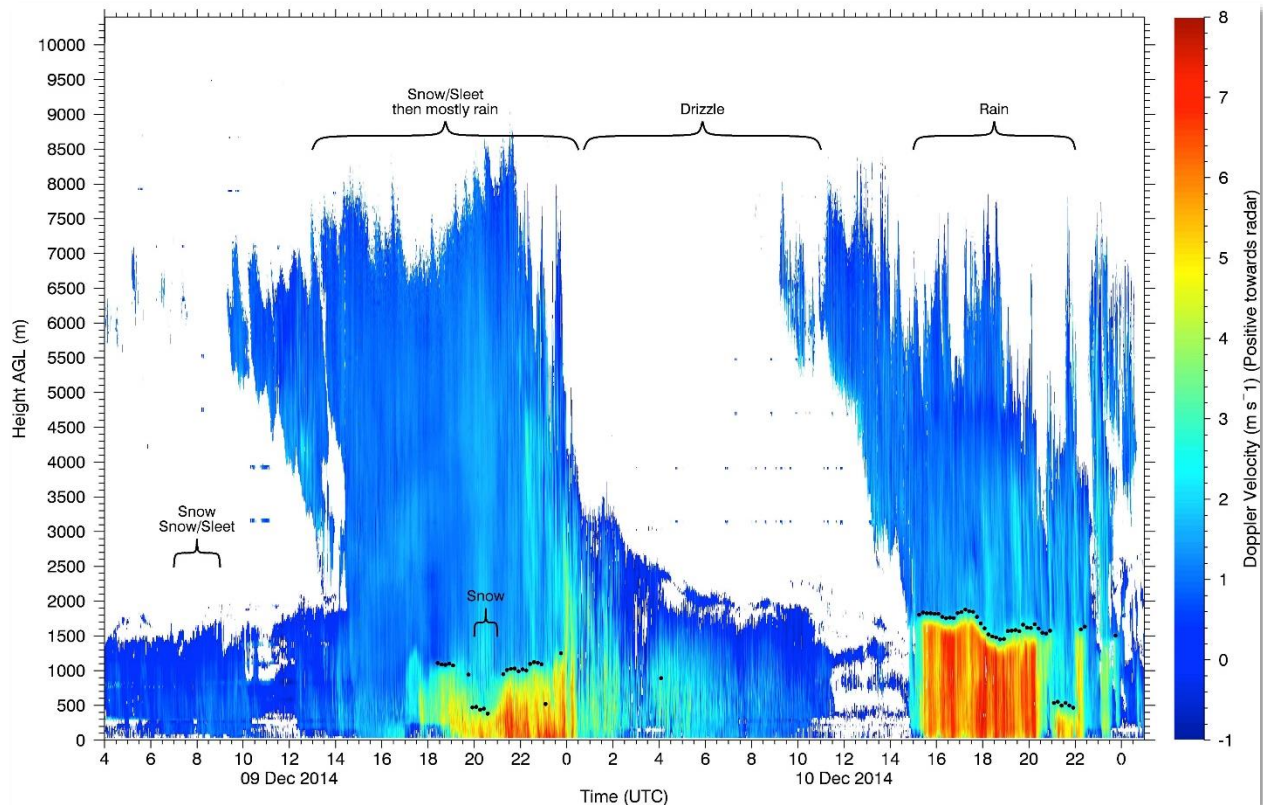


Fig. 9.3: Time-height analysis provided by the NOAA ESRL/PSD of precipitation fall velocity (m s^{-1} ; shaded) at PMH for 0400 UTC 9 December 2014 through 0100 UTC 11 December 2014. The black dots represent the algorithmic location of the precipitation melting level (*i.e.*, snow level) and annotations refer to approximate locations and times discussed in the text.

A melting level was first detected by the PMH SLR at 1800 UTC at ~ 1.1 km AGL, with ice crystals falling at ~ 1 m s^{-1} above ~ 1.1 km, and mixed precipitation and rain falling at $5\text{--}8$ m s^{-1} below 1.1 km. The melting level briefly descended to 0.6 km AGL during 2000–2100 UTC 9 December 2014, in association with a band of higher reflectivity according to the WSR-88D in Gray, Maine (Figure 9.2b), that resulted in moderate wet snow falling at ~ 5 m s^{-1} , before returning to ~ 1.1 km AGL and mostly rain through 0000 UTC 10 December 2014. The melting level likely lowered as a consequence of additional cooling, driven by the absorption of latent heat, as moderate precipitation melted in the layer. Light drizzle was recorded at K1P1, with not enough hydrometeors to detect a melting level at PMH for the remainder of the event through 0700 UTC 10 December 2014.

Additional precipitation that fell later the next day between 1500 and 2300 UTC 10 December contained a melting level that varied between 1.5 and 2.0 km AGL. K1P1

reported light-to-moderate rain without mixed precipitation, which is consistent with the fall velocities below the melting level of $\sim 8 \text{ m s}^{-1}$. Both precipitation events featured a lowering of mid-tropospheric ($\sim 2\text{--}5\text{-km}$) precipitation, indicated by descending fall velocities with time. This pattern is typical of mid- and upper-tropospheric forced precipitation falling into a drier lower-tropospheric air mass that produces moistening, fall streaks (virga) prior to precipitation observed at the surface.

9.2.2. Observations of freezing rain. Freezing rain is a frequent winter-time occurrence over central New England, as advancing warm air aloft advects over surface air that is below freezing to the east of the Northern Appalachian Mountains and within the sheltered river valleys of the White Mountains. The first noteworthy freezing rain event recorded by PMH occurred on 18 – 19 January 2015. A weak surface low-pressure system (Figure 9.4a), located in the Carolinas, included a warm front that extended northeastward along the East Coast, separating cold Arctic air trapped east of the Appalachians from warmer air over the Atlantic Ocean at 1500 UTC 18 January 2015. Weak lower-tropospheric warm air advection (Figure 9.4b) produced precipitation that fell into the cold airmass near the surface, resulting in freezing rain and rain for a significant portion of the Northeast, and two periods of sleet and freezing rain in Plymouth.

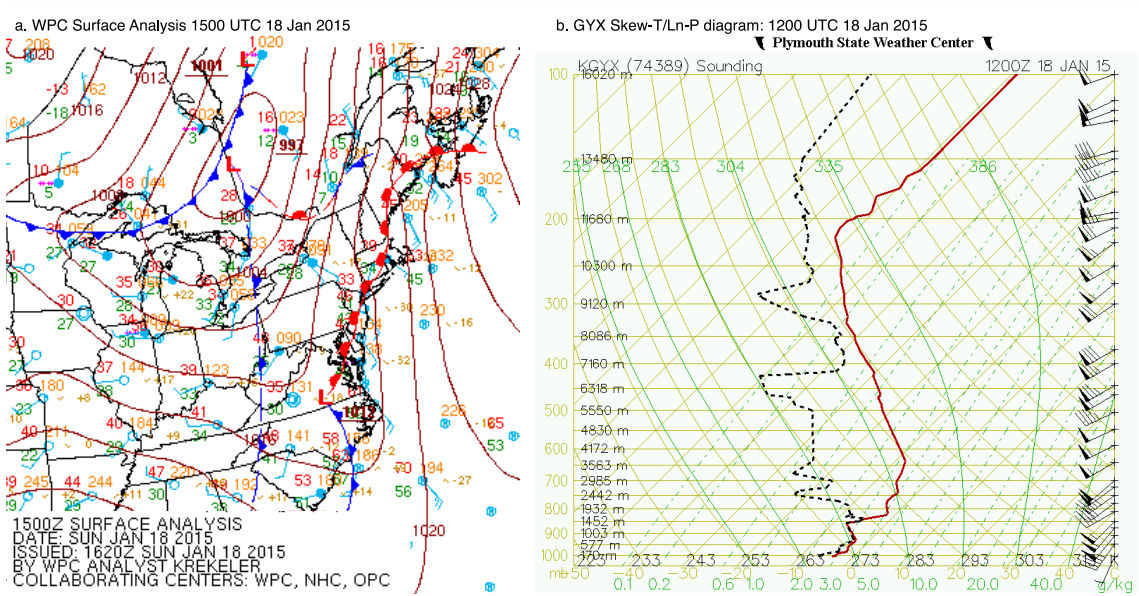


Fig. 9.4: (a) Surface observations and frontal analysis valid at 1500 UTC 18 January 2015 (adapted from imagery provided by the Weather Prediction Center), and (b) Skew- T /Log- p diagram of temperature (red line), dewpoint temperature (dashed black line), and wind (barbs) at Gray (KGYX), Maine at 1200 UTC 18 January 2015 (provided by <http://vortex.plymouth.edu>).

The first period of precipitation at the PMH SLR began between 1600 and 1700 UTC 18 January 2015 as light snow and sleet, with fall velocities of 2–3 m s⁻¹ below ~1.5 km AGL (Figure 9.5), and a surface air temperature of -7°C (not shown). The PMH SLR detected a melting level that varied between 1.0 and 1.3 km AGL as temperatures rose from -6.9°C at 1715 UTC to 0.0°C at 2315 UTC. During this period, fall velocities of 1 m s⁻¹ in the upper troposphere and 2 – 3 m s⁻¹ at the melting level were replaced by fall velocities of 5 – 8 m s⁻¹ below the melting level, suggesting ice crystals melting into raindrops that would later freeze upon contact with the ground. After a short period with freezing drizzle, precipitation resumed as rain and freezing rain in Plymouth from 0100 to 0600 UTC 19 January 2015, as temperatures held between 0.0°C and 1.8°C at PMH and held at ~0.0°C at K1P1 (not shown). The melting level lowered during this time from 1.5 to 0.5 km AGL, as warmer air at upper-levels retreated eastward and colder air advanced from the west. Precipitation ended as the melting level at PMH lowered to the surface.

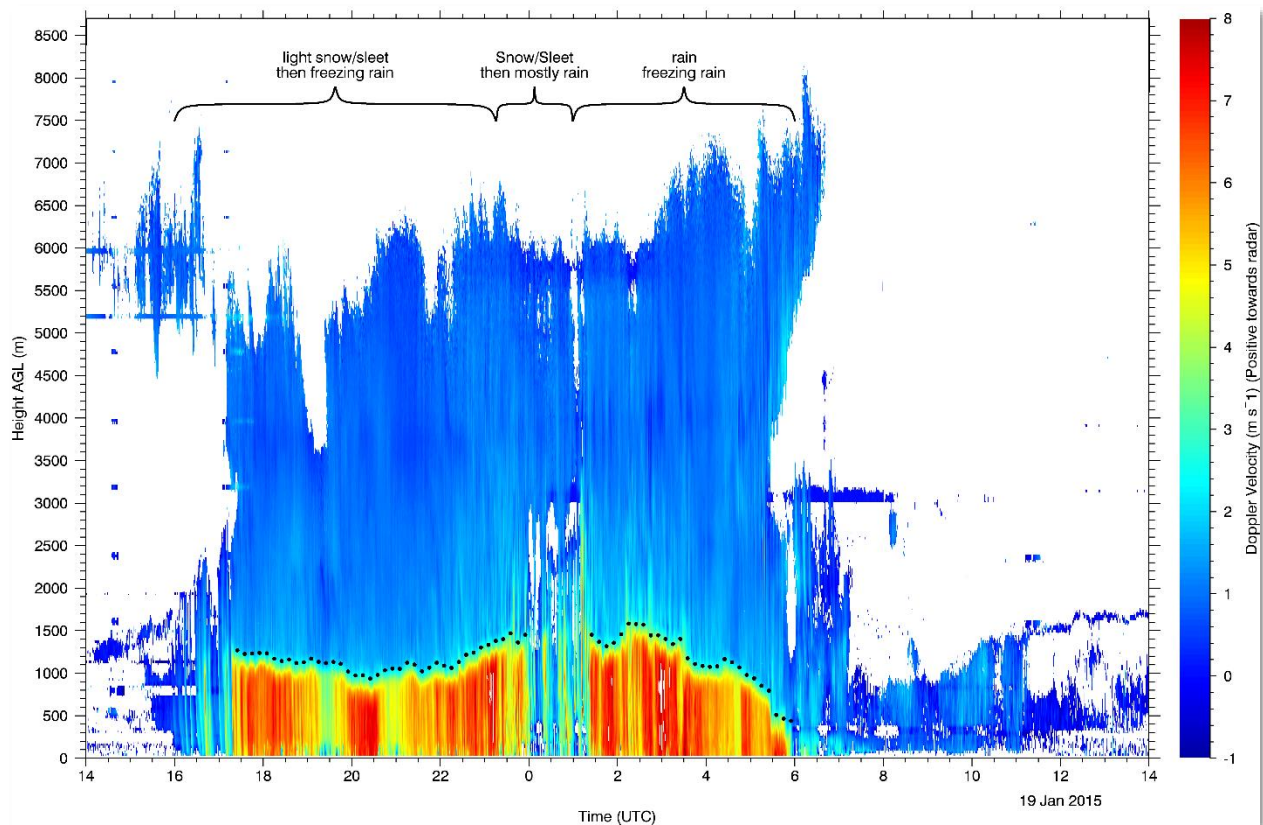


Fig. 9.5. As in Fig. 9.3, except for 1400 UTC 18 January 2015 through 1400 UTC 19 January 2015.

9.3. CSWR Doppler on Wheels (DOW). The Center for Severe Weather Research (CSWR) is part of the National Science Foundation’s Lower Atmospheric Observing Facility (LAOF)³¹. The fleet of mobile Doppler radars were originally constructed to provide close-up observations of tornadoes and severe thunderstorms, at much finer spatial resolutions than the WSR-88D network is capable of producing. The DOWs have since been used for other purposes, such as observing hurricanes and severe winter weather (such as lake-effect snow squalls and synoptic-scale blizzards in the Northeast). In addition to its currently operating DOW-6, DOW-7, and DOW-8 (also known as Rapid-Scan DOW), CSWR also operates a fleet of instrumented vehicles, equipped with standard meteorological instrumentation, which can be used to assemble a mesoscale weather observation network, and approximately 20 rapidly-deployable weather observing “pods” designed to withstand the extreme conditions in and near tornadoes (CSWR 2019).

9.3.1. DOW-6 and DOW-7 are conventional radar systems, using hardware quite similar to (but smaller than) the WSR-88Ds. Both have a transmitted power of 500 kW (from two separate 250 kW magnetron transmitters, and the highest available transmitted power in any mobile X-band radar), which is comparable to the WSR-88D’s peak transmitted power of 750 kW. Their beamwidths are 0.93 degrees, also comparable to the WSR system. Unlike the WSRs, they are capable of both horizontal scans and *vertical* scans (natively producing RHI displays; see Chapter 7, section 7.3.2) (CSWR 2019). Figure 9.6 shows some images of DOW-7 when it was used for education and research over a three-week period, in early 2014, at Plymouth State University.

³¹ See NSF Division of Atmospheric and Geospace Sciences at www.nsf.gov.



Fig. 9.6: Images of the DOW-7 at Plymouth State University. Upper left: Dr. Eric Hoffman with DOW-7 during observations of a severe winter storm. Upper right: Student Alyssa Hammond with DOW-7 during winter storm. Lower left: Outreach event at McAuliffe-Shepard Discovery Center in Concord, New Hampshire. Lower right: DOW-7 at public outreach event at a local secondary school.

Data are collected in up to 1000 range bins along a radial, with a best resolution of 30 meters (similar to the SLR). Both have a variable PRF, with a maximum rate of up to 5000 pulses per second. Both operate at wavelengths slightly longer than 3 centimeters, making them X-band radars (see Chapter 2, Table 2.2). Both are dual-wavelength radars, operating two separate transmitters through a single antenna, mounted on the back of a large, diesel truck (Figure 9.6). The difference between the wavelengths of the two transmitters is on the order of a few millimeters. Both have polarimetric capability, transmitting with linear-diagonal polarization, and separately receiving backscattered horizontal and vertical components. The polarization data are used to produce Z_{DR} , ρ_{HV} (CC), and ϕ_{DP} datatypes (see Chapter 6). Operating two

separate transmitters simultaneously allows for rapid calculations of high-quality dual-pol datatypes. Figure 9.7 shows a schematic of systems operating on these two DOWs.

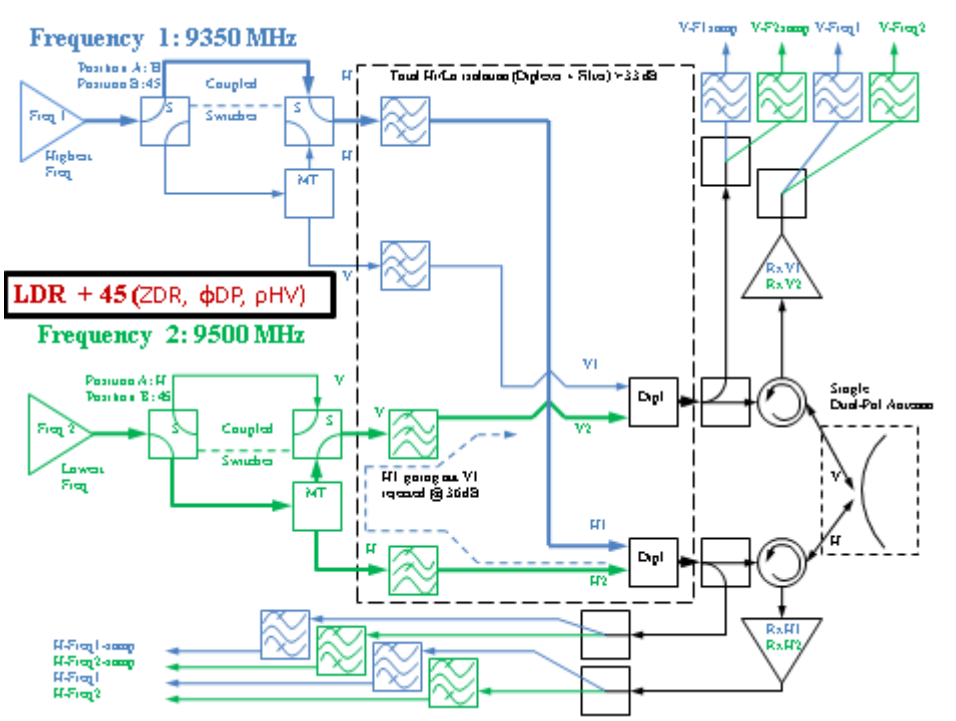


Fig. 9.7: Schematic of DOW-7 system. DOW-6 is quite similar, although the wavelengths of its two transmitters (expressed here in terms of their frequencies) are slightly different. (Credit: CSWR 2019.)

9.3.2. **DOW-8, the mobile Rapid-Scan system, is a multi-beam phased array radar**³². Like the earlier DOWs, the Rapid-Scan DOW is an X-band radar. Its beamwidth is even narrower than the earlier DOWs, and is between 0.8 and 0.9 degrees of azimuth. The scan strategy can complete a volume scan in as little as seven seconds (compare to 4 ½ minutes for the WSR-88Ds), allowing it to scan tornadogenesis events on a timescale that facilitates an improved scientific understanding of the physics at work. Energy from a single transmitter is used to create several simultaneous “pencil” (narrow) beams, each with a unique frequency, which are simultaneously transmitted at different elevation angles (Figure 9.8) from the array. The phased array antenna is rotated horizontally by a turntable, completing a 360-degree sweep in six seconds. Elevation angles (higher than those shown in Figure 9.8) are obtained by tilting the array upward. The array itself is approximately 2.5 meters (8 feet) on a side.

³² Rauber and Nesbitt (2018) also has a brief entry on DOW-8.

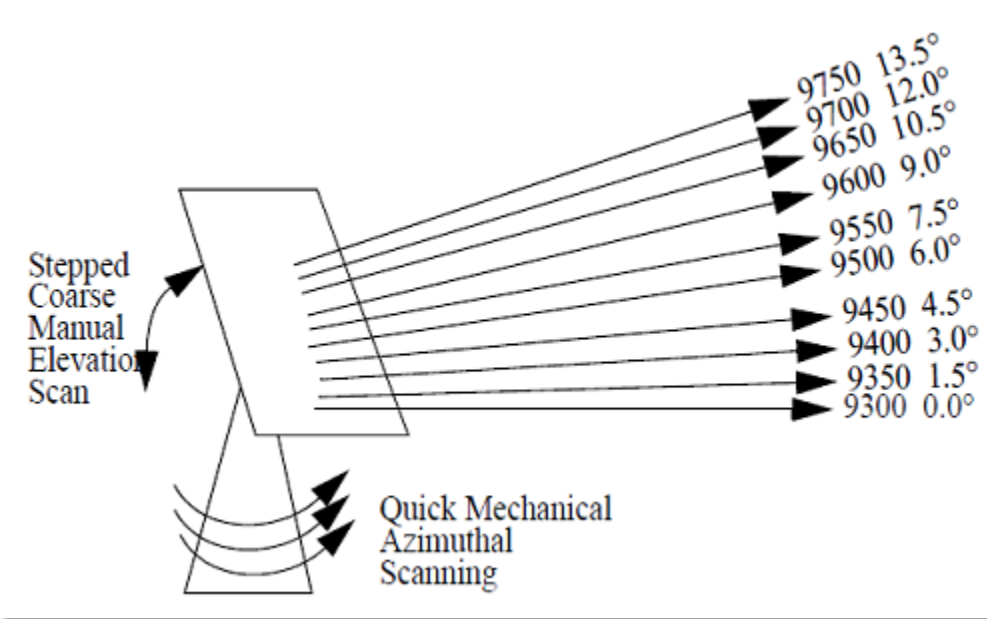


Fig. 9.8: Schematic of DOW-8 phased array antenna. (Credit: CSWR 2019)



Fig. 9.9: Images of Rapid-Scan DOW (DOW-8). (Credit: CSWR 2019.)

9.4. **FAA Terminal Doppler Weather Radar (TDWR)**³³. Low-level wind shear near airports has caused or significantly contributed to the deaths of more than 1400 people worldwide. More than 400 fatalities in the United States resulting from this hazard

³³ Rauber and Nesbitt (2018) also have an entry on the TDWR.

occurred between 1973 and 1985 (NCAR 2019). In the late 1970s, research found that microbursts (intense downdrafts from the bases of thunderstorms) were responsible for the most hazardous forms of wind shear near airports (Figure 9.10). The radial spreading of cold air descending from the base of the thunderstorms causes sharp changes in airflow around aircraft wings. This work eventually led to the development of several wind shear detection systems, among them, the TDWR (NCAR 2019).

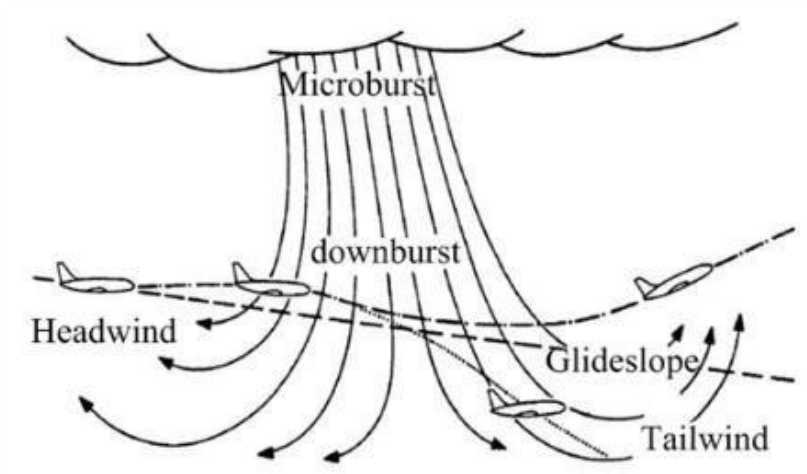


Fig. 9.10: Schematic of thunderstorm downdraft (microburst) resulting in wind shear near an airport. (Credit: Sabzehparvar 2018.)

The TDWR network is a C-band (~5 cm), Doppler-capable radar system operated by the Federal Aviation Administration (FAA). Its primary purpose is detection of hazardous weather conditions within about 135 km (73 nautical miles) of airports, in locations where wind shear or thunderstorms are a regular threat to aviation. It was initially developed in the 1990s at MIT's Lincoln Laboratory for the purpose of real-time detection of wind shear, and in 2004, the National Weather Service developed an agreement with the FAA for expanded use of the TDWR. This agreement resulted in the development of the TDWR Supplemental Product Generator (SPG), a collection of software algorithms for generating Level III products similar to those generated by the WSR-88D system. There were 45 TDWR installations operating in the United States in 2014 (NCEI 2019). These are shown in Figure 9.11. Additional systems have been installed in foreign airports, such as Hong Kong (Shun and Lau 2000).



Fig. 9.11: TDWR locations in the CONUS. (Credit: https://en.wikipedia.org/wiki/Terminal_Doppler_Weather_Radar#media/File:Map_TDWR.svg)

The TDWR transmits at 250 kW (compared to the WSR-88D’s peak of 750 kW) and has a beamwidth of $\frac{1}{2}$ degree (compared to the WSR’s 1-degree beamwidth). Its range resolution (range-bin depth) is 150 meters within 135 km of the RDA and 300 meters between 135 km and 460 km (compare to the WSR’s 250-m range bins). It uses two different Volume Control Patterns: The first (VCP 90) is the “monitor” mode, and the second (VCP 80) is the “hazardous weather” mode (Istok *et al.* ND; NCEI 2019). The “monitor” strategy uses 17 tilt angles (more than the WSR-88D in any VCP), with a maximum tilt angle of 60 degrees (much higher than the WSR-88D’s maximum tilt of $19\frac{1}{2}$ degrees). Figure 9.12 shows examples of TDWR Volume Control Patterns.

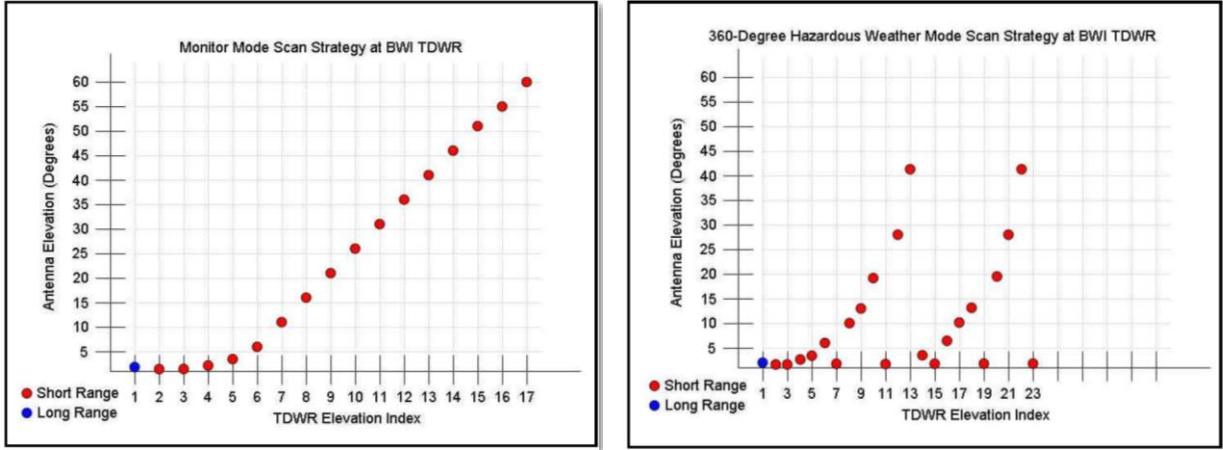


Fig. 9.12: TDWR Volume Control Patterns. (Credit: Istok *et al.* ND.)

Its Maximum Unambiguous Velocity is 20 to 30 knots (10 to 15 ms^{-1}) (NCEI 2019). Figure 9.13 shows a comparison of the same supercell thunderstorms imaged by a TDWR and WSR-88D. The former obviously has higher resolution than the latter, but (because of its shorter wavelength) suffers from much more attenuation of its signal in the region of rainfall.

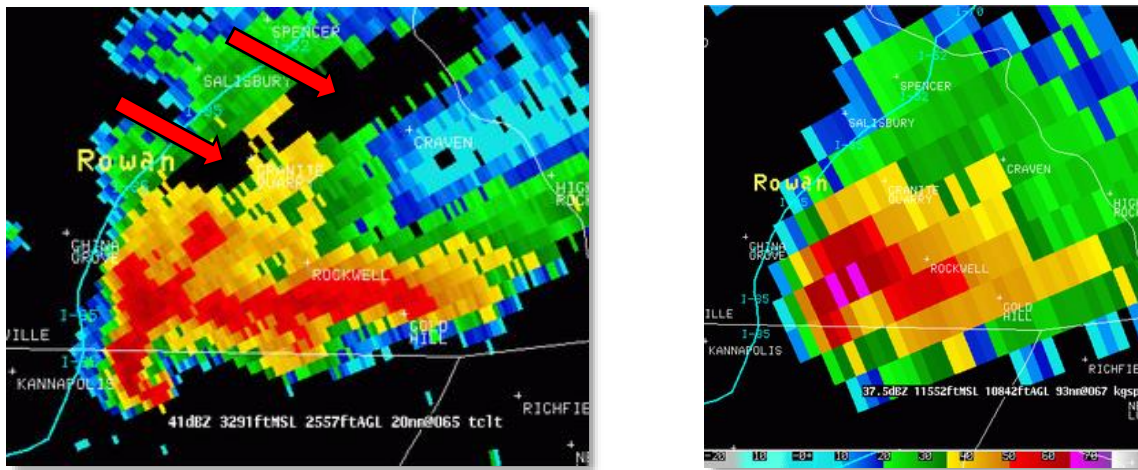


Fig. 9.13: Comparison of the same supercell imaged by TDWR (left) and WSR-88D (right). The TDWR has higher resolution than the WSR-88D, but its signal is heavily attenuated in the heaviest area of precipitation (blacked out areas in left panel, indicated with arrows.)

In 2005, the National Weather Service began working with the Federal Aviation Administration, in a project to combine the data produced by the TDWR network with

the WSR-88D network. This included processing TDWR data into Level III (derived) products very similar to those routinely produced by the WSRs. The deployment of this upgrade to all 45 TDWRs was completed in 2008. While TDWR Level II data (quality-controlled base moments) are *not* archived by the National Centers for Environmental Information (as are WSR-88D Level II data), the TDWR Derived Products *are* and can be downloaded from the NECI website (NCEI 2019).

The following Level III products are available for the TDWRs (NCEI 2019). Refer back to Chapters 7 and 8 to compare these to the analogous WSR-88D products.

Level III Base Moments:

- Digital Base Reflectivity on the lowest three elevation angles, from the RDA out to 48 nautical miles (89 km).
- Long-Range Digital Base Reflectivity on the lowest elevation angle (0.6°), out to 225 nautical miles (417 km).
- Digital Base Radial Velocity on the lowest three elevation angles, from the RDA out to 48 nautical miles (89 km).

Level III storm-cell products:

- Storm Tracking Information, which is similar to the WSR-88D's Storm Cell Information and Tracking (SCIT) output. It includes current location, movement over the previous hour, and forecast movement for up to an hour in the future.
- Storm Structure, which includes maximum reflectivity, maximum velocity at the lowest tilt angle, location, and other attributes.
- Hail Index, including indicators for "hail probable" and "hail positive."
- Other Level III reflectivity-based products: Gridded Vertically-Integrated Liquid, on 2.2 x 2.2 nautical mile (4 x 4 km) rectangular grid, out to 124 nautical miles (230 km); Composite Reflectivity and Enhanced Echo Tops

Level III radial velocity products:

- VAD Wind Profile
- Digital Mesocyclone Detection Algorithm, identifying the existence, location, and height of mesocyclones.
- Tornadoic Vortex Signature, identifying the locations of Gate-to-Gate Shear exceeding defined thresholds.

Precipitation products:

- One Hour Precipitation and Storm Total Precipitation on a $1.1 \text{ nm} \times 1^\circ$ ($2 \text{ km} \times 1^\circ$) polar grid, using the same WSR-88D's legacy Precipitation Processing System (PPS).
- Digital Precipitation Array, similar to the PPS's product.

9.5. **The Canadian operational weather radar network**³⁴. The Canadian operational weather radar network currently consists of 31 installations stretching from the Pacific to Atlantic oceans, and located mostly in the southern half of its geographic area (Environment and Climate Change Canada 2019b). (See Figure 9.14.) The network provides radar coverage for more than 98 percent of the country's population (Meteorological Service of Canada 2019a). Until recently, most were C-band radars, with a maximum range of about 70 nautical miles (128 kilometers) for radial velocity, and 140 nautical miles (240 km) for reflectivity³⁵. In 2011, following original approval in 1998, Environment and Climate Change Canada began a project to initially upgrade the existing C-band radars, and then replace all of them (while adding 12 more) with longer-range S-band radars similar to the WSR-88D. The project is expected to be complete by 2023. The new radars will all be natively dual-pol (Canadian Weather Radar Network 2019).

³⁴ Rauber and Nesbitt (2018) have very brief entries on the Canadian and European operational weather radar networks.

³⁵ The exception was a Doppler-enabled, dual-pol S-band system at McGill University, in Montreal, Quebec, that was used both operationally and for research (McGill JS Marshall Observatory 2019). A newer system has since replaced the original McGill system, in Blainville, outside Montreal.

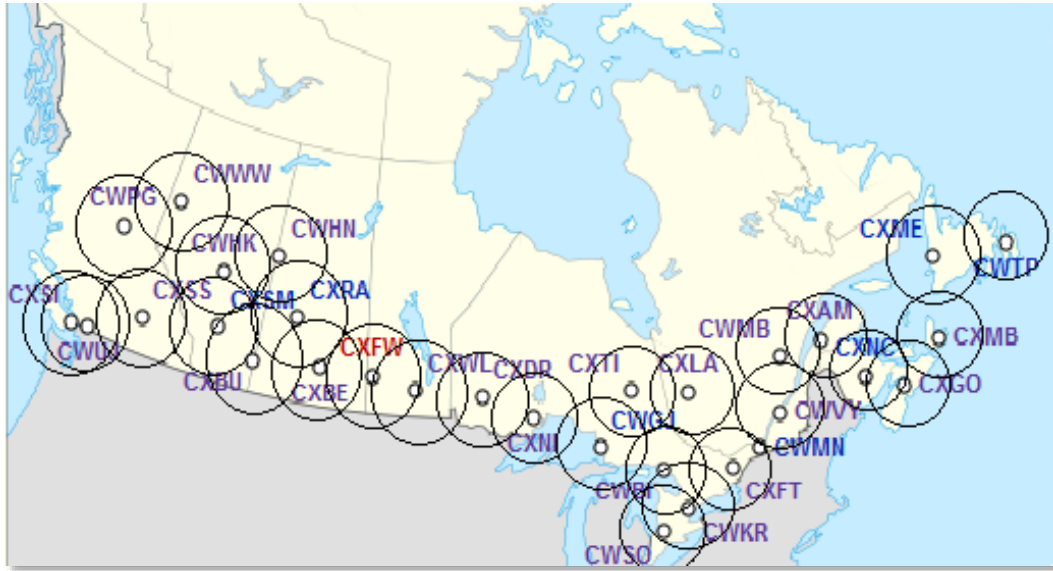


Fig. 9.14: Canadian Weather Radar Network. (Image credit: Pierre cb, <https://commons.wikimedia.org/w/index.php?curid=16128391>)

The original C-band radars utilized two different scan strategies: A “conventional cycle” (for reflectivity) consisting of 24 tilts completed in five minutes, and a “Doppler cycle” (for radial velocity) consisting of four tilt angles (Joe and Lapczak 2002).

The new S-band systems operate at a frequency of 2.7 to 2.9 GHz (about 10 cm), with a peak transmitted power of 750 kW. The PRF is between 250 and 2000 pulses per second, consisting of both short (0.4 μ s) and long (4.5 μ s) Pulse Lengths. The beamwidth is on the order of 1°. The antenna rotates at a maximum speed of 6 revolutions per minute, and is 8.5 meters (about 28 feet) in diameter. The Volume Control Pattern includes 17 tilts, scanned in six minutes. The maximum range for reflectivity volume scans is 162 nautical miles (300 km), and for radial velocity volume scans is 130 nautical miles (240 km). All of these specifications are nearly identical to those of the WSR-88D system. Figure 9.15 shows an example of one of the new S-band systems, in Blainville, Quebec (Canadian Weather Radar Network 2019), and Figure 9.16 shows an ensemble radar image generated by the Meteorological Service of Canada (<https://weather.gc.ca>).



Fig. 9.15: S-band weather radar in Blainville, Quebec. (Credit: Pierre cb)

sNumber	RANK	Rank_Wei...	Category	WDRAFT	BWER	Meso	Hail	VIL	MAXZ	ETOP45	Speed
32	1	6.6	not a...	44.1	26.0	8.1	10.0	113.6	65.50	138.0	6.7
43	2	5.4	SST	39.9	24.0	0.0	8.3	88.1	66.00	126.0	5.7
21	3	5.2	SST	42.6	22.0	0.0	7.5	104.8	67.00	130.0	12.0
37	4	5.0	SST	36.1	22.0	0.0	8.3	76.9	64.50	124.0	4.5
41	5	3.4	SST	21.5	0.0	0.0	5.7	41.0	63.00	103.0	14.5
27	6	3.1	WST	18.4	22.0	0.0	2.3	27.2	59.00	76.0	1.7
11	7	3.1	WST	28.8	0.0	0.0	7.5	57.5	60.00	115.0	6.1
34	8	3.0	SST	25.3	0.0	0.0	4.8	45.0	61.50	100.0	9.4
44	9	2.7	MST	16.0	0.0	0.0	4.1	23.9	55.00	93.0	N/A
sNumber	RANK	Rank_Wei...	Category	WDRAFT	BWER	Meso	Hail	VIL	MAXZ	ETOP45	Speed
32	1	6.6	not_availa...	44.1	26.0	8.1	10.0	113.6	65.50	138.0	6.7

Fig. 9.17: Cell View SCIT. (Credit: Joe N.D.)

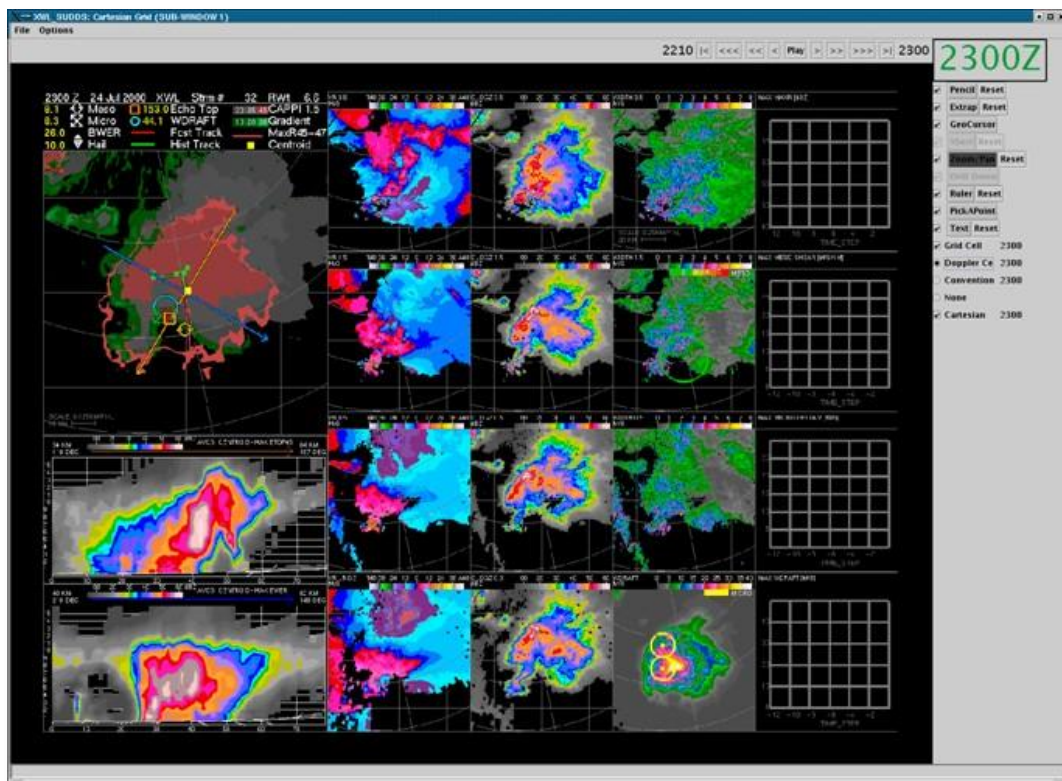


Fig. 9.18: Cell View graphical output. (Credit: Joe N.D.)

Cell View also generates:

- **Hail data**, including maximum hail size, probability of hail, and a severe hail index (see Chapter 7).
- **Downdraft gust potential**.

- **Vertical Cross-Sections** of reflectivity.
- **Storm-relative radial velocity**, similar to the WSR-88D's SRM algorithm output.
- **Velocity Azimuth Display (VAD)**, which creates a wind profile similar to the WSR-88D's VWP.
- **Bounded Weak Echo Regions (BWER)**.
- **Mesocyclone and tornadic vortex** identification.
- **Precipitation accumulations**.

9.6. Weather radar in Europe.

9.6.1. **The OPERA Weather Radar Network.** Thirty different national meteorological services are members of the European National Meteorological Services Network (EUMETNET), of which the Operational Program for Exchange of Weather Radar Information (OPERA) is a part. OPERA makes recommendations about radar hardware and software, facilitates the advancement of meteorological radar science, and coordinates the orderly sharing of weather radar data. OPERA also operates Odyssey (an inaccurate but rather clever acronym for OPERA Radar Data Centre) – an operational data center – that collects radar data from 21 national members in near real-time (Huuskonen *et al.* 2014).

Figure 9.19 shows the locations of OPERA-member operational weather radar installations. Huuskonen *et al.* (2014) describe the current network as “extremely heterogeneous,” meaning that there is a wide variation in the wavelengths of these systems (which includes X-, C-, and S-band installations), as well as in their Doppler and dual-polarization capability. The reasons for this wide variation in type is that each country initially built and continues to be responsible for the funding and upgrades to its individual radar installations, and cooperative sharing and coordination of policy only began as recently as the late 1990s. These differences also make running the continental-scale radar network in Europe a very different problem than running such a network in the United States, where the primary network of WSR-88Ds consists of fundamentally identical components (Huuskonen *et al.* 2014).

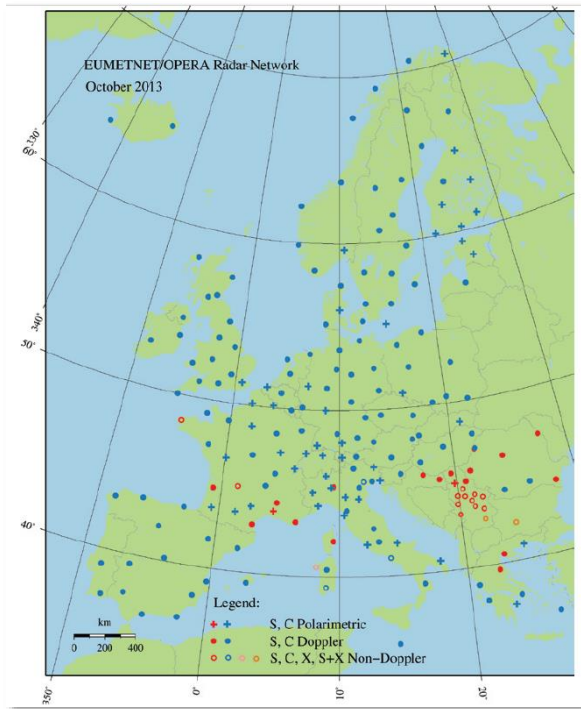


Fig. 9.19: Map of European operational weather radars in OPERA. The network currently consists of a diverse combination of X-, C-, and S-band radars. (Credit: Huuskonen *et al.* 2014.)

As of late October, 2013, there were 202 operational weather radars in the OPERA network. 184 of these were Doppler-enabled, while only 48 were equipped with dual-pol capability. 168 were C-band, and 33 were S-band. Most of the latter were in southern Europe. The median distance between radar installations is 128 km, although (as is obvious from the figure) there is significant variation in the density of the coverage across the continent. Their elevations above sea level vary from only 14.5 meters (on an island in the Norwegian Sea) to 2824 meters (in the Austrian Alps). The median elevation is 256 meters. The beamwidth of all these radars is generally about 1° (Huuskonen *et al.* 2014).

The OPERA Radar Data Centre collects volume scan data (in polar coordinates) from 134 installations in 21 member countries. These include:

- Belgium
- Croatia
- Czech Republic
- Estonia

- Finland
- France
- Germany
- Hungary
- Iceland
- Ireland
- The Netherlands
- Norway
- Poland
- Romania
- Serbia
- Slovakia
- Slovenia
- Spain
- Sweden
- The United Kingdom

The reason Odyssey doesn't use data from *all* 202 radar sites stems from delays in national-level decisions about adapting the radar output to the cooperative project.

The software for Odyssey runs in parallel at two national centers: The first is the British Met Office (in Exeter, England), and the second is at Meteo France (in Toulouse). This is done to ensure continuity in the event of hardware, software, or communications problems. Data sharing between these two centers is performed by the Regional Meteorological Data Communication Network, mainly using the internet (Huuskonen *et al.* 2014).

Output from the cooperating radar systems is used to create continental mosaics of derived data. The mosaic products are on a rectangular grid-coordinate system covering an area 3,800 by 4,400 square kilometers, at a resolution of 2 kilometers. Product types are:

- **Surface rainfall-rate composite**, updated every 15 minutes. (Figure 9.20 shows an example of this product.)

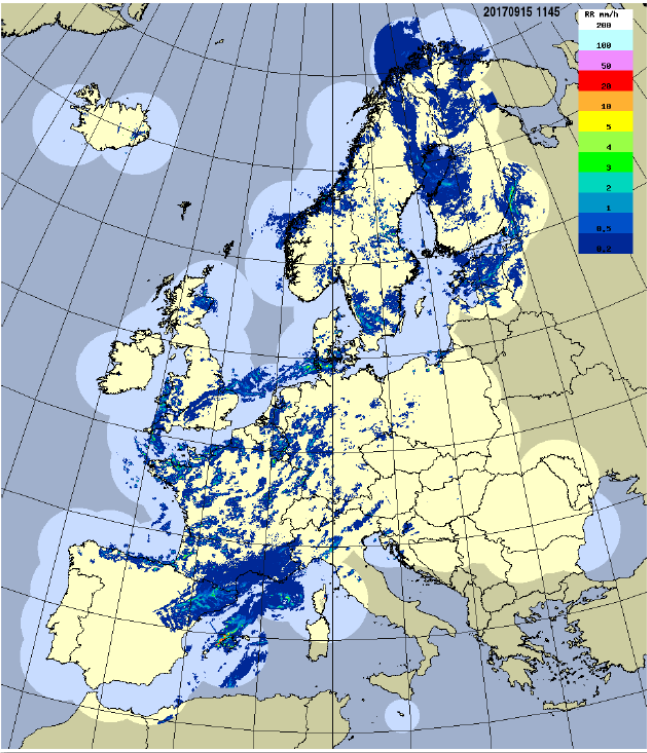


Fig. 9.20: OPERA rainfall rate composite for 15 September 2017, 1145 UTC. (Credit: Peura *et al.* 2017.)

- **Surface rainfall accumulation**, updated once per hour, produced by summing the previous four 15-min rainfall rates.
- **Maximum reflectivity**, updated every 15 minutes. Each pixel in the composite contains the maximum reflectivity at all elevations from all radars contributing to the data for that location.

In 2015, OPERA implemented additional quality control algorithms, including (1) corrections for beam blocking; (2) removal of non-meteorological echoes; and (3) removal of residual clutter. The last of these utilizes satellite data to identify regions of significant clutter (Peura *et al.* 2017).

9.6.2. The Turkish weather radar network. The Turkish State Meteorological Service (TSMS) operates 15 C-band radar installations, in the cities of Afyonkarahisar, Ankara (the capital city), Antalya, Balıkesir, Bursa, Gaziantep, Hatay, Istanbul (the largest city in Turkey), Karaman, İzmir, Muğla, Samsun, Şanlıurfa, Trabzon, and Zonguldak. The first of these was in Ankara, installed in 2001. As of 2016, two more

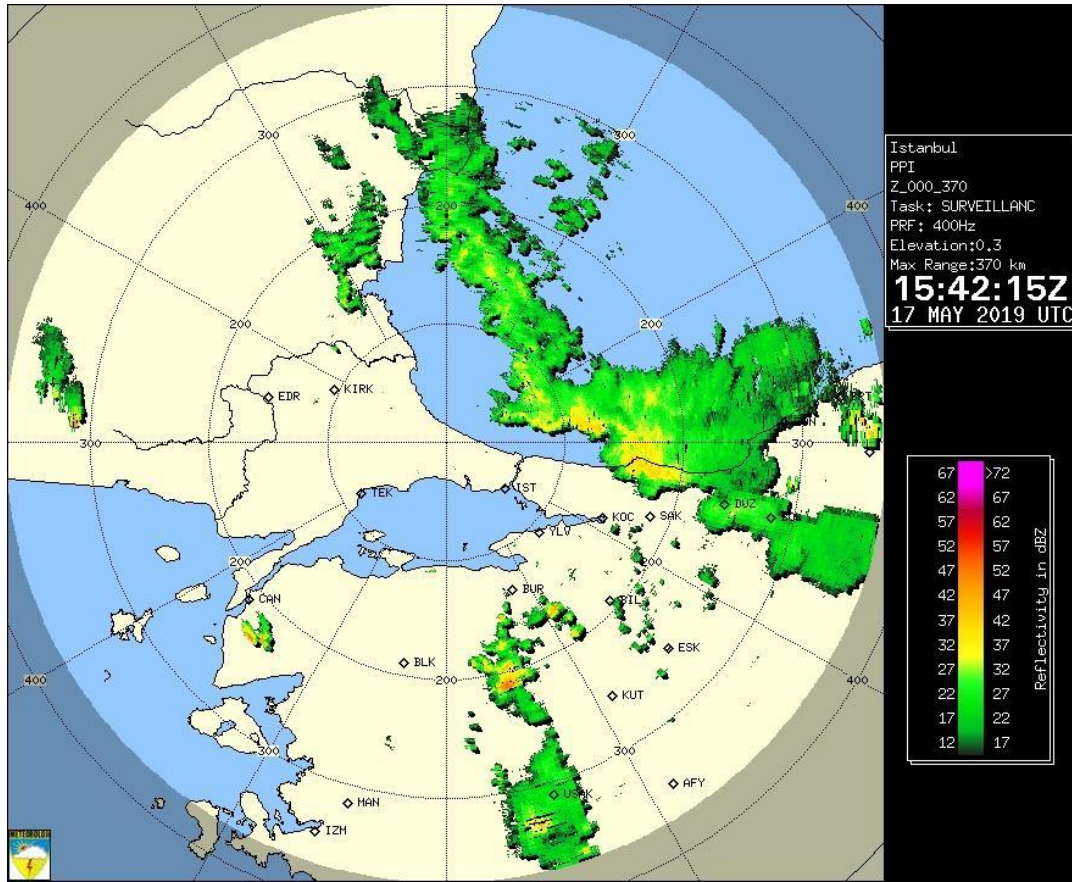


Fig. 9.22: Single-installation reflectivity image produced by the C-band radar in Istanbul, Turkey (<https://mgm.gov.tr/eng/radar.aspx?rG=img&rR=34C&rU=ppi#sfB>).



Fig. 9.23: Ensemble radar image produced by the Turkish State Meteorological Service (<https://mgm.gov.tr/eng/radar.aspx>).

The TSMS also operates a mobile X-band radar at Atatürk airport in Istanbul. The primary purpose of this installation is to test the C-band systems. It can also be used to fill gaps in the stationary C-band network. Figure 9.24 shows this system, as well as typical output showing precipitation echoes (Temir and Macit 2016). Data produced by this system are also available on the TSMS website.

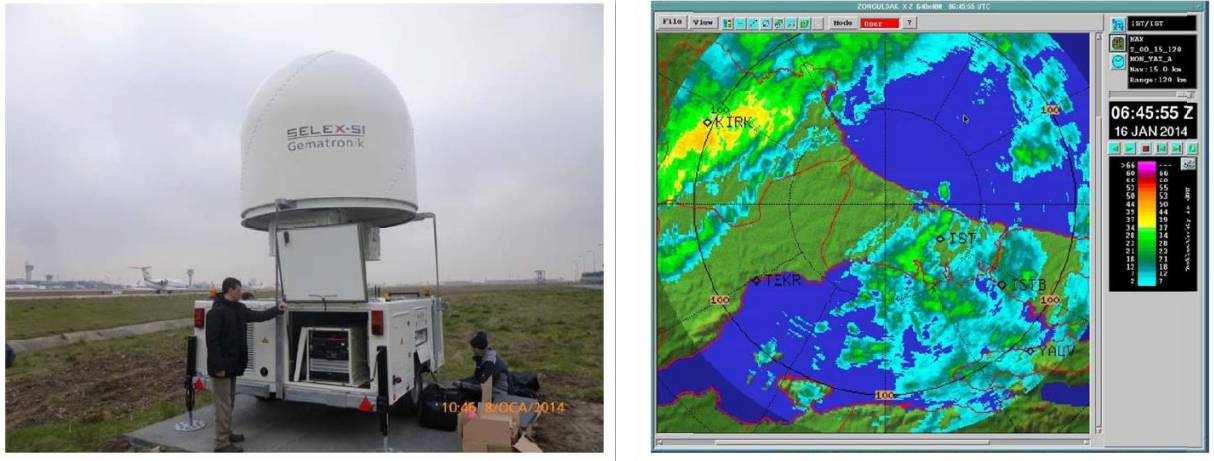


Fig. 9.24: TSMS X-band at Atatürk airport in Istanbul (left), and output with precipitation echoes (right). (Credit: Temir and Macit 2016.)

This completes our introduction to other types of weather radar. In the final chapter, we'll look into weather radar systems in the near future.

Summary. This chapter is an introduction to several additional types of weather radar, including the NOAA Snow Level Radar (SLR), the Center for Severe Weather Research's (CSWR) Doppler on Wheels (DOW), the FAA's Terminal Doppler Weather Radar (TDWR), the Canadian operational weather radar network, and the many kinds of weather radar currently operating in Europe.

The NOAA SLR is an upward-facing, continuously-transmitting S-band radar. It does not scan the region around the antenna in a Volume Control Pattern, but instead focuses on identifying the melting level directly overhead. It transmits at an average power of between 1 and 12 Watts (depending on the specific model), has a vertical range of slightly over 10 kilometers, and returns the vertical velocities of falling precipitation particles in range gates as small as 30 meters. An internal algorithm identifies and tags the elevation at which falling precipitation particles undergo phase transition from a solid to liquid state, by locating the height at which they accelerate from between 1 and 2 ms^{-1} to as much as 8 ms^{-1} .

The CSWR currently operates two different types of DOWs, in addition to its fleet of instrumented vehicles and sturdy, portable weather observing pods. The first type (DOW-6 and DOW-7) are X-band systems, transmitting at two different wavelengths with a combined power output of 500 kW. The second type (DOW-8) is a multi-beam, flat-plate phased array system mounted on a turntable. It can complete a

volume scan in as little as seven seconds, allowing it to study tornadogenesis at a sufficiently fine temporal scale to resolve the relevant physics.

The FAA's Terminal Doppler Weather Radar network consists of 45 C-band, Doppler-capable installations, whose original purpose was to identify wind shear near airports. In 2005, the NWS began working with the FAA to adapt the TDWR network for expanded use. The system was enhanced with a Supplemental Products Generator (SPG), enabling it to generate derived products very similar to the Level III products produced by the WSR-88D RPGs. These products include storm tracking and structure information, similar to that produced by the WSR's SCIT, as well as hail probabilities, VIL, Composite Reflectivity, Enhanced Echo Tops, VAD Wind Profiles, and mesocyclone and TVS products.

The Canadian operational weather network currently consists of 31 permanent installations, located mostly along the country's southern tier. For the time being, it consists of mostly C-band radars, with a maximum range of about 140 nautical miles (240 km), although the government of Canada is carrying out a program to replace them all with S-band systems very similar to dual-pol WSR-88Ds by 2023. Environment and Climate Canada, the Canadian equivalent of the U.S.'s NOAA and the NWS, uses a system for combining data from its operational radars with the rest of its meteorological sensing systems, called the Canadian Radar Decision Support System (CARDS). This system outputs derived products similar to WSR-88D Level III products, such as hail parameters, downdraft gust potential, vertical cross-sections, SRM, and VAD. It also automatically tags Bounded Weak Echo Regions (BWERS), computes mesocyclone and tornadic vortex parameters, and estimates precipitation accumulations.

Weather radar in Europe is a complicated matter. There are several countries involved, each with its own (and unique) weather radar hardware and capabilities. Some are quite advanced, while some are in earlier stages of development. In Western Europe, the Operational Program for Exchange of Weather Radar Information (OPERA) network brings together weather radar data from 21 different countries and produces composites of surface rainfall rate, surface rainfall accumulation, and maximum reflectivity (similar to the WSR-88D's CZ product) as often as once every 15 minutes. In Turkey, a network of 15 C-band radars (some of which are both Doppler and dual-pol enabled) provides coverage for most of the land mass of Asia Minor. The Turkish State Meteorological Service (TSMS) uses data from these systems to produce ensembles of rainfall accumulation and hydrometeor classification. TSMS also operates a portable X-band system at the international airport in Istanbul.

Terms and concepts:

- Automated Surface Observing System (ASOS)
- Automated Weather Observing System (AWOS)
- British Met Office
- Canadian Radar Decision Support System (CARDS)
- Cell View
- Center for Severe Weather Research (CSWR)
- Continuous-wave Doppler radar
- Conventional cycle
- Cooperative Institute for Research in Environmental Sciences (CIRES)
- Digital Base Radial Velocity
- Digital Base Reflectivity
- Digital Mesocyclone Detection Algorithm
- Digital Precipitation Array
- Doppler cycle
- Doppler on Wheels (DOW)
- Doppler vertical velocity
- Earth System Research Laboratory (ESRL) Physical Sciences Division (PSD)
- Environment and Climate Change Canada
- European National Meteorological Services Network (EUMETNET)
- Hydrometeorological Testbed (HMT)
- Lightning Detection Network
- Long-Range Digital Base Reflectivity
- Low-level wind shear
- Meteo France
- National Science Foundation (NSF)
- OPERA Radar Data Centre (Odyssey)
- OPERA Weather Radar Network
- Operational Program for Exchange of Weather Radar Information (OPERA)
- Planetary Boundary Layer (PBL)
- Rapid-Scan DOW
- Servicio Meteorológico Nacional (SMN)
- Signal-to-noise ratio
- Snow Level Radar (SLR)
- Storm-Cell Identification Table (SCIT)

- TDWR Supplemental Product Generator (SPG)
- Terminal Doppler Weather Radar (TDWR)
- Tornadic Vortex Signature
- Turkish State Meteorological Service (TSMS)
- Väisälä
- World Meteorological Organization (WMO)

Study prompts:

1. Discuss the engineering specs and use of the NOAA Snow Level Radar. How is it different from the WSR-88D? How does it detect melting layer height?
2. There are two different types of DOW currently deployed by the Center for Severe Weather Research. What are they and how do they differ? How does the polarization strategy of DOW-6 and DOW-7 differ from the WSR-88D? How does its scan strategy differ from the WSR-88D? How is DOW-8 different from the other two?
3. What was the original motivation for building the network of Terminal Doppler Weather Radars? What was it originally designed to detect? How does the TDWR differ from the WSR-88D? How has the system been modified by the National Weather Service?
4. How many fixed installations are in the Canadian weather radar network? In what part of Canada are most of them located? How do these radar installations differ from U.S. WSR-88D systems? How are they the same? What kinds of derived products do they generate?
5. How many radar sites are in the European OPERA network? How many countries are involved? How does the OPERA radar network differ from the U.S. WSR-88D network? What kinds of problems do the Europeans have to overcome to create their radar network? What kinds of composite products are they generating?
6. Describe the weather radar network operated by the Turkish State Meteorological Service. How many radar installations do they operate? What is

the wavelength of these radar systems? How does their system differ from the U.S. weather radar network?

10. The future of weather radar.

With contributions from Alex Jacques and Paul Johnston.

In the final chapter of this book, we look at the next generation of weather radar and how it will affect operational meteorology.

10.1. The next major development in radar technology is called phased array. The Rapid-Scan DOW (or DOW-8, discussed in the previous chapter), is based on phased array technology, while the other two DOWs currently in service use the conventional single-antenna design.

10.1.1. The concept of array antennas is not new; it was invented during World War II. There are several methods for steering these antennas without using mechanical turntables and tilt mechanisms, and the first electronically-steered radar was the FuMG 41/42 Mammut-1, built in Germany in 1944 (Fenn *et al.* 2000; Wiesback *et al.* 2015). In the 1950s, a method called “phasing” was introduced, vastly increasing the speed with which the beam could be pointed. In 1958, MIT’s Lincoln Laboratory began working on phased array radars. The initial motivation was for tracking satellites, inspired by the successful launch of the world’s first artificial satellite, *Sputnik 1*, by the Soviet Union the previous year. Early MIT designs used a combination of mechanical and electronic beam-steering, but the U.S. Air Force insisted on fully-electronic steering to maximize the ability to track ballistic missiles (Fenn *et al.* 2000).

10.1.2. In 1959, the President’s Science Advisory Committee determined that a credible ballistic missile defense required the ability to track a large number of objects moving at high velocity. The Defense Advanced Research Projects Agency (DARPA, an agency of the United States Department of Defense) funded research for the design and construction of two-dimensional, entirely solid-state radar array steered by computer. DARPA called this the Electronically-Steered Array Radar (ESAR) program, which, in 1960, resulted in the construction of ground-based radar system by Bendix Corporation (Figure 10.1). Additional military phased array radars were built throughout the 1960s and 1970s by Bendix, Raytheon and others, including the AN/FPS-85, which could detect and track ballistic missiles and Earth-orbiting objects at ranges of several

thousand miles. Some of these systems are still in service today (DARPA 2019; Fenn *et al.* 2000).

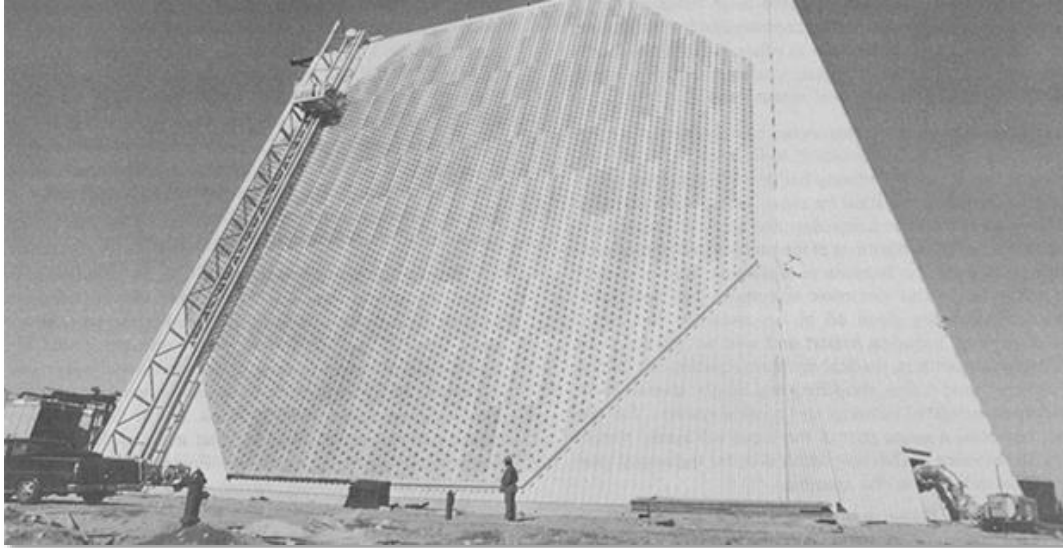


Fig. 10.1: ESAR ground-based phased array radar. This system was originally developed by the U.S. government for military use. Phased array radar was initially a stationary ground-based system, but some types were also deployed on naval vessels beginning in 1973. (Credit: DARPA 2019.)

10.1.3. In the 1980s, Lincoln Laboratories worked with the U.S. Air Force and the U.S. Navy to develop fully-integrated, low-cost, compact Receiver-Transmitter Modules (RTMs), based on gallium arsenide digital circuitry. An RTM is a small printed circuit board in a chassis. To create an array, several of these are mounted on a flat panel. Both General Electric and Raytheon produced several versions of these RTMs (Fenn *et al.* 2000). Additional military phased array systems, some land-based, some portable, and some airborne, were built through the 1980s and 1990s (Fenn *et al.* 2000).

10.2. Civilian meteorological applications of phased array radar in the United States began when the Navy loaned one of its older, ship-mounted systems, called a SPY-1A, to NOAA for research into non-military uses of the device (see Figure 10.2). The SPY-1A antenna had 4352 receiver-transmitter elements, and rested on a turntable (Heinselman *et al.* 2008; Heinselman and Torres 2011). It was capable of scanning a 90-degree wide azimuthal range in one minute or less without moving the turntable (Heinselman *et al.* 2008; Heinselman and Torres 2011). The research into its civilian uses

was accomplished at the National Weather Radar Testbed (NWRT) in Norman, Oklahoma, which began operations in 2003. Because it was capable of performing several functions at the same time, it was called Multi-function Phased Array Radar (MPAR). A descendant of this original antenna is still being used to develop the physical components of the system and the computer algorithms that will enable it, at the NWRT. And the United States is not the only country developing civil MPAR technology. For example, Wada *et al.* (2016) and Mizutani *et al.* (2018) describe the development and fielding of MPAR systems in Japan. Meischner *et al.* (1997) describe European research into phased array and other advanced weather radar systems.

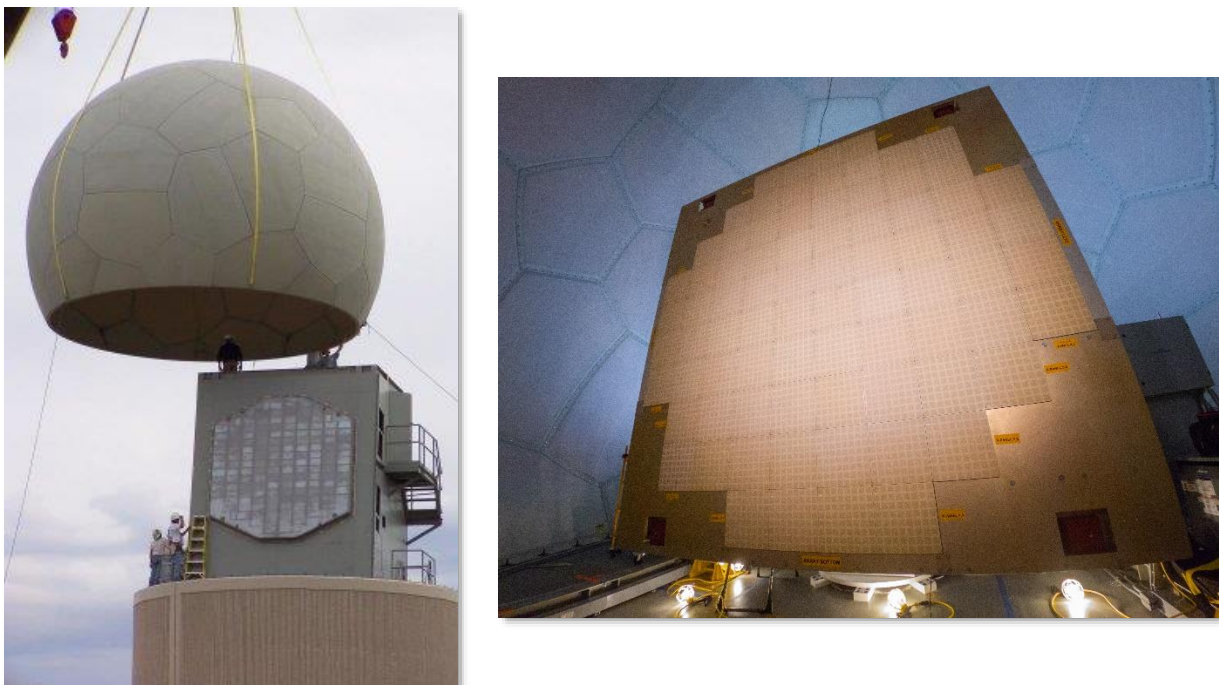


Fig. 10.2: Phased array radar antennas. Left: Original MPAR installation at NSSL (Photo credit: Dr. Sebastian Torres, NOAA/NSSL). Right: ATD flat panel antenna (Photo credit: NOAA/NSSL).

10.2.1. Simultaneous functions include rapid updates to developing weather systems (such as severe convective storms) – resulting in greater warning lead times, conventional volume scans that can be completed in less than a minute – with improved clutter cancellation, and air traffic monitoring (Forsyth *et al.* N.D.). This means that descendants of the NWRT’s MPAR can replace not only the current network of WSR-88Ds, but the TDWR, Air Surveillance Radar (ASR), and (long-range) Air Route Surveillance Radar (ARSR) networks as well (NOAA/NSSL 2014). In total, this is about

550 radar installations, and each of the four member systems has its own management, maintenance, training, and supply logistics programs. MPAR will replace them all with only about 335 installations, which is projected to result in a cost savings of close to five billion dollars over 30 years (OFCM 2006; Weber *et al.* 2007).

10.2.2. The design concept for the completed system is described in Weber *et al.* (2005) and Weber *et al.* (2007): The final version of the phased array will consist of four planar active arrays (a cube), with each face containing 20,000 RTMs in a circular area 8 meters in diameter. There are no magnetron or klystron transmitter tubes, nor are there turntables or tilt-angle mechanisms to point the antenna. Pointing the radar beam is accomplished by selective use of phase shifting. The current to each RTM passes through a phase shifter controlled by a computer. The individual electromagnetic wavefronts from each RTM are spherical, but they combine in front of the antenna array to create a plane wave – a beam of radio waves travelling in a specific direction. The phase shifters delay the emission of radio waves progressively along a line of RTMs so that each one emits its wavefront later than the one before it. This causes the resulting plane wave to be directed at an angle to the antenna's axis. By changing the phase shifts, the computer can instantly change the angle of the beam.

10.2.3. Each RTM has a peak transmitted power of 10 watts, making them comparable to the Snow Level Radar discussed in Chapter 9. With 20,000 RTMs on a side, this is 200 kW on each face of the installation, or 800 kW over all four faces of the cube, comparable to the WSR-88D's 750 kW peak transmitted power. If one RTM fails, it can be easily replaced without shutting down the entire system (OFCM 2006; Weber *et al.* 2008). Pulse Length varies between 1 and 10 μ s. The beamwidth varies between 0.7°, along a line perpendicular to one face of the array, widening to 1°, at a 45-degree angle from the same line (Weber *et al.* 2007).

10.2.4. The system operates in the S-band range, transmitting at three different wavelengths (channels), all near 10 cm. One channel is devoted to aircraft surveillance, one to routine weather volume scans, and the last for “features of special interest,” such as unidentified aircraft and severe weather. Up to 160 beams can be formed from ensembles of RTMs at the same time, by allocating small groups of RTMs to carry out each individual task (Figure 10.3). For example, one set of RTMs may be designated to monitor aircraft arrivals and departures at a nearby airport, while another may be carrying out routine weather surveillance of the entire region. A third set may be

continuously monitoring a severe thunderstorm cell more than a hundred kilometers away (OFCM 2006; Weber *et al.* 2007; Weber *et al.* 2008).

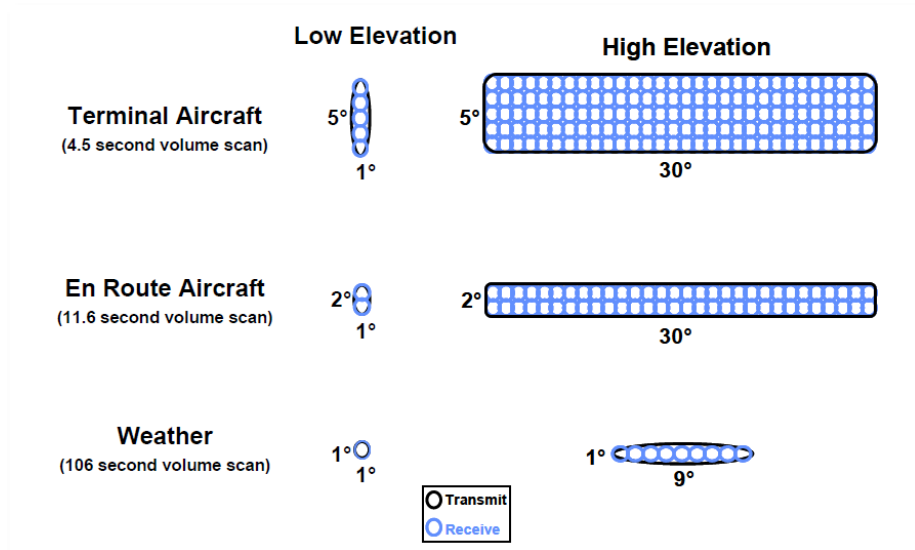


Fig. 10.3. Notional beam patterns for multifunction radar surveillance modes. Cellular objects are RTMs. (Image credit: Weber *et al.* 2008.)

10.2.5. In 2016, the original Navy SPY-1A antenna was replaced by the dual-pol capable Advanced Technology Demonstrator (ATD), a newer phased array flat panel antenna developed by the MIT Lincoln Laboratory (NSSL 2005; Conway *et al.* 2018). Recall that the WSR-88D was retrofitted to transmit linearly-polarized pulses along a diagonal. The final version of the phased array radar may generate dual-pol products by the same means, or it may include a switch that alternates back and forth between horizontally- and vertically-polarized pulses. The former is less expensive, but the latter opens up possibilities for a wider range of dual-pol derived products. (See Rinehart (2004) for a more detailed discussion.)

10.3. Pre-operational meteorological use of phased array radar. In this section, we review three studies examining the performance of the MPAR in development at the NWRT. The high-resolution vertical scan strategies and extremely rapid rate of volume updates made possible by MPAR is yielding a dramatically improved understanding of the physical processes present in severe convective storms. This summary is far from

exhaustive: One study not discussed here is described in Tanamachi *et al.* (2015), which discusses effect of merging storms on a tornadic supercell, as observed using MPAR.

10.3.1. Heinselman *et al.* (2008) report the results of the first detailed investigation into the meteorological capabilities of MPAR. They compare MPAR observations of structure and evolution of three convective storms during the summer of 2006 (a reintensifying supercell, a microburst, and a hailstorm) to those recorded by the WSR-88D in Twin Lakes, OK, about 20 km to the northeast. The MPAR antenna performs VCP 12 (see Chapter 3, Figure 3.6) in 58 seconds, rather than the 258 seconds required by the WSR. Both the MPAR and the WSR-88D transmit near 10 centimeters, and both have a range-resolution of 250 meters.

In the first case, Heinselman *et al.* (2008) reports that the supercell underwent significant evolution during the period of a single WSR-88D volume scan. The MPAR's more rapid volume scan captured the onset of divergent flow on the surface, produced by the forward-flank downdraft, earlier than the WSR-88D imaging the same cell. The MPAR was also better able to detect inflow into the storm's forward flank.

In the second case, the MPAR sampled a wet microburst at a temporal resolution of 34 seconds. There are known precursors to wet microbursts, including (1) rapidly descending reflectivity cores, and (2) strong, deep convergence at mid-levels in the storm cell. These events evolve rapidly, and the 4-6 minute volume scans performed by the WSR-88D and TDWR systems may not be capable of detecting the precursor features before the microburst reaches the surface. The MPAR, scanning at rate of once every 34 seconds, detected the rapidly-descending reflectivity core when it was still aloft, and a few minutes before the onset of strong storm outflow near the surface. The nearby WSR-88D scanned the storm with an update rate of once every five minutes, and therefore missed much of the pre-microburst evolution (Heinselman *et al.* 2008).

In the third case, the MPAR monitored the development of a hailstorm with a temporal resolution of 26 seconds. In this case, the adaptive scanning strategy inherent in MPARs (with *higher* tilt angles possible for sampling the upper portions of storms within 35 km of the RDA, as well as *more* tilt angles for greater vertical detail) was superior to the fixed antenna scan strategies of the WSR-88Ds. During the period of a single WSR-88D volume scan, the top of the storm grew from 5 km AGL to 9 km AGL, and its maximum reflectivity increased from 30 dBZ to 55 dBZ. During another period *shorter* than the WSR-88D volume scan, a Bounded Weak Echo Region developed, indicating an intense, deepening updraft, and maximum reflectivity increased farther to 70 dBZ.

10.3.2. Emersic *et al.* (2011) used the NWRT MPAR system to study the relationship between updrafts, hydrometeors, and lightning flashes in a rapidly evolving, hail-producing thunderstorm in Oklahoma. They combined information from the MPAR with data from the Oklahoma Lightning Mapping Array (OLMA) and the National Lightning Detection Network (NLDN). The MPAR completed volume scans of the hail-producing storm once every 26 seconds, or approximately 10 times faster than the capability of a conventional WSR-88D. Their analysis was the first to compare the electrical characteristics of a hail-producing storm with its reflectivity and radial velocity structure at such fine temporal resolutions. They produced several vertical cross-sections of the cell to study the role of updrafts on temporal scales of less than a minute. Figure 10.4 shows one example of their results.

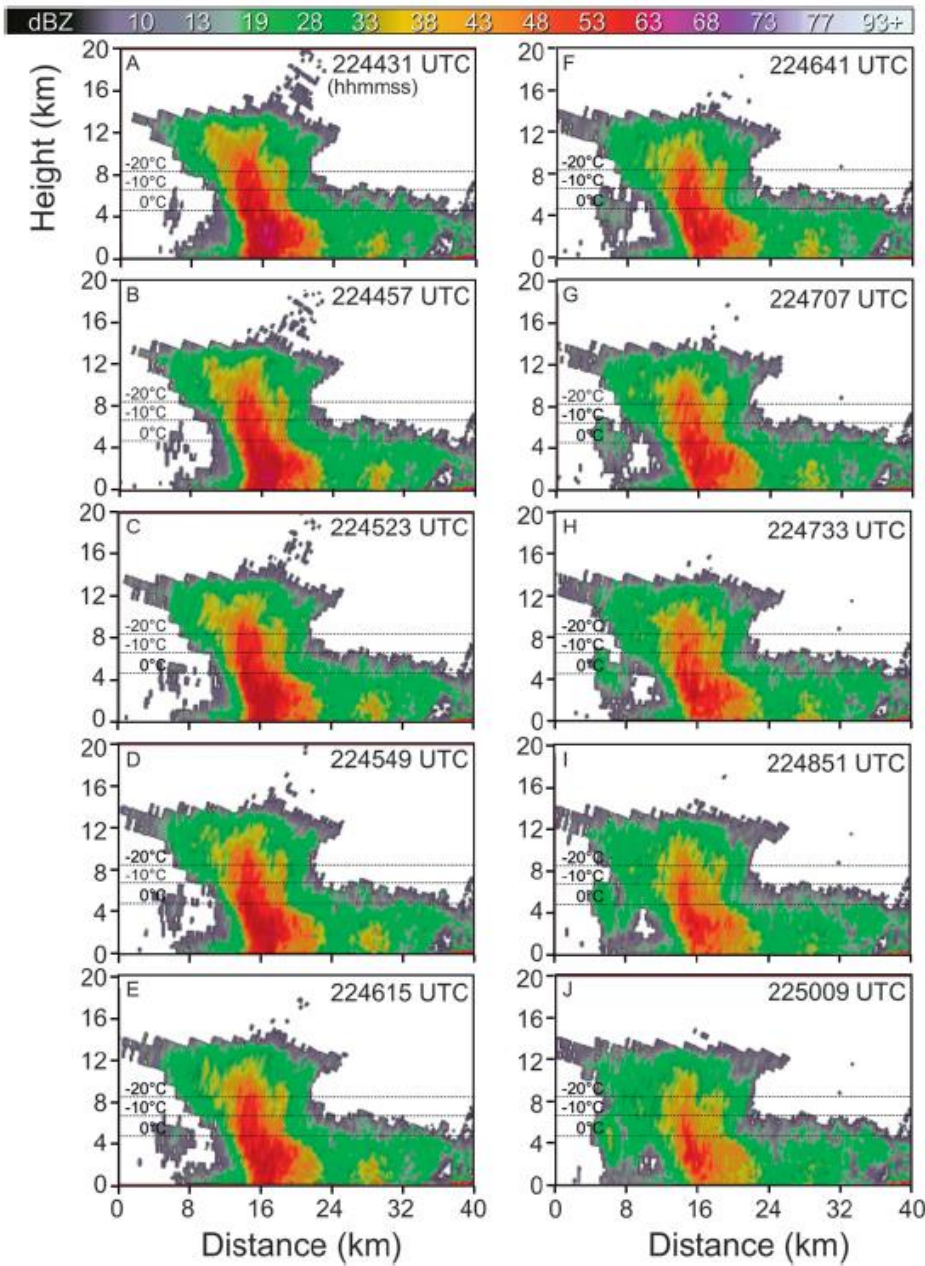


Fig. 10.4: MPAR Vertical cross-sections of rapidly developing, hail-producing thunderstorm, 15 August 2006. Volume scans were completed once every 26 seconds. Times shown are in HHMMSS format. (Credit: Emersic 2011)

10.3.3. Newman and Heinselman (2012) studied an April 2010 wind damage event in Rush Springs, OK, using the NWRT MPAR. The event was also recorded by the WSR-88D in Twin Lakes, OK, and the TDWR system in Norman, OK. It consisted of a low-level circulation associated with a Quasi-Linear Convective System (QLCS) that, while not classified by the Norman, OK Weather Forecast Office as a tornado because of

its relatively large scale (about 2 km in diameter), produced damage consistent with EF Level 1 intensity, as assessed by an independent team. The MPAR was able to sample the Rush Springs circulation at intervals of about two minutes, as compared to the WSR-88D's frequency of about once every 4 ½ minutes, and analysis of the MPAR data suggests that significant changes in QLCSs can occur on time scales of two minutes or less. Further, the scan strategy used by the MPAR included 22 tilt angles, as opposed to the Twin Lakes WSR-88D's 14 tilts, revealing the vertical evolution of the QLCS in much greater detail (Newman and Heinselman 2012).

Newman and Heinselman (2012) conclude that monitoring mid-level features in the QLCS, such as the mid-level or rear-inflow jet, and thus being able to forecast when strong surface winds will occur, requires an amount of volume scan data not available with the current network of WSR-88Ds. The MPAR was able to provide the necessary resolution for observing strong mid-level convergence and a descending reflectivity core (as it did in one of the cases described by Heinselman *et al.* 2008) in sufficient detail to predict the subsequent onset of a strong surface microburst. Thus, the MPAR for the Rush Springs event revealed the precursors for damaging winds, resulting from the QLCS at a level of temporal detail and with an amount of lead time that the conventional WSR-88Ds could not.

10.4. Incorporating phased array radar observations into operational meteorology.

When the author of this text first entered the weather career field, while serving in the U.S. Air Force in the early 1980s, one of the main limiting factors to forecasting was the shortage of high-resolution, rapidly-updated data. Radar data, for example, were manually updated about once each hour, transmitted by remote terminal to a central computer, combined with other data from radar stations, and transmitted back out to the field as a "summary" via facsimile. Observations were typically recorded at 35 minutes past the hour, and the corresponding graphical summary would arrive in a weather office about 20 minutes later. Often, there wasn't enough base radar information to maintain a comfortable level of "situational awareness."

Today, the opposite is true. Satellite data are available in 16 channels (rather than the three that were available in 1982), updated as often as once every five minutes. Radar data update once every four or five minutes and now consist of many more datatypes than the simple reflectivity that was available 35 years ago. There are far more surface observations with higher temporal frequency, and the numerical models (of which there are more now) are far more sophisticated and varied, and update more often. Our problem now is not a *lack* of sufficient data, but data *overload*. To an

operational forecaster working in the field today, the challenge is often deciding what to leave out, rather than the scramble to find more information.

This is not to say that we don't need more and better data. We *do*, especially if we want to continually improve the quality of our work, whose mission is to provide the public and their community leaders with accurate information to help them make good decisions. Everything we do needs to be improved, but the problem then becomes one of managing the resulting avalanche of information. Already, the workload in a NWS Weather Forecast Office can push an individual's cognitive load right up to the point of overload. As phased array radar transitions from research to operational meteorology, we will have to cope with denser volume updates (containing scans at more tilt angles), arriving as often as once every minute.

10.4.1. Impact of high-temporal resolution radar updates on operational forecasters. Wilson *et al.* (2017) considered the impacts of MPAR on operational weather forecasters and their warning decision process, when using 1-, 2-, and 5-min volume updates. Thirty NWS forecasters with an average of 12 years experience, from 25 forecast offices in the U.S. Great Plains region, spent a week working with simulations of rapidly updating volume scan data during the 2015 Phased Array Radar Innovative Sensing Experiment (PARISE). The work was spread out over six weeks, with a subset of the forecasters working a given week based on their availability.

During the week, forecasters worked with data from a series of nine different events: Three were "null" events, three were severe hail and/or wind events, and three were potentially tornadic events. The length of the simulations varied from 19 minutes to slightly longer than an hour. The forecasters were asked to independently interrogate base moments generated by the MPAR in simulated real-time, and issue warnings as they considered necessary. For each of the nine simulations, some forecasters received the 1-minute updates, some the 2-minute updates, and some the 5-minute updates. At the end of the experiment, participants were interviewed in open discussion groups, where they discussed their experiences and made several suggestions (Wilson *et al.* 2017).

Focusing on the 1-min data, the forecasters made positive comments about being able to view storm-scale evolution at a resolution not possible with the WSR-88D. They also stated that they became accustomed to the rapid updates very quickly, although about a third reported initially feeling overwhelmed by the volume of data. This feeling resulted from trying to view *all* base data types (reflectivity, radial velocity, and spectrum width) at *all* tilts as each of the 1-min updates was received, and they quickly realized that they had to begin limiting the types of information they took in with each

update. This “mental filter” was applied differently, depending on the type of event, but was most necessary during a potentially tornadic event, when some of the forecasters settled into closely monitoring the radial velocity reported on the ½ degree elevation angle (Wilson *et al.* 2017).

The consensus among the forecasters participating in PARISE was that the 1-minute data was preferable to the 2-minute and 5-minute MPAR data, in spite of the increased workload. Several of the participants suggested the development of new algorithms that could perform some basic calculations with each update, such as changes in reflectivity cores. Wilson *et al.* (2017) also state that the increased amount of volume data will require the staff of NWS Weather Forecast Offices to redistribute responsibilities during severe weather events – particularly tornadic events – with more individuals involved in evaluating the incoming radar data.

10.4.2. Impact of high-temporal resolution radar updates on warnings and short-term modeling. Computer algorithms can be developed to assist with some of the data evaluation, and help reduce the cognitive load on human weather forecasters. This is the motivation behind the Level III derived products, such as the MDA and the TDA, which identify rotation (at two different scales) in thunderstorms, and alert the forecaster with overlaid graphical symbols. The forecaster is still responsible for acting on the information, but the computer program has helped by identifying the potential trouble areas. Another tool that could be helpful is a system that ingests radar data, and uses it (along with output from large-scale models) to make short-term, storm-scale forecasts.

Supinie *et al.* (2017) discuss the use of rapid-scan MPAR data in storm-scale numerical weather prediction (NWP), and how this supports the National Weather Service’s Warn-on-Forecast (WoF) program, which is working toward including storm-scale NWP in the warning decision process³⁶. In simulations, Yussouf and Stensrud (2010), and Xue *et al.* (2006) showed that fifteen minutes worth of 1-min radar volume scans incorporated into a storm-scale NWP model is enough to significantly shorten the time required to obtain a good analysis of a particular convective storm, and, therefore, increase the lead-time of a severe weather warning.

³⁶ Currently, the National Weather Service does not issue warnings for severe weather (such as tornadoes and severe thunderstorms) until there is a clear radar image of the phenomenon, or the hazard is seen by a spotter. This provides an average of about 13 minutes lead time before a tornado strikes. This is often not enough to reduce loss of life. The Warn-on-Forecast program is working to combine surface, satellite, and radar data into an ideal set of initial conditions for high-resolution (local-scale) computer models that will predict severe weather up to an hour in advance. For more, see https://www.nssl.noaa.gov/news/factsheets/WoF_2015.pdf.

Supinie *et al.* (2017) set out to evaluate and compare the impact of assimilating (1) rapid-scan MPAR reflectivity and radial velocity data, and (2) conventional WSR-88D scans of the same datatypes for a tornadic supercell in Oklahoma, during May, 2011. The radar data from the two types of installations were assimilated into separate storm-scale NWP models once every five minutes, for a 45-minute assimilation period, and 1-hr ensemble forecasts were started after 15, 30, and 45 minutes of radar data assimilation. Root-Mean Square Error (RMSE) and other bulk statistics were then computed by comparing model forecasts of the storm cell with observations of the cell corresponding to the same point in time. Their results indicate that the model forecasts using the MPAR data showed improved skill over those based on the WSR-88D data, particularly for the ensembles started after 15 and 30 minutes of data assimilation. And they attribute the improvement to (1) the greater number of elevation angles possible with the MPAR system, and (2) the MPAR's greater temporal resolution.

Within the context of WoF, a hypothetical real-time prediction system would require 12 or more volume scans that include the storm of interest. For the WSR-88D, this implies nearly an hour's worth of data, but with the MPAR, this could be reduced to as little as 15 minutes. This in turn implies adding at least 30 minutes to lead-times for warnings of severe convective events (Supinie *et al.* 2017).

10.5. Current work assimilating radar data into NWP, and NWP forecasts of radar reflectivity. These are rapidly developing fields, at the forefront of research into improving operational meteorology and its quest for WoF. In the former case, Gao *et al.* (2014) discuss differing methods for assimilating radar data into numerical models. In particular, they note that "effective assimilation of radar data into a NWP model requires advanced data assimilation" (DA) methods. Some DA methods operate in three spatial dimensions, and some over both the three spatial dimensions as well as the dimension of time. They also note that, in a test case involving "real-time convection-resolving forecasts at 1km horizontal spacing over the continental United States," involving the assimilation of both conventional reflectivity and radial velocity from the existing network of WSR-88Ds, clear advantages were demonstrated for storm-scale modeling, and that the use of radar data "clearly represent[s] the future of operational NWP."

Liu *et al.* (2013) discuss the results of assimilating ordinary and "corrected" radar reflectivity from C-band radars in England into 24-hr mesoscale Weather Research and Forecasting (WRF) model forecasts of rainfall. The corrected radar data were obtained by applying a "real-time correction ratio" relating reflectivity to rain gauges, analogous

to the PPS's Precipitation Adjustment Algorithm and the AWIPS Multisensor Precipitation Estimator (see Chapter 8). Additional data from the NCAR Global Data Archive were assimilated, including surface and upper-air pressures, temperatures, water vapor observations, and wind speed observations. They found that the effect of assimilating the NCAR archive data had a more pronounced positive impact on a 24-hr WRF forecast of precipitation than did the radar data (both ordinary and corrected), but that the assimilation of corrected radar data resulted in "some" improvement. They further hypothesized that higher spatial-resolution radar data (in both the horizontal and vertical dimensions) would have had a greater positive impact, as would the assimilation of radial velocity data (Liu *et al.* 2013).

In the United States, the High-Resolution Rapid Refresh (HRRR) model both *ingests* and *forecasts* radar reflectivity data. The current version of HRRR, called HRRRv3 (implemented in July, 2018) is run hourly, and ingests radar data at a spatial resolution of 3 km once every 15 minutes. Forecasts of several conventional model fields (such as wind and pressure) and radar reflectivity are then generated in 15-min intervals out to several hours in the future, at a spatial resolution of 3 km. See https://rapidrefresh.noaa.gov/hrrr/HRRRsubh/Welcome.cgi?dsKey=hrrr_subh_ncep_jet for access to these data. Figure 10.5 shows a sample reflectivity forecast generated using an experimental version of the HRRR. Another experimental version, run at a spatial resolution of 750 meters, is available for the Pacific Northwest region of the United States.

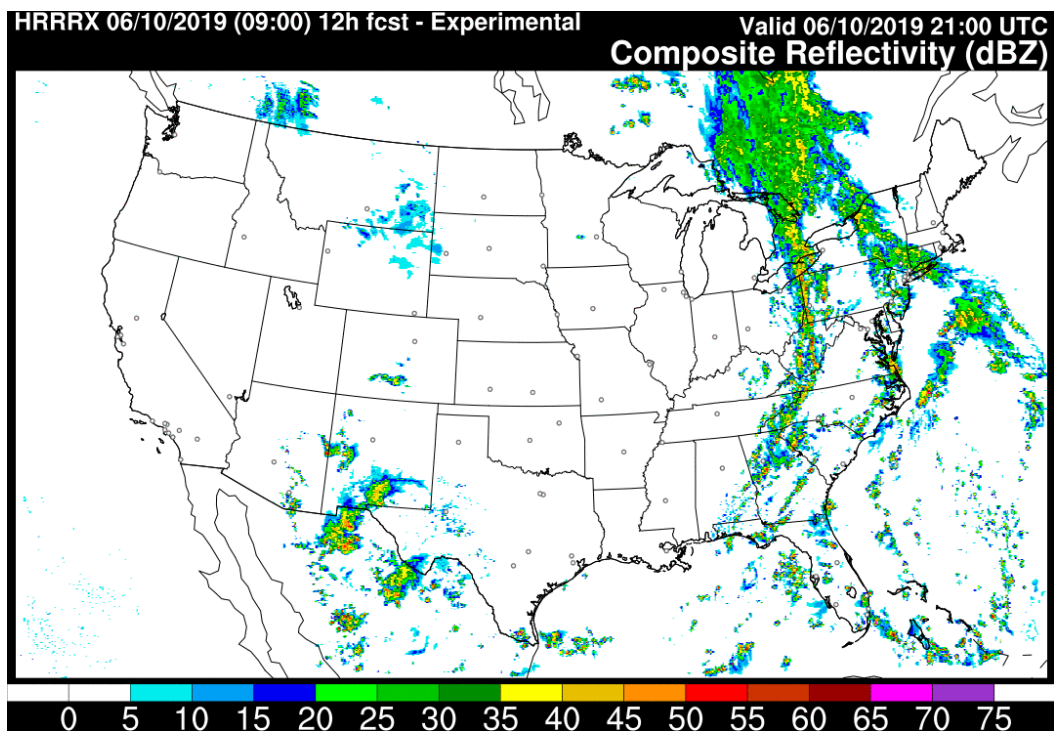


Fig. 10.5: Sample Composite Reflectivity forecast generated by HRRR. (Credit: ESRL, <https://rapidrefresh.noaa.gov/hrrr/>)

Lawson *et al.* (2018) describe a study comparing the effects of WSR-88D radar data assimilation on three different mesoscale models. The first was HRRR version 1 (HRRRv1), run operationally at NCEP, the second was HRRRv2, run in research mode at the beginning of their work but later run operationally at NCEP, and the third was a high spatial-resolution model ensemble system, called the NSSL Experimental Warn-on-Forecast System for Ensembles (NEWSe), which consists of 36 member models. They compared the FAR, POD, CSI, and other skill indicators for these three models using 12 cases (days) with heavy convective weather in the American Midwest and Great Plains regions, for the 0 - 3 hr period following the model initialization time.

Comparing gridded QPF, Lawson *et al.* (2018) showed that the ensemble model system outperformed both versions of the deterministic HRRR model in most situations. They also show that the relative advantage of the ensemble system over the two deterministic models approaches zero by the end of the 3-hr forecast period. This indicates that ensemble modeling, aided by the assimilation of operational radar data, is probably the best approach to achieving the goal of maximizing the short-term advantages of WoF for hazards associated with specific thunderstorms, such as hail, heavy rainfall, strong winds, and tornadoes.

This concludes our introduction to weather radar.

Summary. The next generation of weather radar is called phased array. While not a new idea (it dates back to WW II), it has not been as widely deployed for civilian purposes as conventional radar systems have over the last several decades. This type of radar does not use a single high-powered klystron or magnetron transmitter tube, but instead forms beams of pulsed EMR using hundreds or thousands of low-powered, solid-state Receiver-Transmitter Modules (RTMs) arranged on a flat plate. The ideal phased array radar installation has no rotating turntable or gearing to point or tilt an antenna, but instead relies on very short-term delays in the onset of pulse transmission in adjacent RTMs to point the beam. A complete installation is cube-shaped, with as many as 20,000 RTMs on each of the four vertical faces of the cube. Several beams can be simultaneously formed using small subsets of RTMs on each face of the cube, with each beam carrying out separate functions, such as completing a WSR-88D-like Volume Control Pattern, closely monitoring an individual severe convective storm, or tracking aircraft. The working name of the system is Multi-function Phased Array Radar (MPAR), and it is expected to eventually replace the existing network of WSR-88Ds, and two different FAA aircraft control radar networks.

Because of its ability to complete a volume scan in less than a minute, MPAR has already been used to image developing thunderstorm cells at a high enough temporal resolution to provide insights into the onset of microbursts and the formation of Bounded Weak Echo Regions (BWERs). But the high rate of data generation threatens to overwhelm human weather forecasters, who must intelligently evaluate the incoming data in order to make warning decisions for small geographic areas affected by individual thunderstorm cells. Rapid-refresh, high-spatial resolution computer modeling can assist with the “avalanche” of new data by assimilating Level II radar data (along with other types of meteorological data), and generate products that will help with warning decisions. The Warn-on-Forecast (WoF) program is working on the problem of ingesting the large volumes of data that MPAR will eventually generate, using mesoscale models rerun as often as once an hour, with radar reflectivity and other base moments used as input variables, with the goal of increasing tornado warning lead times to as much as 45 minutes.

Terms and concepts:

- Advanced Technology Demonstrator (ATD)
- Air Route Surveillance Radar (ARSR)
- Air Surveillance Radar (ASR)
- Bendix
- Defense Advanced Research Projects Agency (DARPA)
- Electronically-steered radar
- Electronically-Steered Array Radar (ESAR)
- FPS-85
- High-Resolution Rapid Refresh (HRRR)
- Massachusetts Institute of Technology (MIT) Lincoln Laboratory
- Multi-function Phased Array Radar (MPAR)
- National Lightning Detection Network (NLDN)
- National Weather Radar Testbed (NWRT)
- NSSL Experimental Warning-on-Forecast for Ensembles (NEWSe)
- Oklahoma Lightning Mapping Array (OLMA)
- Phased array
- Phased Array Radar Innovative Sensing Experiment (PARISE)
- Quasi-Linear Convective System (QLCS)
- Receiver-Transmitter Module (RTM)
- SPY-1A
- Warn-on-Forecast (WoF)

Study prompts:

1. Explain the difference between the pointing mechanisms used by conventional and phased array radar systems.
2. Describe the SPY-1A phased array system loaned to NOAA by the U.S. Navy.
3. Explain why the descendants of the NWRT MPAR can replace several existing radar systems at the same time, and why MPAR is much more resilient than a conventional radar system. How many beams will the RTM array be able to simultaneously create?

4. How does the temporal resolution of MPAR compare with that of the WSR-88D? Why are they different? Why is this useful?
5. Describe the National Weather Service's Warn-on-Forecast program, and how MPAR may be able to significantly increase warning lead-times for severe convective weather.

Appendix 1: WSR-88D and TDWR radar list.

With contributions from Stephen Baron.

Sources: <http://www.weather.gov>, <https://vortex.plymouth.edu/myo/rad/tdwr.html>,
<http://apollo.lsc.vsc.edu>, and <http://www.wispa.org>.

Station Name	Call Sign	Type	Agency	Latitude [DMS N]	Longitude [DMS E]	Terrain Elevation [m ASL]	Antenna Height [m AGL]
Aberdeen, SD	KABR	WSR-88D	NWS	45 27 21	-098 24 47	397	20
Aero. Ctr TDWR No. 1, OK		TDWR	FAA	35 24 19	-097 37 31	392	24
Aero. Ctr TDWR No. 2, OK		TDWR	FAA	35 23 34	-097 37 43	394	30
Albany, NY	KENX	WSR-88D	NWS	42 35 11	-074 03 50	557	20
Albuquerque, NM	KABX	WSR-88D	NWS	35 08 59	-106 49 26	1790	20
Altus AFB, OK	KFDR	WSR-88D	DoD	34 21 44	-098 58 35	386	10
Amarillo, TX	KAMA	WSR-88D	NWS	35 14 00	-101 42 33	1094	20
Anchorage/Kenai, AK	PAHG	WSR-88D	FAA	60 43 33	-151 21 05	83	30
Anderson AFB, GU	PGUA	WSR-88D	DoD	13 27 09	144 48 41	80	30
Atlanta, GA	KFFC	WSR-88D	NWS	33 21 49	-084 33 57	262	30
Atlanta, GA	TATL	TDWR	FAA	33 38 48	-084 15 44	293	34
San Antonio, TX	KEWX	WSR-88D	NWS	29 42 14	-098 01 42	193	20
Beale AFB, CA	KBBX	WSR-88D	DoD	39 29 46	-121 37 54	51	10
Bethel, AK	PABC	WSR-88D	FAA	60 47 31	-161 52 35	49	5
Benfield, MD	TBWI	TDWR	FAA	39 05 33	-076 37 48	56	34
Billings, MT	KBLX	WSR-88D	NWS	45 51 14	-108 36 24	1097	10
Binghamton, NY	KBGM	WSR-88D	NWS	42 11 59	-075 59 05	490	20
Birmingham, AL	KBMX	WSR-88D	NWS	33 10 20	-086 46 11	197	30
Bismarck, ND	KBIS	WSR-88D	NWS	46 46 15	-100 45 38	505	20
Boise, ID	KCBX	WSR-88D	NWS	43 29 26	-116 14 08	933	20
Boston, MA	KBOX	WSR-88D	NWS	41 57 21	-071 08 13	36	30
Boston, MA	TBOS	TDWR	FAA	42 09 30	-070 56 01	46	34
Brandywine, MD	TADW	TDWR	FAA	38 41 43	-086 50 42	71	34
Brownsville, TX	KBRO	WSR-88D	NWS	25 54 58	-097 25 08	7	10
Buffalo, NY	KBUF	WSR-88D	NWS	42 56 56	-078 44 12	211	20
Burlington, VT	KCXX	WSR-88D	NWS	44 30 40	-073 10 01	97	30
Camp Humphreys, ROK	RKSG	WSR-88D	DoD	36 57 21	127 01 16	16	20
Cannon AFB, NM	KFDX	WSR-88D	DoD	34 38 07	-103 37 48	1418	10
Cedar City, UT	KICX	WSR-88D	NWS	37 35 27	-112 51 44	3232	30
Charleston, SC	KCLX	WSR-88D	NWS	32 39 20	-081 02 32	26	30
Charleston, WV	KRLX	WSR-88D	NWS	38 18 40	-081 43 23	329	30
Charlotte, NC	TCLT	TDWR	FAA	35 21 39	-080 53 06	246	34
Cheyenne, WY	KCYS	WSR-88D	NWS	41 09 07	-104 48 22	1868	10
Chicago, IL	KLOT	WSR-88D	NWS	41 46 17	-088 05 05	202	20
Cincinnati, OH	KILN	WSR-88D	NWS	39 25 13	-083 49 18	322	30
Cleveland, OH	KCLE	WSR-88D	NWS	41 24 47	-081 51 35	233	20
Cleveland, OH	TLVE	TDWR	FAA	41 17 23	-082 00 28	249	34
Clinton, MD	TDCA	TDWR	FAA	38 45 32	-087 57 43	76	30
Columbia, SC	KCAE	WSR-88D	NWS	33 56 55	-081 07 06	70	30
Columbus, OH	TCMH	TDWR	FAA	40 00 20	-082 42 55	316	34

Columbus AFB, MS	KGWX	WSR-88D	DoD	33 53 48	-088 19 44	148	20
Corpus Christi, TX	KCRP	WSR-88D	NWS	27 47 03	-097 30 40	14	20
Covington, KY	TCVG	TDWR	FAA	38 53 53	-084 34 48	287	30
Crestwood, IL	TMDW	TDWR	FAA	41 39 05	-087 43 47	203	34
Dallas/Ft. Worth, TX	KFWS	WSR-88D	NWS	32 34 23	-097 18 11	208	20
Dallas Love Field, TX	TDAL	TDWR	FAA	32 55 33	-096 58 06	165	24
Davenport, IA	KDVN	WSR-88D	NWS	41 36 42	-090 34 51	230	20
Dayton, OH	TDAY	TDWR	FAA	40 01 19	-084 07 23	282	30
Denver, CO	KFTG	WSR-88D	NWS	39 47 12	-104 32 45	1676	30
Denver, CO	TDEN	TDWR	FAA	39 43 39	-104 31 35	1720	20
Des Moines, IA	KDMX	WSR-88D	NWS	41 43 52	-093 43 22	299	30
Desoto County, MS	TMEM	TDWR	FAA	34 53 45	-089 59 33	113	34
Detroit, MI	KDTX	WSR-88D	NWS	42 41 59	-083 28 18	327	30
Detroit, MI	TDTW	TDWR	FAA	42 06 40	-083 30 54	200	34
Dodge City, KS	KDDC	WSR-88D	NWS	37 45 39	-099 58 08	790	20
Dover AFB, DE	KDOX	WSR-88D	DoD	38 49 32	-075 26 23	15	30
Duluth, MN	KDLH	WSR-88D	NWS	46 50 13	-092 12 35	435	30
Dyess AFB, TX	KDYX	WSR-88D	DoD	32 32 18	-099 15 16	463	10
Edwards AFB, CA	KEYX	WSR-88D	DoD	35 05 52	-117 33 39	841	20
Eglin AFB, FL	KEVX	WSR-88D	DoD	30 33 52	-085 55 17	43	20
El Paso, TX	KEPZ	WSR-88D	NWS	31 52 23	-106 41 53	1251	30
Elko, NV	KLRX	WSR-88D	NWS	40 44 23	-116 48 10	2056	30
Eureka, CA	KBHX	WSR-88D	NWS	40 29 54	-124 17 31	732	30
Evansville, IN	KVWX	WSR-88D	NWS	38 15 37	-087 43 29	190	
Fairbanks, AK	PAPD	WSR-88D	FAA	65 02 06	-147 30 06	791	30
Flagstaff, AZ	KFSX	WSR-88D	NWS	34 34 28	-111 11 52	2261	20
Floyd Bennett Field, NY	TJFK	TDWR	FAA	40 35 20	-073 52 49	2	30
Fort Campbell, KY	KHPX	WSR-88D	DoD	36 44 12	-087 17 06	1756	10
Fort Hood, TX	KGRK	WSR-88D	DoD	30 43 19	-097 22 59	164	10
Fort Polk, LA	KPOE	WSR-88D	DoD	31 09 20	-092 58 33	124	10
Fort Rucker, AL	KEOX	WSR-88D	DoD	31 27 38	-085 27 34	132	10
Fort Smith, AR	KSRX	WSR-88D	NWS	35 17 26	-094 21 42	195	20
Fort Wayne, IN	KIWX	WSR-88D	NWS	41 21 32	-085 42 00	293	25
Fort Lauderdale, FL	TFLI	TDWR	FAA	26 08 36	-080 20 39	2	34
Gaylord, MI	KAPX	WSR-88D	NWS	44 54 26	-084 43 11	446	20
Glasgow, MT	KGGW	WSR-88D	NWS	48 12 23	-106 37 30	694	20
Goodland, KS	KGLD	WSR-88D	NWS	39 22 01	-101 42 01	1113	10
Grand Forks, ND	KMVX	WSR-88D	NWS	47 31 40	-097 19 32	301	20
Grand Junction, CO	KGJX	WSR-88D	NWS	39 03 44	-108 12 50	3046	10
Grand Rapids, MI	KGRR	WSR-88D	NWS	42 53 38	-085 32 41	237	20
Great Falls, MT	KTFX	WSR-88D	NWS	47 27 35	-111 23 07	1132	10
Green Bay, WI	KGRB	WSR-88D	NWS	44 29 54	-088 06 41	208	30
Greer, SC	KGSP	WSR-88D	NWS	34 53 00	-082 13 12	287	30
Hanover, PA	TPIT	TDWR	FAA	40 30 05	-080 29 10	386	34
Hastings, NE	KUEX	WSR-88D	NWS	40 19 15	-098 26 31	602	20
Holloman AFB, NM	KHDX	WSR-88D	DoD	33 04 35	-106 07 22	1287	10
Houlton, ME	KCBW	WSR-88D	NWS	46 02 21	-067 48 23	227	30
Houston, TX	TIAH	TDWR	FAA	30 03 54	-095 34 01	47	30
Houston/Galveston, TX	KHGX	WSR-88D	NWS	29 28 19	-095 04 45	5	20
Huntsville, AL	KHTX	WSR-88D	NWS	34 55 50	-086 05 00	537	15
Indianapolis, IN	KIND	WSR-88D	NWS	39 42 27	-086 16 49	241	20
Indianapolis, IN	TIDS	TDWR	FAA	39 38 14	-086 26 08	229	30

Jackson, KY	KJKL	WSR-88D	NWS	37 35 27	-083 18 47	416	25
Jackson, MS	KDGX	WSR-88D	NWS	32 19 04	-090 04 48	91	20
Jacksonville, FL	KJAX	WSR-88D	NWS	30 29 05	-081 42 07	10	20
Kadena, Okinawa (Japan)	RODN	WSR-88D	DoD	26 18 07	127 54 35	66	30
Kamuela, HI	PHKN	WSR-88D	FAA	20 07 32	-155 46 40	1173	30
Kansas City, MO	KEAX	WSR-88D	NWS	38 48 37	-094 15 52	303	20
Kansas City, MO	TMCI	TDWR	FAA	39 29 55	-094 44 31	317	20
Key West, FL	KBYX	WSR-88D	NWS	24 35 51	-081 42 11	2	20
King Salmon, AK	PAKC	WSR-88D	FAA	58 40 46	-156 37 46	19	20
Knoxville/Tri-Cities, TN	KMRX	WSR-88D	NWS	36 10 07	-083 24 06	408	20
Kohala, HI	PHKM	WSR-88D	FAA	20 07 32	-155 46 41		
Kunsan AB, ROK	RKJK	WSR-88D	DoD	35 55 27	126 37 20	24	30
La Crosse, WI	KARX	WSR-88D	NWS	43 49 22	-091 11 28	392	20
Lajes AB, Azores	LPLA	WSR-88D	DoD	38 43 49	-027 19 18	1016	20
Lake Charles, LA	KLCH	WSR-88D	NWS	30 07 31	-093 12 57	4	20
Las Vegas, NV	KESX	WSR-88D	NWS	35 42 04	-114 53 29	1484	20
Las Vegas, NV	TLAS	TDWR	FAA	36 08 37	-115 00 26	608	20
Langley Hill, WA	KLGX	WSR-88D	NWS	47 07 05	-124 06 26	108	
Laughlin AFB, TX	KDFX	WSR-88D	DoD	29 16 22	-100 16 50	345	10
Leesburg, VA	TIAD	TDWR	FAA	39 05 02	-077 31 46	110	34
Lewisville DFW, TX	TDFW	TDWR	FAA	33 03 53	-096 55 05	169	9
Lincoln, IL	KILX	WSR-88D	NWS	40 09 02	-089 20 13	177	30
Little Rock, AR	KLZK	WSR-88D	NWS	34 50 11	-092 15 44	173	20
Los Angeles, CA	KVTX	WSR-88D	NWS	34 24 42	-119 10 46	831	20
Louisville, KY	KLVX	WSR-88D	NWS	37 58 31	-085 56 38	219	30
Louisville, KY	TSDF	TDWR	FAA	38 02 45	-085 36 38	188	34
Lubbock, TX	KLBB	WSR-88D	NWS	33 39 15	-101 48 51	994	20
Marquette, MI	KMQT	WSR-88D	NWS	46 31 52	-087 32 54	430	30
Maxwell AFB, AL	KMXX	WSR-88D	DoD	32 32 12	-085 47 23	122	30
McCook, IL	TORD	TDWR	FAA	41 47 50	-087 51 31	197	30
Medford, OR	KMAX	WSR-88D	NWS	42 04 52	-122 43 02	2291	10
Melbourne, FL	KMLB	WSR-88D	NWS	28 06 48	-080 39 15	11	20
Memphis, TN	KNQA	WSR-88D	NWS	35 20 41	-089 52 24	86	20
Miami, FL	KAMX	WSR-88D	NWS	25 36 40	-080 24 46	4	20
Miami, FL	TMIA	TDWR	FAA	25 45 26	-080 29 28	3	34
Middleton Island, AK	PAIH	WSR-88D	FAA	59 27 41	-146 18 11	20	10
Midland/Odessa, TX	KMAF	WSR-88D	NWS	31 56 36	-102 11 21	874	10
Milwaukee, WI	KMKX	WSR-88D	NWS	42 58 04	-088 33 02	292	10
Milwaukee, WI	TMKE	TDWR	FAA	42 49 10	-088 02 47	250	34
Minneapolis/St. Paul, MN	KMPX	WSR-88D	NWS	44 50 56	-093 33 56	288	30
Minneapolis/St. Paul, MN	TMSP	TDWR	FAA	44 52 17	-092 55 58	317	24
Minot AFB, ND	KMBX	WSR-88D	DoD	48 23 33	-100 51 54	455	20
Missoula, MT	KMSX	WSR-88D	NWS	47 02 28	-113 59 10	2395	10
Mobile, AL	KMOB	WSR-88D	NWS	30 40 46	-088 14 23	63	20
Molokai, HI	PHMO	WSR-88D	FAA	21 07 58	-157 10 48	416	20
Montague/Ft. Drum, NY	KTYX	WSR-88D	NWS	43 45 20	-075 40 48	597	
Moody AFB, GA	KVAX	WSR-88D	DoD	30 23 25	-083 00 06	53	30
Morehead City, NC	KMHX	WSR-88D	NWS	34 46 34	-076 52 34	9	30
Nashville, TN	KOHX	WSR-88D	NWS	36 14 50	-086 33 45	177	20
Nashville, TN	TBNA	TDWR	FAA	35 58 47	-086 39 42	220	30
New Orleans, LA	KLIX	WSR-88D	NWS	30 20 12	-089 49 32	7	30
New Orleans, LA	TMSY	TDWR	FAA	30 01 18	-090 24 11	1	30

New York City, NY	KOKX	WSR-88D	NWS	40 51 56	-072 51 50	26	30
Nome, AK	PAEC	WSR-88D	FAA	64 30 41	-165 17 42	16	5
Norfolk/Richmond, VA	KAKQ	WSR-88D	NWS	36 59 02	-077 00 26	34	20
North Platte, NE	KLNX	WSR-88D	NWS	41 57 28	-100 34 35	905	20
Oklahoma City, OK	KTLX	WSR-88D	NWS	35 19 59	-097 16 40	370	15
Oklahoma City, OK	TOKC	TDWR	FAA	35 16 34	-097 30 36	364	20
Omaha, NE	KOAX	WSR-88D	NWS	41 19 13	-096 22 00	350	30
Orlando, FL	TMCO	TDWR	FAA	28 20 37	-081 19 13	22	30
Paducah, KY	KPAH	WSR-88D	NWS	37 04 06	-088 46 19	120	30
Pearland, TX	THOU	TDWR	FAA	29 30 59	-095 14 30	11	24
Pendleton, OR	KPDT	WSR-88D	NWS	45 41 26	-118 51 10	462	10
Pennsauken, NJ	TPHL	TDWR	FAA	39 56 57	-075 04 12	103	34
Philadelphia, PA	KDIX	WSR-88D	NWS	39 56 49	-074 24 39	45	20
Phoenix, AZ	KIWA	WSR-88D	NWS	33 17 21	-111 40 12	413	10
Phoenix, AZ	TPHX	TDWR	FAA	33 25 14	-112 09 46	312	20
Pittsburgh, PA	KPBZ	WSR-88D	NWS	40 31 54	-080 13 05	361	20
Pocatello/Idaho Falls, ID	KSFY	WSR-88D	NWS	43 06 21	-112 41 10	1364	10
Portland, ME	KGYX	WSR-88D	NWS	43 53 29	-070 15 23	125	10
Portland, OR	KRTX	WSR-88D	NWS	45 42 53	-122 57 55	479	30
Pueblo, CO	KPUX	WSR-88D	NWS	38 27 34	-104 10 53	1600	10
Raleigh/Durham, NC	KRAX	WSR-88D	NWS	35 39 56	-078 29 23	106	30
Raleigh/Durham, NC	TRDU	TDWR	FAA	36 00 07	-078 41 50	122	34
Rapid City, SD	KUDX	WSR-88D	NWS	44 07 30	-102 49 47	920	30
Reno, NV	KRGX	WSR-88D	NWS	39 45 15	-119 27 44	2530	20
Riverton, WY	KRIW	WSR-88D	NWS	43 03 58	-108 28 38	1698	10
Roanoke, VA	KFCX	WSR-88D	NWS	37 01 28	-080 16 26	874	20
Robins AFB, GA	KJGX	WSR-88D	DoD	32 40 31	-083 21 04	159	20
Sacramento, CA	KDAX	WSR-88D	NWS	38 30 04	-121 40 40	9	30
Saint Louis, MO	KLSX	WSR-88D	NWS	38 41 56	-090 40 58	185	30
Saint Louis, MO	TSTL	TDWR	FAA	38 48 20	-090 29 21	168	30
Salt Lake City, UT	KMTX	WSR-88D	NWS	41 15 46	-112 26 52	1970	30
Salt Lake City, UT	TSLC	TDWR	FAA	40 58 02	-111 55 47	1286	24
San Angelo, TX	KSJT	WSR-88D	NWS	31 22 17	-100 29 33	576	30
San Diego, CA	KNKX	WSR-88D	NWS	32 55 08	-117 02 31	291	20
San Francisco, CA	KMUX	WSR-88D	NWS	37 09 19	-121 53 54	1058	20
San Joaquin Valley, CA	KHNX	WSR-88D	NWS	36 18 51	-119 37 56	74	20
San Juan, PR	TJUA	WSR-88D	FAA	18 06 56	-066 04 41	852	30
San Juan, PR	TSJU	TDWR	FAA	18 28 26	-066 10 46	18	34
Santa Ana Mountains, CA	KSOX	WSR-88D	NWS	33 49 04	-117 38 09	923	15
Seattle/Tacoma, WA	KATX	WSR-88D	NWS	48 11 40	-122 29 45	151	30
Shreveport, LA	KSHV	WSR-88D	NWS	32 27 03	-093 50 29	83	30
Sioux Falls, SD	KFSD	WSR-88D	NWS	43 35 16	-096 43 46	436	10
Sitka, AK	PACG	WSR-88D	FAA	56 51 10	-135 31 45	64	10
South Kauai, HI	PHKI	WSR-88D	FAA	21 53 39	-159 33 08	55	30
South Shore, HI	PHWA	WSR-88D	FAA	19 05 42	-155 34 08	421	20
Spokane, WA	KOTX	WSR-88D	NWS	47 04 49	-117 37 36	727	10
Springfield, MO	KSGF	WSR-88D	NWS	37 14 07	-093 24 02	390	20
State College, PA	KCCX	WSR-88D	NWS	40 55 23	-078 00 13	733	20
Sterling, VA	KLWX	WSR-88D	NWS	38 58 31	-077 28 40	74	25
Tallahassee, FL	KTLH	WSR-88D	NWS	30 23 51	-084 19 44	19	30
Tampa, FL	KTBW	WSR-88D	NWS	27 42 20	-082 24 06	13	20
Tampa, FL	TTPA	TDWR	FAA	27 51 35	-082 31 04	4	24

Topeka, KS	KTWX	WSR-88D	NWS	38 59 49	-096 13 57	417	10
Tucson, AZ	KEMX	WSR-88D	NWS	31 53 37	-110 37 49	1587	30
Tulsa, OK	KINX	WSR-88D	NWS	36 10 30	-095 33 53	204	20
Tulsa, OK	TTUL	TDWR	FAA	36 04 14	-095 49 34	217	34
Vance AFB, OK	KVNX	WSR-88D	DoD	36 44 27	-098 07 40	369	10
Vandenberg AFB, CA	KVBX	WSR-88D	DoD	34 50 17	-120 23 45	373	20
West Palm Beach, FL	TPBI	TDWR	FAA	26 41 17	-080 16 23	6	34
Wichita, KS	KICT	WSR-88D	NWS	37 39 17	-097 26 34	407	10
Wichita, KS	TICH	TDWR	FAA	37 30 26	-097 26 13	387	24
Wilmington, NC	KLTX	WSR-88D	NWS	33 59 22	-078 25 44	20	20
Woodbridge, NJ	TEWR	TDWR	FAA	40 35 37	-074 16 13	6	34
Yuma, AZ	KYUX	WSR-88D	NWS	32 39 43	-114 39 24	53	10

Appendix 2: Forecasting Skill.

For clarity, here we will define remote detection of a given phenomenon as a nowcast, which is a kind of forecast. This is opposed to a direct *in situ* measurement of the phenomenon, which we classify as an observation. The simplest possible scenario that includes forecasts and observations involves binary outcomes, *i.e.* yes/no answers. For example, if a forecast includes a prediction of rain, and rain does in fact occur, this is summarized as a “yes/yes” scenario. Given a statistically-meaningful database of N cases, Table A2.1 summarizes all possible combinations of outcomes.

Table A2.1: Possible combinations of binary forecasts and subsequent observations. The total number of cases (N) is equal to A+B+C+D.

		OBSERVATIONS	
		Yes	No
FORECASTS	Yes	A “Hit”	C “False Alarm”
	No	B “Miss”	D “Correct Non-Event”

Category A is defined as a “hit,” where a positive forecast of some event (such as hail) is verified by later, direct observations. Category B is a “miss,” wherein an unforecast event actually occurs. Category C is a “false alarm,” meaning that the forecast for a given parameter was not verified by later observations. Category D is a correct forecast of something that didn’t happen, called a “correct non-event,” such as a radar-based determination that a particular storm cell would *not* produce warning-threshold hail, and no such hail was subsequently observed with that particular cell.

Given these parameters, the following metrics can be defined. The first is the **Proportion Correct (PC)**, defined as:

$$PC \equiv \frac{A + D}{A + B + C + D} \tag{A2.1}$$

which varies between 0 and 1, the latter being a perfect score. The second is the **Frequency Bias (FB)**, defined as:

$$FB \equiv \frac{A + C}{A + B} \quad (\text{A2.2})$$

which varies between 0 and ∞ . An outcome of 1 indicates a perfect score, and implies both C (false alarms) and B (misses) are equal to zero. If $FB > 1$, the forecaster (or algorithm) is *over*-forecasting the phenomenon. If $FB < 1$, the forecaster is *under*-forecasting the phenomenon (Ghelli 2009).

The next three metrics are commonly used and closely related to one another (Gerapetritis and Pelissier ND, Gerapetritis and Pelissier 2004, Ghelli 2009, AMS 2012, Schaefer 1990). The first of this is **Probability of Detection (POD)**, defined by:

$$POD \equiv \frac{A}{A + B} \quad (\text{A2.3})$$

which varies between 0 and 1, with the latter being a perfect score. This captures information about the likelihood that a given phenomenon will be forecast at all. The next is the **False Alarm Rate (FAR)**, given by:

$$FAR \equiv \frac{C}{A + C} \quad (\text{A2.4})$$

which also varies between 0 and 1. If FAR is equal to zero, then every positive forecast of a phenomenon is verified by subsequent observations. In an ideal world, every forecast technique would report a POD of 1, and a FAR of zero. The **Critical Success Index (CSI)** combines these metrics by:

$$CSI \equiv \frac{A}{A + B + C} \quad (\text{A2.5})$$

which, like POD and FAR, varies between 0 and 1, with 1 being a perfect score. After several steps, it can be shown that CSI is also a function of POD and FAR, given by:

$$CSI \equiv \frac{1}{\frac{1}{(1 - FAR)} + \frac{1}{POD} - 1} \quad (\text{A2.6})$$

Given the more complicated (and realistic) possibility that a simple yes/no isn't sufficient for describing an outcome, the **Skill Score (SS)** can be used, which is defined by:

$$SS \equiv 1 - \frac{E_f}{E_{refr}} \quad (A2.7)$$

where E_f is the root-mean square (or absolute) errors associated with a particular forecaster or forecasting technique, and E_{refr} is the RMS error associated with a reference technique. (Climatological tables are often used as the reference technique.) If $SS > 0$, then $E_f < E_{refr}$, and the forecasting technique has greater skill than the reference technique (AMS 2012). Ghelli (2009) defines several more parameters that can also be used to gauge skill in these cases.

Appendix 3: Visualizing radar data with IDV and GR2Analyst

Contributed by Christopher Hohman.

A3.1. Integrated Data Viewer (IDV).

A3.1.1. **History.** In September 2002, the Integrated Data Viewer software package was completed and released by The University Corporation for Atmospheric Research (UCAR), in Boulder, Colorado. The project was funded by the National Science Foundation. The software has gone through several updates since its initial release, and it is still completely free for anyone to download under the terms of the GNU Lesser General Public License (<https://www.gnu.org/licenses/old-licenses/lgpl-2.1.en.html>). IDV was created to allow easy manipulation and visualization of atmospheric data, including radar and upper air data, satellite imagery, surface analyses, and others. It allows users to create graphical displays ranging from simple 2-D maps of upper-level geopotential heights, to 3-D displays of radar mosaics.

The scope of this appendix is to describe basic methods of obtaining and visualizing radar data using IDV. For more detailed basic instructions in navigating the display, including how to move the field of view, zooming in and out, resetting the image, and other basic functions, follow the link below:

<https://www.unidata.ucar.edu/software/idv/docs/workshop/installandstart/basics/index.html>

A3.1.2. Setting up and running IDV on a computer.

- Point the web browser to www.unidata.ucar.edu/software/idv/.
- Click the link on the left hand side of the page labelled “Download.”
- Under IDV downloads click, “Current Release.”
- If using a Windows computer, select the download link that says “IDV Installer for 64-bit Windows XP/Vista/10.” If using a Linux computer, select “IDV Installer for Linux.”
- Once the file is downloaded, open it. A prompt may appear with a message that asks for your permission to open IDV. Select “Run.”
- The display shown in Figure A3.1 should appear on the screen:

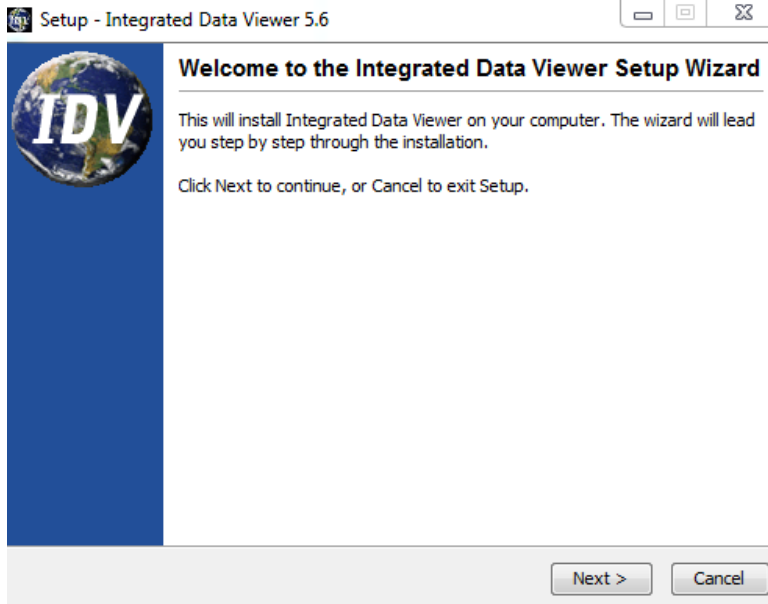


Fig. A3.1: IDV initial set-up screen.

- Select "Next." Accept the license agreement, decide where to install IDV, and whether a desktop icon is needed. Once these decisions are made, the installation will begin.
- Open IDV once installation is completed. The following two windows will open (Figure A3.2):

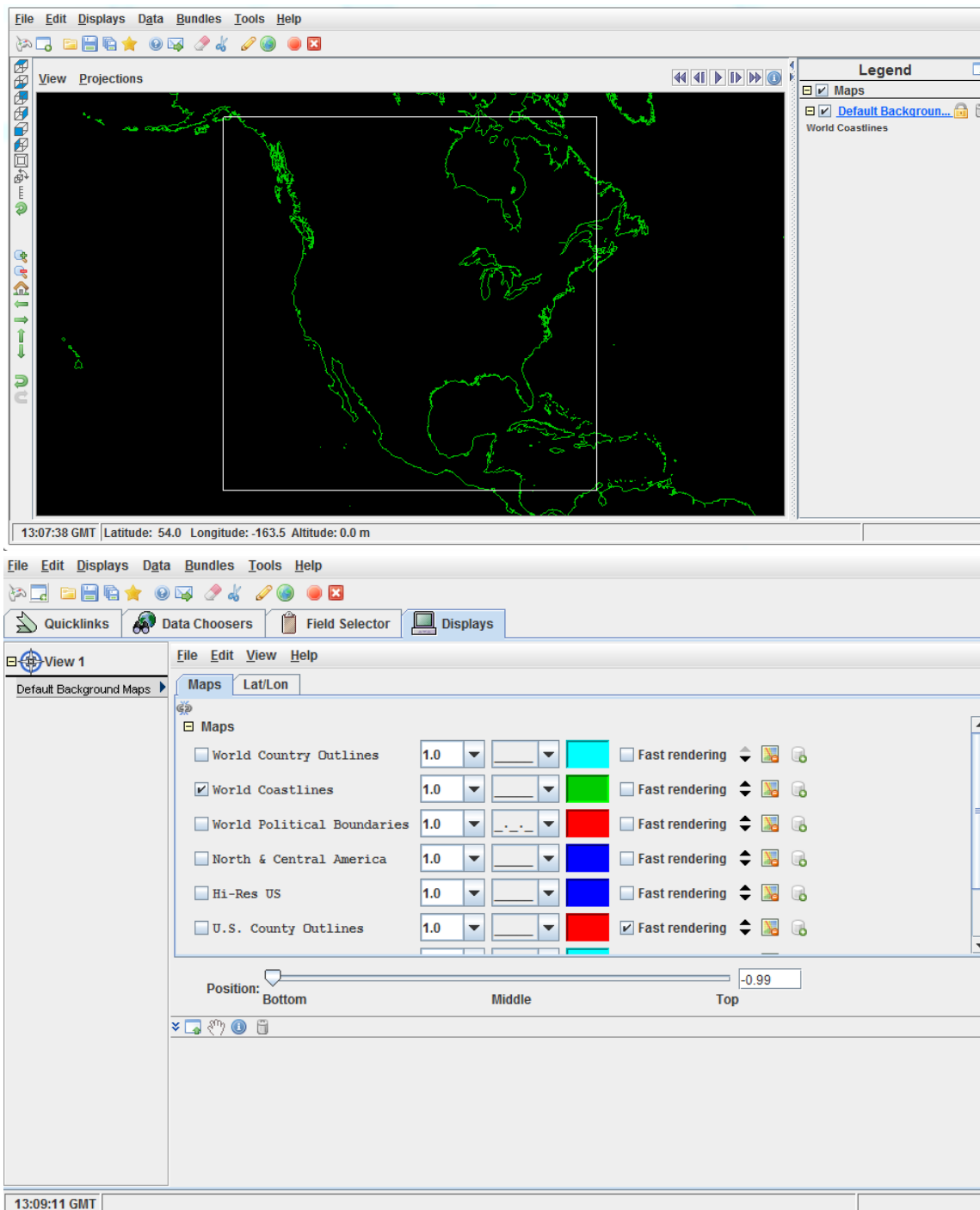


Fig. A3.2: IDV opening screens.

A3.1.3. Obtaining Radar Data.

A3.1.3.1. **Retrieving *current* radar data.** Click the “Data Choosers” tab. Scroll down the left side and see “Radar.” The “Radar” chooser contains three sub-tabs

for choosing radar data. The first is NEXRAD Level III data (derived products) on remote Abstract Data Distribution Environment (ADDE) servers, NEXRAD Level II/III data (quality-controlled base moments and derived products) from the local computer's file system, or a remote Thematic Real-time Environmental Distributed Data Services (THREDDS) Data Server (Figure A3.3).

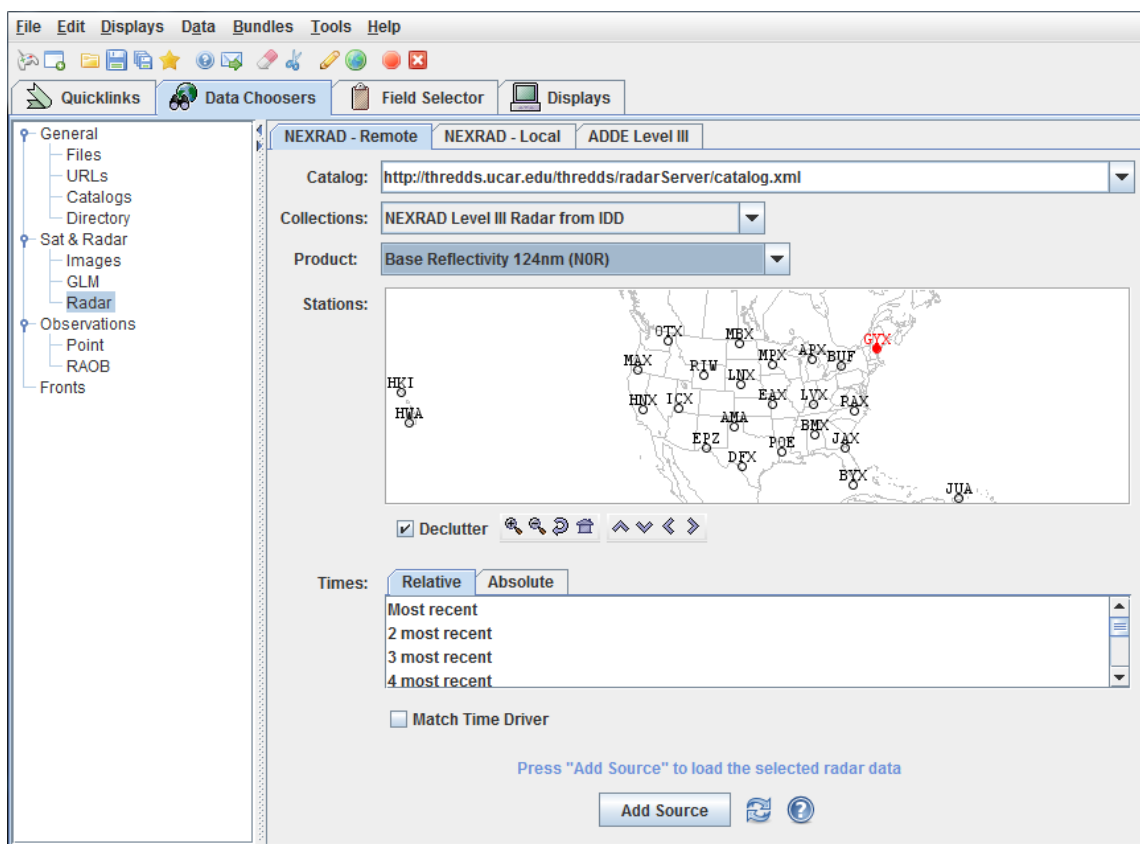


Fig. A3.3: Options for selecting radar data.

- Select the “NEXRAD – Remote” tab.
- Decide which “Catalog” (listings of data holdings on remote data servers), “Collection” (selecting Level II or III data) and “Product” (specific radar product) to use (Figure A3.3).
- Select the desired RDA by clicking on its 3-letter identifier.
- There are two options for determining time stamps. The first option is using the “Relative” tab underneath the Stations map. One can select the most recent scan, the two most recent scans, three most recent, etc.

- The “Absolute” tab is the second way to determine time stamps. It allows the user to select scans at specific times. This option is depicted below. (Figure A3.4).

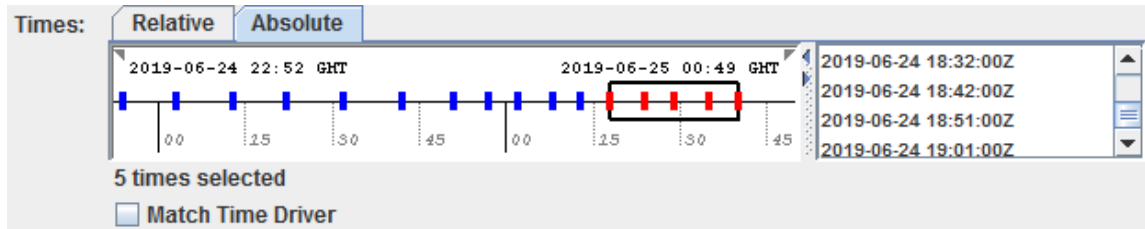


Fig. A3.4. Use of “Absolute” time tab.

- Load the data with the “Add Source” button.

A3.1.3.2. **Retrieving archived radar data.** The National Center for Environmental Information (NCEI) has archived radar data including the Next Generation Weather Radar System (NEXRAD, *i.e.* WSR-88D) and Terminal Doppler Weather Radar (TDWR) networks. Data are free and available from all weather radar systems in the United States.

- Point the internet browser to <https://www.ncdc.noaa.gov/data-access/radar-data>
- Select “Download Radar Data.”
- There are multiple ways to select data to best suit one’s needs. WSR-88D and TDWR sites can be selected via a list, or be searched by county, state, and (postal) zip code. For most orders, using the “Select by Map” option will suffice.
- In the “Select by Map” option, there is a display of all current RDAs, represented by blue dots. Click on the blue dot associated with the desired RDA.
- After choosing an RDA, a new page will load asking for more information. Using the pull-down menus, select the desired date. Below that, select the radar product in the scroll-down menu.
- Once the datatype is chosen, select “Create Graph.”
- In the new page, enter an email address for the data to be sent to. Once finished, select “Order Data.” Depending on the current volume of requests, this can take minutes or hours.
- Once the data are sent to an accessible email address, download it onto a computer. Move this data into a known location so it is easy to find in IDV.
- In IDV, select the “Data Choosers” tab.

- Select “Radar” on the left-hand side.
- Select the “NEXRAD - Local” tab (Figure A3.5):

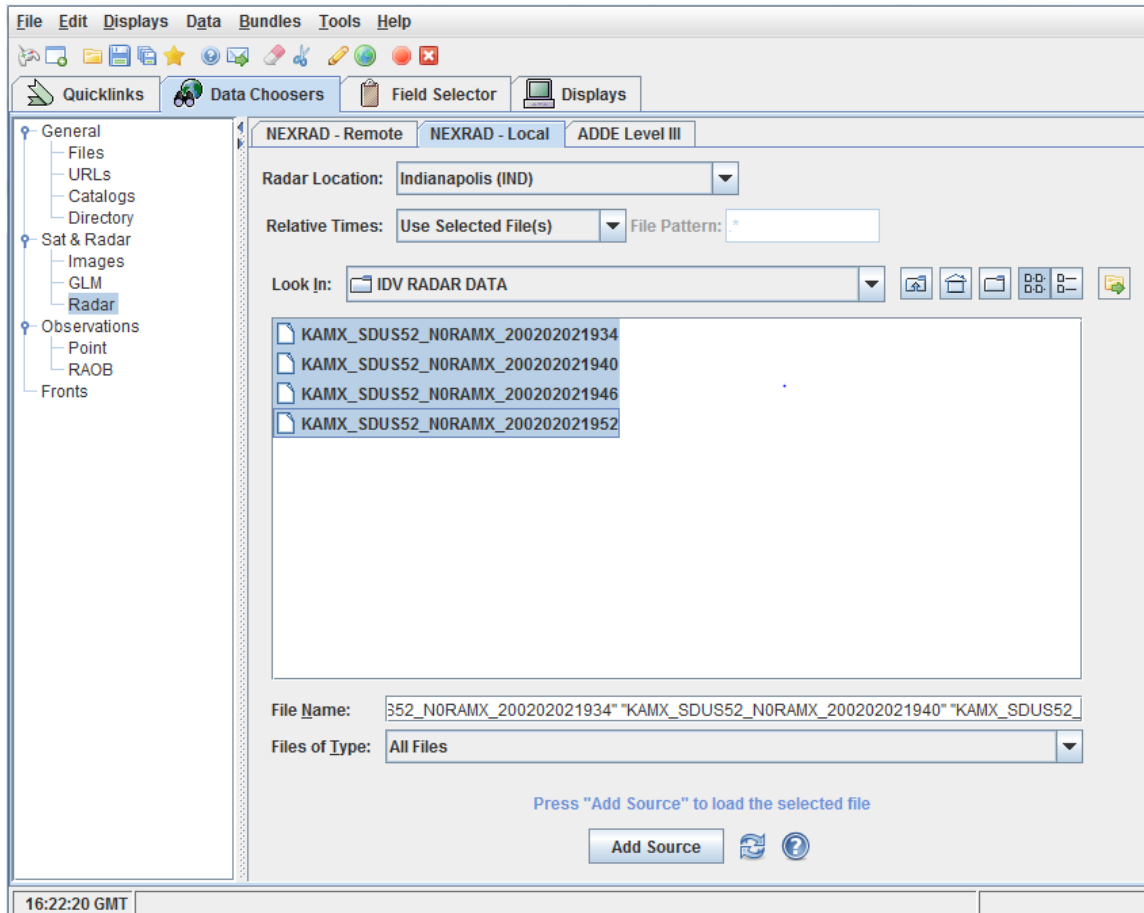


Fig. A3.5: Loading archived radar data from a local directory.

- Navigate to the file location using the “Look in” pull-down menu.
- Once the files are located, select relative times by using the 2 most recent, 3 most recent, etc. There is also the option to simply source specific files. (This is done in the example shown in Figure A3.5.)
- Select “Add Source.”

A3.1.3.3. Selecting Level III data from an ADDE server.

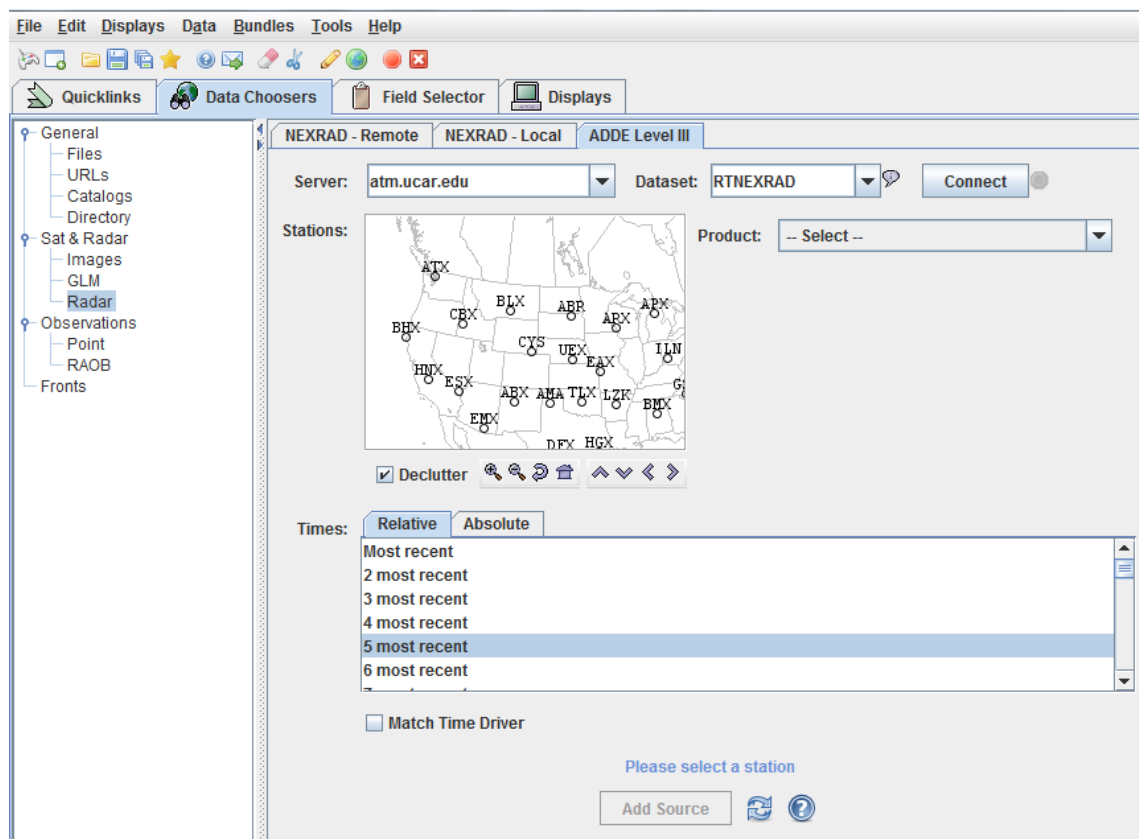


Fig. A3.6: Loading Level III data.

- Select the server and dataset desired, then use the “connect” button to query the ADDE server.
- Use the product pull down menu to decide which Level III datatype to use.
- Stations will populate in the U.S. map. Use the magnifying glass buttons to zoom in and out, and the arrow buttons to move around the map. Select the desired RDA by clicking on it.
- Similar to the NEXRAD - Remote tab described above, both “Relative” and “Absolute” time stamp options are available.
- Once the desired dataset is acquired, select “Add Source.”

A3.1.4. **Basic 2-D visualization.** Once the desired data have been selected by one of the three means described above, navigate to the “Field Selector” tab. This tab is the staging area for visually displaying radar products. In the example below (Figure A3.7), Level II data from the KCRP station are displayed.

This example describes a reflectivity display, however all of the other products (radial velocity, correlation coefficient, etc.) can be displayed by following the same procedure.

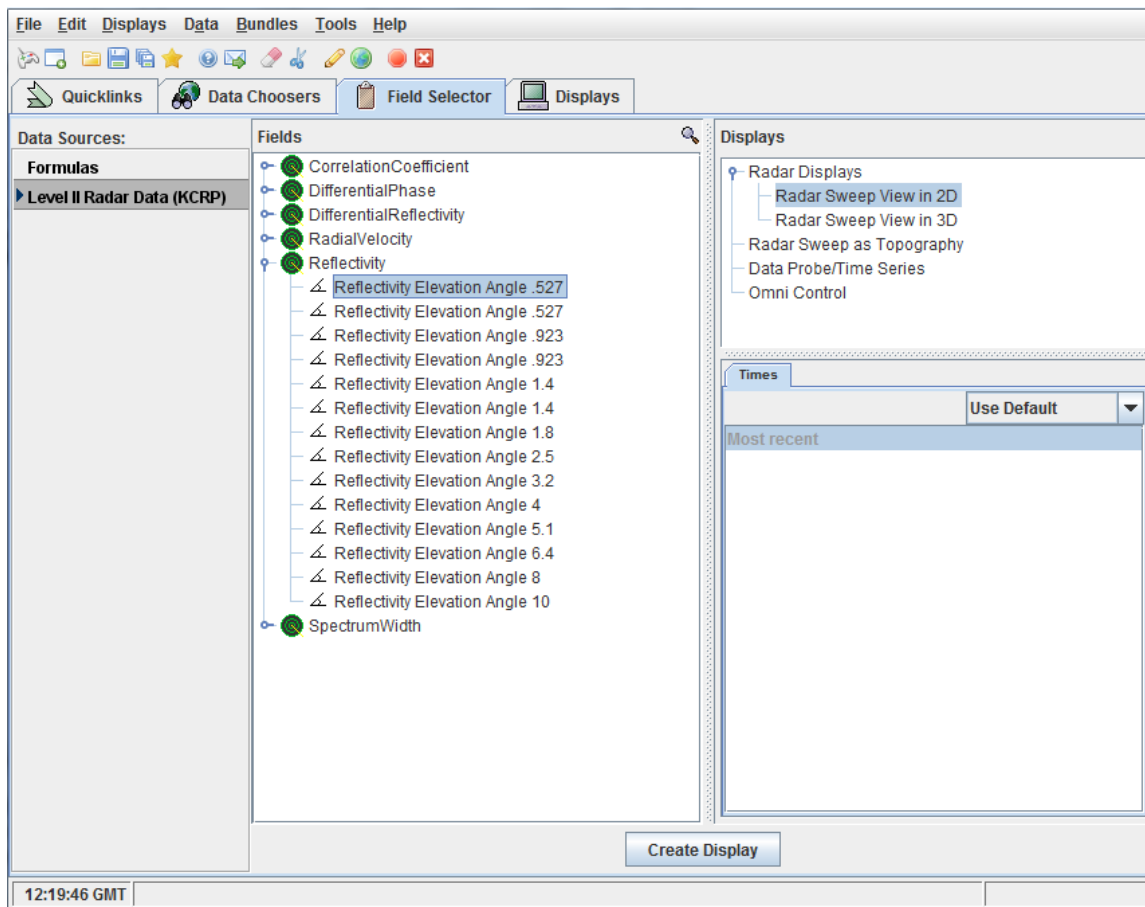


Fig. A3.7: Selecting IDV display of KCRP 0.5° reflectivity.

The left-hand side of this tab shows “Data Sources.” This is where all station data loaded into the current IDV session are cataloged. One can easily navigate between different RDAs by simply clicking on the data source. (In this example, data for only one RDA are loaded.) The “Fields” section displays every product available from the current data source. Clicking on the blue key next to one of these products will drop down into specific radar elevation angles. Select a desired elevation angle by clicking on it. On the right-hand side in the “Displays” section select “Radar Sweep View in 2-D.” Finally, select “Create Display.” This will project the desired product onto a map surrounding the radar (Figure A3.8).

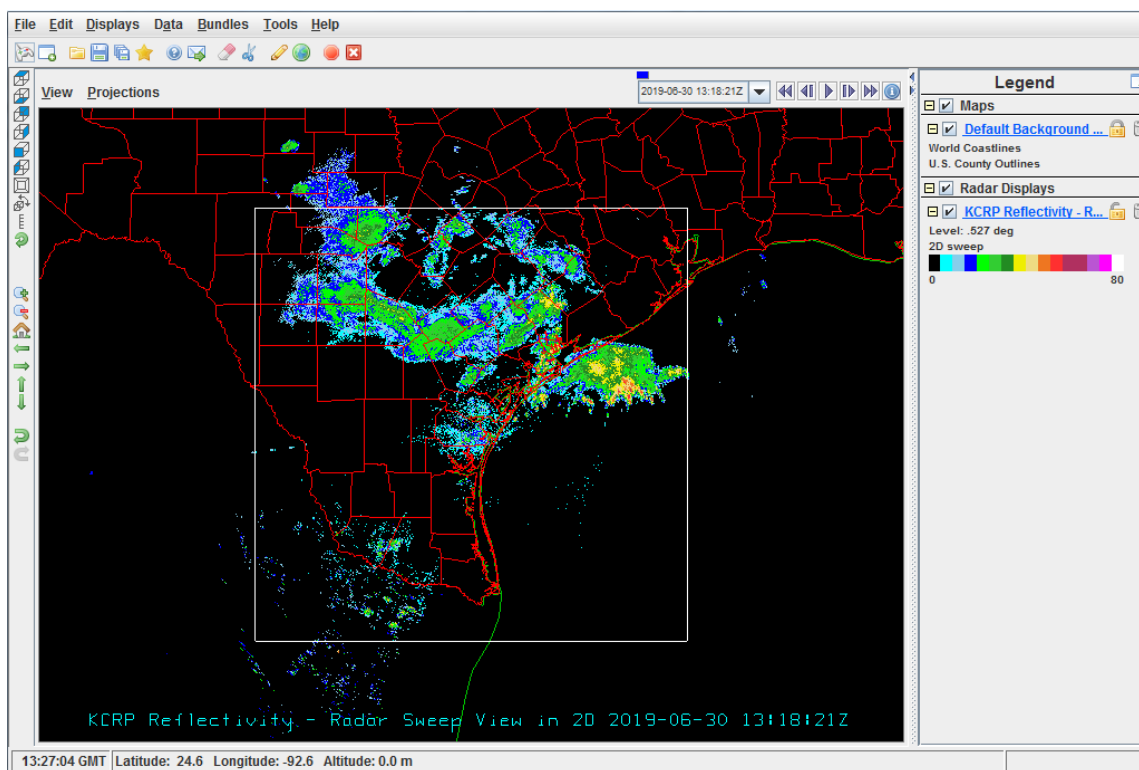


Fig. A3.8: 2-D display of 0.5 ° tilt reflectivity.

A3.1.5. **Changing the color scheme.** Changing the range, texture quality, and color scheme is done in the “Displays” tab. The color scheme is changed by selecting the button next to “Color Table” (Figure A3.9).

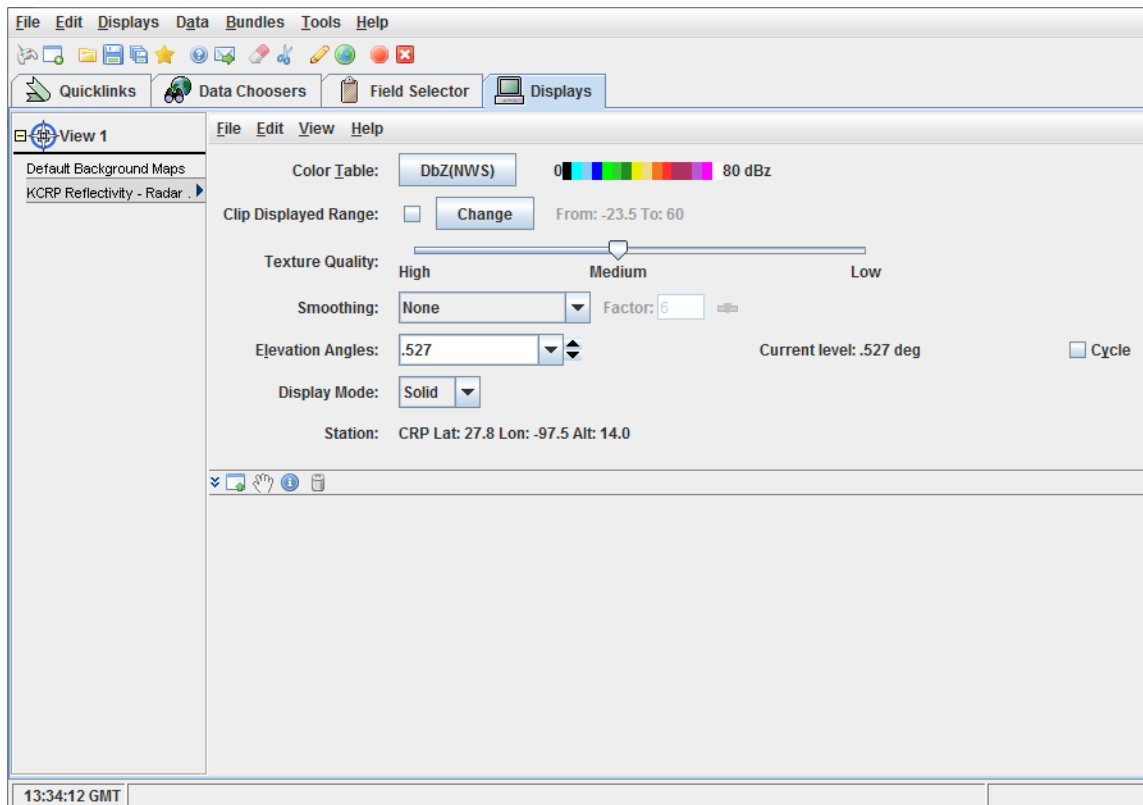


Fig. A3.9: Changing color scheme.

A drop-down menu will appear; select “Edit Color Table.” This will open a new window allowing the color scheme to be edited. Select a color by using the rainbow scale in the bottom left, then determine the exact shade in the box next to it. Once the exact color has been determined, click on any one of the boxes above. This will change it to that exact color (Figure A3.10). Click “Apply” to save these new color settings.

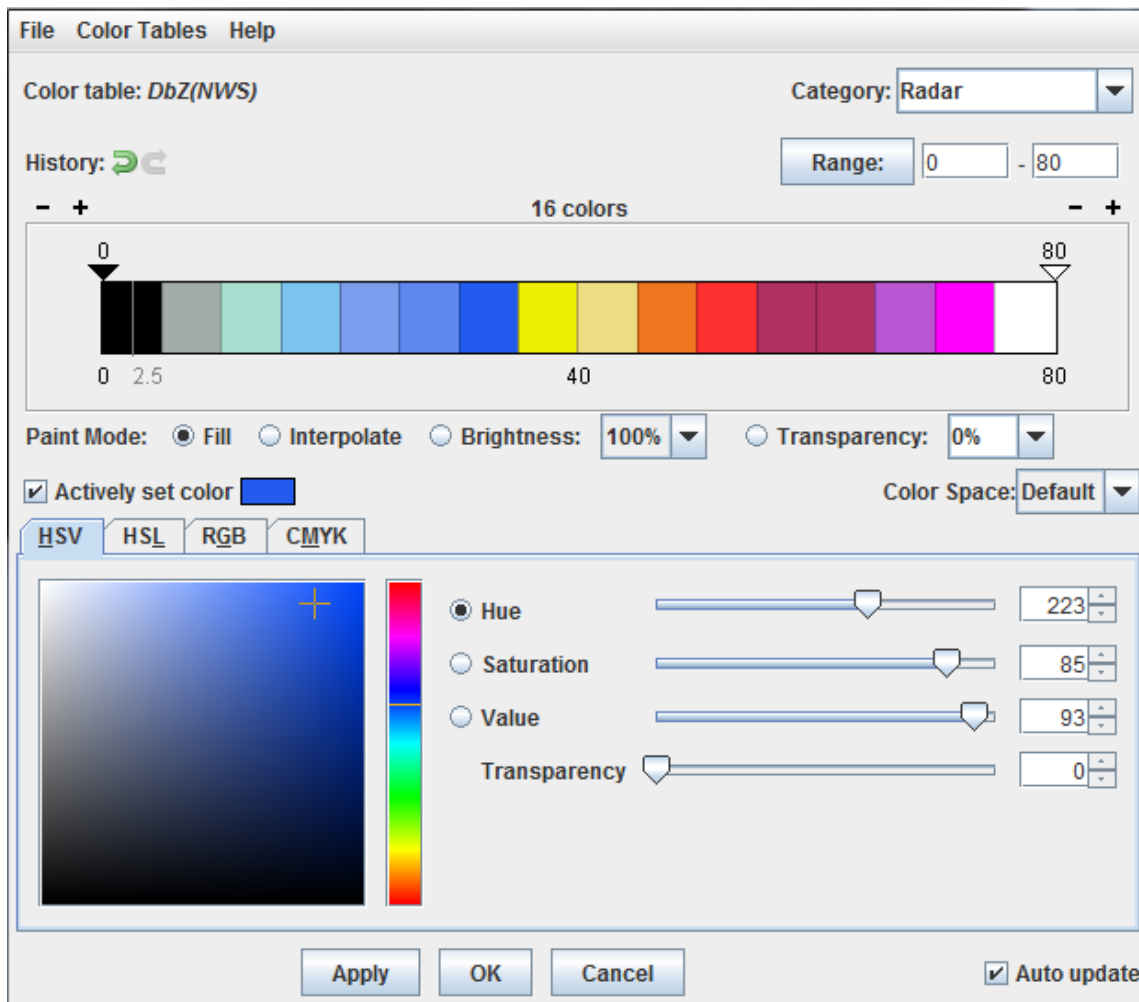


Fig. A3.10: Adjusting color scheme.

A3.1.6. **Basic 3-D visualization.** 3-D displays are created using a method very similar to that of 2-D displays. The only difference is selecting the 3-D option in the Field Selector tab. Determine the exact radar tilt angle, then in the Displays section select "Radar Sweep in 3-D" (Figure A3.11).

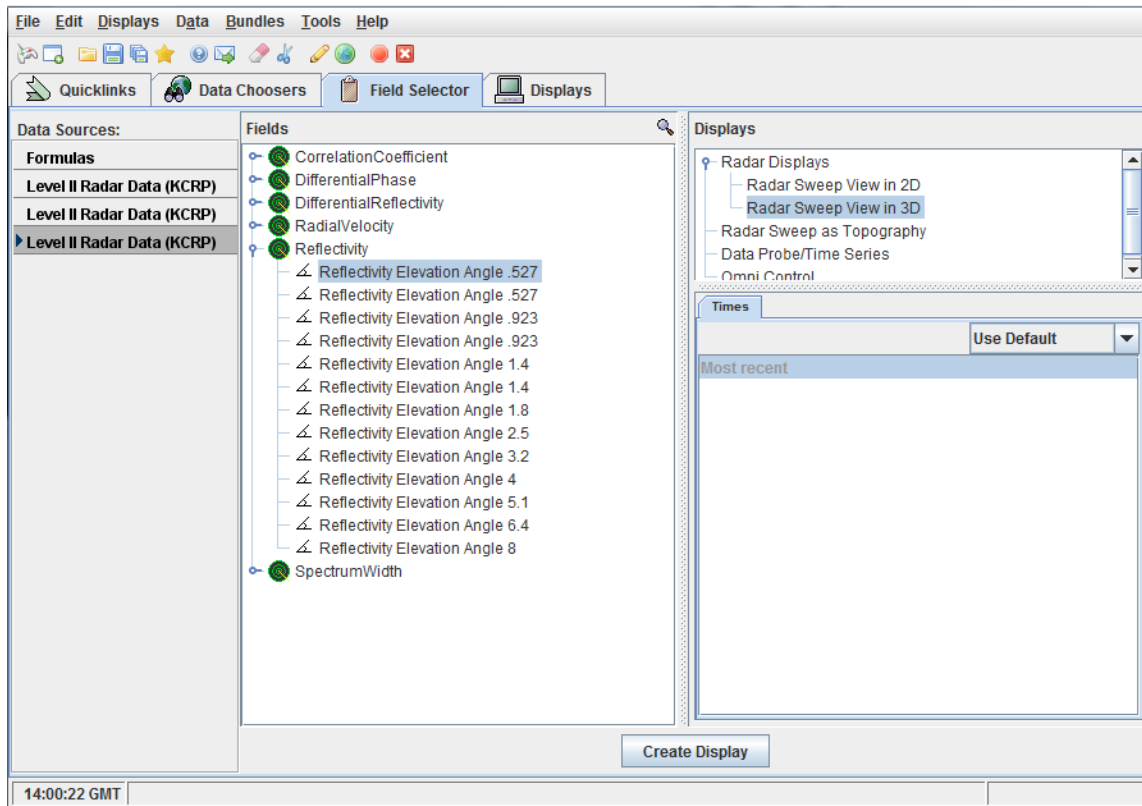


Fig. A3.11: Setting up 3-D displays.

Select "Create Display," and a 3-D radar sweep will be created for the RDA (Figure A3.12).

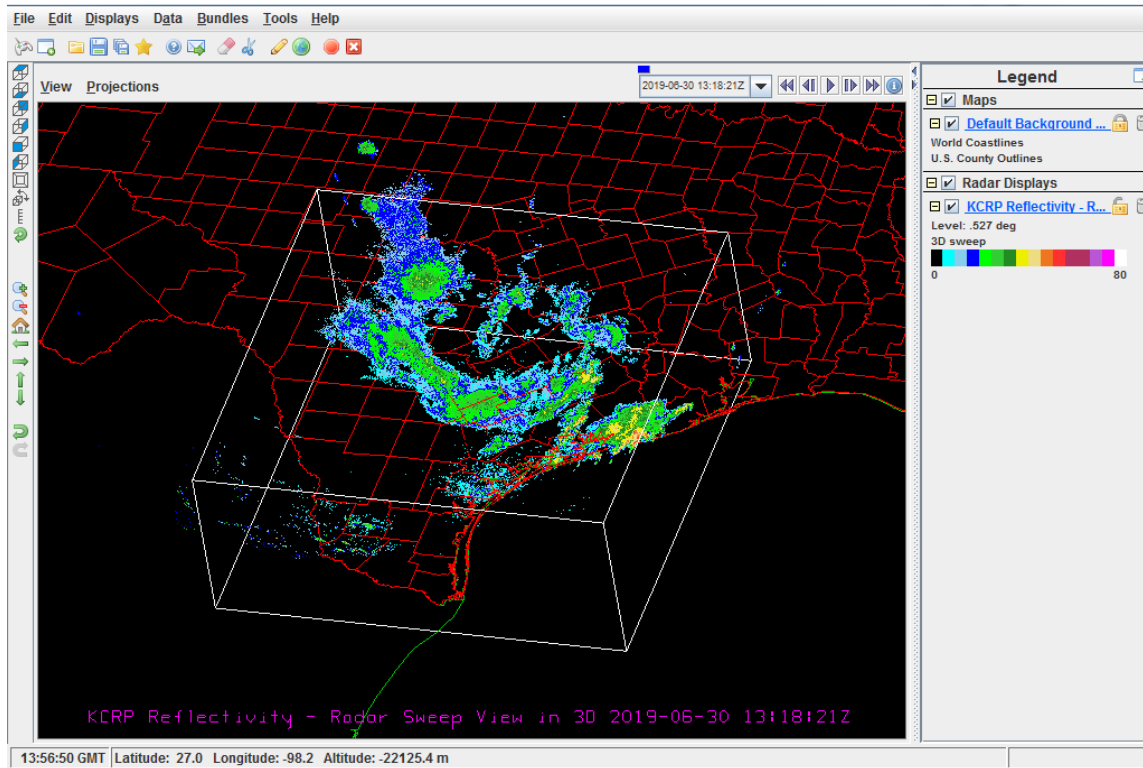


Fig. A3.12: 3-D radar display of reflectivity at a single tilt angle.

Multiple tilt angles can be displayed simultaneously, by navigating back to the “Field Selector” tab, and selecting a new radar scan to display. IDV will automatically display the new scan on top of the previous one (Figure A3.13).

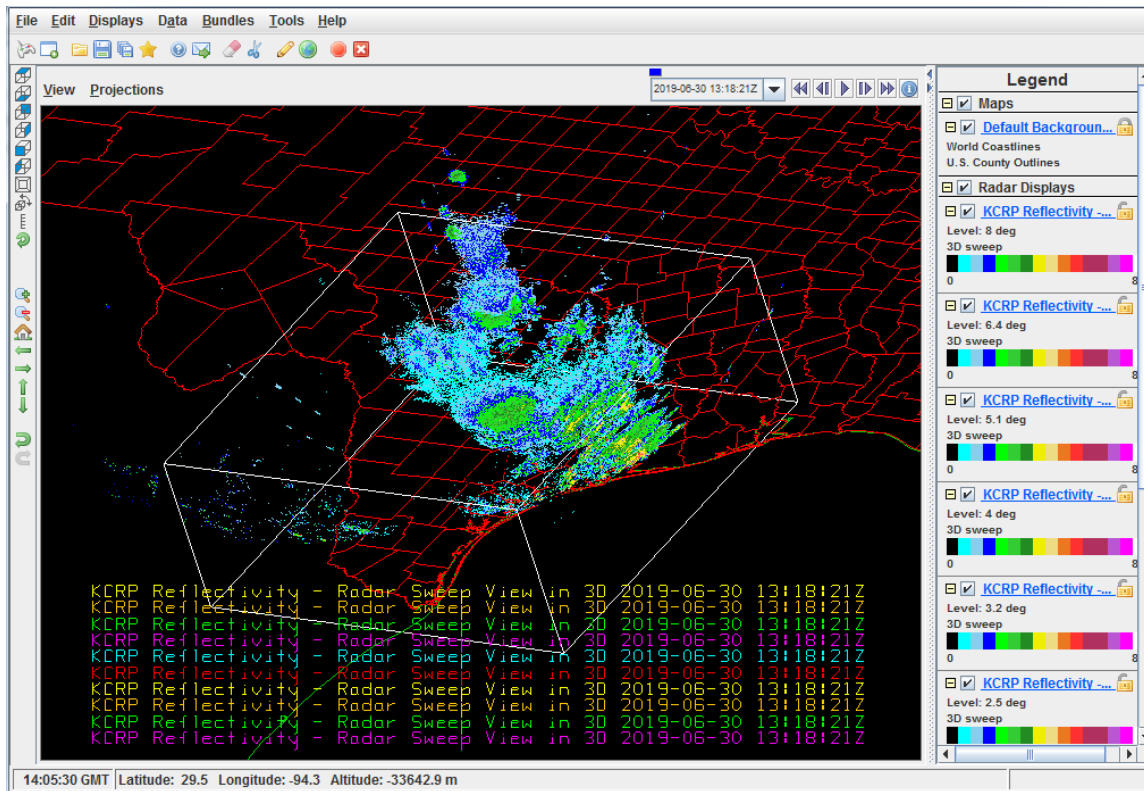


Fig. A3.13: Display of reflectivity at multiple tilt angles.

A3.1.7. Creating a cross-section. IDV can create a vertical cross-section display from Level II radar data. This display is possible in both a 2-D and 3-D plot. The vertical cross-section display is constructed from the cross-section line and radials from several tilt angles available in a WSR-88D Level II datafile. IDV can create a cross-section with any Level II data. In this example, reflectivity will be used.

- Create a radar display via one of the means described above. For this example, a 2-D display will be used.
- Select “Reflectivity” then in the “Displays” tab, select “Radar Cross-Section” (Figure A3.14).

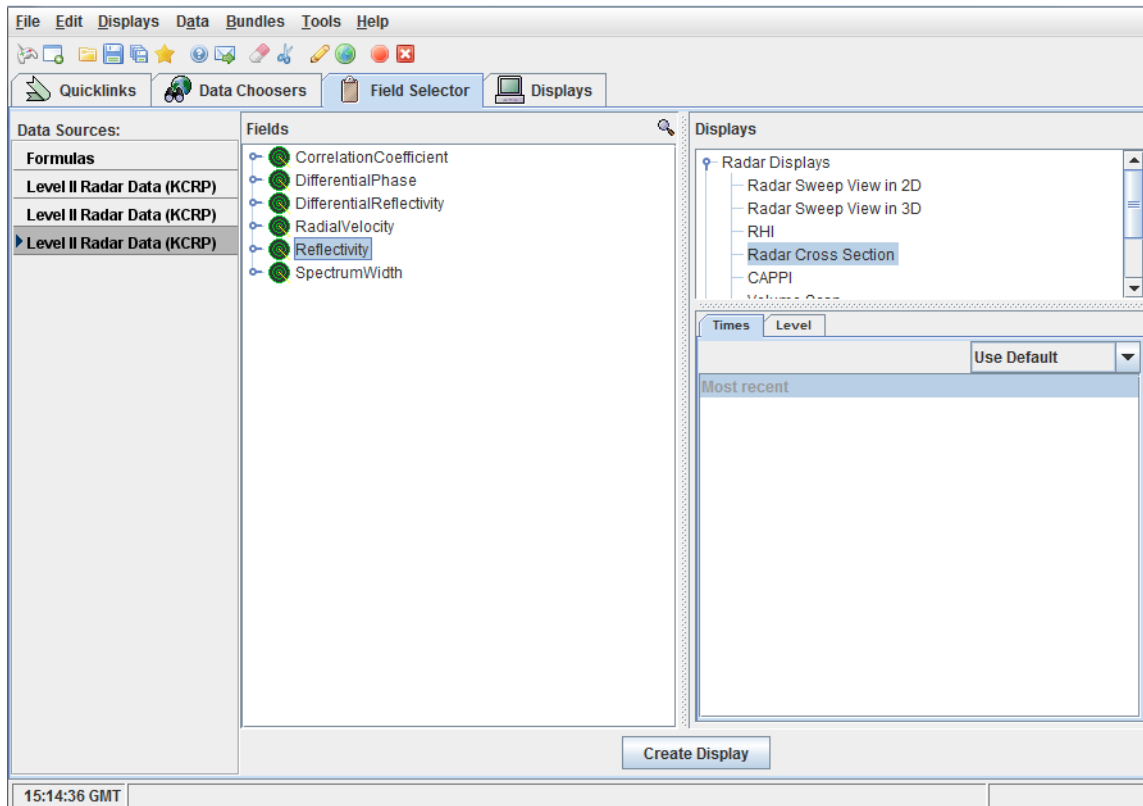


Fig. A3.14: Radar cross-section tool in IDV.

- Select “Create Display.”
- The default cross-section will be created. IDV automatically centers it directly over the RDA. To move the cross-section, navigate to the radar display.
- Figure A3.15 shows the cross-section tool that will appear over the radar. The triangle will move the cross-section, the cross and square on either side of the line will move their respective ends of the cross-section. To stretch the cross-section to cover a larger or shorter distance, move the cross or square.



Fig. A3.15: Cross-section tool.

- In this example, the cross-section is stretched across most of the display (Figure A3.16).

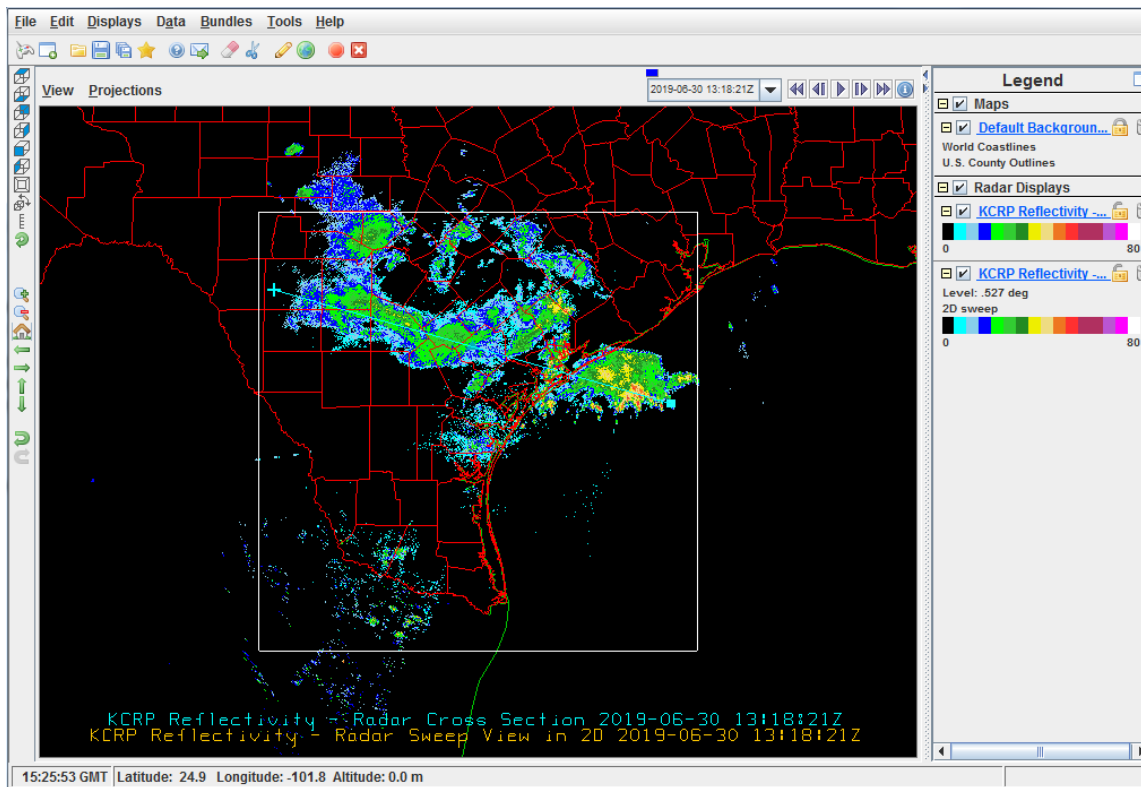


Fig. A3.16: Location of cross-section (indicated by white line running diagonally through the image).

- Viewing the cross-section can be done in multiple ways. The first is by rotating the display to see the cross-section above the 2-D radar display. (Figure A3.17).

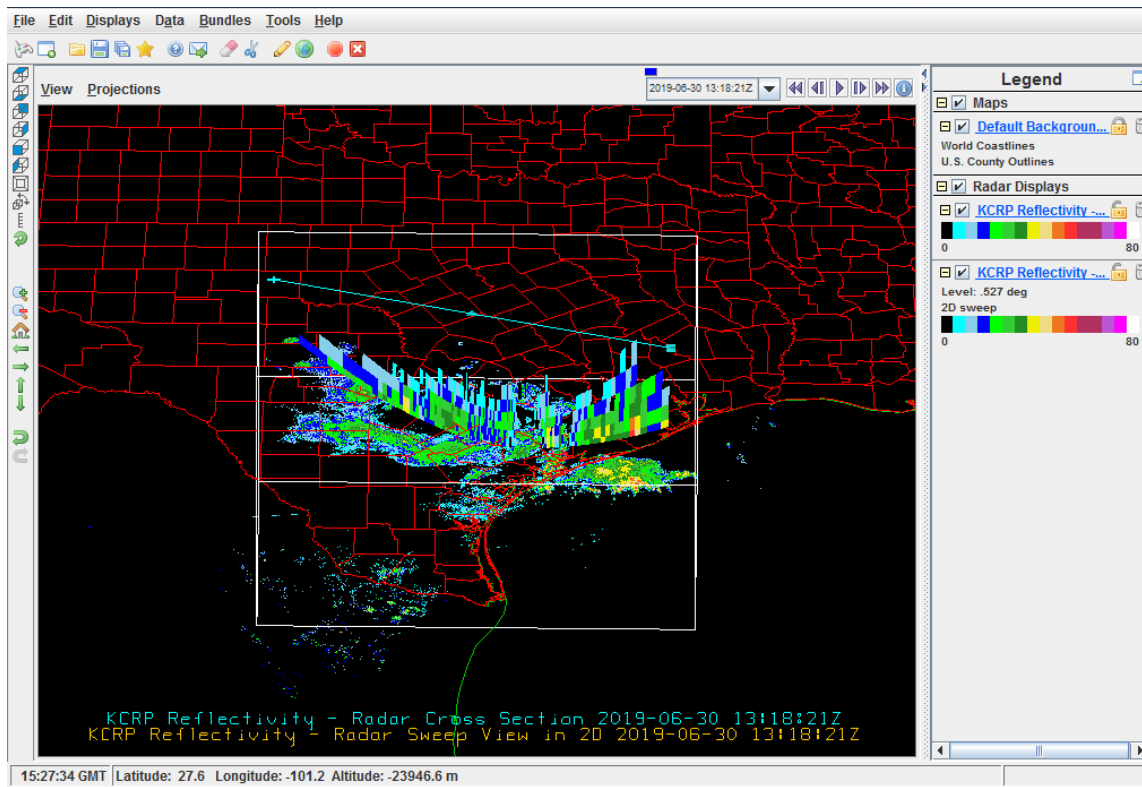


Fig. A3.17: Displaying Reflectivity Cross-Section above corresponding 2-D display.

- The second way is viewing the cross-section in the “Display” tab (Figure A3.18). This one shows more information about the cross-section itself, including a scale for horizontal distance along the transect on the x-axis, and the altitude of the scan on the y-axis.

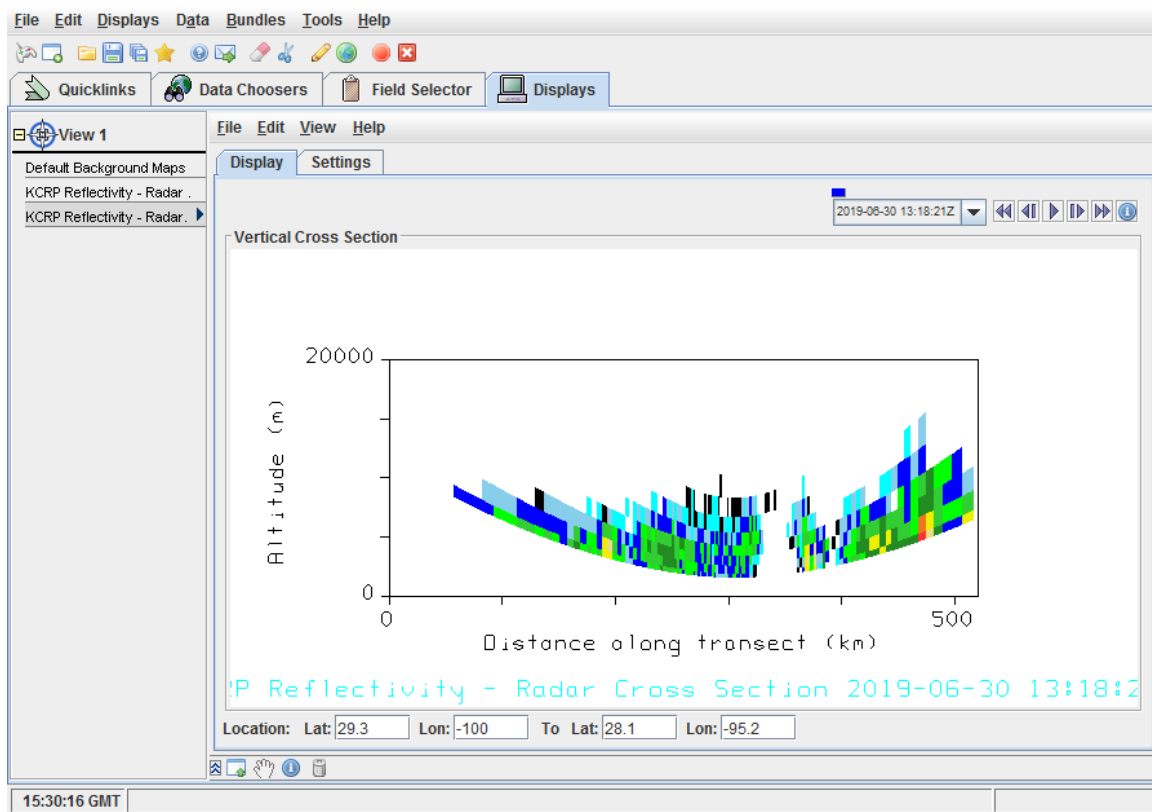


Fig. A3.18: Reflectivity Cross-Section in IDV.

A3.2. GR2Analyst.

A3.2.1. **History.** GR2Analyst is a proprietary radar data processing and display program, developed by Gibson Ridge Software, LLC. This program, first released in March of 2005, is designed specifically for Level II, Level III and dual-pol radar data. The software can view real-time or archived data in much the same way as Integrated Data Viewer (IDV). Unlike IDV, this program requires the purchase of a license. There is a free 21-day trial period available that has the same capabilities as the paid version.

As in the IDV section above, the scope of this section of the appendix is to describe basic methods of obtaining and visualizing radar data using GR2Analyst. This does not include basic skills such as zooming in and out, moving the field of view, resetting images, etc. GR2Analyst has a lot of additional products that can be overlaid onto basic displays as well. This section will not focus on advanced skills, but rather how to render simple 2-D and 3-D displays from any desired RDA.

To learn basic GR2Analyst skills, point an internet browser to:

<https://www.weather.gov/media/top/GR%20for%20Dummies%202.70.pdf>

A3.2.2. Installation.

- Navigate to the following URL: http://www.grlevelx.com/gr2analyst_2/
- Scroll down to the middle of the page to the *Downloads* section.
- Click on the following link labeled “GR2Analyst 2 Setup (8.5MB).”
- The GR2Analyst setup program will automatically download.
- A prompt with a message may appear that asks for permission to install GR2Analyst. If so, select yes.
- At this point, the window shown in Figure A3.19 will appear:

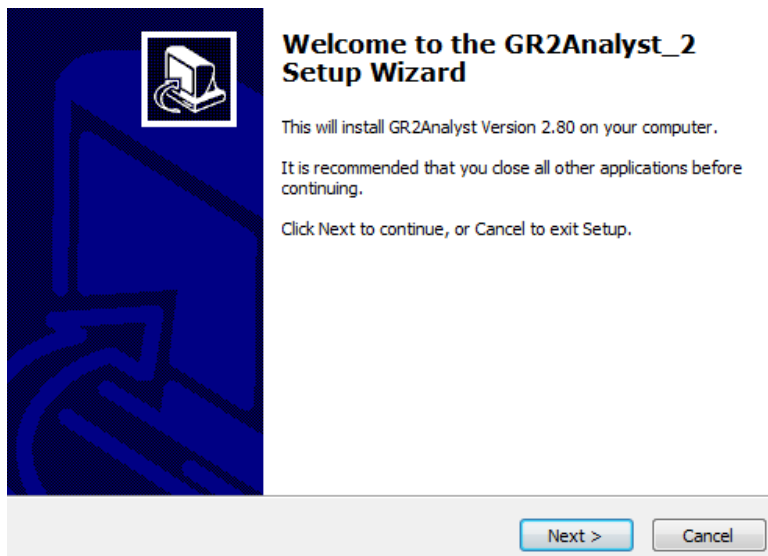


Fig A3.19: Setup Wizard for GR2Analyst.

- Accept the license agreement, and finish installing GR2Analyst by clicking Next.
- When GR2Analyst is first opened, a prompt will ask which radar data feed to use. The Iowa state feed should suffice for most applications, but if a different source is preferred, select “Use a different L2 feed ...” The feed can be changed at any time by going to “File” then “Configure Polling” and finally “Add.”
- If installed correctly, and the Iowa state feed is selected, the window shown in Figure A3.20 will appear:

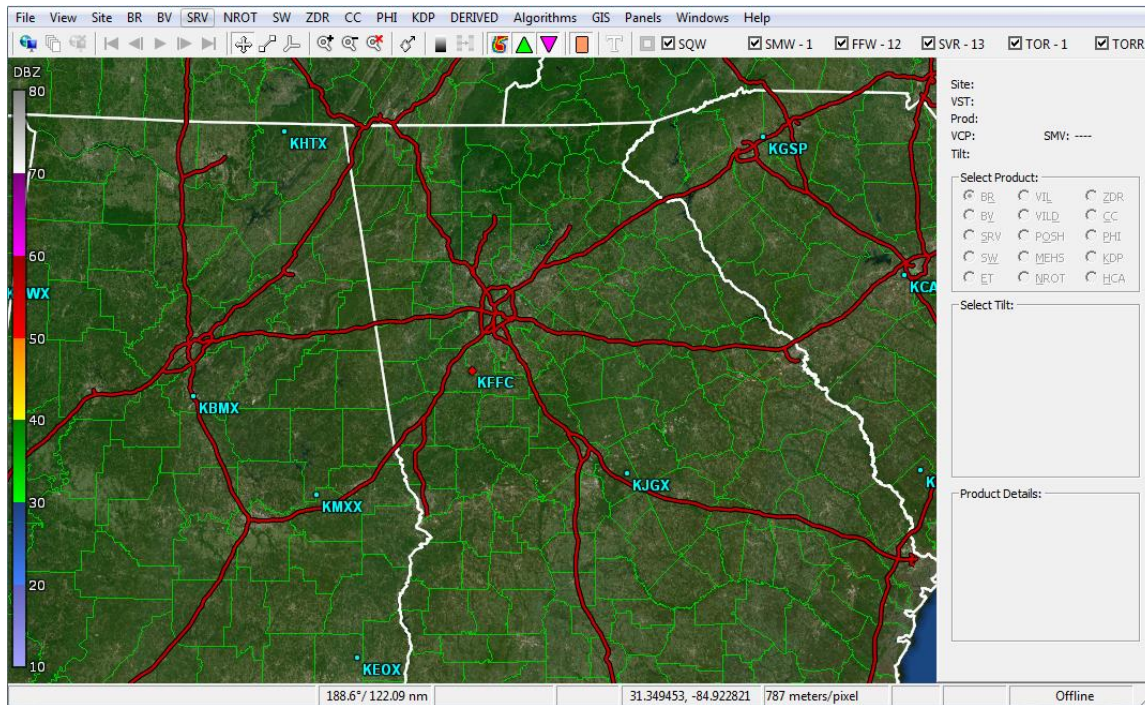


Fig A3.20: Default window from the first run of GR2Analyst.

A3.2.3. **Obtaining Radar Data.** There are two ways to obtain radar data. The first operates within the GR2Analyst program itself, and the second loads archived radar data from a local file source.

A3.2.3.1. **Retrieving current radar data.** This section will discuss how to retrieve current radar data using GR2Analyst.

- Make sure that GR2Analyst is set to use a data feed (described above). The default method from Iowa State will work for most applications.
- In the top left corner, select the “Site” option (Figure A3.21).

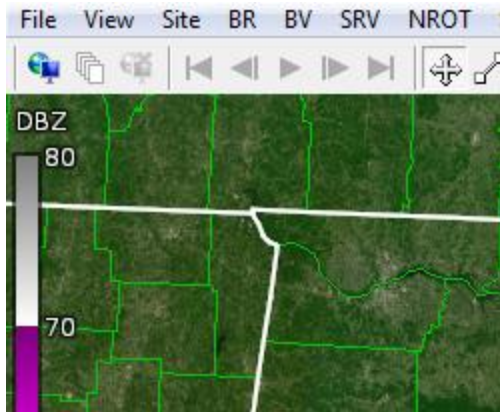


Fig A3.21: Zoomed in view of the top left menu.

- In the subsequent drop down menu, click “Select...”
- A new window listing every WSR-88D RDA in the United States will appear (Figure A3.22).

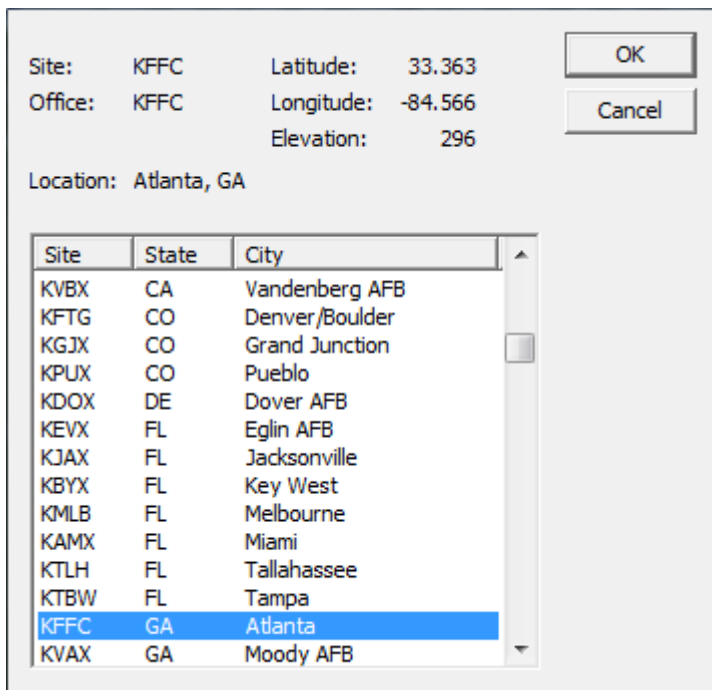


Fig. A3.22: List of RDAs available in GR2Analyst.

- Select the desired RDA, and click OK.

- Once selected, the main window will automatically move to display the location of the selected RDA.
- Make sure that the “Start Polling” button has been selected (icon with the globe in the top tool bar). This will allow GR2Analyst to feed current radar data into the display (Figure A3.23).



Fig. A3.23: Location of Polling Button.

- Once the data have been feed into the program, the current 2-D display will appear (Figure A3.24):

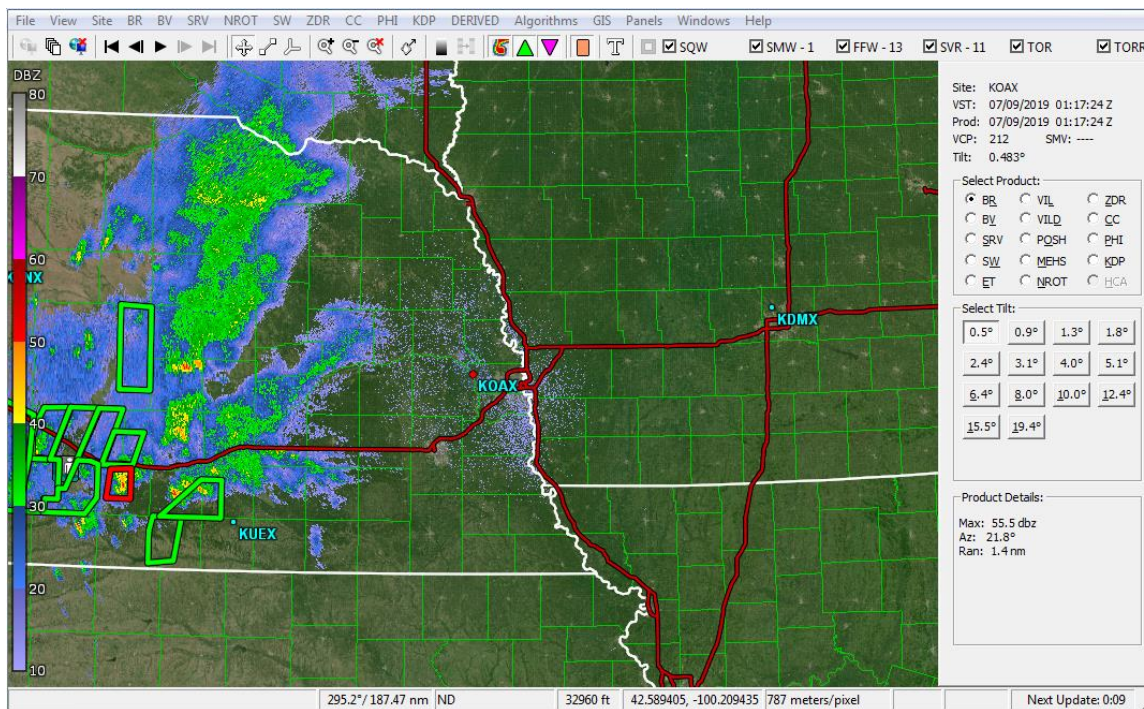


Fig. A3.24: 2-D display of base reflectivity (BR) observed by the Omaha, NE (KOAX) RDA.

A3.2.3.2. Retrieving archived radar data. The National Center for Environmental Information (NCEI) has archived radar data that are free and available from all weather radar systems in the United States. Retrieving archived data is similar to the procedure described in the IDV section.

- Point the internet browser to <https://www.ncdc.noaa.gov/data-access/radar-data>
- Select “Download Radar Data.”
- There are multiple ways to select data best suited to the user’s needs. One can select WSR-88D and TDWR sites via a list, or one can search by county, state, and (postal) zip code. For most orders, using the “Select by Map” option will suffice.
- In the “Select by Map” option, there is a display of all current RDAs, represented by blue dots. Click on the blue dot associated with the desired RDA.
- After choosing an RDA, a new page will load asking for more information. Using the pull-down menus, select the desired date, and product.
- Once the datatype is chosen, select “Create Graph.”
- In the new page, there are two options to either direct download, or order the data. Selecting “Direct Download” will open a new window with download links to the desired data. Entering an E-mail address, and selecting “Order Data” will send the selected files directly to the entered E-mail. Either option works, but ordering data typically takes longer.
- There are two ways to load data into GR2Analyst. The first option is to select the file, drag it over the display, then drop the file into the data viewer. The display will render shortly after.
- The second option is to load it via a GR2Analyst menu. First, select the “File” option in the left-hand corner. In the drop down menu, select “Open.” This will open a file locator window. Navigate to the saved files, and click “Open” again (Figure A3.25).

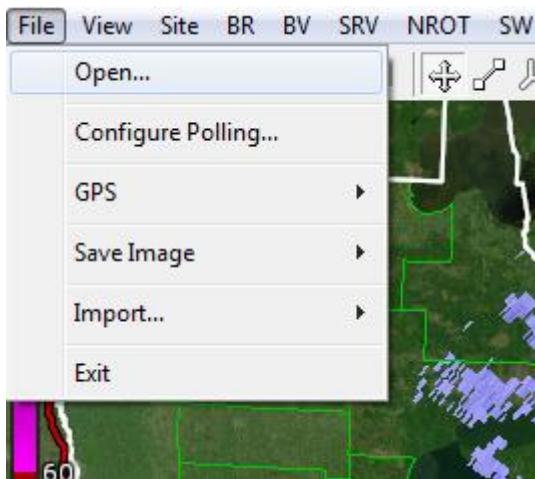


Fig. A3.25: How to open a local file in GR2Analyst.

A3.2.4. Basic 2-D visualization. Once the data have been fed into GR2Analyst, whether the data are current or archived, the 2-D display will automatically appear on the screen. If current data have been fed in, there will also be boxes representing NWS weather statements (usually watches, warnings, advisories, etc., as shown in Figure A3.24). The following will describe basic navigation around 2-D displays.

The right hand side of the display is where the desired products are selected. At the top, there is general information about the radar describing its station identifier, time of radar scan, current tilt angle, etc. Below that is the “Select Product” section. This is where datatypes for the current radar scan are available. Simply click the button next to a desired product, and it will automatically be rendered.

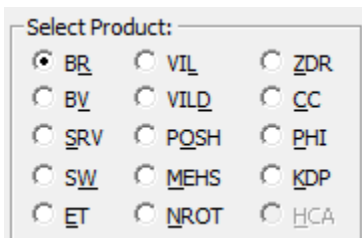


Fig. A3.26: List of all Level II, Level III and dual-pol radar products available in GR2Analyst.

Below is a list of the product acronyms:

- BR: Base Reflectivity (Level II)
- BV: Base (Radial) Velocity (Level II)
- SRV: Storm Relative Mean Radial Velocity (Level III)
- SW: Spectrum Width (Level II)
- ET: Echo Tops (Level III)
- VIL: Vertically-Integrated Liquid (Level III)
- VILD: Vertically-Integrated Liquid Density (Level III)
- POSH: Probability of Severe Hail (Level III)
- MEHS: Maximum Expected Hail Size (Level III)
- NROT: Normalized Rotation (specific to GR2Analyst)
- Z_{DR}: Differential Reflectivity (dual-pol)
- CC: Correlation Coefficient(dual-pol)
- PHI: Differential Propagation Phase (dual-pol)
- K_{DP}: Specific Differential Phase (dual-pol)

- HCA: Hydrometeor Classification Algorithm (Level III; dual-pol)³⁷

The following figures show a few examples of dual-pol radar products available in GR2Analyst.

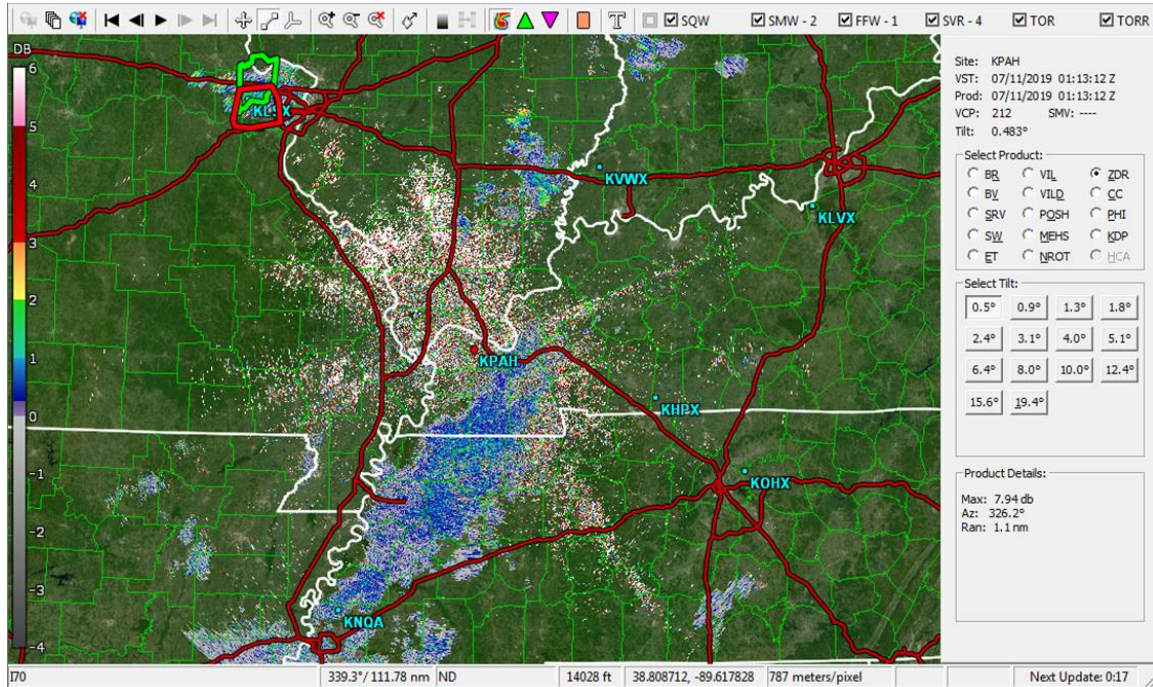


Fig. A3.27: Differential Reflectivity (Z_{DR}) from the Paducah, KY (KPAH) radar.

³⁷ See Chapter 8.

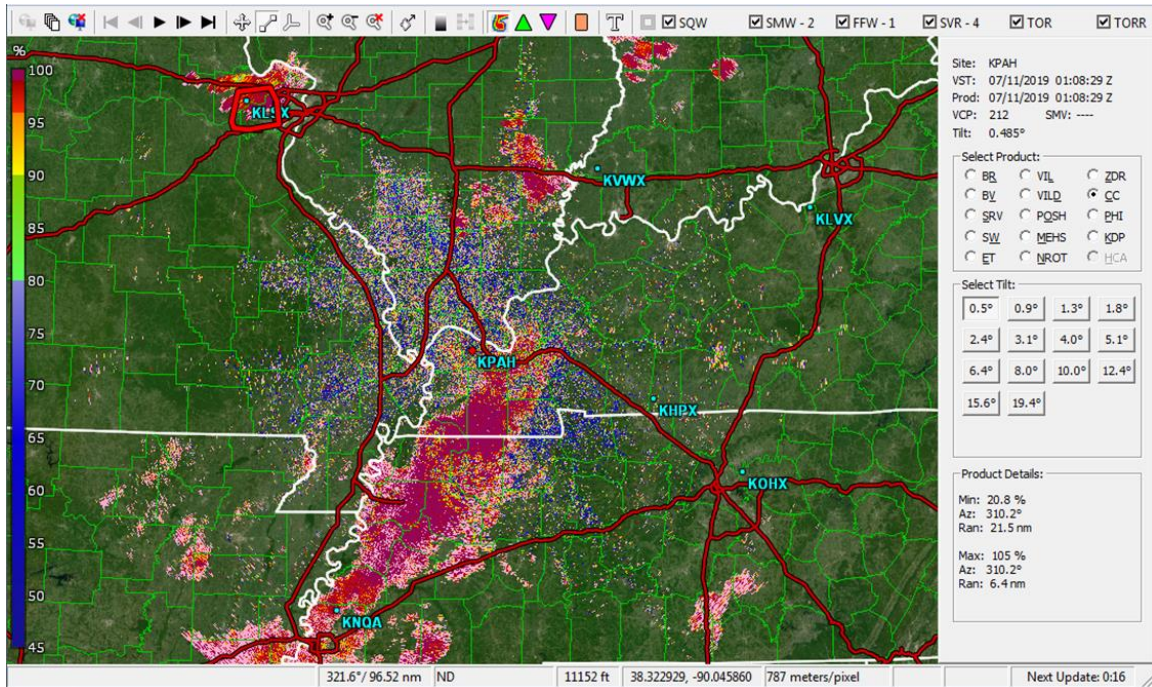


Fig. A3.28: Correlation Coefficient (CC) from the Paducah, KY (KPAH) radar.

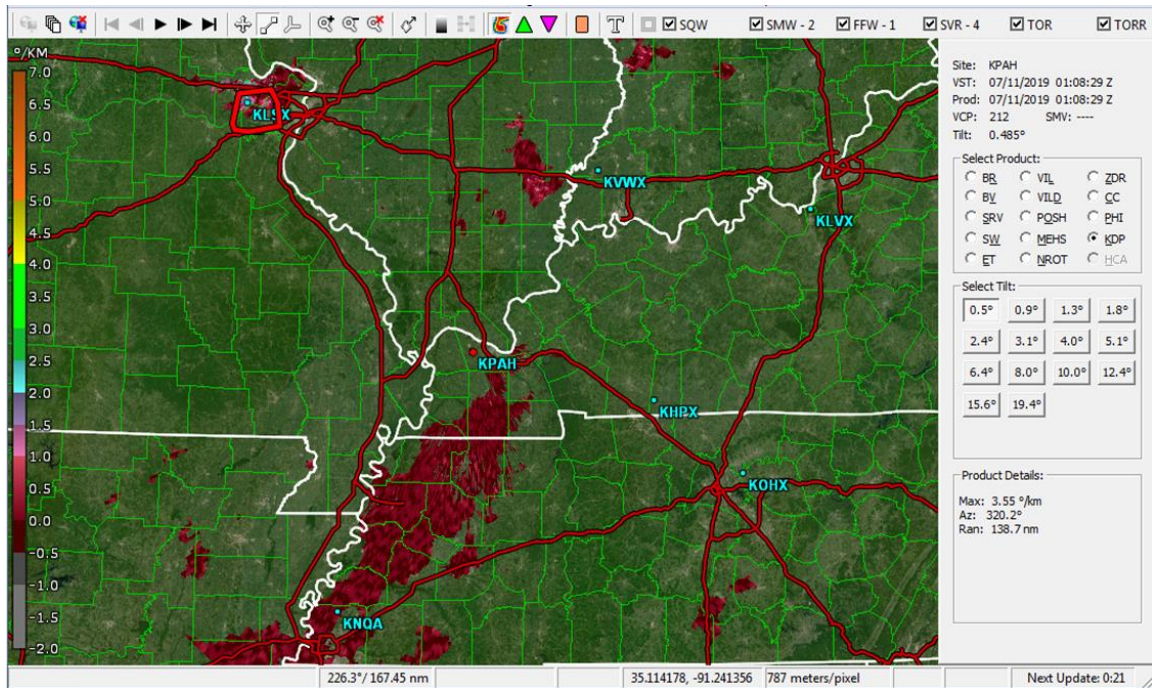


Fig. A3.29: Specific Differential Phase (K_{DP}) from the Paducah, KY (KPAH) radar.

A useful feature in GR2Analyst is the ability to create multiple display panels (Figure A3.30). This allows the user to view radar products from the same volume scan

side by side. To do this, select the “Panels” option in the top tool bar. A drop down menu will appear, allowing the user to select one, two, and four panel displays.

To change the radar product, click on an individual panel. Navigate to the “Select Product” section, and click on the desired product. The radar image will automatically render in the selected panel. Figure A3.30 shows an example of BR, CC, Z_{DR} , and K_{DP} from the KFWS RDA in a four panel display.

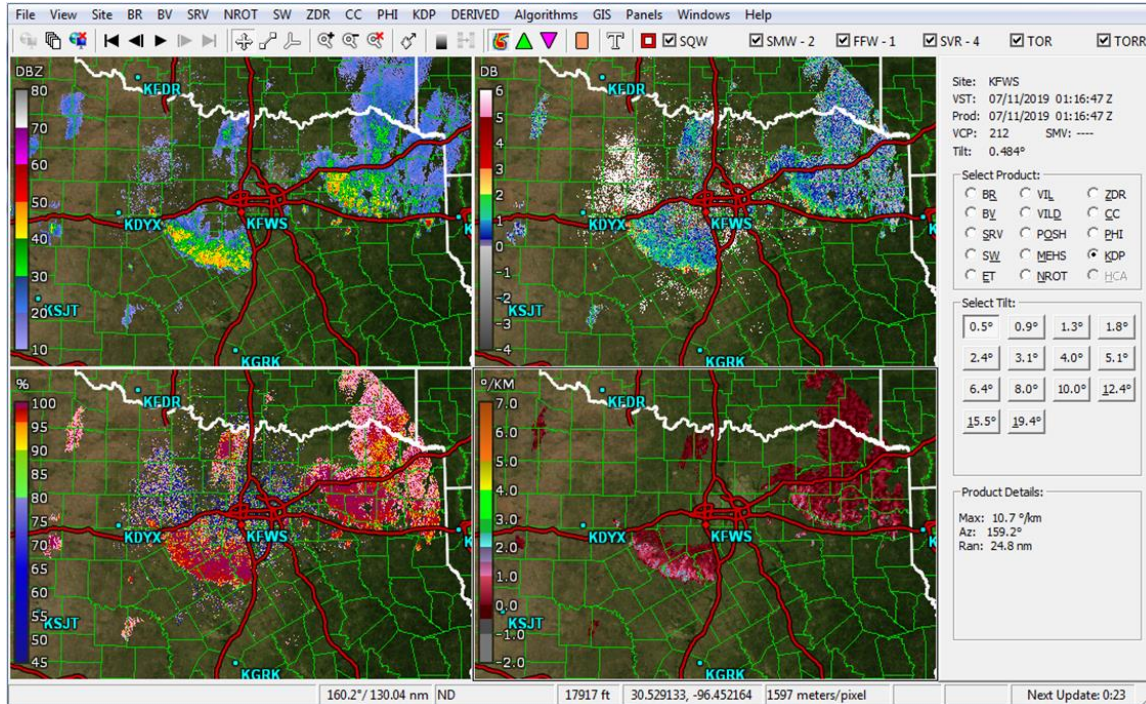


Fig. A3.30: Four panel display of BR, CC, Z_{DR} , and K_{DP} from the Dallas/Fort Worth, TX (KFWS) radar.

Following the product section, the radar tilt can be specified. This can be done by clicking on the corresponding tilt button. In the example below (Figure A3.31), the 0.9° angle is selected:

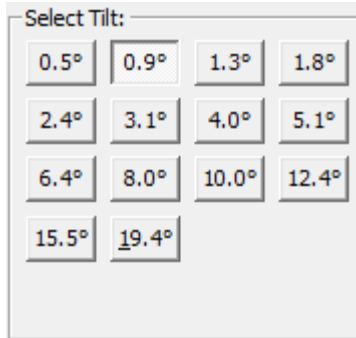


Fig. A3.31: Selecting Radar Tilt angles in GR2Analyst.

A3.2.5. Basic 3-D Visualization. The hallmark of GR2Analyst’s 3-D visualization is its “Volumetric Mode.” This allows users to view a 3-D scan of a selected area within a storm. It is a very effective way to visualize the composition of thunderstorms, tornados, and extra-tropical cyclones.

- Begin by feeding in radar data via one of the two means described above.
- Once the desired radar data have been chosen, there should be a 2-D display of base reflectivity. In the example below, KMVX radar was chosen (Figure A3.32).

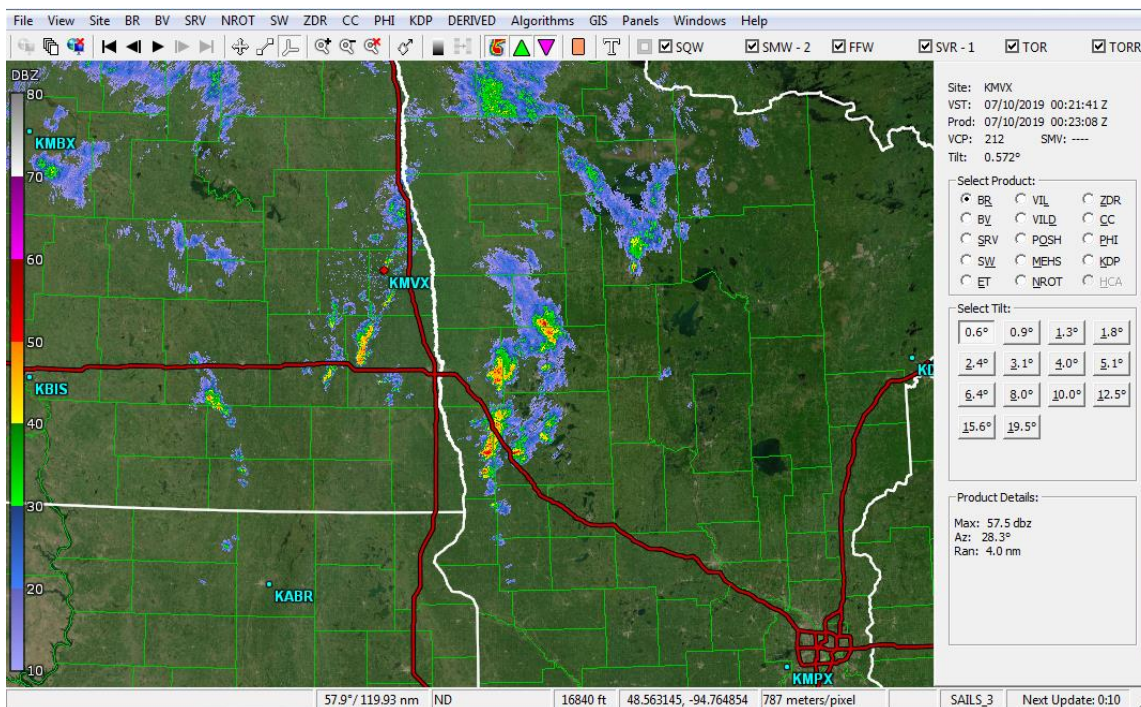


Fig. A3.32: 2-D display of ordinary reflectivity from the Grand Forks, ND (KMVX) RDA.

- Select the “Volumetric Mode” button from the toolbar (Figure A3.33). This is the Y-shaped button to the left of the magnifying glass icons.



Fig. A3.33: Location of the Volumetric Mode tool.

- Once the button is selected, the cursor will become a cube shape. Draw the volumetric scan box by holding down the left mouse button. Drag the cursor to create a box around the desired area, and release the button. A new window will appear near the middle of the screen with the desired volume scan rendered in 3-D (Figure A3.34).

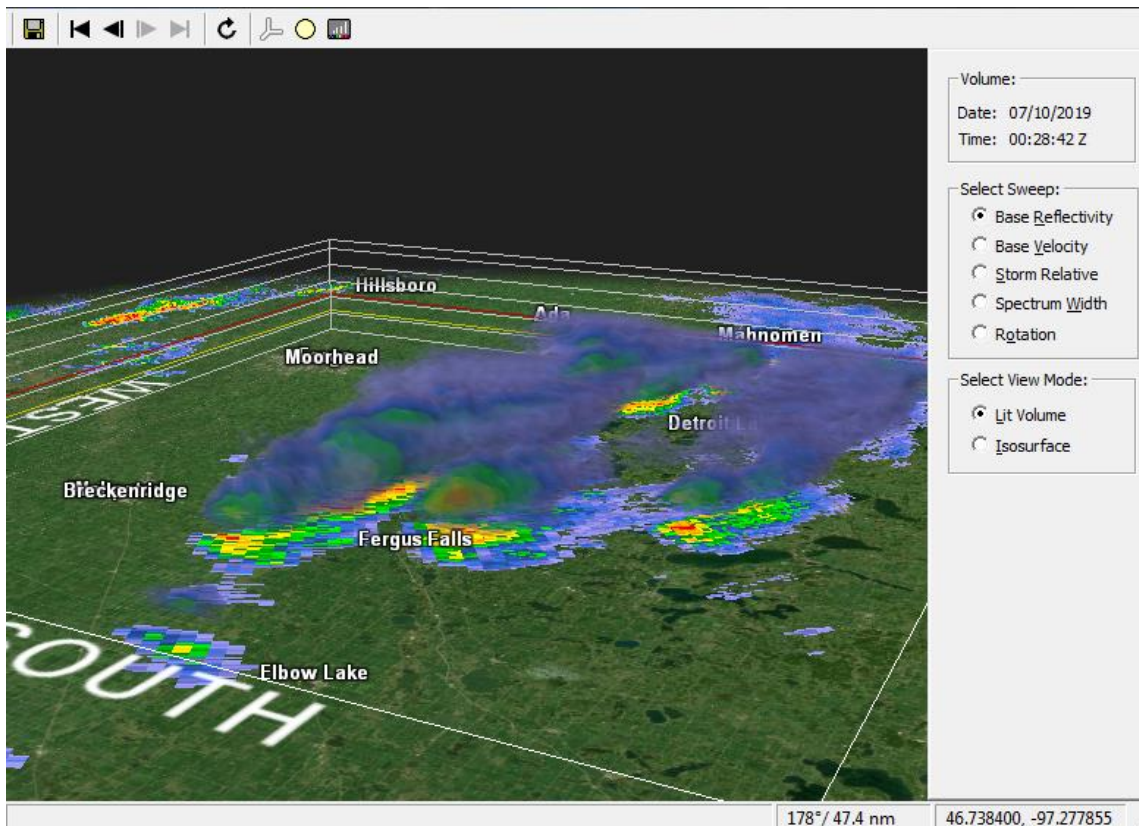


Fig. A3.34: 3-D rendering of base reflectivity from Grand Forks, ND (KMXV) in Volumetric Mode.

- On the right hand side of the viewer, five radar products can be selected.

- The “Select View Mode” section allows the user to pick between two different view modes. The first one is “Lit Volume.” This mode allows the user to view multiple layers and adjust the opacity, dimming or darkening of different reflectivity levels.
- To change the opacity, select the “Volume Alpha Tool” (Figure A3.35). This is done by clicking the icon that resembles a bar graph in the top toolbar.



Fig. A3.35: Location of Volume Alpha Tool.

- The Volume Alpha Tool for Lit Volume is essentially an opacity curve. At the bottom of the curve, opacity is 0% and the top is 100%. Use the cursor to draw lines for the desired opacity at certain reflectivity values. Below is a depiction of the changed opacity curve for Figure A3.34, and how it affected the display.



Fig. A3.36: Opacity curve where low reflectivity values have lower opacity, and high reflectivity values have higher opacity.

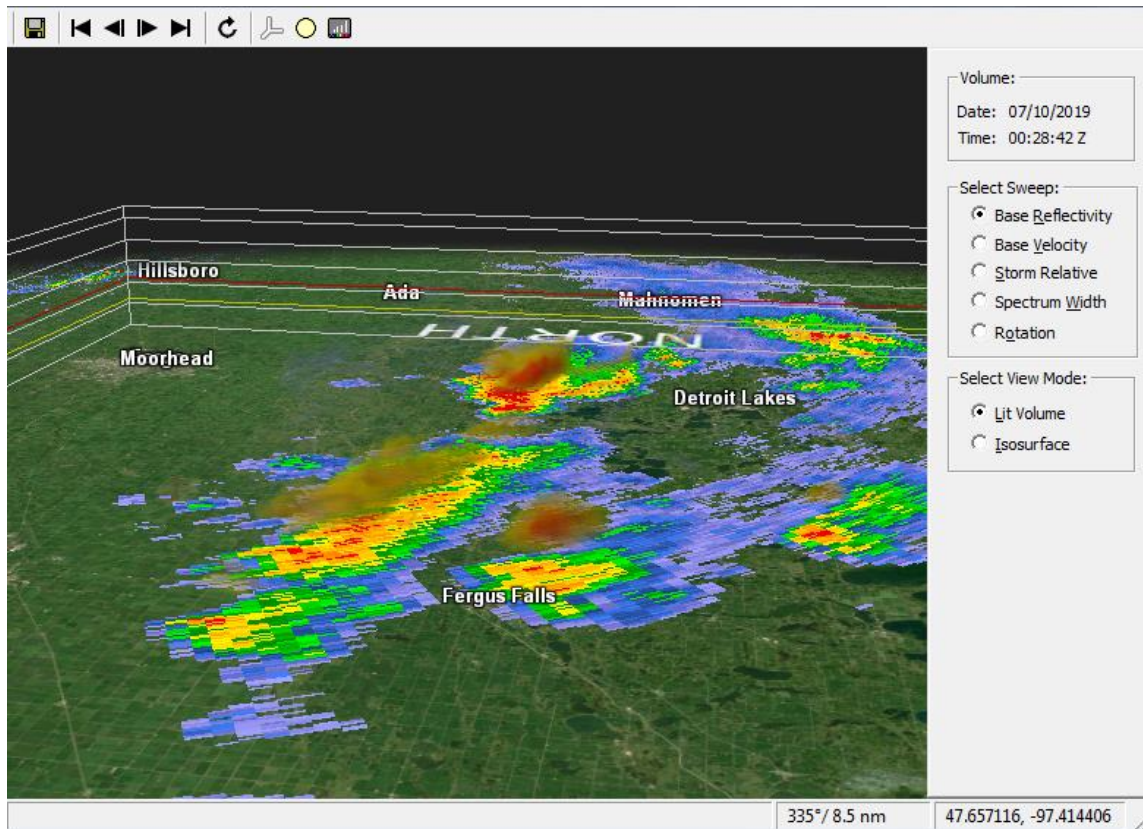


Fig. A3.37: Display of low reflectivity with lower opacity, and high reflectivity with higher opacity.

- The second view mode is “Isosurface.” This view allows the user to isolate specific reflectivity values. To do this, open the same Volume Alpha Tool as described above.
- Instead of drawing opacity lines, simply slide the arrow at the bottom to a desired reflectivity value, as shown in Figure A3.38. This will make the viewer only display that specific value.

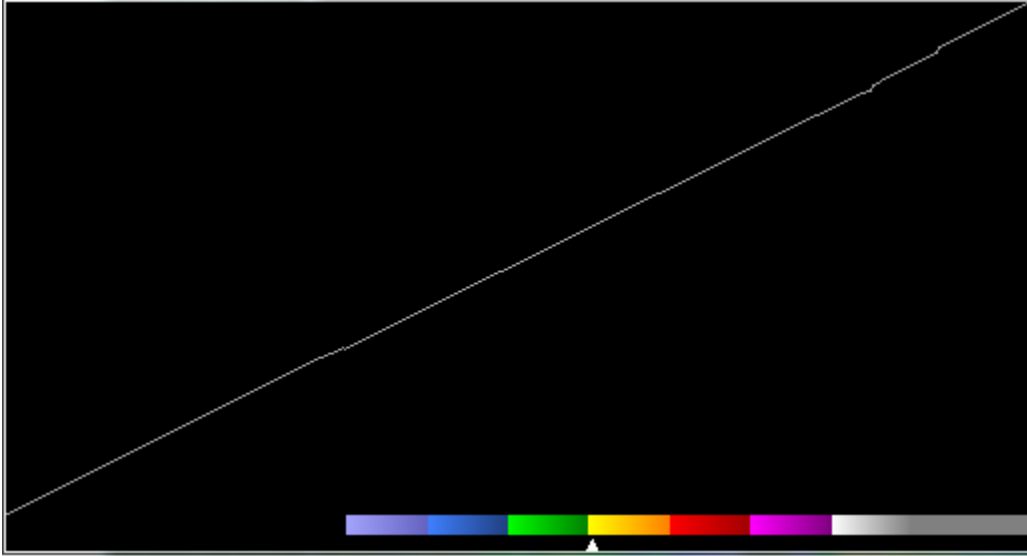


Fig. A3.38: Volumetric Alpha Tool with medium reflectivity values selected .

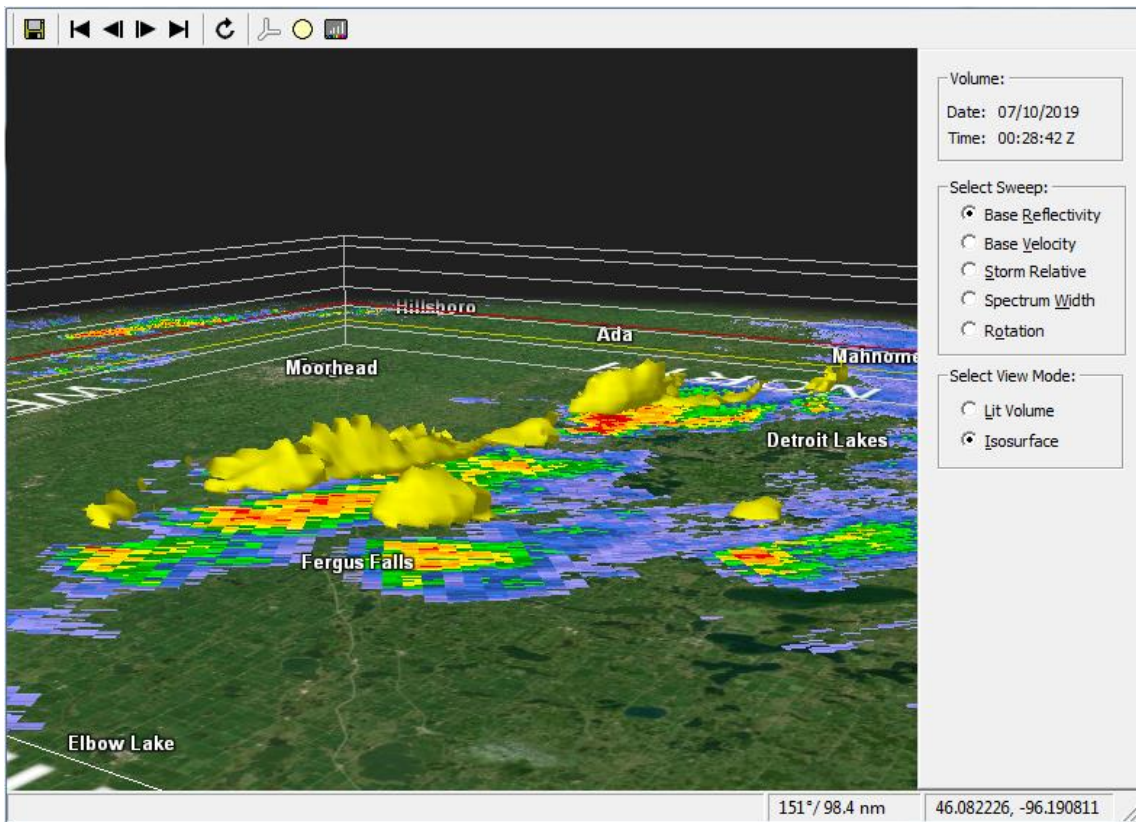


Fig. A3.39: KMXV 3-D display with a medium reflectivity Isosurface.

A.3.2.6. **Cross-sections.** The cross-section tool can be used to create vertical displays of radar data. This function is outlined below. Base reflectivity was used in this example.

- In the tool bar at the top of the window, select the “Cross Section Mode” button. The icon is a line with two squares at each end (Figure A3.40).



Fig. A3.40: Location of the cross-section tool.

- To create the cross-section, click and drag the computer mouse. Draw the line through the desired location, and then release the mouse button when finished.
- A window will open up with the new cross-section. An example is shown in Figure A3.41.

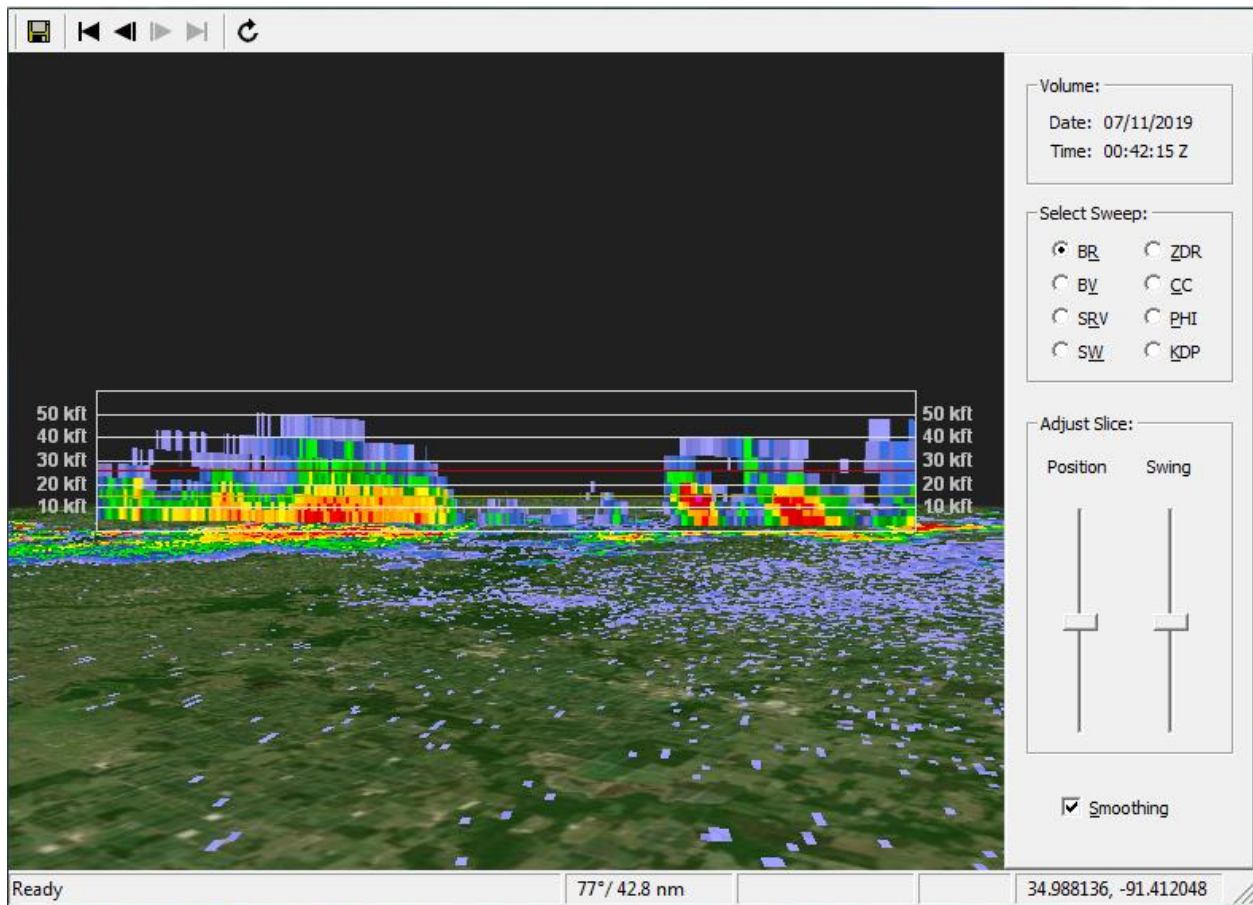


Fig. A3.41: Vertical cross-section of a thunderstorm system.

- There are two tools that one can use to edit the cross-section. The first is the “Swing” option. This allows the user to swivel the cross-section around its left axis.
- The last is the “Position” tool. This moves the cross-section horizontally either toward or away from the user’s viewing position.

References:

_____, 2012: A statistical evaluation of the accuracy of forecasts or the effectiveness of detection techniques, *Meteorology Glossary*, American Meteorological Society, accessed March, 2019. [Available on-line at <http://glossary.ametsoc.org/wiki/Skill>]

Ashley, W., A. Krmenc, and R. Schwantes, 2008: Vulnerability due to nocturnal tornadoes, *Weather and Forecasting*, **23**, 795 – 807.

Atlas, D. (ed.), 1990: Radar in Meteorology, American Meteorological Society, 806 pgs.

Baidar, S., S. Tucker, M. Beaubien, and R. Hardesty, 2018: The optical autocovariance wind LIDAR, Part II: Green OAWL (GrOAWL) airborne performance and validation, *Journal of Atmospheric and Oceanic Technology*, **35**, 2099 – 2116, DOI: 10.1175/JTECH-D-18-0025.1.

Beard, K., 1976: Terminal velocity and shape of cloud and precipitation drops aloft. *Journal of the Atmospheric Sciences*, **33**, 851 – 864.

Böhm, H., 1989: A general equation for the terminal fall speed of solid hydrometeors. *Journal of the Atmospheric Sciences*, **46**, 2419 – 2427.

Brown, R., and V. Wood, 2012: The Tornadic Vortex Signature: An Update, *Weather and Forecasting*, **27**, 525 – 530.

Burgess, D., and L. Lemon, 1990: Severe Thunderstorm Detection by Radar, in Atlas, D. (ed.) Radar in Meteorology, American Meteorological Society, 619 – 647.

Center for Severe Weather Research (CSWR), 2019: Website, accessed April, 2019. [Available on-line at www.cswr.org]

Campbell, L., W. Steenburgh, P. Veals, T. Letcher, and J. Minder, 2016: Lake-effect mode and precipitation enhancement over the Tug Hill Plateau during OWLeS IOP2b, *Monthly Weather Review*, **144**, 1729 – 1748.

Canadian Weather Radar Network, 2019: Accessed 2019. [Available on-line at https://en.wikipedia.org/wiki/Canadian_weather_radar_network and ipfs.io/ipfs/QmXoypizFiJnKlWHCnL72vedxjGDDP1mXWo6uco/wiki/Canadian_weather_radar_network.html]

Chrisman, J., 2012: WSR-88D Supplemental Adaptive Intra-Volume Low-Level Scan (SAILS), DQ Decision Brief, accessed May 2019. [Available on-line at https://www.roc.noaa.gov/WSR88D/PublicDocs/NewTechnology/SAILS_DQ_Presentation_Nov_2012.pdf]

Conway, M., D. Du Russel, A. Morris, and C. Perry, 2018: Multifunction phased array radar advanced technology demonstrator nearfield test results, *2018 IEEE Radar Conference (RadarConf18)*, accessed April 2019. [Available on-line at <http://ieeexplore.ieee.org/document/8378771>]

Cunningham, J., W. Zittel, R. Lee, and R. Ice, 2013: Methods for identifying systematic differential reflectivity (Z_{DR}) biases on the operational WSR-88D network, *36th Conference on Radar Meteorology*.

Defense Advanced Research Projects Agency (DARPA), 2019: Phased array radar, accessed May, 2019. [Available on-line at <https://www.darpa.mil/about-us/timeline/phased-arrays>]

Dye, J., and B. Martner, 1978: The relationship between radar reflectivity factor and hail at the ground for northeast Colorado storms, *Journal of Applied Meteorology*, **17**, 1335 – 1341.

Emersic, C., P. Heinselman, P., D. MacGorman, and E. Bruning, 2011: Lightning activity in a hail-producing storm observed with phased-array radar, *Monthly Weather Review*, **139**, 1809 – 1825.

Environment and Climate Change Canada, 2019a: Backgrounder – Weather Monitoring Infrastructure, accessed May 2019. [Available on-line at <http://www.ec.gc.ca/default.asp?lang=En&n=592AB94B-1&news=06F87DOA-4ECO-41F2-99EE-7298555FCEA65>]

Environment and Climate Change Canada, 2019b: Canadian Weather Radar, accessed May, 2019. [Available on-line at http://weather.gc.ca/radar/index_e.html]

Fenn, A., D. Temme, W. Delaney, and W. Courtney, 2000: The development of phased-array radar technology, *Lincoln Laboratory Journal*, **12** (2), 321 – 340.

Foote, G. B., and P.S. DuToit, 1969: Terminal velocity of raindrops aloft, *Journal of Applied Meteorology*, **8**, 249–253.

Forbes, G., 1981: On the reliability of hook echoes as tornado indicators, *Monthly Weather Review*, **109**, 1457 – 1466.

Forsyth, D., J. Kimpel, D. Zrnica, S. Sandgathe, F. Pfeil, J. Heimmer, T. McNellis, J. Crain, A. Shapiro, J. Belville, and W. Brenner, N.D.: The National Weather Radar Testbed (Phased-Array), accessed May, 2019. [Available on-line at https://www.researchgate.net/publication/238108994_BUILDING_THE_NATIONAL_WEATHER_RADAR_TESTBED_PHASED-ARRAY]

Fournier, J., 1999: Reflectivity-rainfall relationships in operational meteorology, Tallahassee Florida WFO, U.S. National Weather Service, accessed 2019. [Available on-line at <https://www.weather.gov/tae/research-zrpaper>]

Fulton, R., J. Breindenbach, D. Seo, D. Miller, and R. O'Bannon, 1998: The WSR-88D rainfall algorithm, *Weather and Forecasting*, **13**, 377 – 395.

Fujita, T., 1986: Mesoscale classifications – Their history and their application to forecasting. *Mesoscale Meteorology and Forecasting* (P. S. Ray, Ed.), 18 - 35.

Gao, J., D. Stensrud, L. Wicker, M. Xue, and K. Zhao, 2014: Storm-scale radar data assimilation and high resolution NWP, *Advances in Meteorology*, **2014**, 1 – 3.

Gerapetritis, H., and J. Pelissier, ND: The critical success index and warning strategy, NOAA/National Weather Service, accessed April, 2019. [Available on-line at <https://ams.confex.com/ams/pdfpapers/70691.pdf>]

Gerapetritis, H., and J. Pelissier, 2004: On the behavior of the Critical Success Index, (NOAA) Eastern Region Technical Attachment No. 2004-03, accessed April, 2019. [Available on-line at <https://www.weather.gov/media/erh/ta2004-03.pdf>]

Ghelli, A., 2009: Verification of categorical predictands, 4IWVM - Tutorial Session, accessed April, 2019. [Available on-line at <https://www.swpc.noaa.gov/sites/default/files/images/u30/Verification%20of%20Categorical%20Predictands.pdf>]

Giangrande, S., and A. Ryzhkov, 2008: Estimation of rainfall based on the results of polarimetric echo classification, *Journal of Applied Meteorology and Climatology*, **47**, 2445 – 2462.

Gorgucci, E., S. Gianfranco, and V. Chandrasekar, 1999: A procedure to calibrate multiparameter weather radar using properties of the rain medium, *IEEE Trans. On Geoscience and Remote Sensing*, **37** (1), Jan 1999.

Gunn, R., and G. Kinzer 1949: The terminal velocity of fall for water droplets in stagnant air, *Journal of Meteorology*, **6**, 243 – 248.

Heinselman, P., D. Priegnitz, K. Manross, T. Smith, and R. Adams, 2008: Rapid sampling of severe storms by the National Weather Radar Testbed Phased-Array Radar, *Weather and Forecasting*, **23**, 808 – 824.

Heinselman, P., and S. Torres, 2011: High-temporal resolution capabilities of the National Weather Radar Testbed Phased-Array Radar, *Journal of Applied Meteorology and Climatology*, **50**, 579 – 593.

Holton, J., 2004: *An Introduction to Dynamic Meteorology*, Elsevier Academic Press, 535 pgs.

Houdas, Y., 1991: Doppler, Buys-Ballot, Fizeau. Historical note on the discovery of the Doppler's Effect, *Annales de Cardiologie et d'Angéiologie*, **40** (4), pp. 209 – 213.

Huuskonen, A., E. Saltikoff, and I. Holleman, 2014: The operational radar network in Europe, *Bulletin of the American Meteorological Society*, NN, 897 – 907, DOI: 10.1175/BAMS-D-12-00216.1

Ice, R., J. Cunningham, and A. Heck, 2013: Polarimetric weather radar – engineering challenges, accessed March, 2019. [Available on-line at https://www.roc.noaa.gov/wsr88d/PublicDocs/Publications/PolarWX_Calibration_Eng_Challenges_Ice_radar2013_rv2.pdf]

Ice, R., A. Heck, B. McGuire, L. Richardson, W.D. Zittel, R. Lee, and J. Cunningham, 2015, Polarimetric weather radar antenna calibration using solar scans, accessed April, 2019. [Available on-line at https://www.roc.noaa.gov/wsr88d/PublicDocs/Publications/PolarmetricWXRadar_Cal_Using_SolarScans_Ice_31EIP_T_Jan2015_final.pdf]

Istok, M., W. Blanchard, T. Granger, and A. Stern, ND: Radar information enhancements for the NWS operational user, accessed May, 2019. [Available on-line at <https://ams.confex.com/ams/pdfpapers.71169.pdf>]

Johnston, P., J. Jordan, A. White, D. Carter, D. Costa, and T. Ayers, 2016: The NOAA FM-CW snow level radar. *Journal of Atmospheric and Oceanic Technology*, **34**, 249 – 267.

Joe, P., ND: The CARDS system description and algorithms, accessed 2019. [Available on-line at <https://slideplayer.com/slide/7463767/>]

Joe, P., and S. Lapczak, 2002: Evolution of the Canadian Operational Radar Network, *Proceedings, 2nd European Conference on Radar in Meteorology and Hydrology (ERAD)*, 370 – 382.

Jorgensen, D., and P. Willis, 1982: A Z-R relationship for hurricanes, *Journal of Applied Meteorology*, **21**, 356 – 366.

Katz, T., and P. Henry, 1990: Radar Meteorology at Radiation Laboratory, MIT, 1941 – 1947, in Atlas, D. (ed.), *Radar in Meteorology*, 16 – 21.

Kidder, S., and T. Vonder Harr, 1995: *Satellite Meteorology – An Introduction*. Academic Press, 466 pgs.

Lawson, J., J. Kain, N. Yussouf, D. Dowell, D. Wheatley, K. Knopfmeier, and T., Jones, 2018: Advancing from convection-allowing NWP to Warn-on-Forecast: Evidence of progress, *Weather and Forecasting*, **33**, 599 – 607.

Lapedes, D. (Ed.), 1976: *McGraw-Hill dictionary of scientific and technical terms*, McGraw-Hill, 1634, A26 p.

Lee, H., E. Kim, and S. Kim, 2016: Anomalous propagation echo classification of imbalanced radar data with support vector machine, *Advances in Meteorology*, **5**, 1 – 13, DOI: 10.1155/2016/4129708.

Lee, H., and S. Kim, 2016: Decision tree ensemble classifiers for anomalous propagation echo detection, *Joint 8th International Conference on Soft Computing and Intelligent Systems (CSIS) and 17th International Symposium on Advanced Intelligent Systems (ISIS)*, DOI: 10.1109/SCIS-ISIS.2016.0089.

Lee, R., and A. White, 1998: Improvement of the WSR-88D mesocyclone algorithm, *Weather and Forecasting*, **13**, 341 – 351.

Lenning, E., H. Fuelberg, and A. Watson, 1998: An evaluation of WSR-88D severe hail algorithms along the northwestern Gulf Coast, *Weather and Forecasting*, **13**, 1029 – 1045.

Lide, D., 1997: CRC Handbook of Physics and Chemistry, CRC Press.

Liu, J., M. Bray, and D. Han, 2013: A study of WRF radar data assimilation for hydrological rainfall prediction, *Hydrology and Earth Systems Sciences*, **17**, 3095 – 3110, DOI: 10.5194/hess-17-3095-2013.

Loconto, A., 2005: Improvements of warm-season convective wind forecasts at the Kennedy Space Center and Cape Canaveral Air Force Station, Master's Thesis, Plymouth State University, 79 pgs, accessed March, 2019. [Available on-line at http://vortex.plymouth.edu/conv_winds/Loconto_thesis.pdf]

Lubchenco, J., and J. Hayes, 2012: New technology allows better extreme weather forecasts, accessed May, 2019. [Available on-line at <https://www.scientificamerican.com/article/a-better-eye-on-the-storm>]

Marshall, J., R. Langille, and W. Palmer, 1947: Measurement of rainfall by radar, *Journal of Meteorology*, **4**, 186–192.

Marshall, J., and W. Palmer, 1948: The distribution of raindrops with size, *Journal of Meteorology*, **5**, 165–166.

Maxwell, J., 1865: A dynamical theory of the electromagnetic field, *Philosophical Transactions of the Royal Society of London*, 155: 459 – 512. [Available on-line at <https://royalsocietypublishing.org/doi/10.1098/rstl.1865.0008>]

McCarthy, P., and D. Patrick, 2008: Improved thunderstorm detection, tracking and assessment products for Environment Canada radars, *24th Conference on Severe Local Storms*, Savannah, Georgia.

McGill JS Marshall Radar Observatory, 2019: McGill S-band radar, accessed May 2019. [Available on-line at <http://www.radar.mcgill.ca/facilities/mcgill-radar.html>]

Meischner, P. (ed.), 2004: *Weather Radar – Principles and Advanced Applications*, Springer, 337 pgs.

Meischner, P, C. Collier, A. Illingworth, J. Joss, and W. Randeu, 1997: Advanced weather radar systems in Europe: The COST 75 action, *Bulletin of the American Meteorological Society*, 78 (7), 1411 – 1430.

Meteorological Service of Canada, 2019: That National Radar Program, accessed May, 2019. [Available on-line at https://web.archive.org/web/20060615050828/http://www.msc-smc.ec.gc.ca/projects/nrp/index_e.cfm]

Miller, S., 2015: *Applied Thermodynamics for Meteorologists*, Cambridge University Press, 385 pgs.

Mitchell, E., S. Vasiloff, G. Stumpf, A. Witt, M. Eilts, J. Johnson, and K. Thomas, 1998: The National Severe Storms Laboratory Tornado Detection Algorithm, *Weather and Forecasting*, 13, 352 – 366.

Mizutani, F., T. Ushio, W. Yoshikawa, S. Shimamura, H. Kikuchi, M. Wada, S. Satoh, and T. Iguchi, 2018: Fast-scanning phased-array weather radar with angular imaging technique, *IEEE Transactions on Geoscience and Remote Sensing*, 56 (5), 2664 – 2673.

Morsi, S., and A. Alexander, 1972: An investigation of particle trajectories in two-phase flow systems. *Journal of Fluid Mechanics*, 55, 193 – 208.

National Centers for Atmospheric Research (NCAR), 2019: Wind shear detection and alerting, accessed April, 2019. [Available on-line at ral.ucar.edu/sites/default/files/public/media/files/wind-shear-broch-2018-08.pdf]

National Centers for Environmental Information (NCEI), 2019: Terminal Doppler Weather Radar – Supplemental Product Generator (TDWR-SPG), accessed April, 2019. [Available on-line at www.ncdc.noaa.gov/data-access/radar-data/tdwr]

National Severe Storms Laboratory (NSSL), 2005: New radar technology can increase tornado warning lead times, accessed April, 2019. [Available on-line at http://web.archive.org/web/20060509134036/http://www.norman.noaa.gov/publicaffairs/backgrounders/backgroundounder_par.html]

Newman, J., and P. Heinselman, 2012: Evolution of a quasi-linear convective system sampled by phased array radar, *Monthly Weather Review*, **140**, 3467 – 3485.

NOAA, 2016: Snow Level Radar, accessed April 2019. [Available online at <https://www.esrl.noaa.gov/psd/psd2/technology/snow-level-radar.html>.]

NOAA/NSSL, 2014: Multi-function Phased Array Radar and Cylindrical Polarized Phased Array Radar, accessed May, 2019. [Available on-line at <https://www.ofcm.gov/groups/MPAR/references/Final/%20MPAR%20Congressional%20Report%20FY14.pdf>]

O'Connor, J., and E. Robertson, 2007: Heinrich Rudolf Hertz, accessed May, 2019. [Available on-line at http://www-history.mcs.st-andrews.ac.uk/Biographies/Hertz_Heinrich.html]

Office of the Federal Coordinator of Meteorological Services and Supporting Research (OFCM), 2006: Research and development for multi-function phased array radar (MPAR), FCM-R25-2006, Silver Springs, Maryland.

Ohanian, H., 1987: Modern Physics. Prentice-Hall, Inc., 543 pgs.

Parry, D., 2010: NRL History – November 1930, News Releases from the U.S. Naval Research Laboratory, U.S. Naval Research Laboratory, accessed May, 2019. [Available on-line at <https://www.nrl.navy.mil/news/releases/nrl-history-november-1930>]

Peura, M., M. Martet, A. Huuskonen, L. Delobbe, B. Lipovscak, H. Leijnse, and E. Saltikoff, 2017: OPERA – Harmonizing the European weather radar network, accessed May 2019. [Available on-line at <https://ams.confex.com/ams/38RADAR/webprogram/Paper320437.html>]

Pond, N., 2004: *The Tube Guys, Russ Cochran (pub.)*, 447 pgs.

Puca, S., and Coauthors, 2014: The validation service of the hydrological SAF geostationary and polar satellite precipitation products, *Natural Hazards and Earth System Sciences*, 871 – 889, doi: 10.5194/nhess-14-871-2014.

Radar Operations Center (ROC), 2019: WSR-88D Service Life Extension Program, accessed May 2019. [Available on-line at <https://www.roc.noaa.gov/WSR88D/SLEP/SLEP.aspx>]

Radar Operations Center (ROC), 2019b: NEXRAD technical information, accessed May 2019. [Available on-line at <https://www.roc.noaa.gov/WSR88D/Engineering/NEXRADTechInfo.aspx>]

Radartutorial.eu, 2019: Overview of radar transmitter, accessed May 2019. [Available on-line at <http://www.radartutorial.eu/08.transmitters/Radar%20Transmitter.en.html>]

Ralph, F. M., and Coauthors, 2016: CalWater field studies designed to quantify the roles of atmospheric rivers and aerosols in modulating U.S. West Coast precipitation in a changing climate. *Bulletin of the American Meteorological Society*, **97**, 1209 – 1228.

Rasmussen, R., and A. Heymsfield, 1987: Melting and shedding of graupel and hail, Part II: Sensitivity study, *Journal of the Atmospheric Sciences*, **44**, 2764 – 2782.

Rasmussen, R., M. Dixon, S. Vasiloff, F. Hage, S. Knight, J. Vivekanandan, M. Xu, 2003: Snow nowcasting using a real-time correlation of radar reflectivity with snow gauge accumulations. *Journal of Applied Meteorology*, **42**, 20-36.

Rauber, R., and S. Nesbitt, 2018: *Radar Meteorology – A First Course*. John Wiley & Sons, Ltd., 461 pgs.

Rinehart, R., 2004: *Radar for Meteorologists*, 4th Ed. Rinehart Publications, 482 pgs.

Rogers, R. and M. Yau, 1989: A Short Course in Cloud Physics (3rd Ed.), Butterworth-Heinemann, 290 pgs.

Rosenfeld, D., D. Wolff, and D. Atlas, 1993: General probability-matched relations between radar reflectivity and rain rate, *Journal of Applied Meteorology*, **32**, 50-72.

Ryzhkov, V., S. Ginagrande, V. Melnikov, and T. Schuur, 2005: Calibration Issues of Dual-Polarization Radar Measurements, *Journal of Atmospheric and Oceanic Technology*, **22**, 1138 - 1155.

Sabzehparvar, M., 2018: Dynamic response of the aircraft to wind shear using multi-points loading approach, *Archive of Mechanical Engineering*, **18** (2), 243 - 252.

Schaefer, J., 1990: The Critical Success Index as an indicator of warning skill, *Weather and Forecasting*, **5**, 570 - 575.

Shun, C., and S. Lau, 2000: Terminal Doppler Weather Radar (TWDR) observations of atmospheric flow over complex terrain during tropical cyclone passages, *Hong Kong Observatory Reprint 365*, 12 pgs.

Small, A., 2005: A Brief History of Radar Meteorology, semester project, Radar Meteorology, Plymouth State University.

St. Jean, D., 2012: Personal Communication, in the form of his unpublished presentation *Dual Polarization: Base Moments and Hurricane Sandy*. St. Jean was the Science and Operations Officer (SOO) of the Gray, Maine NWS Weather Forecast Office at the time, and shared this presentation with my Radar Meteorology course.

Stumpf, G., A. Witt, E. Mitchell, P. Spencer, J. Johnson, M. Eilts, K. Thomas, and D. Burgess, 1998: The National Severe Storms Laboratory Mesocyclone Detection Algorithm for the WSR-88D, *Weather and Forecasting*, **13**, 304 - 326.

Supinie, T., N. Yussouf, Y. Jung, M. Xue, J. Cheng, and S. Wang 2017: Comparison of the analysis and forecasts of a tornadic supercell storm from assimilating phased-array radar and WSR-88D observations, *Weather and Forecasting*, **32**, 1379 - 1401, DOI: 10.1175/WAF-D-16-0159.1.

Swingle, D., 1990: Weather Radar in the United States Army's Fort Monmouth Laboratories, in Atlas, D. (ed.), *Radar in Meteorology*, 7 - 15.

Tanamachi, R., P. Heinselman, and L. Wicker, 2015: Impacts of a storm merger on the 24 May 2011 Reno, Oklahoma tornadic supercell, *Weather and Forecasting*, **30**, 501 - 523.

Taub, H. and D. Schilling, 1986: *Principles of Communication Systems*. McGraw-Hill, 759 pgs.

Temir, I., and A. Macit, 2016: Turkish weather radar network, accessed May 2019. [Available on-line at https://www.wmo.int/pages/prog/www/IMOP/publications/IOM-116_TECO-2014/Session%201/P1_51_Temir_TurkishWxRadarNet.pdf]

Tucker, S., C. Weiner, S. Baidar, and R. Hardesty, 2018: The optical autocovariance wind LIDAR, Part I: OAWL instrument development and demonstration, *Journal of Atmospheric and Oceanic Technology*, **35**, 2079 - 2097, DOI: 10.1175/JTECH-D-18-0024.1.

Vasiloff, S., 2001: WSR-88D performance in northern Utah during the winter of 1998-1999, Part I: Adjustments to precipitation estimates, NOAA/Western Regional Technical Attachment 01-03, 5 pp.

Wada, M., H. Yonekubo, T. Ushio, S. Satoh, A. Adachi, and S. Tsuchiya, 2016: Development of phased-array weather radar: Field trial, dual-pol, and how it reduces disaster, accessed May 2019. [Available on-line at https://www.wmo.int/pages/prog/www/IMOP/publications/IOM-125_TECO_2016/Session_2/K2A_Wada_Toshiba.pdf]

Waldvogel, A., B. Federer, and P. Grimm, 1979: Criteria for the detection of hail cells, *Journal of Applied Meteorology*, **18**, 1521 - 1525.

Warning Decision Training Branch, 2005: Distance Learning Operations Course (DLOC).

Warning Decision Training Branch, 2008: RDA/RPG Build 10.0 Training, 41 pgs.

Warning Decision Training Branch, 2018: Dual-polarization radar principles and system operations (version 1109), 94 pgs.

Warning Decision Training Division, 2019: Radar and applications training materials, accessed May, 2019. [Available on-line at <https://training.weather.gov/wdtd/courses/index.php>]

Weber, M., J. Cho, J. Herd, and M. Vai, 2005: Multi-function phased array radar for U.S. civil-sector surveillance needs, Preprints, *32nd Conference on Radar Meteorology*, Albuquerque, NM, American Meteorological Society, CD-ROM, 12R.2.

Weber, M., J. Cho, J. Herd, J. Flavin, W. Benner, and G. Torok, 2007: The next-generation multimission U.S. surveillance radar network, *Bulletin of the American Meteorological Society*, **88**, 1739 – 1752, DOI: 10.1175/BAMS-88-11-1739.

Weber, M., J. Cho, J. Flavin, J. Herd, and Michael V., 2008: Multi-function phased array radar for U.S. civil-sector surveillance needs, Federal Aviation Administration under Air Force Contract FA8721-05-C-0002.

White, A. B., and Coauthors, 2013: A twenty-first-century California observing network for monitoring extreme weather events, *Journal of Atmospheric and Oceanic Technology*, **30**, 1585 – 1603.

White, A. B., J. R. Jordan, B. E. Martner, F. Ma. Ralph, and B. W. Bartram, 2000: Extending the dynamic range of an S-band radar for cloud and precipitation studies. *Journal of Atmospheric and Oceanic Technology*, **17**, 1216 – 1234.

White, A. B., D. J. Gottas, E. T. Strem, F. M. Ralph, P. J. Neiman, 2002. An automated brightband height detection algorithm for use with Doppler radar spectral moments, *Journal of Atmospheric and Oceanic Technology*, **19**, 687 – 697.

Whiten, R., P. Smith, S. Bigler, K. Wilk, and A. Harbuck, 1990: History of operational use of weather radar by U.S. weather services, Part I: The Pre-NEXRAD era, *Weather and Forecasting*, **13**, pp. 219 – 243.

Wiesbeck, W., S. Leen, M. Younis, G. Krieger, and A. Moriera, 2015: Radar 2020: The Future of Radar Systems, *IEEE International Geoscience and Remote Sensing Symposium (IGARSS) 2015*, Milano, Italy. [Available on-line at <https://www.researchgate.net/publications/272027572>]

Wilson, K., P. Heinselman, and C. Kuster, 2017: Considerations for phased-array radar data use within the National Weather Service, *Weather and Forecasting*, **32**, 1959 – 1965, DOI: 10.1175/WAF-D-17-0084.1.

Witt, A., M. Eilts, G. Stumpf, J. Johnson, E. Mitchell, and K. Thomas, 1998: An enhanced hail detection algorithm for the WSR-88D, *Weather and Forecasting*, **13**, 2764 – 2782.

Wood, V., and R. Brown, 1983: Single Doppler velocity signatures: An atlas of patterns in clear air, widespread precipitation and convective storms, NOAA Tech. Memo ERL NSSL-95, 71 pgs.

Xue, M., M. Tong, and K. Droegemeier, 2006: An OSSE framework based on ensemble square-root Kalman filter for evaluating impact of data from radar networks on thunderstorm analysis and forecast, *Journal of Atmospheric and Oceanic Technology*, **23**, 46-66, doi: 10.1175/JTECH1835.1.

Yussouf, N., and D. Stensrud, 2010: Impact of phased-array radar observations over a short assimilation period: Observing system simulation experiments using an ensemble Kalman filter, *Monthly Weather Review*, **140**, 562 – 587, doi: 10.1175/MWR-D-10-05074.1.

Index

- 2-D circulations, 197
- 2-D Shear Feature, 190
- 3D Strength Rank, 193

- A2D, 48
- absorption, 29
- adaptable parameters, 162, 189, 199
- Advanced Technology Demonstrator, 272
- Advanced Weather Interactive Processing System, 41
- Air Route Surveillance Radar, 271
- Air Surveillance Radar, 271
- Air Traffic Control, 164
- alias number, 89
- alternating current, 23
- AN/APS-2F, 12
- AN/CPS-9, 12
- AN/FPS-85, 269
- analog-to-digital conversion, 48
- angular frequency, 27
- Anomalous Propagation, 60, 77
- antenna, 41, 42, 44
- antenna gain, 51
- Antenna Scan Strategy, 45
- anticyclonic, 112
- AOR, 223
- AP, 60, 77
- APQ-13, 11
- Archive Level I, 40
- Archive Level II, 40, 66, 71
- Archive Level III, 40
- Area of Responsibility, 223
- area threshold, 218
- array antennas, 268
- ARSR, 271
- ASOS, 223
- ASR, 271
- Atatürk airport, 262
- ATC, 164
- ATD, 272
- Automated Surface Observing Systems, 223
- Automated Weather Observing Systems, 223
- average received signal power, 68
- average transmitted power, 43
- AWIPS, 41
- AWOS, 223
- Axis Powers, 10

- backing, 102
- backscattered EMR, 44
- Backward-S zero isodop, 104
- band width, 68
- base moments, 48
- beam centerline, 45
- Bell Telephone Laboratories, 11
- below-beam effects, 215
- Bendix, 269
- Bias Tables, 223
- biological targets, 128
- blockhouse, 42
- blueshifting, 34
- Boot, Henry, 10
- Bounded Weak Echo Regions, 171
- Bragg scattering, 30
- bright banding, 215
- British Air Ministry, 10
- British Met Office, 10
- broad-band communications, 41, 69
- Brunt-Väisälä frequency, 77
- BWER, 171

- CAA, 101
- Canadian operational weather radar network, 251
- Canadian Radar Decision Support System, 254
- Canadian Weather Radar Network, 251
- Cant Angle, 125
- CARDS, 254
- CAT, 173
- Category 0, 218
- Category 1, 218
- Category 2, 218
- C-band, 14, 28
- CC, 140
- CD, 67
- Cell View, 254
- cell-based Vertically Integrated Liquid, 156
- cell-based VIL, 156
- Center for Severe Weather Research, 242
- centroid, 155
- channel capacity, 68
- CIRC, 193
- circular polarization, 32
- CIRES, 236
- clear-air mode, 218
- clutter suppression, 71

Clutter Suppression Algorithm, 74
 clutter suppression pattern, 69
 coherent radar, 56
 cold air advection, 101
 cold rain process, 140
 Combined Attributes Table, 173
 complex conjugate, 141
 component (reflectivity), 155
 Composite Reflectivity, 172
 Cone of Silence, 47
 confluence, 105
 conical ice crystal, 127
 constructive interference, 30
 Continuous Doppler, 67
 Continuous Surveillance, 67
 continuous-wave Doppler radar, 236
 conventional cycle, 252
 convergence, 112
 Convergence Vector, 189
 Cooperative Institute for Research in
 Environmental Sciences, 236
 Co-Polar Cross-Correlation Coefficient, 140
 CP2, 121
 CPLT, 193
 Critical Success Index, 195, 291
 CS, 67
 CSA, 74
 CSI, 195, 291
 CSWR, 242
 cyclonic, 112
 CZ, 172

 DARPA, 268
 decibel, 50
 Defense Advanced Research Projects Agency,
 268
 Department of Defense, 16
 derived products, 48, 152, 173, 260, 273
 DHR, 228
 Differential Propagation Phase, 134
 Differential Reflectivity, 127
 diffuse reflection, 31
 diffluence, 105
 Digital Base Radial Velocity, 250
 Digital Base Reflectivity, 250
 Digital Hybrid Scan Reflectivity, 228
 Digital Mesocyclone Detection Algorithm, 251
 Digital Precipitation Array, 251
 Digital Precipitation Rate, 229
 Digital VIL, 166
 dipole antenna, 8, 23
 divergence, 112

 DoD, 16
 Doppler cycle, 252
 Doppler Dilemma, 66
 Doppler Effect, 8, 33
 Doppler frequency shift, 34
 Doppler on Wheels, 242
 Doppler vertical velocity, 236
 Doppler Wind Lidar, 235
 Doppler, Christian Andreas, 8
 DOW, 242
 DPR, 229
 drop diameter, 49
 dropsize distribution, 49
 dual polarization, 18
 dual-pol, 54, 123
 dual-polarization radar, 122
 Dual-Polarization Z-R Relationship, 210
 dual-wavelength radar, 121
 ducting, 31, 80
 duplexer, 9, 42, 43
 DWL, 235

 Earth System Research Laboratory, 236
 East Cool Season Z-R Relationship, 209
 Echo Free Vaults, 171
 EET, 175
 EF Level 1, 276
 electrical field, 8, 23
 electrical permittivity of free space, 25
 electromagnetic radiation, 8, 22
 electromagnetic spectrum, 22
 electromagnetic waves, 8, 24
 Electronically-Steered Array Radar, 268
 electronically-steered radar, 268
 Elevated TVS, 198
 EMR, 8, 22
 engineering method (for determining
 polarization bias), 215
 Enhanced Echo Tops, 175
 Enhanced Precipitation Preprocessor, 219
 Environment and Climate Change Canada, 251
 Environmental Winds Table, 92
 EPre, 219
 equivalence of range and elevation, 99
 ESAR, 268
 ESRL, 236
 ETVS, 198
 EUMETNET, 256
 European National Meteorological Services
 Network, 256
 exclusion zones, 219
 expanded search, 92

Experimental Warn-on-Forecast System for Ensembles, 281
 FAA, 16
 False Alarm Rate, 291
 FAR, 187, 195, 291
 Feature, 188, 192, 198
 feature tracking, 193
 feature type, 201
 Federal Aviation Administration, 12
 first-guess radial velocity, 48
 Fizeau, H. Louis, 8
 flat panel, 269
 Forward-S zero isodop, 103
 FPS-77, 11, 14
 freezing rain, 240
 frequency, 8, 28
 Frequency Bias, 291
 Fujita, 101
 FuMG 41/42 Mammot-1, 268

 Gate-to-Gate Shear, 196
 Gate-To-Gate Velocity Difference, 189
 General Electric Corporation Research Laboratory, 11
 geometric scattering, 30
 giant hail, 146
 GR2Analyst, 310
 grass level, 60
 graupel, 128
 Gridded VIL, 164
 Ground Clutter, 31, 60
 GTGVD, 189

 hail detection (dual-wavelength), 121
 Hail Detection Algorithm, 160
 hail identification (dual-polarization), 130
 Hail Kinetic Energy, 161
 Hail Signal (dual-wavelength), 122
 HCA, 224
 HCI, 41, 69
 HDA, 160
 Heavy rain, 138
 Hertz, Heinrich Rudolf, 8
 High-Resolution Rapid Refresh, 280
 High-Resolution VIL, 166
 hook echo, 186
 horizontal reflectivity, 127
 HRRR, 280
 Hülsmeier, Christian, 9
 Human Control Interface, 41, 69
 Hybrid Scan, 219
 hybrid target, 86
 Hydrometeor Classification Algorithm, 224
 Hydrometeorological Testbed, 236
 hydrometeors, 18

 Ideal Gas Law, 77
 imaginary number line, 141
 Incorrect hardware calibration, 214
 Index of Refraction, 25
 Integrated Data Viewer, 293
 isodop, 98

 K_{DP} , 134
 klystron transmitter tube, 10, 43

 LAN, 71
 laser ceilometer, 235
 Layer Composite Reflectivity Maximum, 173
 Legacy Z-R relationships, 208
 Level III products, 152
 LIDAR, 235
 Lightning Detection Network, 254
 Lincoln Laboratory, 247
 linear polarization, 32, 123
 linear reflectivity, 49
 Local Area Network, 71
 logarithmic reflectivity, 50
 logarithmic scale, 50
 Long-Range Digital Base Reflectivity, 250
 Lower Atmospheric Observing Facility, 242
 low-level V_{GTG} , 201
 low-level wind shear, 246
 LRM, 173

 magnetic field, 8, 23
 magnetic permeability of vacuum, 25
 magnetron transmitter tube, 43
 magnetron transmitter tube, 10
 main lobe, 45
 Marconi, Guglielmo, 9
 Marshall-Palmer relationship, 208
 Massachusetts Institute of Technology, 11
 Master System Control Function, 41, 69
 Maximum Expected Hail Size, 161
 Maximum Precipitation Rate Allowed, 220
 Maximum Unambiguous Range, 44
 Maximum Unambiguous Velocity, 58
 Maxwell, James Clerk, 8
 MCS, 160
 MDA, 187
 MDA Rapid Update, 195
 MEHS, 161

melting layer, 130
 Melting Layer Detection Algorithm, 225
 Melting layer identification, 130
 MESO, 193
 mesocyclone, 67, 193
 Mesocyclone Detection Algorithm, 187
 Mesocyclone Strength Index, 192
 mesoscale, 101
 Mesoscale Convective System, 160
 meso- α , 101
 meso- β , 101
 meso- γ , 101
 METAR, 145
 Météo France, 258
 METEOROLOGICAL Aerodrome Reports, 145
 microscale, 101
 microwave line-of-sight, 68
 micro- α , 101
 mid-level wind maxima, 106
 Mie scattering, 30
 Minimum Reflectivity Threshold, 153
 MIT, 11
 mixed precipitation, 215
 MLDA, 225
 MLOS, 68
 MPAR, 270
 MPE, 223
 MPRA, 220
 MRL-5M, 121
 MRU, 195
 MSCF, 69
 MSI, 192
 Multi-function Phased Array Radar, 270
 Multisensor Precipitation Estimator, 223

 narrow-band communications, 41, 70
 National Centers for Environmental Information, 13
 National Hurricane Center, 13
 National Lightning Detection Network, 274
 National Oceanic and Atmospheric Administration, 71
 National Science Foundation, 242
 National Severe Storms Laboratory, 187
 National Weather Radar Testbed, 270
 National Weather Service, 11
 Naval Research Laboratory, 9
 NCEI, 71
 NEWSe, 281
 NEXRAD, 15
 NEXRAD Imagery Dissemination System, 16
 NIDS, 16

 Nine-point average, 91
 NLDN, 274
 NOAA, 71
 NOAA Snow Level Radar, 236
 NOAAPort, 71
 non-meteorological echoes, 143
 notch width, 75
 NSSL, 187
 number density, 135
 NWRT, 270
 NWS, 16

 Odyssey, 256
 OHP, 220
 Oklahoma Lightning Mapping Array, 274
 OLMA, 274
 One Hour Precipitation, 220, 229, 251
 One Time Requests, 69
 OPERA Radar Data Centre, 256
 OPERA Weather Radar Network, 256
 Operational Program for Exchange of Weather Radar Information, 256
 Operational Support Facility, 214
 OSF, 214
 overlaid echoes, 84

 PAA, 220
 PAA2, 223
 PARISE, 277
 partial beam filling, 213
 PBL, 237
 PDF, 218
 peak transmitted power, 43
 PEC, 210
 period, 27
 phase angle, 27
 phase shift, 48, 55
 phased array, 43, 268
 Phased Array Radar Innovative Sensing Experiment, 277
 phasor diagrams, 55
 Physical Sciences Division, 236
 Plan Position Indicator, 13
 Planck's constant, 29
 Planetary Boundary Layer, 237
 POD, 163, 291
 POH, 160
 Polarimetric Echo Classification, 210
 polarization, 31, 122
 polarization diverse, 32
 POSH, 162
 power ratio, 87

Power-Amplifier-Transmitter, 43
 Power-Oscillator-Transmitter, 43
 power-weighted average, 58
 PPI, 13
 PPS, 216, 217
 PRA, 219
 Precipitation Accumulation Algorithm, 220
 Precipitation Adjustment Algorithm, 223
 precipitation category, 218
 Precipitation Detection Function, 218
 precipitation mode, 218
 Precipitation Processing System, 216, 217
 Precipitation Rate Algorithm, 219
 President's Science Advisory Committee, 268
 PRF, 44, 67
 Probability of Detection, 163
 Probability of Hail, 160
 Probability of Severe Hail, 162
 Probert-Jones Radar Equation, 30, 50
 Product Distribution Communications, 70
 Proportion Correct, 290
 PSD, 236
 Pulse Length, 45
 Pulse Repetition Frequency, 44
 Pulse-Pair Processing, 55
 pulse-to-pulse phase shift, 56

 QLCS, 275
 QPE, 216, 227
 Quantitative Precipitation Estimator, 216, 227
 Quasi-Linear Convective System, 275

 radar, 10
 RADAR, 9
 Radar Data Acquisition, 41
 Radar Echo Classifier, 219
 Radar Operations Center, 123
 Radar Products Generator, 41, 69
 Radar Wind Profilers, 235
 Radial continuity check, 91
 radial velocity, 16, 34, 54, 89
 RADio Detection And Ranging, 9
 RADio Direction And Ranging, 9
 Radio-Acoustic Sounding Systems, 235
 rainfall rate, 33, 52
 rainfall rate algorithms, 216
 rainfall rates during outages, 224
 rain-hail mix, 138
 Randall, John, 10
 range bin, 48
 range folding, 80
 Range Height Indicator, 168

 Range Unfolding Algorithm, 84
 Rapid-Scan DOW, 245
 RASS, 235
 Rayleigh scattering, 30
 Raytheon, 12
 RCS, 167
 RDA, 41, 42
 RDA maintenance terminal, 42, 43
 real number line, 141
 REC, 219
 receiver, 9, 42
 Receiver-Transmitter Module, 269
 redshifting, 35
 reference pulse, 56
 Reflection, 31
 reflectivity, 13, 48, 49, 50
 Reflectivity Cross-Section, 167
 reflectivity threshold, 218
 refraction, 30
 Regional Meteorological Data Communication
 Network, 258
 residual clutter, 75
 returned power, 11, 44, 51
 RHI, 168
 Right-Hand Rule, 57
 R_{max} , 44, 81
 RMSE, 183
 ROC, 215
 Root-Mean Square Error, 183
 Rosenfeld Z-R Relationship, 209
 rotation, 112
 Rotational velocity, 191
 Royal Meteorological Society, 10
 RPG, 41, 69
 RTM, 269
 RUA, 84
 RWP, 235

 SAILS, 46
 S-band, 12, 13, 28
 scattering, 29
 SCCS, 155
 SCIT, 152
 SCSS, 153
 SCTS, 157
 segment, 153
 separation of charge, 23
 Service Life Extension Program, 18
 Servicio Meteorológico Nacional, 234
 severe hail, 160
 Severe Hail Index, 161
 Shannon-Hartley Theorem, 68

Shear (in the MDA), 189
 Shear Segment, 188
 SHI, 161
 side lobes, 45
 signal processor, 42
 signal strength, 140
 signal-to-noise ratio, 60
 size parameter, 29
 Skill Score, 292
 SLEP, 18
 sloping wind maxima, 106
 SLR, 236
 SMN, 234
 Snell's Law, 30
 Snow Level Radar, 236
 SODAR, 235
 Sources of rainfall rate errors, 212
 Specific Differential Phase, 134
 spectrum width, 48, 59
 specular reflection, 31
 speed of light, 8, 24, 27, 28
 SPG, 247
 Sputnik 1, 268
 SPY-1A, 269
 SR, 189
 SRM, 178
 SS, 292
 Steamship Dorchester, 9
 Storm Position Forecast Subfunction, 158
 Storm Total Precipitation, 220, 229, 251
 Storm-Cell Centroid Subfunction, 155
 Storm-Cell Identification Table, 254
 Storm-Cell Information and Tracking, 152
 Storm-Cell Segment Subfunction, 153
 Storm-Cell Tracking Subfunction, 157
 Storm-Relative Mean Radial Velocity, 178
 storm-scale numerical weather prediction, 278
 STP, 220
 strength attributes, 201
 Strength Rank, 187, 189
 subrefraction, 78
 superrefraction, 77, 78
 Supplemental Adaptive Intra-Volume Low-Level Scan, 46
 Sym, 183
 Symmetry, 183
 synoptic scale, 101

 Taylor, Albert, 9
 TDA, 195
 TDA Rapid Update, 200
 TDWR, 18, 246

 TDWR Derived Products, 250
 TDWR Supplemental Product Generator, 247
 telemobiloscope, 9
 Terminal Doppler Weather Radar, 18, 246
 terminal fall speed, 52
 texture parameter, 210
 THP, 221
 Three Hour Precipitation, 221
 thunderstorm updrafts, 131
 tornadic debris, 147
 tornadic debris ball, 132
 Tornadic Vortex Signature, 198
 Tornado Detection Algorithm, 195
 Tornado Strength Index, 200
 transmitted power, 51
 transmitter, 9, 42, 43
 TRU, 200
 TSMS, 259
 Turkish State Meteorological Service, 259
 Turkish weather radar network, 259
 turntable, 44
 TVS, 198

 U.S. Air Force, 14
 U.S. Army Signal Corp, 12
 ULR, 174
 United States Navy, 12
 User Selectable Precipitation, 221
 User-Selectable Layer Reflectivity Maximum, 174
 USP, 221

 VAD, 92, 180
 VAD Slant Range, 181
 VAD Wind Profile, 92, 183
 Väisälä, 235
 Varian, Russell and Sigurd, 10
 VCP, 44, 46
 VCS, 178
 VDA, 90
 veering, 102
 velocity alias, 88, 90
 Velocity Azimuth Display, 92, 180
 velocity couplet, 92, 196
 Velocity Cross-Sections, 178
 Velocity dealiasing, 87
 Velocity Dealiasing Algorithm, 90
 Velocity Difference, 189
 velocity folding, 88
 vertical reflectivity, 127
 Vertically-Integrated Liquid, 164
 Very Small Aperture Terminal, 69

V_{GTG} , 197
 VIL, 156
 VIL Density, 166
 VILD, 166
 virga, 173, 216
 virtual potential temperature, 78
 V_{max} , 58
 Volume Control Pattern, 44, 45
 V_r , 16, 54
 VSAT, 69
 VWP, 92, 183

w , 59
 WAA, 100
 warm air advection, 100
 warm rain process, 140
 Warning Threshold, 162
 Warn-on-Forecast, 278
 WARP, 71
 Watson-Watt, Robert Alexander, 10
 wave analogy, 22
 wave guide, 43
 wave number, 27
 wavefront, 271
 wavelength, 27, 28
 Weather and Radar Processor, 71
 Weather Bureau, 11
 weather clutter, 11
 Weather Forecast Office, 42
 Weather Research and Forecasting, 280
 Weather Surveillance Radar – 1988 Doppler, 15
 Weather Surveillance Radar 1957, 13
 West Cool Season Z-R Relationship, 209
 Western Allies, 10
 wet microburst, 273
 wet radome, 214
 WFO, 42

WMO, 234
 WoF, 278
 World Meteorological Organization, 234
 WRF, 280
 WSR-1, 12
 WSR-1A, 12
 WSR-3, 12
 WSR-4, 12
 WSR-57, 12
 WSR-88D, 15
 WT, 162

X-band, 11, 28

Young, Leo, 9

Z_{DR} , 127
 zero isodop, 97
 zeroth alias, 57
 Z-estimate errors, 213
 Z_H , 127
 Z-R Relationship, 54
 Z-R Relationship errors, 215
 Z_V , 127

Δf_{dop} , 34
 $\Delta\phi$, 56
 ϵ_0 , 25
 ϕ , 27
 ϕ_{DP} , 134
 κ , 27
 λ , 27
 μ_0 , 25
 ρ_{HV} , 140
 ω , 27

About the Author



Sam Miller with the WSR-57 console on display at the 100th Annual Meeting of the American Meteorological Society in Boston, Massachusetts, January, 2020. (Photo by Eric Hoffman.)

Sam Miller began his career in meteorology as a weather observer in the U.S. Air Force (USAF) in 1982. In 1984 he attended the weather forecaster school at Chanute Air Force Base, Illinois, and graduated with honors. Between 1982 and 1989, he worked as a USAF weather observer in Maine, and as a forecaster in northern California, upstate New York, and at the joint US-Turkish airbase outside Adana, Turkiye. He eventually earned the rank of Technical Sergeant, and left the USAF in 1989 after more than ten years on active duty.

After leaving the USAF, Miller attended the University of New Hampshire and earned a Bachelor of Science in Physics (1996), a Master of Science in Earth Sciences: Oceanography (1999), and a Ph.D. in Earth Sciences (2003), while also working as a

weather observer in Portsmouth, New Hampshire, a research scientist at the university, and a teacher in New Hampshire's public university system.

From 2003 to 2005, Miller was a weather forecaster with the U.S. National Weather Service in Anchorage, Alaska. Since 2005, he has served as a professor of meteorology at Plymouth State University, in New Hampshire, where he teaches courses in introductory atmospheric science and climatology, meteorological analysis, atmospheric thermodynamics, instrumentation, weather forecasting, satellite meteorology, and radar meteorology.

In 2017, Miller became an American Meteorological Society (AMS) Certified Consulting Meteorologist, and now serves on the AMS's governing Board of Certified Consulting Meteorologists. In 2018, he earned a Master of Business Administration from Plymouth State University, in New Hampshire.

Miller is a member of Phi Beta Kappa, has published papers on the subjects of the sea breeze and the physics of water vapor, as well as a textbook titled Applied Thermodynamics for Meteorologists (available from Cambridge University Press), and has worked extensively as a meteorological consultant in legal matters.



Eric Hoffman (left) photographing Sam Miller (right) with the WSR-57 console (center) on display at the 100th Annual Meeting of the American Meteorological Society in Boston, Massachusetts, January, 2020. (Photo by Lourdes Aviles.)